Power Supply Design and Waveform Targeting for Dielectric Barrier Discharge Reactors

Henry O'Keeffe

A thesis submitted for the degree of Doctor of Philosophy

Department of Electronic and Electrical Engineering

The University of Sheffield

September 2024

Abstract

This thesis explores the development of efficient power supplies for high-efficacy dielectric barrier discharge (DBD) ozonisers, with a focus on designing and generating controllable waveforms to optimise ozone production.

One useful technology for building DBD power supplies is the piezoelectric transformer, a two-port electromechanical device similar to a magnetic transformer, that can be modelled with an electrical equivalent circuit. A global-optimiser-based method to determine the equivalent circuit parameters of piezoelectric transformers and resonators is developed to aid in power supply design. Three parameterisation methods are explored, including an improved cost function, refinement of parameters, and particle swarm optimisation (PSO). The research shows that these methods can more accurately extract the circuit parameters than those shown previous literature, aiding design and simulation of DBD reactor power supplies.

Piezoelectric resonators are one-port electromechanical devices which are high Q-factor resonators. A novel piezoelectric-resonator-based power supply for operation with low input voltage is also designed. A dielectric barrier discharge reactor is parameterised to determine its equivalent linear-model component values, which are used in conjunction with parameters from three different piezoelectric resonators to develop a new system model. This model is then used to design a novel power supply which uses only the piezoelectric resonator for voltage gain. This power supply is then tested in conjunction with the DBD reactor to validate its performance.

This thesis also explores how a biharmonic waveform can be used to change the frequency spectrum of the reactor input waveform to improve the efficacy of the reactor and overall system efficacy. A technique called selective harmonic generation (SHG) is presented to create a periodic pulse-train containing precisely controllable harmonics up to the switching frequency. Two experiments with DBD reactors are performed, one using a high-voltage magnetic transformer as the voltage gain device and the other using a piezoelectric transformer to validate this technique.

Finally, global optimisers using hardware in the loop tune the biharmonic input waveform parameters and flowrate of the input gas to improve the efficacy of ozone production in a DBD reactor. A novel hardware-in-the-loop system is developed to explore the effects of varying these parameters on reactor conditions.

The main contribution of this work comes from the development of a new biharmonic tailored waveform technique which is shown to improve ozone generation. A second contribution includes the novel piezoelectric resonator-based power supply that has many applications beyond chemical reactors. Other contributions include the piezoelectric and reactor modelling which have applications beyond ozonisers.

Contents

Table of Figures

Table of Tables

Nomenclature

Abbreviations

Abbreviation	Description
AC	Alternating current
ASCII	American standard code for information interchange
AWG	Arbitrary waveform generation
CHBMLC	Cascaded H-bridge multilevel converter
CO	Carbon monoxide
CO_2	Carbon dioxide
DBD	Dielectric barrier discharge
DC	Direct current
ELV	Extra low voltage
EMI	Electromagnetic interference
FFS	Fundamental frequency switching
GaN	Gallium nitride
H_2O	Dihydrogen monoxide
HIL	Hardware-in-the-loop
HV	High voltage
IGBT	Insulated-gate bipolar transistor
LCS	Low current switching
MOSFET	Metal-oxide-semiconductor field-effect transistor
NH_3	Ammonia
NOx	Nitrogen oxides
PEEK	Polyether ether ketone
PR	Piezoelectric resonator
PS	Pattern search
PSFB	Phase-shifted full bridge
PSO	Particle swarm optimisation
PSU	Power supply unit
PT	Piezoelectric transformer
PWM	Pulse-width modulation
PZT	Lead zirconate titanate

RMS	Root-mean-squared
SHG	Selective harmonic generation
Sw	Switch (MOSFET)
THD	Total harmonic distortion
UART	Universal asynchronous receive / transmit
USB	Universal serial bus
UV	Ultraviolet
ZVS	Zero voltage switching

Symbols

Symbol	Description	Units
a	A number representing one pulse	-
A_0	DC component of the waveform used in SHG	V
A_n	Imaginary part of the harmonic amplitude	V
B_n	Real part of the harmonic amplitude	V
C	RLC-branch capacitance for a PT or PR equivalent circuit model	nF
$c_{1\text{-}4}$	Constants used to fit models of the DBD reactor	*Various*
C_A	Additional capacitance added to the DBD reactor in the PR-based PSU	nF
C_D	Capacitance in the linearised DBD model	pF
C_o	Output capacitance for a PT or PR equivalent circuit model	pF
C_P	Input capacitance for a PT or PR equivalent circuit model	nF
C_R	DBD reactor capacitance measured at a voltage below the ignition threshold	pF
C_S	Current sense capacitance	pF
d	A number representing a datapoint used in fitting models	-
$E_{\%}$	Average magnitude of the error ratio used in fitting PR and PT models	
E_{abs}	Average absolute error used in fitting PR and PT models	Ω
E_{MS}	Mean square error used in fitting DBD reactor models	-
f	Fundamental frequency	kHz
F_A	Flowrate of air feedstock	ℓpm
F_d	Calculated data for fitting a model	*Various*
f_{sw}	Switching frequency	Hz
$\boldsymbol{G}$	Vector of Fourier series equations to solve	
H_n	Amplitude of the nth harmonic in a harmonic controlled waveform	V
I_{CD}	Reactive part of the current flowing into the linearised DBD model	A
I_I	Instantaneous inverter output current	A
I_R	Reactor current	A
I_W	Current flowing through R	A
j	Imaginary unit, the square root of minus one	-
K	Number of modelled resonant modes for a PT or PR	-

k	A number representing the resonant mode of a PT or PR	-
K_c	Transformer coupling factor	-
L	RLC-branch inductance for a PT or PR equivalent circuit model	mH
L_P	Parasitic inductance in the experimental setup for the PR-based PSU	μH
m	A number representing one Newton iteration	-
M_d	Measured data for use in fitting a model	*Various*
M_m	Mean of measured data used in fitting a model	*Various*
N	Turns ratio in the PT equivalent circuit model	-
n	A number representing one harmonic	-
N_D	Number of data points used in fitting the models of the DBD reactor	-
N_p	Number of pulses per cycle in a pulse-train	-
P_I	PT input power	W
P_R	DBD reactor power	W
P_W	Power dissipated in the PR	W
Q_{RLC}	RLC-branch quality factor for a PT or PR equivalent circuit model	-
R	RLC-branch resistance for a PT or PR equivalent circuit model	Ω
R^2	Coefficient of determination	-
R_D	Resistance in the linearised DBD reactor model	kΩ
R_G	Variable resistance in the conventional DBD reactor model	kΩ
R_S	Current sense resistor resistance	Ω
S	The waveform used in SHG	V
s	The complex variable equal to $2\pi jf$	Radians/s
T	Total time for measured data	s
V_{CS}	Current sense capacitor voltage	kV
V_{DC}	DC bus voltage	V
V_I	Instantaneous inverter output voltage	V
V_{In}	nth harmonic component of the RMS inverter output voltage	V
V_{Irms}	RMS inverter output voltage considering only controlled harmonics	V
V_R	Instantaneous DBD reactor voltage	kV
V_{Rn}	nth harmonic component of the RMS reactor voltage	V
V_{Rrms}	RMS DBD reactor voltage	V
V_{RS}	Current sense resistor voltage	V

$Z_{in(s\text{-}c)}$	Calculated input impedance of a PT (output short circuited) or PR	Ω
$Z_{in(s\text{-}c)M}$	Measured input impedance of a PT (output short circuited) or PR	Ω
$Z_{out(s\text{-}c)}$	Calculated output impedance of a PT (input short circuited) or PR	Ω
$Z_{out(s\text{-}c)M}$	Measured output impedance of a PT (input short circuited) or PR	Ω
β	Impedance of a PT or PR RLC branch	Ω
γ	Fourier series contribution of a pulse on the imaginary axis	V
ΔV	Change in voltage	V
η_c	Concentration efficacy	ppm/W
η_r	Quantitative efficacy of only the reactor	g/kWh
η_s	Quantitative efficacy of the system	g/kWh
θ	Phase angle	Radians
λ	Fourier series contribution of a pulse on the real axis	V
ϕ_{Ea}	End of pulse *a*	Radians
$\boldsymbol{\phi}_m$	Vector of switching angles	Radians
ϕ_{Sa}	Start of pulse *a*	Radians
ψ_n	Phase of the *n*th harmonic	Radians
ω_0	Resonant frequency	Radians/s
ω_B	Bandwidth	Radians/s

1 Introduction

This thesis explores the engineering of power supplies for dielectric barrier discharge (DBD) reactors, with a focus on tailoring waveforms to optimise DBD reactor efficiency. These reactors are used for many applications but in this thesis DBD reactors are used for the generation of ozone (O_3).

Ozone (O_3) is a reactive chemical species of oxygen formed from three oxygen atoms [1.1] shown in Fig. 1.1. Ozone breaks down to form short-lived oxygen radicals which readily combine with organic compounds, altering their composition. This has led to applications in toxic-gas treatment [1.2], medicine [1.1], water sterilisation and filtration [1.2], [1.3], and many others where ozone's ability to destroy organic compounds can be utilised [1.2]. Ozone is currently most efficiently produced in a dielectric barrier discharge (DBD) reactor [1.4].

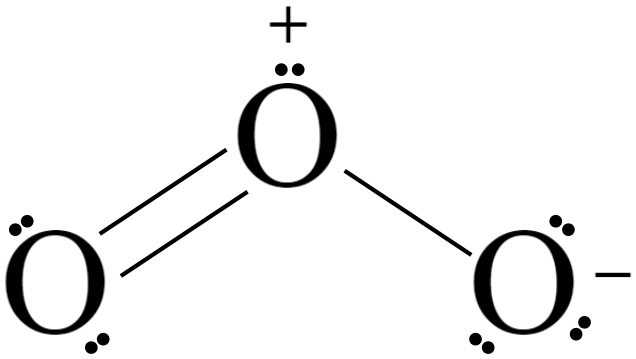

Fig. 1.1 Lewis structure for ozone (made by author)

DBD reactors used for ozone generation (ozonisers) vary in size from benchtop devices for laboratory use or applications like sterilising surfaces generating 10 g of ozone per hour (g/hr), through to room-sized units that can produce 250 kg/hr for water treatment on a large scale [1.5].

A DBD ozoniser uses high-voltage, usually sinusoidal, alternating current provided by some type of power supply creating a non-thermal plasma (Fig. 1.2) to break down the oxygen molecules in a dry air or oxygen enriched feedstock. This monatomic oxygen then reforms into O_3. The dry or oxygen-enriched air can be made relatively inexpensively from the atmosphere using refrigeration-cycle air driers or pressure-swing-adsorption based oxygen concentrators. For reactors that use air as a feedstock, the majority of the value of the ozone produced comes from the electricity required to make it [1.6]. This makes both the high efficiency of the power supply and high efficacy (grammes of ozone produced per kilowatt-

hour of electrical energy, g/kWh) of the reactor itself critical in reducing the cost of the ozone produced.

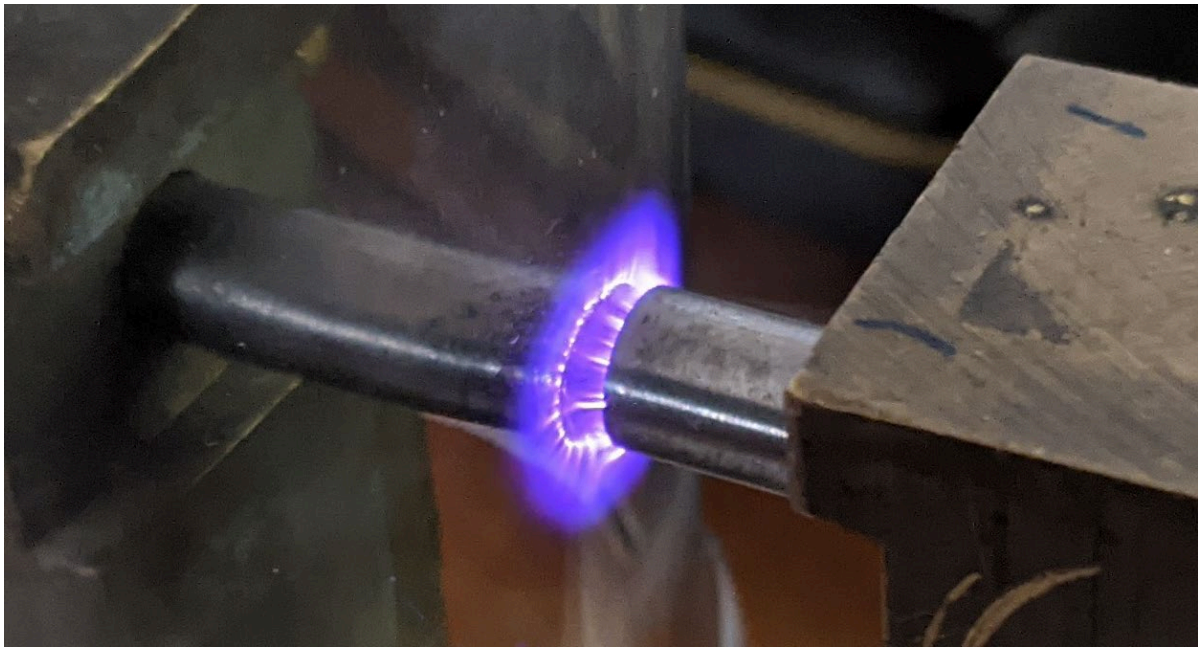

Fig. 1.2 Photograph of DBD plasma in air (photograph by author)

1.1 Aims and Thesis Outline

This work aims to improve the system efficacy of small-scale DBD ozonisers by developing new power supply topologies, investigating the effects of different waveforms on the efficacy of DBD reactors and the techniques used to generate these waveforms.

Work towards these aims is split up into four main technical chapters. The topics they cover are illustrated in Fig. 1.3. Chapter 4 covers an improved method of modelling piezoelectric devices, which are often used to step up voltages in DBD power supplies [1.7], [1.8]. This work is used in Chapter 5, where it allows an accurate model of a piezoelectric resonator and a DBD reactor to be used to design, build and validate a novel DBD power supply.

Chapter 6 presents a method of generating pulse-trains with precisely controllable harmonic content up to and including the switching frequency. This technique, selective harmonic generation (SHG) is used to provide biharmonic waveforms with several controllable characteristics to DBD reactors via a conventional transformer and a piezoelectric transformer in different experiments, where the efficiency of the power supply and the effect of the waveforms on the efficacy of the reactor are validated.

Chapter 7 explores the use of a global optimiser to find the most efficacious sets of biharmonic waveform parameters for DBD reactors, helping maximise the benefits of the controllable waveforms presented in Chapter 6.

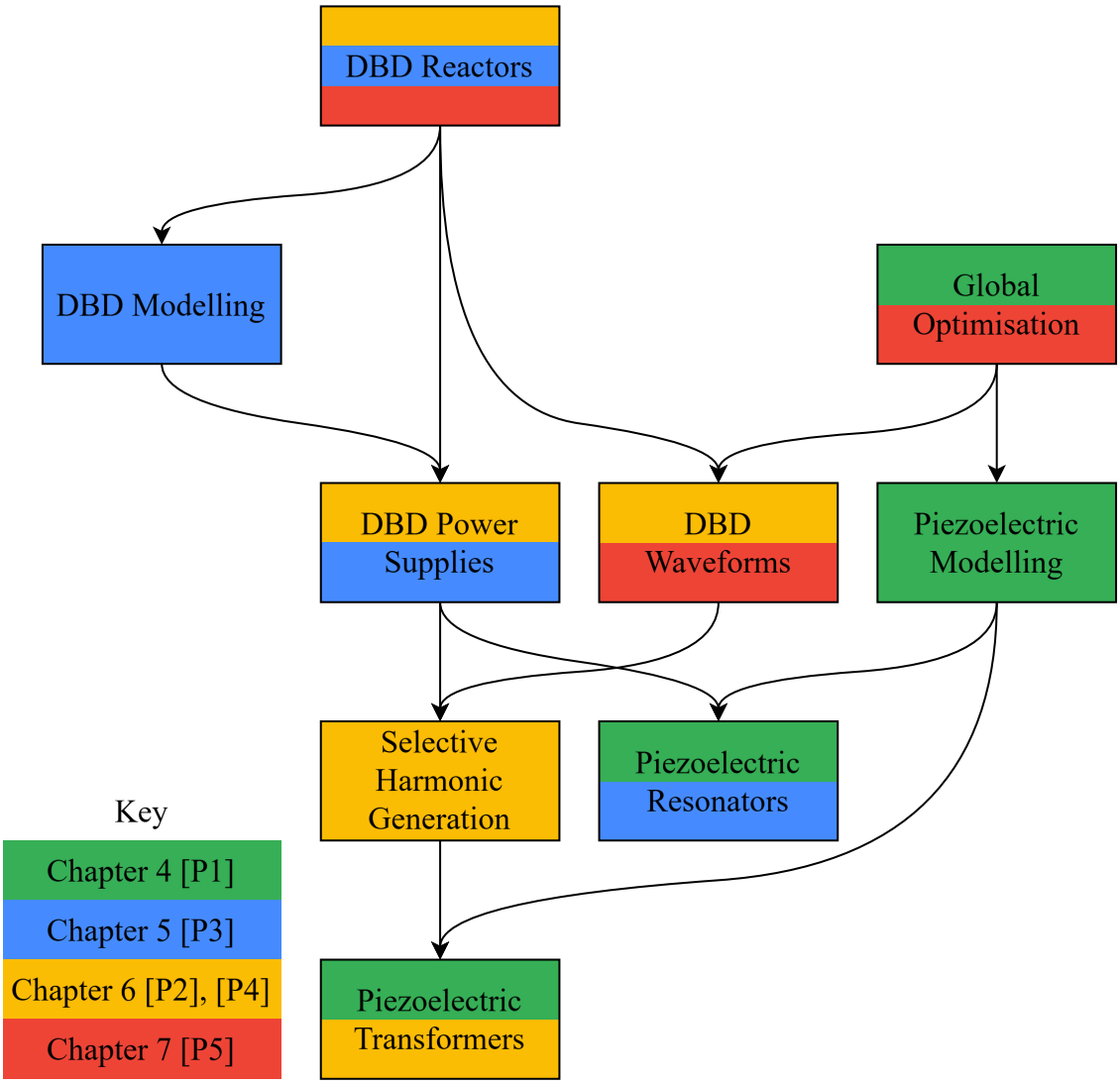

Fig. 1.3 Thesis topic breakdown. Publications in the key are found in Section 1.2.

Supporting these main chapters are the introduction in Chapter 1; a literature review in Chapter 2; a description of the experimental equipment, including the reactors used and developed for this work in Chapter 3 and a conclusion in Chapter 8.

1.2 Publications

1.2.1 Published

[P1] **Henry O'Keeffe**, Martin P. Foster, and Jonathan N. Davidson, 'Parameterisation methods for piezoelectric transformer equivalent circuit models', in *11th International*

Conference on Power Electronics, Machines and Drives (PEMD 2022), Newcastle, UK: IET Digital Library, 2022, pp. 764–768. DOI: 10.1049/icp.2022.1152

[P2] **Henry O'Keeffe**, Martin P. Foster, and Jonathan N. Davidson, 'Selective harmonic generation for dielectric barrier discharge reactors', in *13th International Conference on Power Electronics, Machines and Drives (PEMD 2024)*, Nottingham, UK: IET Digital Library, Jun. 2024, p. 576, DOI: 10.1049/icp.2024.2210

[P5] **Henry O'Keeffe**, Fahad J Rehman, Thomas D Holmes, Jonathan N Davidson, Martin P Foster, and William B.J. Zimmerman, 'Targeted-Waveform Optimisation for Ozonising Dielectric Barrier Discharge Reactors', *Ozone: Science & Engineering*, pp. 1–9, Jan. 2025, DOI: 10.1080/01919512.2025.2453579.

1.2.2 Under Review

[P3] **Henry O'Keeffe**, Martin P. Foster, and Jonathan N. Davidson, 'Piezoelectric Resonator Based Power Supply for an Ozone-Generating Dielectric Barrier Discharge Reactor', submitted to *IEEE Transactions on Plasma Science*

1.2.3 Awaiting Submission

[P4] **Henry O'Keeffe**, Martin P. Foster, and Jonathan N. Davidson, 'Selective Harmonic Generation for a Piezoelectric-Transformer-Based Dielectric Barrier Discharge Power Supply'

1.3 Contribution

The novel contributions of this research are:

- Three improved parameterisation techniques for piezoelectric devices are presented in Chapter 4 and [P1], allowing more accurate parameters to be determined and used to design novel DBD reactor power supplies.
- An efficient, compact new DBD reactor power supply design is developed in Chapter 5 [P3]. This design is based on piezoelectric resonators and uses the parameterisation techniques developed in Chapter 4.
- Two further DBD reactor power supplies are developed in Chapter 6 [P2], [P4], one using magnetic transformers and the other using a piezoelectric transformer. These power supplies use selective harmonic generation to tailor the waveshape, allowing the efficacy of the reactor to be explored and optimised with a large number of controllable input parameters.

- A hybrid hardware-in-the-loop global optimiser approach is presented in Chapter 7 [P5]. Biharmonic waveform parameters are optimised to maximise DBD reactor efficacy. This optimiser integrates particle swarm optimisation and pattern search for improved parameter selection.

These developments contribute significantly towards the efficient production of ozone with potential applications in water treatment, surface disinfection, healthcare, and environmental remediation, helping to reduce energy consumption costs associated with both small and large-scale DBD reactor operation.

1.4 References

[1.1] S. Maftuhah, A. Rahardian, M. Masfufah, E. Yulianto, S. Sumariyah, and M. Nur, 'Experimental Study on Medical Ozone Generation in Double Dielectric Barrier Discharge (DDBD) with Spiral-Spiral Electrodes', in *Proceedings of 2nd International Conference on Chemical Process and Product Engineering*, Semarang, Indonesia, 2019.

[1.2] U. Kogelschatz, 'Dielectric-barrier Discharges: Their History, Discharge Physics, and Industrial Applications', *Plasma Chemistry and Plasma Processing*, vol. 23, no. 1, pp. 1–46, 2003.

[1.3] A. Hafeez, N. Shezad, F. Javed, T. Fazal, M. S. Rehman, and F. Rehman, 'Developing multiplexed plasma micro-reactor for ozone intensification and wastewater treatment', *Chemical Engineering and Processing - Process Intensification*, vol. 162, p. 108337, 2021.

[1.4] K. Nassour, M. Brahami, S. Nemmich, N. Hammadi, N. Zouzou, and A. Tilmatine, 'Comparative Experimental Study between Surface and Volume DBD Ozone Generator', *Ozone: Science & Engineering*, vol. 38, no. 1, pp. 70–76, 2016.

[1.5] Veolia, 'Ozonia* Range Ozone Systems'. Accessed: Sep. 03, 2024. [Online]. Available: https://estore.watertechnologies.com/document/document/contentdownload/?document_name=SZ20017_EN.pdf

[1.6] A. Ried, J. Mielcke, and A. Wieland, 'The Potential Use of Ozone in Municipal Wastewater', *Ozone: Science & Engineering*, vol. 31, no. 6, pp. 415–421, Nov. 2009, doi: 10.1080/01919510903199111.

[1.7] Z. Salam, M. Facta, and M. Amjad, 'Design and implementation of a highly efficient DBD ozonizer using the single switch resonant converter with piezoelectric transformer', in *2013 Twenty-Eighth Annual IEEE Applied Power Electronics Conference and Exposition (APEC)*, Mar. 2013, pp. 1596–1600. doi: 10.1109/APEC.2013.6520510.

[1.8] K. Teranishi, N. Shimomura, S. Suzuki, and H. Itoh, 'Development of dielectric barrier discharge-type ozone generator constructed with piezoelectric transformers: effect of dielectric electrode materials on ozone generation', *Plasma sources science & technology*, vol. 18, no. 4, pp. 045011-045011 (10), 2009, doi: 10.1088/0963-0252/18/4/045011.

2 Literature Review

2.1 Introduction

This chapter explains the background to this work and consists of a review of the literature across the topics explored in this thesis. A diagram of the topics covered in this literature review and how they relate to one another is shown in Fig. 2.1.

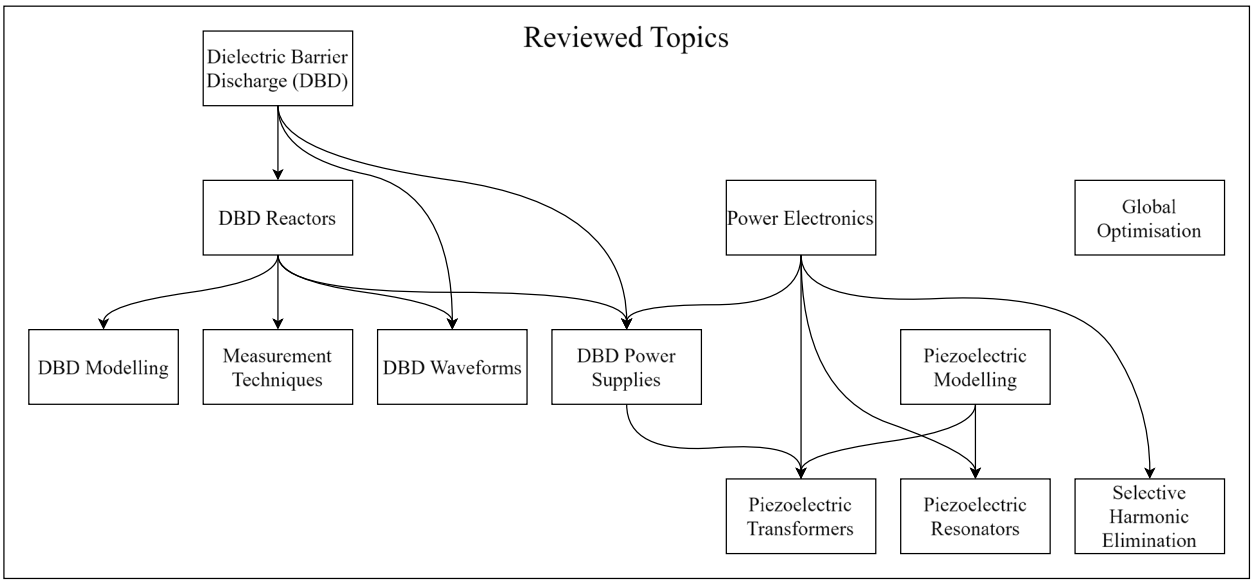

Fig. 2.1 An overview of reviewed topics

2.2 Plasma and Dielectric Barrier Discharge

An arc discharge is formed between two conductive electrodes when the voltage (AC or DC) is sufficiently high to cause dielectric breakdown of the gas in the gap between them. This discharge has a nonlinear resistance with a negative trend [2.1], causing a high current to flow through the gap, limited only be the impedance of the voltage source and the low impedance of the plasma. The large power dissipated further heats the plasma and lowers its impedance [2.2], resulting in runaway heating. This effect would cause destruction of parts and equipment in the vicinity of the high-temperature plasma in a reactor, although in some applications it is intended.

There are many applications for arc discharge; for example, welding and cutting metals, fusing optical fibre, and fire ignition. High-temperature plasma has been used for producing chemicals, for example nitric acid in the Birkeland-Eyde process [2.3], but the ability to

control the products formed in such a plasma is limited, and some products, such as ozone, will be broken down after formation by the high-temperature [2.4].

A different type of plasma discharge, dielectric barrier discharge (DBD), was discovered in 1857 by Siemens [2.5] according to one of the most prolific contributors to the field of DBD plasmas, Kogelschatz, in [2.6]. This kind of electrical discharge requires that there are one or more dielectric layers between the electrodes, in addition to the gap. A high voltage (HV) bipolar waveform is applied to the electrodes (Fig. 2.2), causing a small current to flow through the reactor due to its capacitance. A charge builds up on the surface of the dielectric until the potential difference across the gap adjacent to the charge carrier exceeds the breakdown voltage of the gas in the gap, causing localised discharge called streamers or plasma filaments through the gas. Each filament exists for tens of nanoseconds [2.7], but usually at least one filament is generated per electrical cycle.

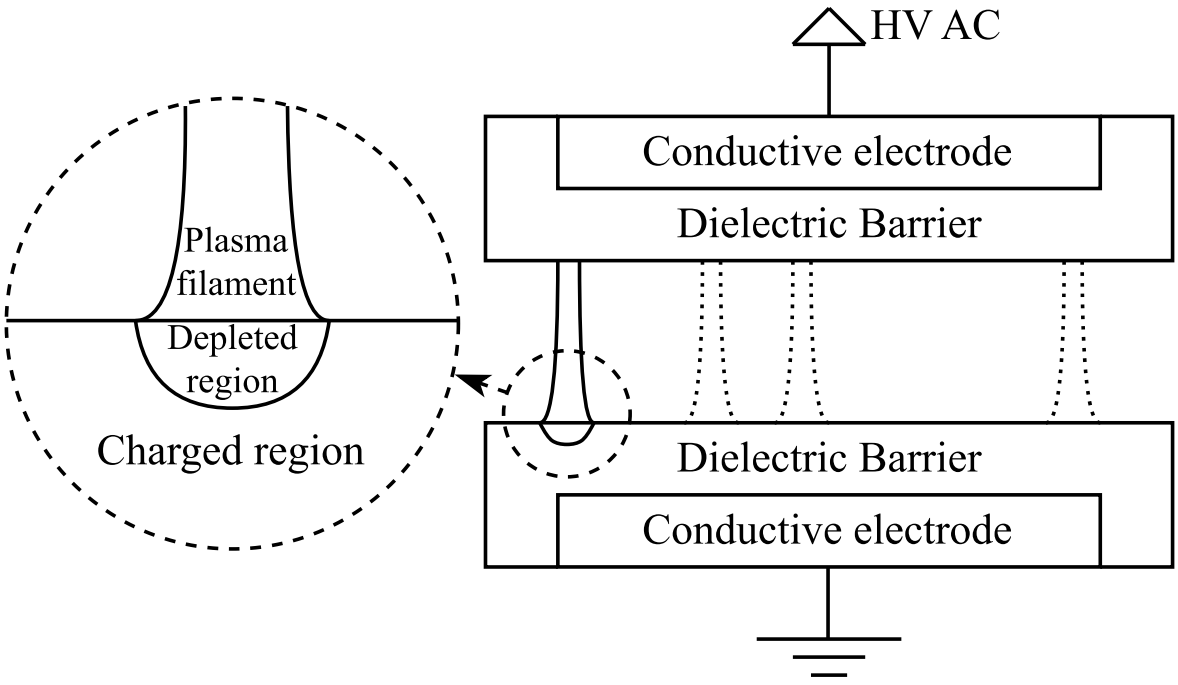

Fig. 2.2 An example of a simple DBD set-up (made by author)

In Fig. 2.3, current and voltage waveforms for weak DBD plasma can be seen in the upper plot, where there are approximately four plasma filaments per cycle, seen on the reactor current waveform. A strong DBD plasma is shown in the lower plot, where there are many more plasma filaments per cycle.

This discharge reduces the charge on the dielectric to the point the voltage across the gap can no longer support further discharge. The current flowing though the largely capacitive reactor

causes charge to build up again until another discharge occurs. Compared to arc discharge, this cycle of charge and discharge limits the energy supplied to the gas and the resultant plasma. This type of plasma is known as non-thermal, or cold plasma and is favourable for ozone generation [2.8], as it prevents high temperature from prematurely breaking down any ozone formed [2.4].

Specific applications for this type of plasma include the sterilisation of equipment [2.9], anti-microbial food treatment [2.10], in the catalysis of reactions in chemical engineering [2.11] and for producing chemicals like ozone from a feed gas in a DBD reactor.

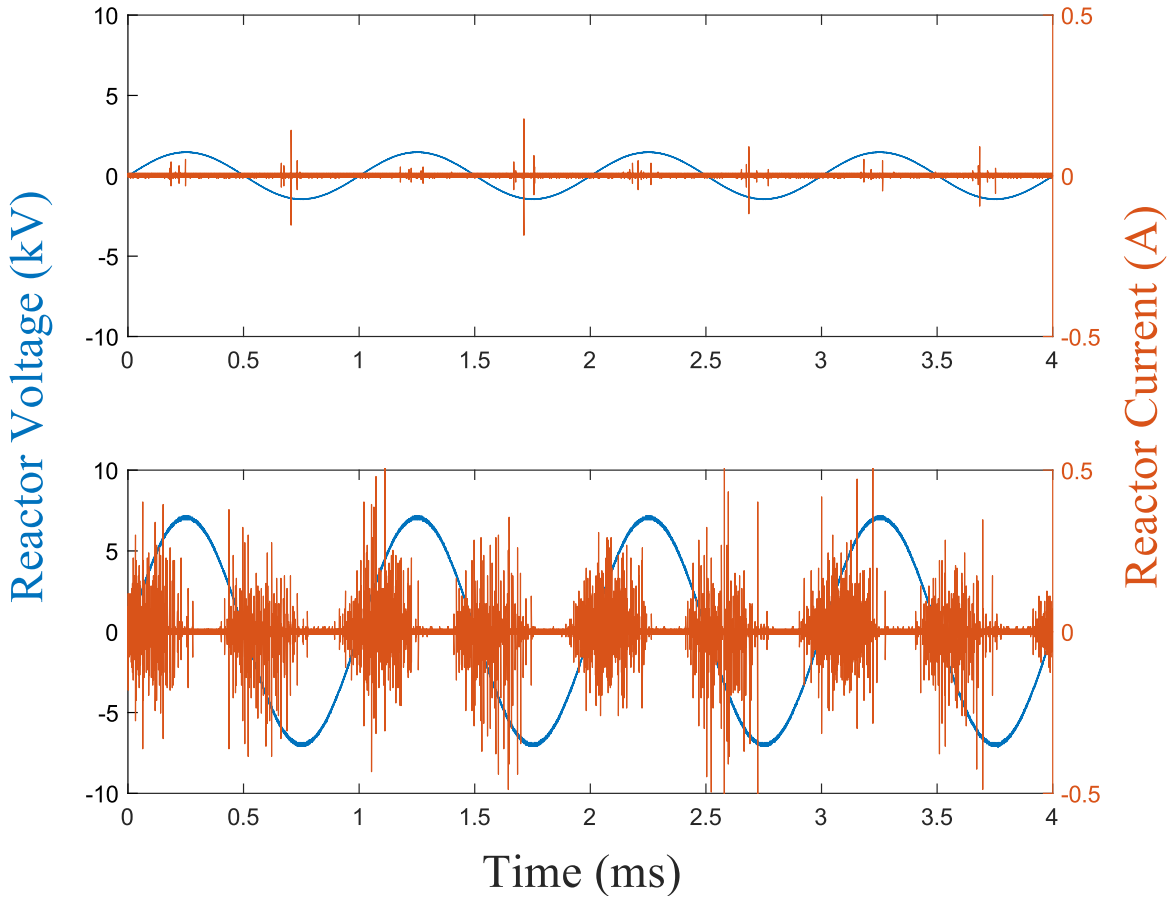

Fig. 2.3 Experimental DBD current and voltage waveforms: upper a weak plasma and lower a strong plasma (data and figure by author)

2.3 DBD Reactors

DBD reactors are used in myriad applications, including efficient generation of ozone with oxygen or air as the feedstock [2.9], the destruction of unwanted chemicals [2.12] or biological materials [2.13] and the production of high-value chemicals. In some reactors this is done directly, for example ozone is often produced from air or oxygen using just the

reactor, whilst other reactors may use an intermediate gas to carry energetic chemical species to another chemical where further reactions occur.

DBD reactors use DBD to produce reactive chemical species, which can recombine to form new chemicals. The main (and first) application of this is in the generation of ozone [2.14], where these reactors are more efficient than other techniques such as oxygen photolysis by ultra-violet radiation [2.8]. Other researchers have explored the production of other chemicals by DBD, for example nitrous oxide in [2.15].

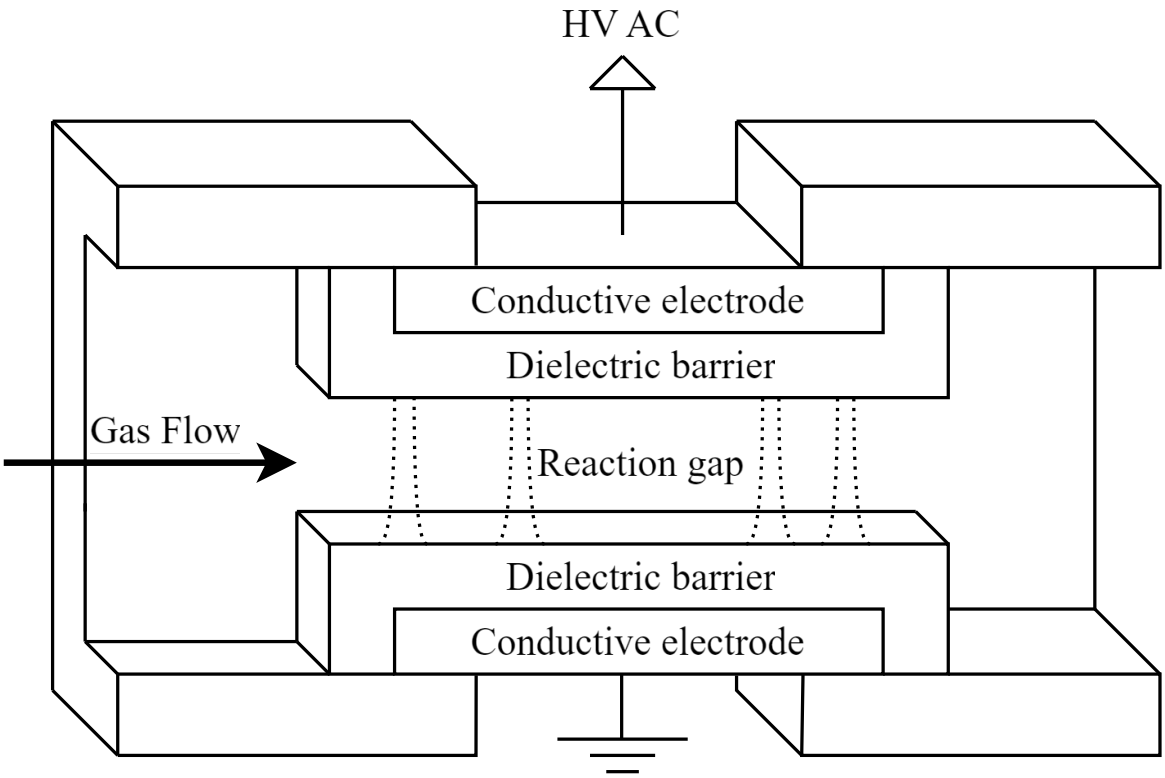

Fig. 2.4 Cut-away diagram of a simple DBD reactor (made by author)

The structure of a DBD reactor (Fig. 2.4) usually consists of a pair of electrodes with one or more insulating layers between them, with at least one of the layers being a dielectric (e.g., glass, quartz or ceramic) and one of the electrodes exposed to gas (air or oxygen for ozone generation). A structure around the electrodes allows the gas into the reactor, where it passes over or across the electrodes in the reaction gap, before exiting the reactor.

A reactor can either be symmetrical (electrodes of the same type) or asymmetrical (electrodes of differing types e.g. one conductive, and one with a dielectric coating). Fig. 2.4 shows a symmetrical reactor, and Fig. 2.5 shows an example of a symmetrical DBD plasma. One plasma filament extends between the two electrodes.

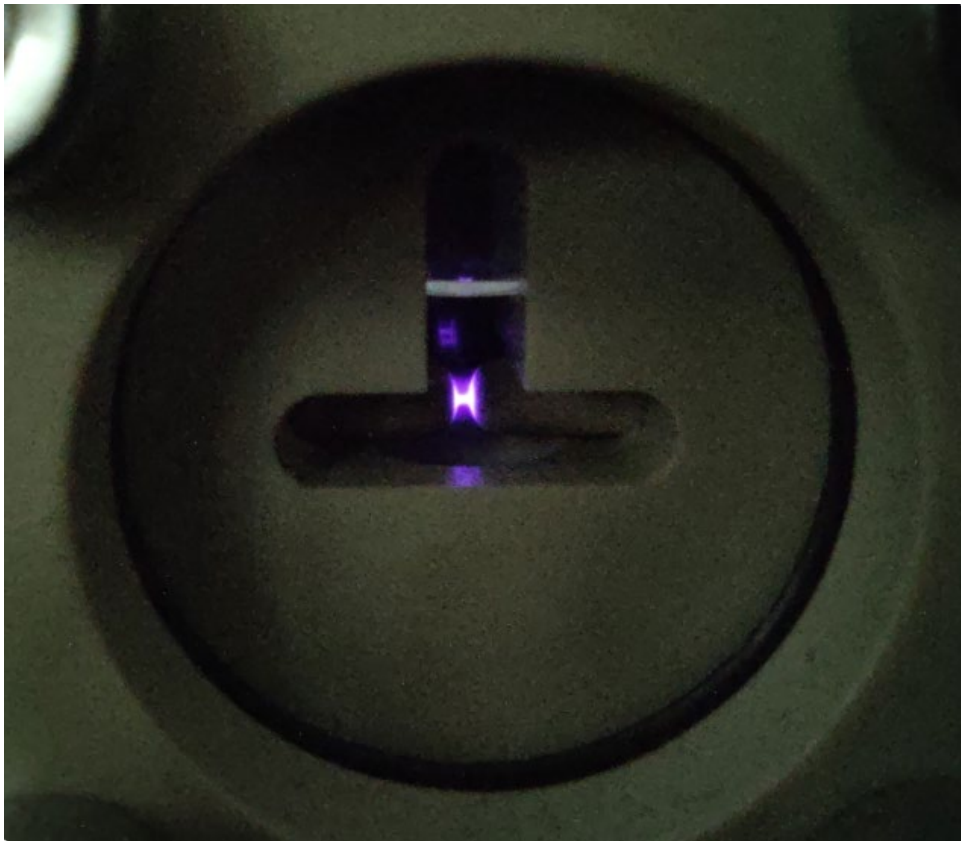

Fig. 2.5 Photograph of a symmetrical, air, DBD plasma in a DBD reactor (by author)

The electrical input to a DBD reactor must have sufficient voltage to cause breakdown of the gas in the gap, i.e. it must be greater than the ignition voltage, and is usually bipolar to allow current flow to reset the charge on the dielectric. The input voltage and frequency of DBD reactors vary over a wide range depending on design requirements. The parameters of some examples from literature are shown in Table 2.1, showing that peak operating voltages range from 700 V to 6 kV, frequency ranges from 5 kHz to 57.5 kHz over power ranges of 0.15 W to 240 W.

Table 2.1 DBD ozoniser parameters from literature

Ref	Voltage (kVpk)	Frequency (kHz)	Power (W)	PSU efficiency (%)	Ozoniser efficacy (g/kWh)
[2.8]	3–6	25	12–53*	-	-
[2.16]	2.3–4.3	19	32–1015	≤ 81	-
[2.17]	2.4–3	26.3	0.3–3	-	≤ 140 (air) ≤ 223 (O_2)
[2.18]	0.8–1.25	53.4	1.4–4	90	≤ 3.4 (O_2)
[2.19]	5	5*	0.15–1	-	≤ 206 (air) ≤ 414 (O_2)
[2.20]	3.44	45–57.5	9.2–40.4	30–85	4.5–21
[2.21]	0.7	15.6	1	50	6 (O_2)

* Subject to caveat explained in the reference

Several metrics are used for measuring the efficacy (effectiveness) of ozone generation. The most common is a ratio of a quantity of ozone generated and the energy used to produce the ozone, e.g. g/kWh, [2.12], [2.17], [2.22] usually measured at the input of the reactor. In this work, η_r and η_s are used to represent this metric, for quantitative efficacy only considering the reactor, and considering the whole system respectively. Another useful metric is the ratio of the ozone concentration to power which is measured in units of ppm/W [2.23] and is represented by the symbol η_c. Usually η_c is used when the flowrate is kept constant and is therefore proportional to η_r, as in [2.24]. If a reaction is limited by the concentration of ozone, for example by a gas/liquid interface area that is independent of flowrate, η_c might be more useful than η_r, regardless of flowrate.

2.3.1 Reactor Power Measurement

Two main methods of measuring DBD reactor power used in literature are the Lissajous technique and the Pearson technique [2.19], [2.25], [2.26].

The Lissajous technique uses the voltage across the current sense capacitor, V_{CS} and the reactor input voltage V_R and equation (2.1) to determine reactor power.

$$P_R = \frac{C_S}{T}\int_{t=0}^{T} V_R(t)\, dV_{CS}(t) = \frac{C_S}{T}\int_{t=0}^{T} V_R \frac{dV_{Cs}}{dt} dt \tag{2.1}$$

This method is based on integrating the area enclosed by the Lissajous figure (Fig. 2.6) made using the voltage (V_{CS}) across a current sense capacitor (C_S) and the reactor voltage (V_R). T is the length of time over which the data is recorded. An example experimental setup diagram for measuring reactor power is shown in Fig. 2.7.

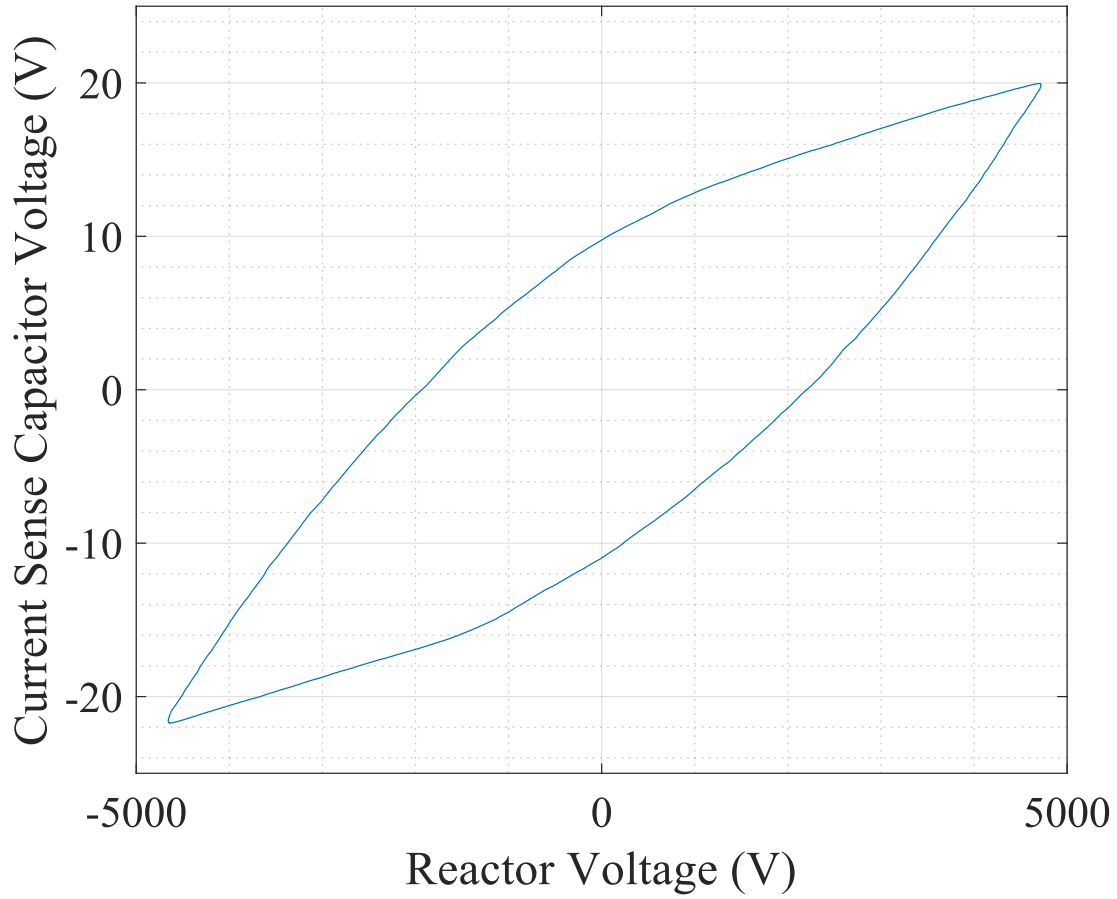

Fig. 2.6 An experimental Lissajous figure of a DBD reactor in operation found using the average over many cycles (by author)

The Pearson technique involves measuring the reactor current, I_R, directly using a current transformer (commonly manufactured by Pearson), then calculating the average power using

$$P_R = \frac{1}{T}\int_{t=0}^{T} V_R I_R dt \tag{2.2}$$

In [2.19], the Pearson technique is shown to be less accurate than the Lissajous technique due to the limited bandwidth of a current transformer when compared to the ability of a high-quality capacitor to accumulate charge from discharges with a significant high-frequency spectral component.

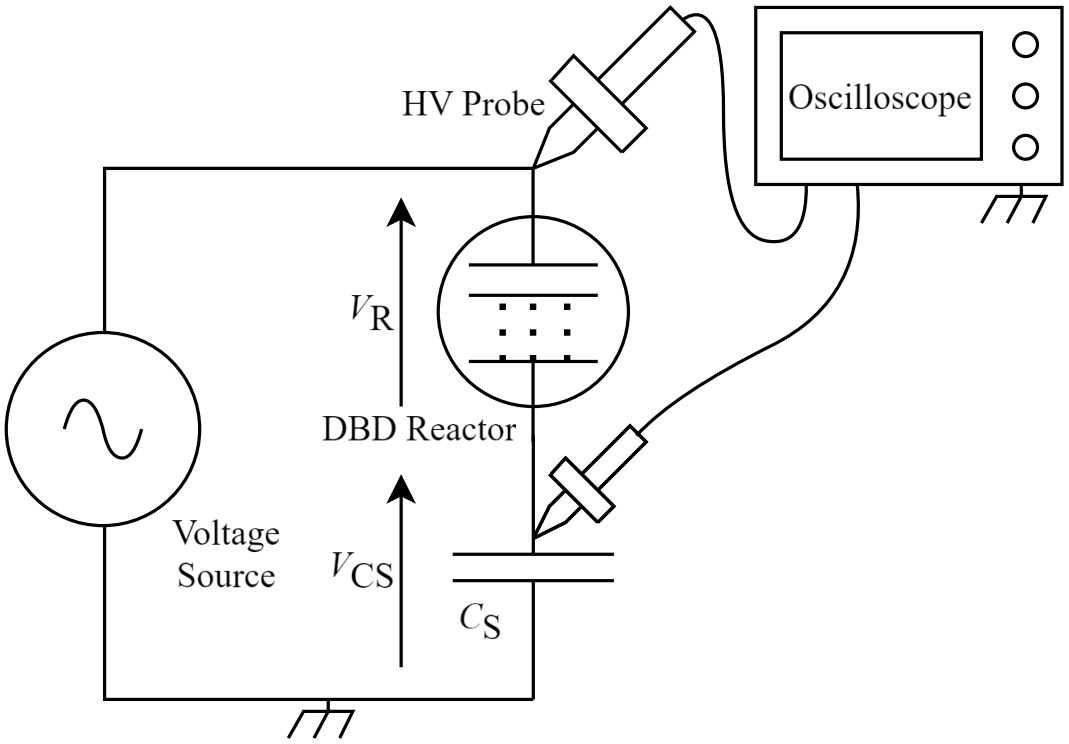

Fig. 2.7 An example DBD reactor power measurement test setup (diagram made by author)

2.3.2 DBD Reactor Modelling

DBD reactors are commonly modelled electrically as a pair of series capacitors with a variable resistance connected in parallel with one of the capacitors [2.27], [2.28], [2.26], as shown in Fig. 2.8a. Over the course of an electrical cycle, the resistance, R_G, is varied, simulating the ignition of the plasma and its varying intensity.

In the simplest non-linear model, R_G is changed continuously over the electrical cycle, representing the bulk charge transfer by the many individual plasma filaments [2.29]. More complex models simulate each individual discharge to allow for greater accuracy [2.26].

In [2.22], Alonso, et al. introduced a simplified the model of the DBD reactor, the parallel RC network shown in Fig. 2.8b, allowing it to be used in linear systems, at the cost of a reduced accuracy (e.g. high-frequency current fluctuations from discharge cannot be modelled). In addition, a reactor with an input voltage lower than the ignition voltage can be modelled as purely capacitive [2.30].

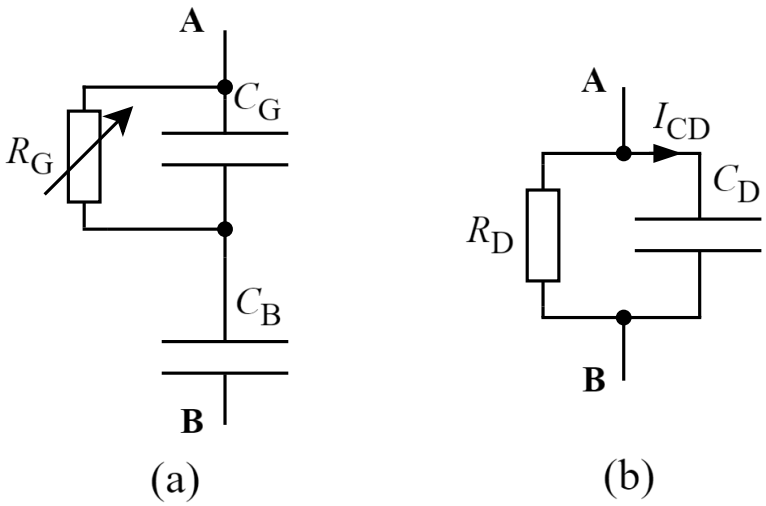

Fig. 2.8 (a) Conventional DBD reactor model and (b) linearised, high-frequency DBD reactor model (diagram made by author)

The high-frequency linear model can be parameterised using the input power to the reactor. Measurements of the power using the Lissajous method (Section 2.3.1), for example, correspond to the power dissipated in R_D therefore

$$R_D = \frac{V_R^2}{P_R} \tag{2.3}$$

where V_R is the RMS voltage applied to the reactor and P_R is the measured input power to the reactor. The capacitance, C_D, can be found from the reactive part of the input current, I_{CD}, flowing into the reactor:

$$C_D = \frac{I_{CD}}{2\pi f V_R} \tag{2.4}$$

where f is the frequency of the sinusoidal input waveform.

The plasma discharges cause significant stochastic electrical noise: both radiating electromagnetic interference (EMI) and creating noise on the input current waveform, although this cannot be modelled in the linearised, high-frequency model.

2.4 DBD Waveforms

The AC waveform used to power DBD reactors is usually sinusoidal, and the voltage is necessarily high enough to cause the gas in the reaction gap (Fig. 2.4) to undergo dielectric breakdown, usually >1 kV. The frequency varies depending on the reactor and its application. A higher frequency allows for greater plasma formation as the number of discharges per

period is independent of frequency; the higher the frequency, the higher the number of periods per second, and the more discharges occur per second [2.31]. This usually results in greater ozone production at higher frequencies, at the cost of a more complex power supply (PSU) and increased input power. For example, medium power reactors (<100 kW) may use a frequency in the kHz [2.32], or even MHz, [2.33], due to the reduction in size and weight of high-frequency PSUs compared to line frequency PSUs. A large (>100 kW) reactor for wastewater treatment might operate at line frequency (50/60 Hz) due to the ease of obtaining high voltage directly from the grid, although even in these larger installations, PSUs operating at higher frequencies have become common [2.12].

For radio frequency, sub-atmospheric-pressure plasmas, researchers have been able to adjust the waveform by altering the harmonic content to achieve controllable DC-self-bias and control the location of the high-intensity plasma. In [2.34], Heil, et al, present this technique and provide a theoretical model derivation and numerical simulation. In more recent work, [2.35] focuses on the effects of the time-domain waveshape on the plasma in the spatiotemporal domain. In [2.36], this technique is applied to oxygen plasma, and the effects of different fundamental frequencies are also explored. The effect of the waveform on the energy efficiency of generating certain chemical species is investigated in [2.37].

There has also been research on the effects of waveform on atmospheric DBD plasmas: in [2.38] Seri, et al explore the effect of input waveform on ozone production using an indigo probe.

2.5 DBD Power Supplies

DBD reactors require a high-voltage, high frequency, usually sinusoidal AC supply. As with most power supply applications, high efficiency is a concern, and in portable applications, a small size and low component count is also a requirement. To achieve the high voltage output, a transformer is usually used for voltage gain.

Power supply topologies used for DBD include the resonant LLCC half-bridge (Fig. 2.9) [2.39], a transformer-coupled LC resonant H-bridge [2.40] and the phase-shifted full bridge [2.20] amongst others. As with other types of power supply, resonance of what would otherwise be considered parasitic components (e.g. transformer leakage inductance) allows high efficiency and results in a sinusoidal output voltage with low harmonic distortion and a higher gain than would be achieved with a conventional H-bridge design.

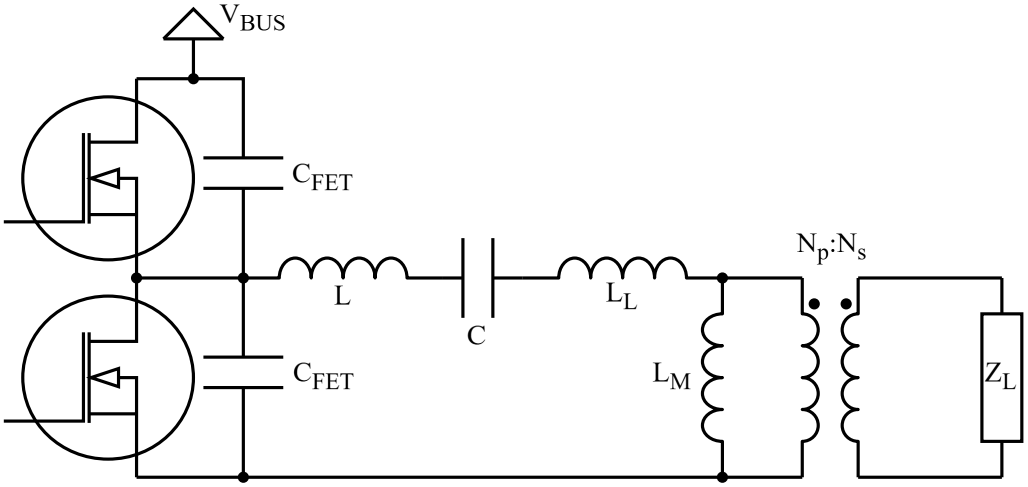

Fig. 2.9 An example of an LLCC topology (author-produced)

As DBD reactor power is proportional to the frequency of the reactor input waveform [2.9] and power generally has a positive correlation with ozone generation, a higher frequency power supply can be used to obtain a higher production rate in an ozone-generating reactor.

For small, portable DBD reactors, a simple topology such as the single-switch resonant flyback converter presented in [2.21] can be used, although the topology was only demonstrated with 50% efficiency.

In [2.16], a resonant series-parallel converter is presented where a series LC tank drives a parallel LC tank and achieves zero-current switching (ZCS). This topology is transformer-coupled, with the transformer accounting for a large part of the total losses and system volume.

Traditional low power high voltage power supplies designed for DBD frequently use resonance to achieve high efficiency with a very low range of available output frequencies and waveforms [2.41] [2.17]. The DBD lamp driver presented in [2.39] is a resonant LLCC half-bridge topology (see Fig. 2.9) which allows for high efficiency at the relatively high power of 100 W. The effects of parasitics on the output waveform and efficiency is explored and various techniques are used to reduce the impact of the parasitics on efficiency for the presented topology. The resonant frequency can be adjusted by changing circuit components, however the waveshape will always be a pulsed sinusoid.

In [2.40], an LC resonant H-bridge topology is used to drive a 300 W ozoniser at a voltage of 5 kV. The circuit is transformer-coupled, with a series inductor and capacitor parallel to the transformer primary. The H-bridge was driven with a fixed 180-degree phase-shift, and duty-

cycle of 30%, allowing a large deadtime in which the primary tank current is allowed to flow through the IGBT co-pack diode. Examination of the switching waveforms suggests that whilst they do not achieve zero-voltage switching (ZVS), the current at the switching events is low, achieving low current switching (LCS). This results in a reported efficiency of 86%. The reported total harmonic distortion (THD) was 1.33%, however this seems to have been derived from the simulation results, and the output waveform has a notably more distorted waveform.

As the resonant H-bridge in [2.40] is designed to have a continuous sinusoidal output, there is scope for the output power to be varied by adjusting the duty-cycle. A phase-shifted full bridge (PSFB) topology may also help achieve this as in [2.20] where a PSFB is used to determine the effects of frequency on output power efficiency and efficacy, amongst others. Linear, positive relationships between frequency and power, frequency and efficiency, frequency and yield, and frequency and efficacy are demonstrated.

A low power single switch design for portable ozone generation is presented in [2.21]. The single MOSFET, supplied from an extra low voltage (ELV) DC supply, switches the primary of a flyback transformer with an unrectified output, the capacitance on the secondary from the reactor and turn to turn parasitics forming a resonant circuit with the transformer leakage inductance. As the load is known and constant (designed to work with a specific reactor), the MOSFET can be switched at a fixed frequency and duty cycle making the supporting circuitry extremely simple and inexpensive. Efficiency was reported to be poor, at only 50%, but with a low output power of 1 W. The design is compact and inexpensive; however, it provides a pulsed half-sine output with limited range of output powers (output power can be changed by varying the DC input voltage).

Both push-pull and class-E amplifiers are explored for use in DBD ozone generators in [2.42]. The push-pull inverter is driven at resonance with presumably the magnetising inductance of the transformer at approximately 15 W depending on the reactor configuration. No efficiency results are given; however, it seems that even a simple push-pull circuit driving a transformer without any extra components can still achieve good efficiency given the size of the heatsinks photographed. There is even less information on the performance of the class E amplifier. It is demonstrated being driven at resonance; however, it has a lower output voltage than the push-pull assuming it was driven from the same supply voltage, but according to the performance figures, has a higher ozone output.

Whilst researching the difference between DBD reaction provided by current and voltage-controlled supplies, Le Wang, *et al*. in [2.43] use a simple transformer coupled H-bridge to power the reactor.

A DBD lamp may require more adjustment of input voltage, for example for varying brightness. In [2.44] a novel, dual, two-switch flyback converter to provide bipolar pulsed-sinusoid supply to the DBD lamp with adjustable output power is presented. The pulsed supply is designed to increase the efficiency of the lamp, unfortunately at the expense of the efficiency of the driver. The amplitude and pulse-width are not independently variable by the power supply, however.

In [2.45], a current-fed parallel-resonant push-pull inverter is presented with a closed loop control system and over-current protection. The feedback for the closed loop is derived from the transformer tap voltage, which is proportional to the transformer input voltage, and therefore the output power. Whilst this form of closed loop control is simple and easy to implement whilst providing isolation between each side of the transformer, it neglects the transformer leakage inductance. In addition, the method of sensing the tap voltage (low pass filtering to obtain a DC voltage to compare) slows the response time and requires the closed loop control to have a low bandwidth: a step response of approximately 10 ms is presented. If such a system were used to create a variable sinusoidal supply, the bandwidth would likely need increasing to provide adequate performance.

2.5.1 High Voltage Waveform Generation

To provide highly variable waveforms (waveshape, voltage and frequency), an exploration of high voltage waveform generation techniques has been carried out. These include topologies with a low efficiency such as the class B amplifier driven by a low voltage arbitrary waveform generator (AWG) which can be implemented in two main ways; with several devices capable of medium voltage operation being used in series, or by using one device per voltage rail (two for a push/pull output stage) that can withstand the full rail voltage.

With the low output power, and the high cost of high bandgap devices capable of withstanding 10 kV, thermionic valves could be used in a simple push/pull output. In [2.46] such an amplifier is constructed however the bandwidth is poor, limited to 1 kHz, and the output impedance is considerable. A modern version of such an amplifier could be made from a small number of highly integrated components, and with improvements in bandwidth,

voltage limits and slew rate, a system with a thermionic output stage could provide a useful and inexpensive AWG, if one with a low efficiency. For example, the original design required several batteries as isolated power supplies to supply the heater current as well as local power supplies for the op-amps; a modern design could utilise small, isolated DC/DC converters, reducing the size, maintenance cost, and eliminating problems with low voltage on the heaters from a discharged battery.

Another linear amplifier option with cascaded output devices has been the subject of more recent research. In [2.47] a cascaded linear amplifier is presented using opto-isolation to drive op-amps which themselves provide the output stage. This approach has several benefits, such as fewer components on the output, and a greater performance due to the high optimisation of integrated circuits. Unfortunately, op-amps with an output voltage ±>100 V are not readily available, so a system capable of ±5 kV output would require an impractical number of series-connected stages.

A similar approach is taken in [2.48], however the output stage is formed from N-channel MOSFETs, driven by an optocoupled cascode allowing an output voltage of ±12 kV. As expected, the harmonic distortion is higher than the design with op-amp output stages, but as the output MOSFETs are rated to 4 kV, few stages are needed for operation at high voltage.

Another linear amplifier is shown in [2.49]. This is a current amplifier with an asymmetrical voltage output (+10 kV −300 V) designed for pulsed operation. Like in [2.47], op amps are used but here they drive cascaded IGBTs. An additional optocoupler is used locally in the low voltage section of each output stage to linearise the local voltage response by using feedback from the output of the extra optocoupler. As this amplifier is current controlled and designed to have a capacitive load, the output has not been optimised for large rate of change of voltage.

A novel approach to the linear amplifier is presented in [2.50]. The multilevel transformer coupled design results in a theoretical efficiency of 91.49% and achieved a measured efficiency of 87%. The transformer coupling makes it unsuitable for an arbitrary output with low frequency components, in addition to requiring additional electronics on the output to provide a DC bias.

Modern high bandgap switching devices are not readily available in high enough voltages to make a single H-bridge inverter (to form a class D amplifier for example) with sufficient

output voltage. However, like with a linear amplifier, there are ways to use multiple switching devices to increase the output voltage: in [2.51] a class D amplifier is demonstrated that uses series-connected single-switch diode-clamped isolated levels followed by a full bridge to allow an AC output. The low voltage of each level allows fast switching devices to be used to provide a pulse-width modulated (PWM) output that is then LC filtered and inverted at the baseband frequency, reducing the switching requirements of the high voltage output switches compared to a simple H-bridge inverter.

A variant on the cascaded H-bridge multilevel converter (CHBMLC, Fig. 2.10) is presented in [2.52]. Here, half-bridge sections are used, rather than full-bridges and so needs twice the number of voltage sources for a bipolar output. The design is capable of an output voltage of 14 kV_{pk} as each level has a DC bus of 1.4 kV. This output voltage coupled with the use of IGBTs for the output switches results in a low PWM frequency of 8 kHz.

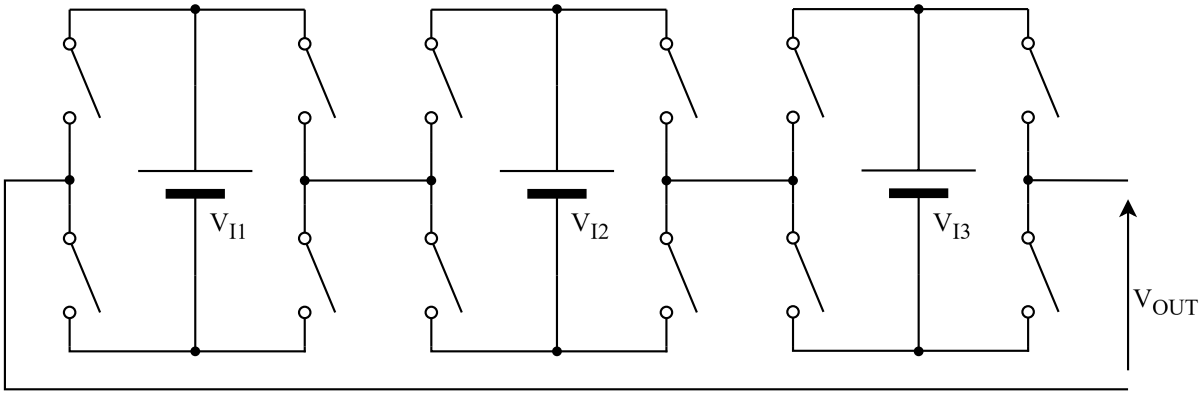

Fig. 2.10 A simplified example of the CHBMLC topology (author-produced)

A more conventional CHBMLC is presented in [2.53]. The system has a ±14.4 kV output and a bandwidth of 20 kHz, powered from several isolated 12 V batteries each boosted to 600 V by a flyback transformer. Due to the limitations of the controller (and the IGBT switches), a PWM scheme is not used, instead fundamental frequency switching (FFS) is used, where each switch is only on for one period during the switching cycle. This has the advantage of being simple to implement and efficient due to the reduction of switching losses over the higher frequency needed for PWM, however harmonic distortion is high in comparison. The authors do not measure this directly but use the high voltage AWG for driving a DBD plasma reactor.

2.6 Harmonic-Controlled Waveforms

Patel and Hoft introduced a technique to eliminate unwanted harmonics in an inverter pulse-train in 1973 [2.54], as an alternative to commonly used modulation schemes like PWM. This method involves estimating a possible solution for switching angles that may generate the required fundamental waveform with low harmonic content, then using an iterative numeric solver on the Fourier series expansion of the pulse-train to improve this estimation. They were able to zero the 5th, 7th, 11th, 13th and 17th harmonics in a 3-level inverter with a frequency modulation ratio of 10 pulses per fundamental cycle.

Due to improvements in computational technology, far more harmonics can now be zeroed using this method, and even extended to multi-level inverters [2.55], [2.56].

2.7 Piezoelectric Resonators

Piezoelectric devices use the electromechanical properties of a piezoelectric material to convert electrical energy to mechanical energy and vice versa. Such devices exploit mechanical resonance whose natural frequency is dependent on the material parameters and geometry.

A piezoelectric resonator (PR) is a one-port device and thus cannot provide voltage gain without additional components. An external voltage applied to the PR causes the material to deform. Mechanical resonance, coupled to the electrical domain by the piezoelectric properties of the material, allows it to be electrically modelled with the Van Dyke equivalent circuit shown in Fig. 2.11 [2.57], [2.58].

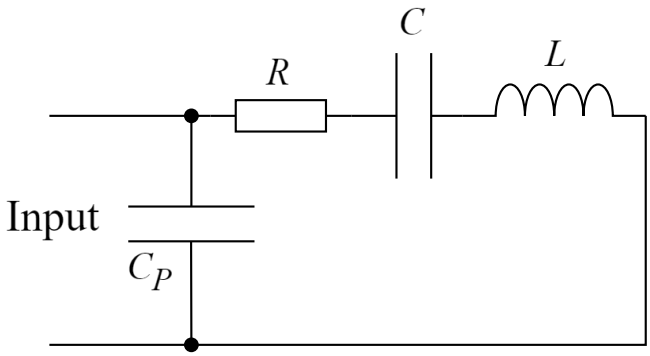

Fig. 2.11 Van Dyke equivalent circuit model of a piezoelectric resonator (made by author)

Due to the properties of the piezoelectric material, a high Q-factor of over 600 can be achieved for a lead zirconate titanate (PZT) resonator [2.58]. This makes the equivalent circuit unrealisable with electrical components in a volume comparable to the resonator. For

example, a PZT resonator with a volume of 11.87 mm^3, which has parameters R = 4.45 Ω, C = 75.2 pF, and L = 1.51 mH, is used in the DC-DC converter described in [2.59].

2.8 Piezoelectric Transformers

Piezoelectric transformers (PTs) are an alternative to conventional electromagnetic transformers for low-power voltage conversion (power supply) applications. They operate by converting electrical energy into mechanical stress within a piezoelectric material, taking advantage of mechanical resonances. The PT may be a three-terminal device with no separation between primary and secondary or a four-terminal device with isolated primary and secondary sections [2.60].

In the most basic design, monolithic piezoelectric material is used, featuring three electrical connections: one for the input, another acting as a common ground and the final connection being the output terminal. By altering the placement of the electrical contacts along with the geometry of the device, it is possible to obtain the desired voltage gain.

PTs can achieve high efficiency due to their resonant operation and have been used to provide voltage gain for driving low-power DBD reactors. For example, in [2.18], Salam et al. report 90% power supply efficiency for a 4 W reactor driving a DBD reactor, resulting in 3.6 g/kWh of ozone production with pure oxygen as the feedstock. Since piezoelectric materials do not rely on magnetic properties, these transformers can withstand extreme temperature conditions [2.61], making them suitable for use even in harsh environments.

Due to the capacitance of the PT, any driving circuit usually has a series inductor to reduce switching losses. This inductor adds size and weight to the system and represents a source of additional power loss.

A PT can be electrically modelled by the Mason equivalent circuit model. The simplified Mason equivalent circuit of a PT can be seen in Fig. 2.12.

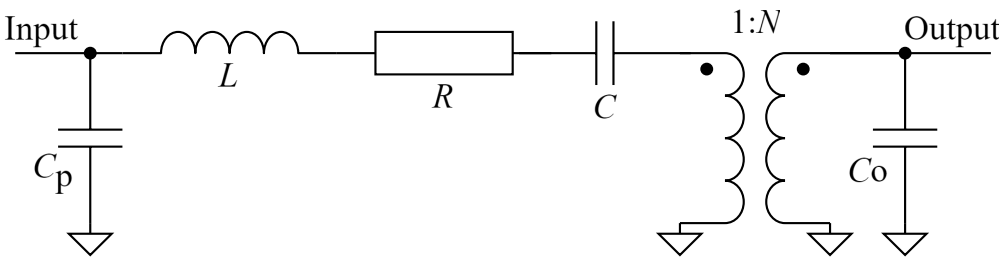

Fig. 2.12 Mason equivalent circuit model (made by author)

The component values can be obtained by calculation from mechanical properties [2.62], [2.63] or by performing electrical measurements of the transformer [2.64]. The latter is usually more accurate as tolerances associated with the materials specifications and manufacturing processes can be accounted for.

2.9 Global Optimisation Techniques and Applications

Part of the work in this thesis explores the use of global optimisation algorithms to improve DBD reactor performance, as well as improve the parametrisation of piezoelectric devices.

Global optimisation is a process of finding the best solution to a problem, or a solution close to the best, subject to certain constraints, usually using heuristic algorithms. A heuristic global optimiser can be used to improve the performance of many systems with well-defined inputs and at least one measurable output metric. Most heuristic optimisation algorithms are used either to determine optimum system parameters of a simulated system [2.65] or tune a control system, with the system being usually simulated or physical hardware (hardware in the loop, HIL) [2.66]. One such use is documented in [2.67], where a genetic algorithm is used to optimise the performance of an aerofoil. Optimisation algorithms have also been used to adjust voltage waveforms to obtain some desirable outcome. For example, in [2.68], a gate-drive waveform is adjusted to achieve high efficiency in an inverter for solar power by way of a global optimiser.

Two popular categories of optimisation algorithm are evolutionary algorithms and direct-search algorithms. Particle swarm optimisation (PSO), described in [2.69], is an evolutionary algorithm inspired by the social behaviour of birds. In PSO, a “swarm” of particles move through the search-space and interact with each other, where each particle represents a vector of variables providing a potential solution to the problem. The algorithm iteratively updates the position of particles within the search-space based on the optimum solution found by that particle and the global best solution, causing the particles to tend towards better solutions over several iterations. PSO has demonstrated good performance when operating on problems with multiple variables.

Pattern search (PS), [2.70], is a direct-search optimisation technique that uses a systematic approach to explore the parameter space around a given initial point. From a given starting point, this technique searches along each dimension of the problem, where a dimension represents one variable. The optimiser moves through the search-space in steps dependent on

the success of the previous step. This success is defined only by whether the solution at the newer point is better than the current best.

As PSO is seeded with random particle locations covering the valid search-space, this allows the optimiser to cover a large area, helping to ensure that a global minimum is found. The PS technique, however, starts with a given starting point and iteratively moves towards the optimum solution, thoroughly covering the parameter space, but making it more susceptible to becoming stuck in local minima.

2.10 Output Gas Sensing

For a closed loop reaction system, a method of determining the quantity of the output gasses is required. Metal oxide sensors are inexpensive, available and the subject of current research, as reviewed in [2.71]. In this review, an overview is given on sensors for detecting carbon dioxide (CO_2), carbon monoxide (CO), nitrogen oxides (NO_x), and ammonia (NH_3). Although the expected output products of a DBD reactor with air as the input would be mostly reactive compounds of oxygen and nitrogen, other components of air such as CO_2 and H_2O would breakdown and provide small quantities of other compounds. The ability to sense these, or at least the ability to sense a lack of one of the input compounds in the output, could allow a better understanding of the reaction pathways.

Another method of sensing gasses such as nitrogen dioxide is with an electrochemical sensor. Here the gases to be sensed are absorbed into an electrolyte where they are then oxidised or reduced, allowing an electric current to flow though the electrolyte. In [2.72], both a plate and tube of stabilised zirconia are used to create sensors intended to detect nitrogen oxides in exhaust gasses. The authors had trouble obtaining adequate performance when barium nitrate was used on one electrode, however other compounds had more success, and changed the relative sensitivity of NO_2 and NO. If several similar sensors were used with different electrode coating compounds, the differential measurement would allow the concentrations of the nitrogen oxides to be determined independently.

A recent review of zirconium-based electrochemical sensors is presented in [2.73]. In this review, a mixed potential sensor is reported which utilises a thin gold layer to cause only NO_2 to give a positive voltage change (ΔV), whilst other compounds cause a negative ΔV. Whilst this increases the selectivity of the sensor, either other gasses must be scrubbed from the

sensor stream, or more than one kind of sensor must be used to avoid other species (like NO) from reducing the sensor output voltage, giving the impression of a lower NO_2 concentration.

A popular and accurate (±1%) method of sensing ozone used in commercial ozone monitors involves the transmittance of 254 nm UV [2.74]. The gas is sampled and fed through a chamber with a mercury-lamp-based UV light source opposing a photodiode. As ozone strongly attenuates light at this wavelength, comparing the output from the photodiode with sampled ozone in the chamber against the same signal with an ozone-free reference gas in the chamber allows the concentration of ozone to be calculated.

2.11 Commercial Ozone Generation

Ozone generators are available commercially. Small devices designed to generate and dissipate a small amount of ozone into the surrounding air are available from retailers such as Amazon [2.75]. An example of this type of device is the Murata MHM502, a device designed to generate 45 mg/hr of ozone whilst consuming 4.6 W at 12 V DC [2.76]. This corresponds to an ozone generation efficacy of 9.8 g/kWh. The design of this device suggests it uses corona discharge to produce the ozone.

Larger units are also available for applications such as treating pool water. One such device is the VMUS-4, sold by Oxidation Technologies LLC [2.77]. This device can be wall-mounted and can produce 10 g/hr or 19,000 ppm at 4 ℓpm with pure oxygen as the feedstock. Power consumption is not specified, and the website repeatedly claims it uses corona discharge to generate the ozone; however, it also mentions it uses a quartz dielectric barrier, and the pictures of the discharge suggest it is DBD. A journal article linked at the bottom of the webpage, [2.78], is also about DBD.

An example of an ozone generator for laboratory use is the triogen LAB2B [2.79] sold by Asynt. This device can generate 4 g/hr of ozone with 10 ℓpm of dry air, consuming 105 W, according to the datasheet. This corresponds to an efficacy of 38 g/kWh. This datasheet also states that it uses corona discharge but then mentions a dielectric and a high-frequency power supply, suggesting there may be some confusion about the difference between types of partial discharge outside academia.

2.12 Summary

This literature review discusses the use of dielectric barrier discharge (DBD) reactors in various applications such as ozone generation, chemical synthesis, and plasma treatment. DBD reactors are used to produce reactive chemical species by applying a high-voltage electrical discharge to a gas or mixture of gases.

DBD reactors typically consist of two electrodes with one or more insulating layers between them, including at least one dielectric layer such as glass, quartz, or ceramic. The reactor structure allows gas to flow into the reaction gap, where it interacts with the electrical discharge.

DBD reactors have various applications in fields such as chemical synthesis, plasma treatment, and water treatment. The review highlights some of these applications, including ozone generation for water treatment, air purification, and laboratory use.

The use of different DBD reactor models is discussed, including a simple model consisting of two series capacitors with a variable resistance in parallel with one capacitor. More complex models can simulate individual plasma filaments and their varying intensity over time, however only the linear model is used in this thesis to allow modelling and simulation of the system in Chapter 5.

Various metrics used to measure the efficacy of ozone generation by DBD reactors are discussed, including the ratio of ozone generated to energy used (g/kWh) and the ratio of ozone concentration to power (ppm/W). These metrics are used in chapters 5, 6 and 7.

This review also discusses different methods for measuring reactor power, including the Lissajous technique and the Pearson technique. The Lissajous technique is based on integrating the area enclosed by a voltage-charge plot and is used in chapters 5, 6 and 7 due to its improved accuracy over the Pearson technique, which involves measuring the reactor current directly using a current transformer.

The different high-voltage waveform generation techniques used to power DBD reactors are discussed. These include resonant half-bridge topologies, phase-shifted full bridge topologies, and linear amplifier designs using class B amplifiers with cascaded output devices.

Piezoelectric transformers and resonators are another alternative for low-power voltage conversion applications, such as powering small DBD reactors. The use of PRs in a novel

power supply is demonstrated in Chapter 5. PTs can achieve high efficiency due to their resonant operation and have been used to generate ozone in previous literature.

The history of selective harmonic elimination was explored and is adapted in this thesis into selective harmonic generation, where is used in Chapter 6 with a piezoelectric transformer to provide controllable biharmonic waveforms.

Also discussed are global optimisation techniques that will be applied to the parameterisation of piezoelectric devices and improve the performance of DBD reactors in chapters 4 and 7 respectively. These include evolutionary algorithms like particle swarm optimisation (PSO) and direct-search algorithms like pattern search (PS).

The literature review also covers output gas sensing methods, including metal oxide sensors, electrochemical sensors and transmittance-based sensors which are used to measure ozone concentrations produced by DBD reactors. Quantification of DBD reactor output is particularly important in Chapter 7, where it is part of a hardware-in-the-loop system.

2.13 Conclusion

Several research gaps have been highlighted by this literature review:

- Prior literature lacks a method for accurately determining the equivalent circuit parameters of piezoelectric transformers and resonators when multiple resonant branches are to be modelled. In addition, heuristic techniques such as global optimisation could improve the existing methods of PT and PR parameterisation.
- There is a lack of research on power supplies that use piezoelectric resonators for voltage gain, particularly at low input voltages. These could be utilised in portable or small-scale DBD applications.
- While the mathematical concept behind selective harmonic generation is known (as selective harmonic elimination), there is no previous research on its application to generate voltage waveforms to explore the impact of ozone generation efficacy in a DBD reactor, for example.
- A hardware-in-the-loop control system could be made using global optimisation that can dynamically adjust DBD reactor input parameters to optimise performance, particularly in terms of ozone generation efficacy.

2.14 References

[2.1] K.-J. Tseng, Y. Wang, and D. M. Vilathgamuwa, 'An experimentally verified hybrid Cassie-Mayr electric arc model for power electronics simulations', *IEEE Trans. Power Electron.*, vol. 12, no. 3, pp. 429–436, May 1997, doi: 10.1109/63.575670.

[2.2] W. Marszalek and Z. W. Trzaska, 'Dynamical Models of Electric Arcs and Memristors: The Common Properties', *IEEE Trans. Plasma Sci.*, vol. 45, no. 2, pp. 259–265, Feb. 2017, doi: 10.1109/TPS.2016.2645879.

[2.3] I. Remsen and H. Renoup, 'The Oxidation of Atmospheric Nitrogen with Reference to the Manufacture of Nitrates and Nitric Acid', *Am. Chem. J.*, vol. 35, pp. 358–367, 1906.

[2.4] H. Itoh, M. Taguchi, and S. Suzuki, 'Thermal decomposition of ozone at high temperature leading to ozone zero phenomena', *J. Phys. Appl. Phys.*, vol. 53, no. 18, p. 185206, 2020, doi: 10.1088/1361-6463/ab71a9.

[2.5] W. Siemens, 'Ueber die elektrostatische Induction und die Verzögerung des Stroms in Flaschendrähten', *Ann. Phys.*, vol. 178, no. 9, pp. 66–122, 1857, doi: 10.1002/andp.18571780905.

[2.6] U. Kogelschatz, B. Eliasson, and W. Egli, 'From ozone generators to flat television screens: history and future potential of dielectric-barrier discharges', in *14th International Symposium on Plasma Chemistr*, Prague, Czech Republic, 1999.

[2.7] F. Peeters and T. Butterworth, 'Electrical Diagnostics of Dielectric Barrier Discharges', in *Atmospheric Pressure Plasma - From Diagnostics to Applications. IntechOpen*, 2018. doi: 10.5772/intechopen.80433.

[2.8] K. Nassour, M. Brahami, S. Nemmich, N. Hammadi, N. Zouzou, and A. Tilmatine, 'Comparative Experimental Study between Surface and Volume DBD Ozone Generator', *Ozone Sci. Eng.*, vol. 38, no. 1, pp. 70–76, 2016.

[2.9] U. Kogelschatz, 'Dielectric-barrier Discharges: Their History, Discharge Physics, and Industrial Applications', *Plasma Chem. Plasma Process.*, vol. 23, no. 1, pp. 1–46, 2003.

[2.10] K. Obileke *et al.*, 'Recent advances in radio frequency, pulsed light, and cold plasma technologies for food safety', *Journal of food process engineering*, vol. 45, no. 10. John Wiley & Sons, Inc, Hoboken, USA, p. n/a, 2022. doi: 10.1111/jfpe.14138.

[2.11] Y. Zeng, G. Chen, B. Liu, H. Zhang, and X. Tu, 'Unraveling Temperature-Dependent Plasma-Catalyzed CO_2 Hydrogenation', *Ind. Eng. Chem. Res.*, vol. 62, no. 46, pp. 19629–19637, Nov. 2023, doi: 10.1021/acs.iecr.3c02827.

[2.12] X. Ma *et al.*, 'Plasma Assisted Catalytic Conversion of CO2 and H2O Over Ni/Al2O3 in a DBD Reactor', *Plasma Chem. Plasma Process.*, vol. 39, pp. 109–124, 2019.

[2.13] A. Hafeez, N. Shezad, F. Javed, T. Fazal, M. S. Rehman, and F. Rehman, 'Developing multiplexed plasma micro-reactor for ozone intensification and wastewater treatment', *Chem. Eng. Process. - Process Intensif.*, vol. 162, p. 108337, 2021.

[2.14] U. Kogelschatz, 'Advanced Ozone Generation', in *Process Technologies for Water Treatment*, S. Stucki, Ed., Boston, MA: Springer US, 1988, pp. 87–118. doi: 10.1007/978-1-4684-8556-1_9.

[2.15] X. Tang *et al.*, 'N2O Formation Characteristics in Dielectric Barrier Discharge Reactor for Environmental Application: Effect of Operating Parameters', *Energy Fuels*, vol. 31, no. 12, pp. 13901–13908, Dec. 2017, doi: 10.1021/acs.energyfuels.7b02428.

[2.16] T. Jakubowski, M. Holub, and S. Kalisiak, 'Resonant inverter with resonance frequency tracking for DBD plasma reactor supply', *Eur. Phys. J. - Appl. Phys.*, vol. 61, no. 2, p. 24304, Feb. 2013, doi: 10.1051/epjap/2012120430.

[2.17] K. Teranishi, S. Suzuki, and H. Itoh, ‘A novel generation method of dielectric barrier discharge and ozone production using a piezoelectric transformer’, *Jpn. J. Appl. Phys.*, vol. 43, no. 9 B, pp. 6733–6739, 2004, doi: 10.1143/JJAP.43.6733.
[2.18] Z. Salam, M. Facta, and M. Amjad, ‘Design and implementation of a highly efficient DBD ozonizer using the single switch resonant converter with piezoelectric transformer’, in *2013 Twenty-Eighth Annual IEEE Applied Power Electronics Conference and Exposition (APEC)*, Mar. 2013, pp. 1596–1600. doi: 10.1109/APEC.2013.6520510.
[2.19] T. Homola, V. Prukner, P. Hoffer, and M. Šimek, ‘Multi-hollow surface dielectric barrier discharge: an ozone generator with flexible performance and supreme efficiency’, *Plasma Sources Sci. Technol.*, vol. 29, no. 9, p. 95014, 2020, doi: 10.1088/1361-6595/aba987.
[2.20] P. Hothongkham and V. Kinnares, ‘High-voltage high-frequency power supply using a phase-shifted PWM full bridge inverter fed ozone generator with constant applied electrode voltage’, in *The 2010 International Power Electronics Conference - ECCE ASIA*, Sapporo, Japan, 2010.
[2.21] J. Alonso, J. Cardesin, E. Corominas, M. Rico-Secades, and J. Garcia, ‘Low-power high-voltage high-frequency power supply for ozone generation’, *IEEE Trans. Ind. Appl.*, vol. 40, no. 2, pp. 414–421, 2004.
[2.22] J. M. Alonso, M. Valdés, A. J. Calleja, J. Ribas, and J. Losada, ‘High Frequency Testing and Modeling of Silent Discharge Ozone Generators’, *Ozone Sci. Eng.*, vol. 25, no. 5, pp. 363–376, 2003, doi: 10.1080/01919510390481685.
[2.23] R. Peyrous and R.-M. Millot, ‘Ozone generation in oxygen by corona discharges in a point-to-plane gap subjected to a chopped DC positive voltage’, *J. Phys. Appl. Phys.*, vol. 14, no. 12, p. 2237, Dec. 1981, doi: 10.1088/0022-3727/14/12/012.
[2.24] R. Barni, I. Biganzoli, E. Dell’Orto, and C. Riccardi, ‘Effects of a pulsed operation on ozone production in dielectric barrier air discharges’, *Lett. Appl. NanoBioscience*, vol. 3, no. 2, pp. 167–171, 2014.
[2.25] Z. Fan, H. Yan, Y. Wang, Y. Liu, H. Guo, and C. Ren, ‘Breakdown characteristics of atmospheric dielectric barrier discharge in gas flow condition’, *Phys. Plasmas*, vol. 25, no. 5, p. 053517, May 2018, doi: 10.1063/1.5018331.
[2.26] H. Jakob and M. Kim, ‘Electrical Model for Complex Surface DBD Plasma Sources’, *IEEE Trans. Plasma Sci.*, vol. 49, no. 10, pp. 3051–3058, 2021, doi: 10.1109/TPS.2021.3110437.
[2.27] U. N. Pal *et al.*, ‘Electrical modelling approach for discharge analysis of a coaxial DBD tube filled with argon’, *J. Phys. Appl. Phys.*, vol. 42, no. 4, p. 045213, Jan. 2009, doi: 10.1088/0022-3727/42/4/045213.
[2.28] R. Valdivia-Barrientos, J. Pacheco-Sotelo, M. Pacheco-Pacheco, J. S. Benítez-Read, and R. López-Callejas, ‘Analysis and electrical modelling of a cylindrical DBD configuration at different operating frequencies’, *Plasma Sources Sci. Technol.*, vol. 15, no. 2, p. 237, Mar. 2006, doi: 10.1088/0963-0252/15/2/008.
[2.29] A. V. Pipa, J. Koskulics, R. Brandenburg, and T. Hoder, ‘The simplest equivalent circuit of a pulsed dielectric barrier discharge and the determination of the gas gap charge transfer’, *Rev. Sci. Instrum.*, vol. 83, no. 11, pp. 115112–115112, 2012, doi: 10.1063/1.4767637.
[2.30] M. Ponce, J. Aguilar, J. Fernandez, E. Beutelspacher, J. M. Calderon, and C. Cortes, ‘Linear and non linear models for ozone generators considering electrodes losses’, in *2004 IEEE 35th Annual Power Electronics Specialists Conference*, Piscataway NJ: IEEE, 2004, pp. 810-814 Vol.1. doi: 10.1109/PESC.2004.1355853.

[2.31] T. C. Manley, 'The Electric Characteristics of the Ozonator Discharge', *Trans. Electrochem. Soc.*, vol. 84, no. 1, pp. 83–96, 1943, doi: 10.1149/1.3071556.
[2.32] J. M. Alonso, J. Garcia, A. J. Calleja, J. Ribas, and J. Cardesin, 'Analysis, design, and experimentation of a high-voltage power supply for ozone generation based on current-fed parallel-resonant push-pull inverter', *IEEE Trans. Ind. Appl.*, vol. 41, no. 5, pp. 1364–1372, 2005, doi: 10.1109/TIA.2005.853379.
[2.33] I. G. Koo, J. H. Cho, and W. M. Lee, 'Influence of the Gas Humidity on the Uniformity of RF-Powered Atmospheric-Pressure Low-Temperature DBD Plasmas', *Plasma Process. Polym.*, vol. 5, no. 2, pp. 161–167, 2008, doi: 10.1002/ppap.200700068.
[2.34] B. G. Heil, U. Czarnetzki, R. P. Brinkmann, and T. Mussenbrock, 'On the possibility of making a geometrically symmetric RF-CCP discharge electrically asymmetric', *J. Phys. Appl. Phys.*, vol. 41, no. 16, p. 165202, Jul. 2008, doi: 10.1088/0022-3727/41/16/165202.
[2.35] B. Bruneau, T. Novikova, T. Lafleur, J. P. Booth, and E. V. Johnson, 'Ion flux asymmetry in radiofrequency capacitively-coupled plasmas excited by sawtooth-like waveforms', *Plasma Sources Sci. Technol.*, vol. 23, no. 6, p. 065010, Aug. 2014, doi: 10.1088/0963-0252/23/6/065010.
[2.36] A. Derzsi *et al.*, 'Power coupling mode transitions induced by tailored voltage waveforms in capacitive oxygen discharges', *Plasma Sources Sci. Technol.*, vol. 26, no. 3, p. 034002, Feb. 2017, doi: 10.1088/1361-6595/aa56d6.
[2.37] I. Korolov, Z. Donkó, G. Hübner, Y. Liu, T. Mussenbrock, and J. Schulze, 'Energy efficiency of voltage waveform tailoring for the generation of excited species in RF plasma jets operated in He/N 2 mixtures', *Plasma Sources Sci. Technol.*, vol. 30, no. 9, p. 095013, Sep. 2021, doi: 10.1088/1361-6595/ac1c4d.
[2.38] P. Seri *et al.*, 'Influence of the voltage waveform's shape and on-time duration on the dissolved ozone produced by a DBD bubble reactor', *Plasma Sources Sci. Technol.*, vol. 28, no. 3, p. 035001, Mar. 2019, doi: 10.1088/1361-6595/ab024f.
[2.39] M. Meisser, M. Paravia, W. Heering, and R. Kling, 'Resonance behaviour of a pulsed electronic control gear for dielectric barrier discharges', in *5th IET International Conference on Power Electronics, Machines and Drives (PEMD 2010*, 2010.
[2.40] G. Udhayakumar, M. R. Rashmi, K. Patel, G. P. Ramesh, and A. Suresh, 'Implementation of high-frequency high-voltage power supply for ozone generator system using embedded controller', in *2016 International Conference on Circuit, Power and Computing Technologies (ICCPCT*, Nagercoil, India, 2016.
[2.41] X. Bonnin, J. Brandelero, N. Videau, H. Piquet, and T. Meynard, 'A High Voltage High Frequency Resonant Inverter for Supplying DBD Devices with Short Discharge Current Pulses', *IEEE Trans. Power Electron.*, vol. 29, no. 8, pp. 4261–4269, 2014, doi: 10.1109/TPEL.2013.2295525.
[2.42] M. Facta, Z. Salam, A. Jusoh, and Z. B. Buntat, 'Improvement in ozone generation with low voltage high frequency power converters', in *2008 IEEE 2nd International Power and Energy Conference*, Johor Bahru, Malaysia, 2008.
[2.43] L. Wang, X. Tang, S. Luan, and S. Chen, 'Comparison and Analysis of DBD-Ozonizers Powered by Current and Voltage-Mode Power Supplies', in *6th International Conference on Power Electronics Systems and Applications (PESA*, China: Hong Kong, 2015.
[2.44] A. El-Deib, F. Dawson, G. v Eerden, S. Bhosle, and G. Zissis, 'Current Controlled Driver for a Dielectric Barrier Discharge Lamp', in *The 2010 International Power Electronics Conference*, Sapporo, Japan, 2010.

[2.45] J. M. Alonso and C. Ordiz, ‘High-Voltage Closed-Loop Power Supply for Ozone Generators’, *EPE J.*, vol. 19, no. 2, pp. 45–51, 2009.
[2.46] P. T. Krein, D. J. Kervinf, and J. M. Crowley, ‘An improved high-voltage waveform generator’, *J. Phys. [E]*, vol. 16, pp. 1234–1237, 1983.
[2.47] J. Liu, D. Zhang, M. Wang, L. Huang, and D. Zhao, ‘A Cascaded Linear High-Voltage Amplifier Circuit for Dielectric Measurement’, *IEEE Trans. Ind. Electron.*, vol. 63, no. 3, pp. 1834–1841, 2016.
[2.48] Y. Shyur, N. J. Fitch, J. A. Bossert, T. Brown, and H. J. Lewandowski, ‘A high-voltage amplifier for traveling-wave Stark deceleration’, *Rev. Sci. Instrum.*, vol. 89, no. 084705, 2018.
[2.49] T. Hom and J. Melbert, ‘A 10-kV Linear Current-Mode Power Amplifier for Capacitive Actuators’, *IEEE Trans. Instrum. Meas.*, vol. 61, no. 1, pp. 2–8, 2012.
[2.50] B. Chen, W. Gao, Y. Chen, C. Tian, Y. Zhou, and G. Xue, ‘A High Efficiency Linear Power Supply with Pure Sine Wave for High Voltage Test’, *Electronics*, vol. 10, no. 1, 2021.
[2.51] Y. Hou, W. Sun, A. Ren, and S. Liu, ‘Design of High-Voltage Switch-Mode Power Amplifier Based on Digital-Controlled Hybrid Multilevel Converter’, *Act. Passive Electron. Compon.*, p. 9, 2016.
[2.52] P. Lei, Y. Mingtian, L. Geqi, and Z. Qiaogen, ‘A High Voltage Multi Level Arbitrary Waveform Generator for Insulation Testing’, *IEEE Trans. Dielectr. Electr. Insul.*, vol. 26, no. 2, pp. 405–411, 2019.
[2.53] F. A. Dragonas, G. Neretti, P. Sanjeevikumar, and G. Grandi, ‘High-Voltage High-Frequency Arbitrary Waveform Multilevel Generator for DBD Plasma Actuators’, *IEEE Trans. Ind. Appl.*, vol. 51, no. 4, pp. 3334–3342, 2015.
[2.54] H. S. Patel and R. G. Hoft, ‘Generalized Techniques of Harmonic Elimination and Voltage Control in Thyristor Inverters: Part I--Harmonic Elimination’, *IEEE Trans. Ind. Appl.*, vol. IA-9, no. 3, pp. 310–317, May 1973, doi: 10.1109/TIA.1973.349908.
[2.55] Z. Salam, Y. S. Soon, and Y. Saleem, ‘On the improved computational speed and convergence of the Newton Raphson iteration method for selective harmonics elimination PWM applied to cascaded multilevel inverter with equal and non-equal DC sources’, *COMPEL - Int. J. Comput. Math. Electr. Electron. Eng.*, vol. 32, no. 3, pp. 901–922, Jan. 2013, doi: 10.1108/03321641311305827.
[2.56] M. S. A. Dahidah, G. Konstantinou, and V. G. Agelidis, ‘A Review of Multilevel Selective Harmonic Elimination PWM: Formulations, Solving Algorithms, Implementation and Applications’, *IEEE Trans. Power Electron.*, vol. 30, no. 8, pp. 4091–4106, Aug. 2015, doi: 10.1109/TPEL.2014.2355226.
[2.57] J. D. Boles, J. J. Piel, N. Elaine, J. E. Bonavia, J. H. Lang, and D. J. Perreault, ‘Piezoelectric-Based Power Conversion: Recent Progress, Opportunities, and Challenges.’, in *IEEE Custom Integrated Circuits Conference (CICC*, Newport Beach, CA, USA, 2022.
[2.58] J. S. Kim, K. Choi, and I. Yu, ‘A New Method of Determining the Equivalent Circuit Parameters of Piezoelectric Resonators and Analysis of the Piezoelectric Loading Effect’, *IEEE Trans. Ultrason. Ferroelectr. Freq. CONTROL*, vol. 40, no. 4, pp. 424–426, 1993.
[2.59] J. D. Boles, J. E. Bonavia, J. H. Lang, and D. J. Perreault, ‘A Piezoelectric-Resonator-Based DC–DC Converter Demonstrating 1 kW/cm Resonator Power Density’, *IEEE Trans. Power Electron.*, vol. 38, no. 3, pp. 2811–2815, 2023, doi: 10.1109/TPEL.2022.3217773.
[2.60] A. V. Carazo, ‘Piezoelectric Transformers: An Historical Review’, *Actuators*, vol. 5, no. 2, p. 12, 2016.

[2.61] J. Forrester *et al.*, ‘Performance of PZT-based piezoelectric transformers for use in high-temperature converters’, in *11th International Conference on Power Electronics, Machines and Drives (PEMD 2022)*, Jun. 2022, pp. 41–46. doi: 10.1049/icp.2022.1012.
[2.62] Y. Huang, W. Huang, Q. Wang, and X. Su, ‘Research on the Equivalent Circuit Model of a Circular Flexural-Vibration-Mode Piezoelectric Transformer With Moderate Thickness’, *IEEE Trans. Ultrason. Ferroelectr. Freq. Control*, vol. 60, no. 7, pp. 1538–1543, 2013.
[2.63] D. J. Falimiaramanana, F. E. Ratolojanahary, J. E. Lefebvre, L. Elmaimouni, and M. Rguiti, ‘2D Modeling of Rosen-type Piezoelectric Transformer by Means of a Polynomial Approach’, *IEEE Trans. Ultrason. Ferroelectr. Freq. Control*, 2020.
[2.64] J. Forrester, J. Davidson, M. Foster, and D. Stone, ‘Equivalent Circuit Parameter Extraction Methods for Piezoelectric Transformers’, in *21st European Conference on Power Electronics and Applications*, Genova, Italy, 2019.
[2.65] Prem Prakash and Dheeraj K Khatod, ‘Optimal sizing and siting techniques for distributed generation in distribution systems: A review’, *Renew. Sustain. Energy Rev.*, vol. 57, pp. 111–130, 2016.
[2.66] H. Nobahari, S. A. Kordkheili, and S. S. Afshari, ‘Hardware-in-the-loop optimization of an active vibration controller in a flexible beam structure using evolutionary algorithms’, *J. Intell. Mater. Syst. Struct.*, vol. 25, no. 10, pp. 1211–1223, 2014.
[2.67] F. Boria, B. Stanford, S. Bowman, and P. Ifju, ‘Evolutionary Optimization of a Morphing Wing with Wind-Tunnel Hardware in the Loop’, *AIAA J.*, vol. 47, no. 2, pp. 399–409, 2009.
[2.68] S. Bhowmick, R. Vasu, S. K. Chattopadhyay, and C. Chakraborty, ‘A PSO-Based Optimized Hybrid PWM Strategy for a Binary Asymmetric Cascaded H-Bridge Photovoltaic Inverter With Single PV Source Per Phase’, *IEEE J. Emerg. Sel. Top. Power Electron.*, vol. 12, no. 2, pp. 1654–1665, Apr. 2024, doi: 10.1109/JESTPE.2023.3347643.
[2.69] J. Kennedy and R. Eberhart, ‘Particle Swarm Optimisation’, in *IEEE International Conference on Neural Networks*, Perth, Australia, 1995.
[2.70] R. Hooke and T. A. Jeeves, ‘“Direct Search” Solution of Numerical and Statistical Problems’, *J. ACM*, vol. 8, no. 2, pp. 212–229, Apr. 1961, doi: 10.1145/321062.321069.
[2.71] G. F. Fine, L. M. Cavanagh, A. Afonja, and R. Binions, ‘Metal Oxide Semi-Conductor Gas Sensors in Environmental Monitoring’, *Sensors*, vol. 10, pp. 5469–5502, 2010.
[2.72] H. Kurosawa, Y. Y., N. Miura, and N. Yamazoe, ‘Stabilized zirconia-based NO, sensor operative at high temperature’, *Solid State Ion.*, vol. 79, pp. 338–343, 1995.
[2.73] T. Liu, X. Wang, L. Li, and J. Yua, ‘Review—Electrochemical NOx Gas Sensors Based on Stabilized Zirconia’, *J. Electrochem. Soc.*, vol. 164, pp. 610–619, 2017.
[2.74] 2B Technologies, Inc., ‘Ozone Monitor Operation Manual Model 202’. 2017. Accessed: Aug. 28, 2024. [Online]. Available: https://2btech.io/wp-content/uploads/docs/manuals/model_202_revJ.pdf
[2.75] ‘Tesiplz Car Air Purifier,Negative Ion Ozone Generator UV Light 3 Modes Reusable Air Freshener,Portable USB Touch Small Desktop Odor Removal Machine,Home Automotive Deodorizer,No Filter Required’. Accessed: Aug. 28, 2024. [Online]. Available: https://www.amazon.co.uk/Tesiplz-Generator-Freshener-Automotive-Deodorizer/dp/B0BWDLJD3C?th=1
[2.76] Murata Manufacturing Co., Ltd., ‘MHM502 series / Ozonizer module’. [Online]. Available: https://www.murata.com/products/productdata/8802734145566/M13X-MHM502-DS-PDF.pdf

[2.77] Oxidation Technologies LLC., Accessed: Aug. 28, 2024. [Online]. Available: https://www.oxidationtech.com/vmus4.html
[2.78] V. I. Gibalov and G. J. Pietsch, ‘On the Performance of Ozone Generators Working with Dielectric Barrier Discharges’, *Ozone Sci. Eng.*, vol. 28, no. 2, pp. 119–124, May 2006, doi: 10.1080/01919510600559419.
[2.79] Asynt Ltd., ‘Laboratory Ozone Generator’. 2023. Accessed: Aug. 28, 2024. [Online]. Available: https://www.asynt.com/wp-content/uploads/2023/07/Asynt-Laboratory-Ozone-Generator-V2.0.pdf

3 Experimental Equipment

3.1 Introduction

This chapter describes the equipment used in the experiments described in the later chapters. Equipment used during experimental validation includes the DBD reactor, oscilloscopes for waveform monitoring and power calculation, a personal-computer-based controller, a means of monitoring the output of the reactor and a power supply or waveform generator and amplifier. A general experimental setup block diagram is shown in Fig. 3.1.

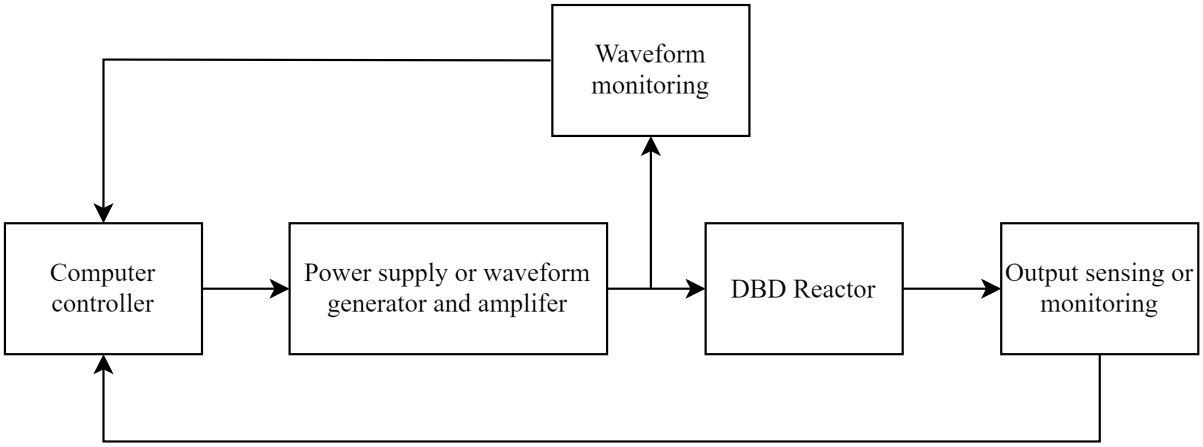

Fig. 3.1 General DBD experimental setup

This chapter also describes the components of the custom power supplies used in this thesis. These include three piezoelectric resonators (PRs), two piezoelectric transformers (PTs), a conventional HV transformer, and a GaN inverter. Also used are an off-the-shelf arbitrary waveform generator (AWG) and a high voltage (HV) amplifier.

3.2 DBD (Dielectric Barrier Discharge) Reactors

In this thesis, two DBD reactors are used in the experimental sections to validate various hypotheses. Since the reactors are significantly different to each other they are described in their own sections.

3.2.1 Coaxial Reactor

The coaxial ozone producing reactor (ozoniser) was designed and made by the author, seen in Fig. 3.2. An alumina (aluminium oxide) coating on an aluminium electrode (labelled A in Fig. 3.2) forms the dielectric and brass is used for the second electrode (labelled B).

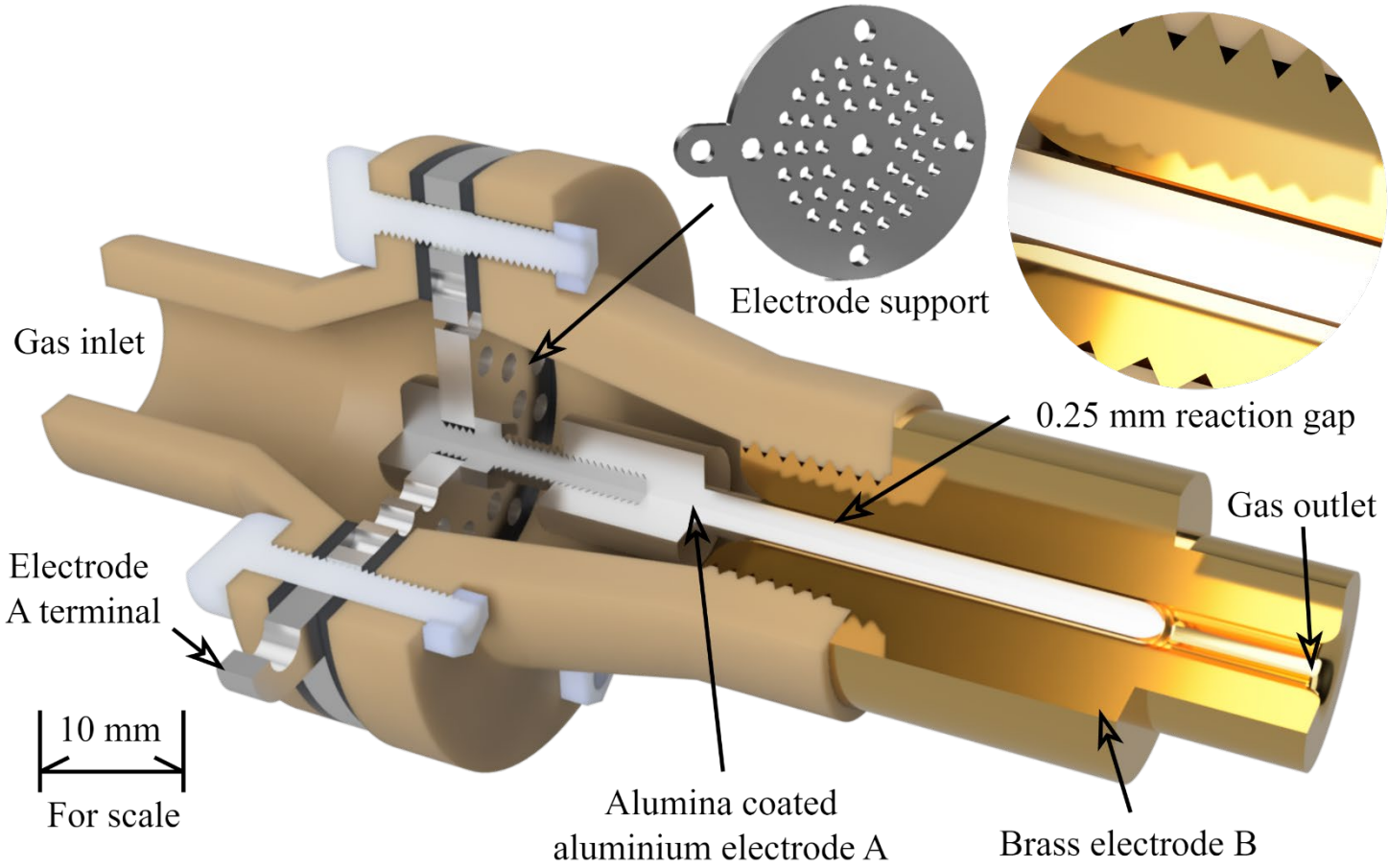

Fig. 3.2 Cut-away 3D model of the coaxial DBD reactor

Table 3.1 Coaxial DBD reactor specifications

Inner electrode diameter	3 mm
Alumina dielectric thickness	~ 60 µm
Average electrode gap distance	0.25 mm
Electrode active length	20 mm
Maximum reactor power	5 W
Maximum reactor voltage	1.5 kV_{RMS}

The key dimensions and parameters of the coaxial reactor can be seen in Table 3.1 and the design can be seen in Fig. 3.2. The gas enters the reactor inlet on the left, passing through holes in the electrode A support, where it then travels through the reaction gap between electrodes A and B, before exiting the reactor. Electrode A is constructed from aluminium with a dielectric layer of alumina (aluminium oxide) surrounding it and electrode B is constructed from brass with no surface treatment. The plastic pieces coloured light brown in Fig. 3.2 are made from nylon plastic. The gas outlet is on the right of the reactor (see Fig. 3.2) and was connected to an ozone monitor to quantify the output of the reactor. A photograph of the reactor in an experimental setup can be seen in Fig. 3.3.

This reactor was designed and made by the author to use components (the piece with the gas inlet, the electrode support and electrode A) that were left-over from previous research. Other parts (electrode B and its threaded partner) were turned by the author from brass and nylon feedstock for use in the reactor. Electrode A was aligned in the centre of electrode B by manipulating the electrode support via the gas inlet until concentricity was observed through the gas outlet (lit via the inlet).

This reactor is used where a low plasma ignition voltage is required yet can generate a reasonable quantity of ozone due to the large active area of electrode A in this configuration. (A previous design in Fig. 2.5 has a pair of these electrodes end to end.)

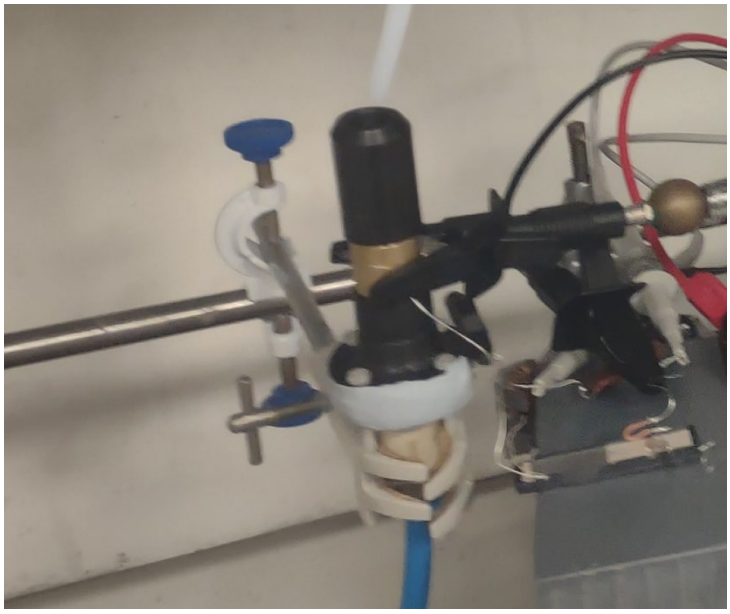

Fig. 3.3 Coaxial DBD reactor shown in an experimental setup. Gas is fed in the bottom; the ozone monitor is fed from the top. A PT is powering the reactor.

This reactor has a very thin dielectric barrier of ~60 µm (see Table 3.1), which results in a low plasma ignition voltage (a useful amount of DBD occurs <1 kV_{RMS}). This makes it suitable for lower-voltage power supplies. It also has a large active surface area for high ozone production. However, this reactor type does not allow the DBD to be monitored from the outside since the reaction gap is enclosed by the brass electrode. It should also be noted that the thin dielectric layer is more susceptible to degradation at higher reactor power.

3.2.2 Biaxial Reactor

The second, biaxial, reactor used in these experiments is asymmetrical with a pair of 3 mm diameter cylindrical electrodes, one alumina (aluminium oxide) and one aluminium. The reaction gas flows between the electrodes, separated by a reaction gap of approximately 0.25 mm. The main body of the reactor is constructed from PEEK plastic with a quartz window on the front to allow the DBD to be seen to verify operation. The design of the reactor can be seen in Fig. 3.4. Specifications can be seen in Table 3.2.

This reactor has a thicker dielectric than the coaxial design, making it more suitable for higher voltage power supplies and operation for long periods of time without any changes in performance due to degradation of the electrodes.

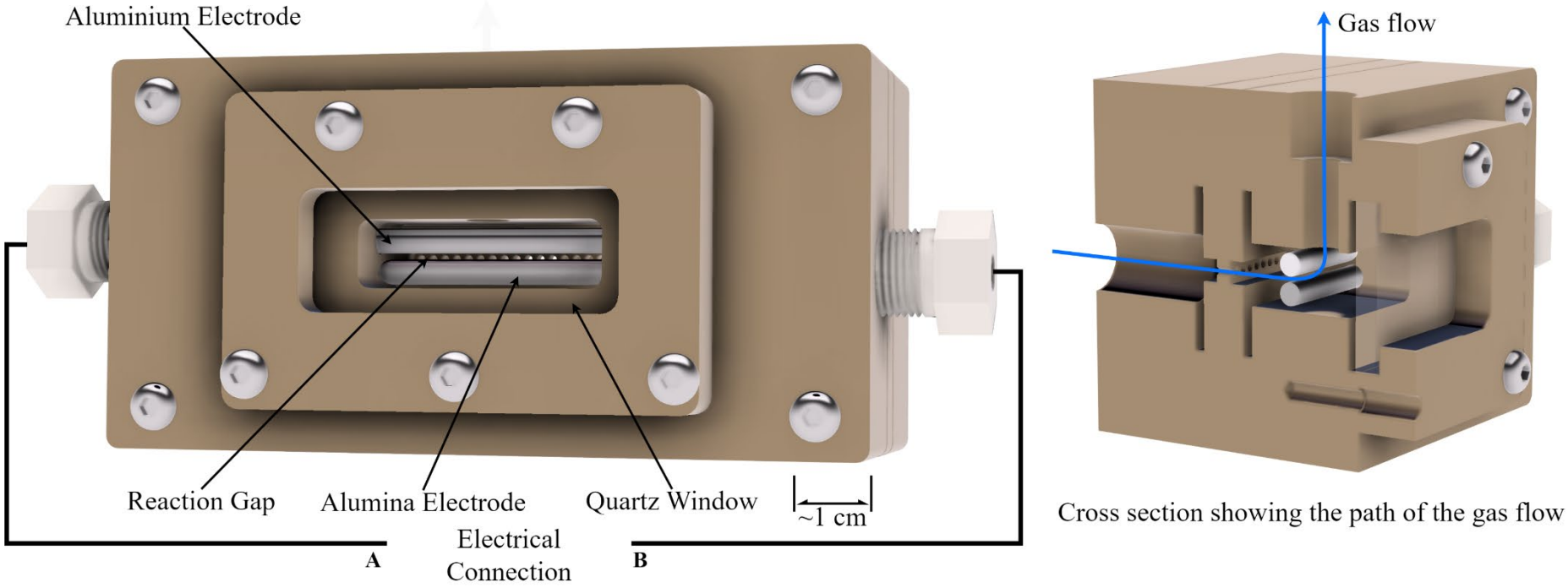

Fig. 3.4 3D model of the biaxial DBD Reactor

This reactor was designed by Thomas Holmes (post-doctoral research associate) and Mario Dorna (chemical engineering technician) to allow a larger surface area than their previous design (Fig. 2.5), whilst still being able to observe the plasma via the quartz window. A different electrode with thicker dielectric than that of the coaxial reactor was used to allow the reactor to operate at higher power. Solidworks, Autodesk Fusion 360 and OnShape were used to design and render these reactors.

A photograph of the reactor in operation can be seen in Fig. 3.5.

Table 3.2 Biaxial DBD reactor specifications

Electrode diameter	3 mm
Alumina dielectric thickness	0.675 mm
Average electrode gap distance	0.25 mm
Electrode active length	20 mm
Maximum reactor power	15 W
Maximum reactor voltage	5 kV_{RMS}

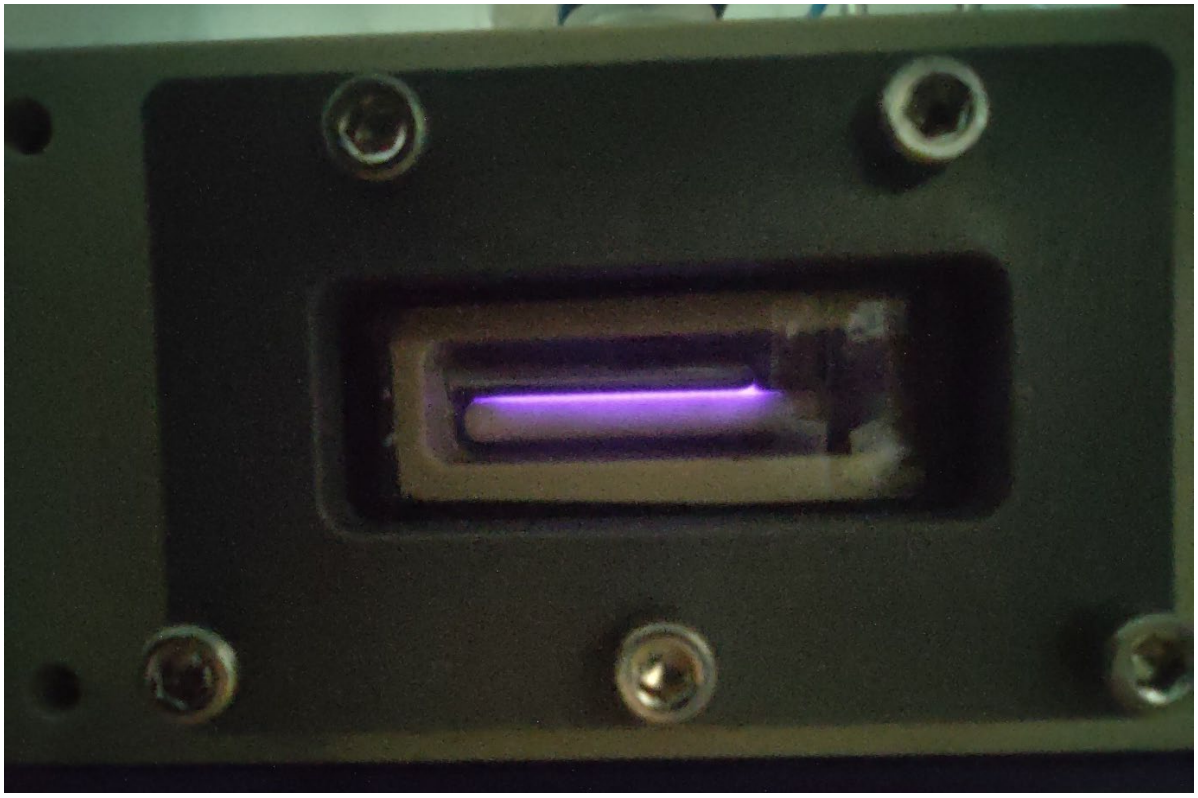

Fig. 3.5 Photograph of the biaxial reactor in operation

3.3 Piezoelectric Transformers

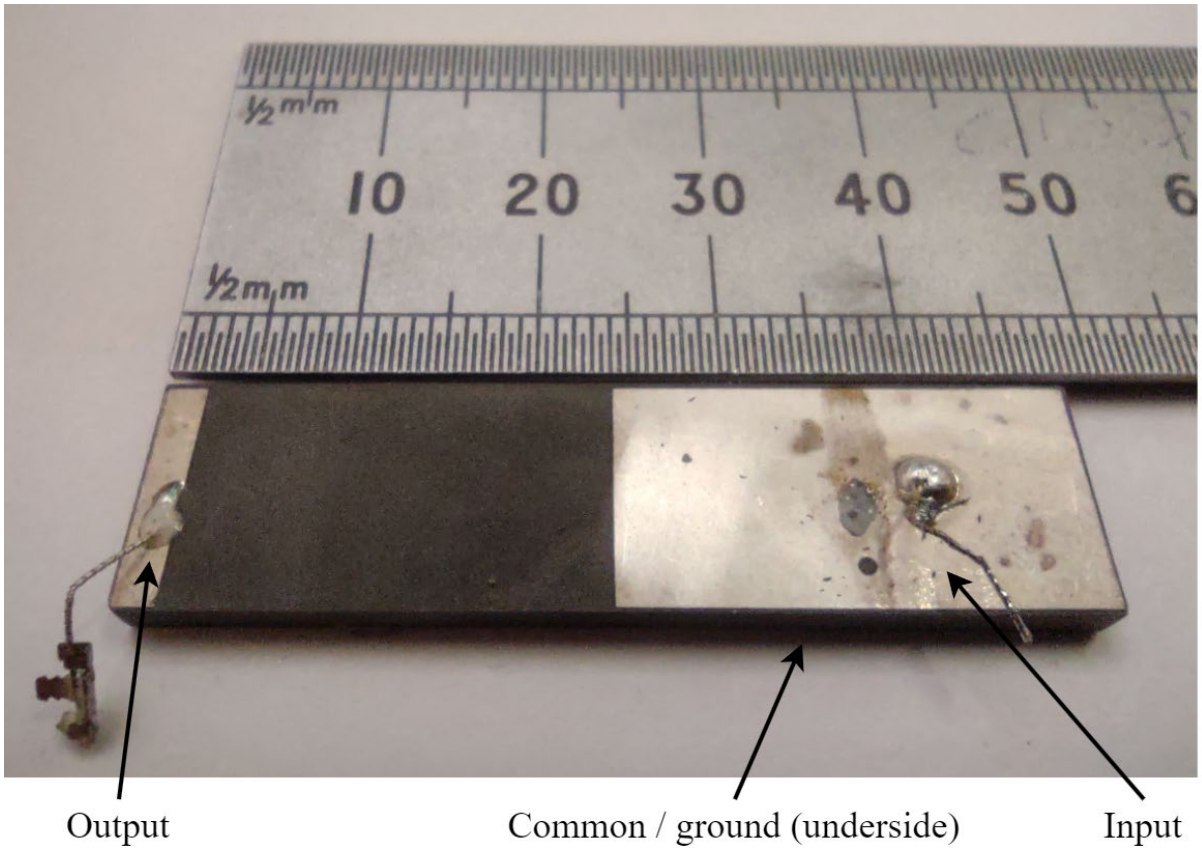

Fig. 3.6 Photograph of the STEMiNC SMSTF71P12S8 piezoelectric transformer with labelled electrodes

The STEMiNC SMSTF71P12S8 [3.1] Rosen-type piezoelectric transformer (PT) is used in Chapter 6 to provide the required voltage gain for the reactor. A photograph of the device is shown in Fig. 3.6. The gain spectrum of the device was measured using a Bode 100 analyser and is shown in Fig. 3.7. As can be seen from gain magnitude curve (blue), two resonant modes exist, one at 36 kHz and another at 72 kHz, each providing a high voltage gain. The second resonant mode occurs at approximately twice the frequency of the first resonant mode.

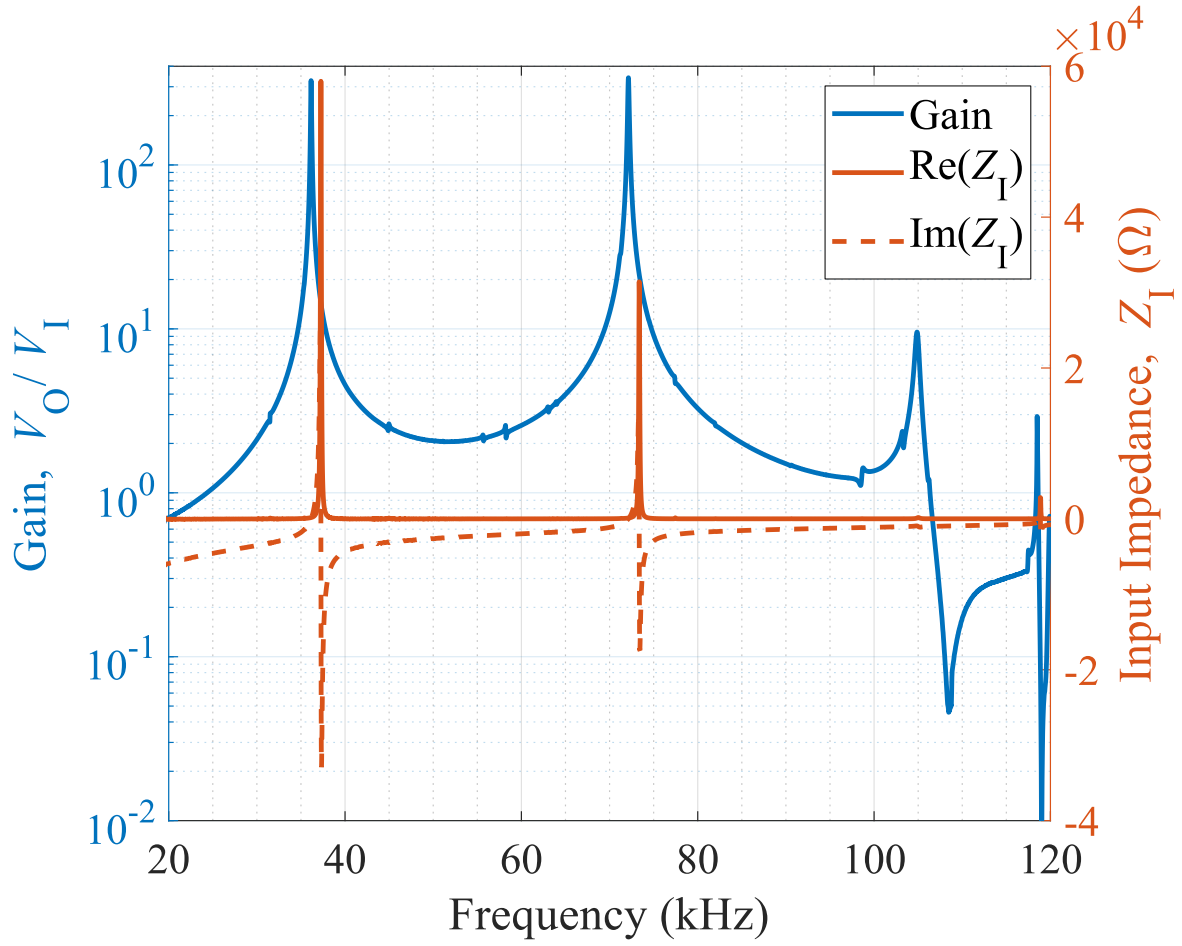

Fig. 3.7 Piezoelectric transformer (STEMiNC SMSTF71P12S8) gain and input impedance

The real, Re(Z_I), and imaginary, Im(Z_I), parts of the input impedance Z_I are shown in solid orange and dashed orange respectively in Fig. 3.7. The peak gain occurs when the input impedance is low (~200 Ω). This contrasts with a conventional transformer where the magnetising inductance is relatively high. For a PT, the low input impedance could result in high current and high power dissipated. However, there is still significant gain at frequencies between the resonant and anti-resonant points for each resonant mode (36-37 kHz and 72-73 kHz) where the impedance is much higher, allowing lower losses and high efficiency.

This PT was parameterised using Technique 3 shown in Chapter 4. These parameters are shown in the extended Mason equivalent circuit model of this PT in Fig. 3.8.

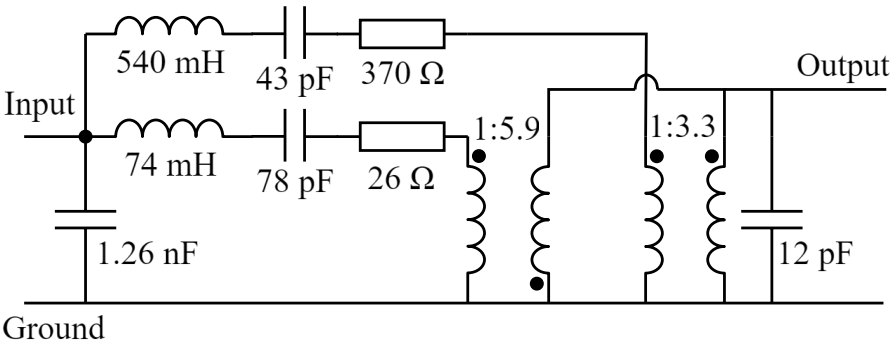

Fig. 3.8 Equivalent circuit of the STEMiNC SMSTF71P12S8 piezoelectric transformer

A second PT, a small SMMTF85P1S50 was used to test the parameterisation methods in Chapter 4. A photograph of this PT is shown in Fig. 3.9. The parameters can be found in Section 4.6.

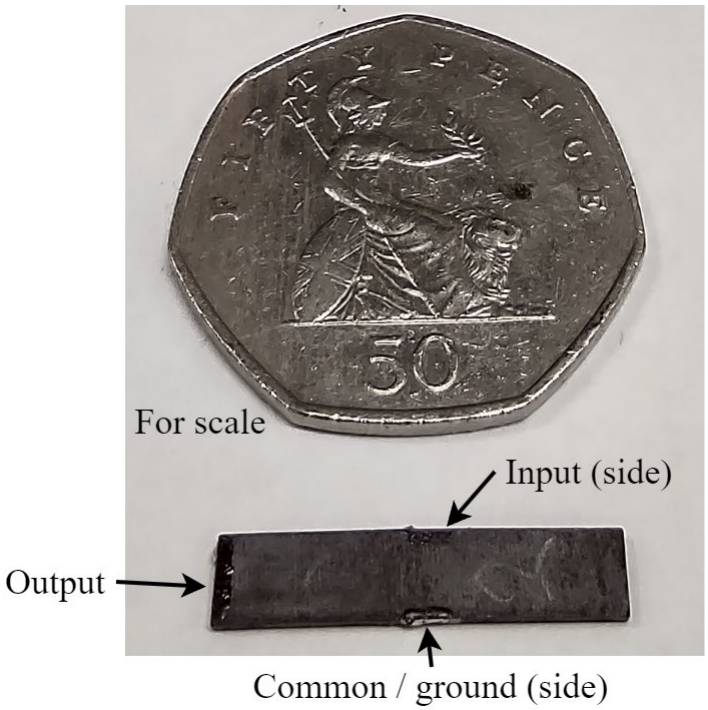

Fig. 3.9 Photograph of the SMMTF85P1S50 PT with a 50p piece for scale and labelled electrodes

3.4 Piezoelectric Resonators

In this thesis the performance of three PR devices from STEMiNC were investigated as described in Chapter 5 where they are used to provide voltage magnification. A photograph comparing the size of each PR is in Fig. 3.10, highlighting the difference in their dimensions.

In Fig. 3.10, the resonators can be seen as they were used, in custom holders. These holders were designed by the author to hold the resonators via sprung electrical contacts in the centre

of the resonator, allowing them to vibrate freely without touching the sides of the holder as this might contribute to energy loss through friction. The holders were intended to provide an electrical contact to the resonator (soldering is also possible); provide some level of protection for the resonator; reduce friction on the resonator; and decrease the influence of the resonators' environment on the resonators' equivalent circuits.

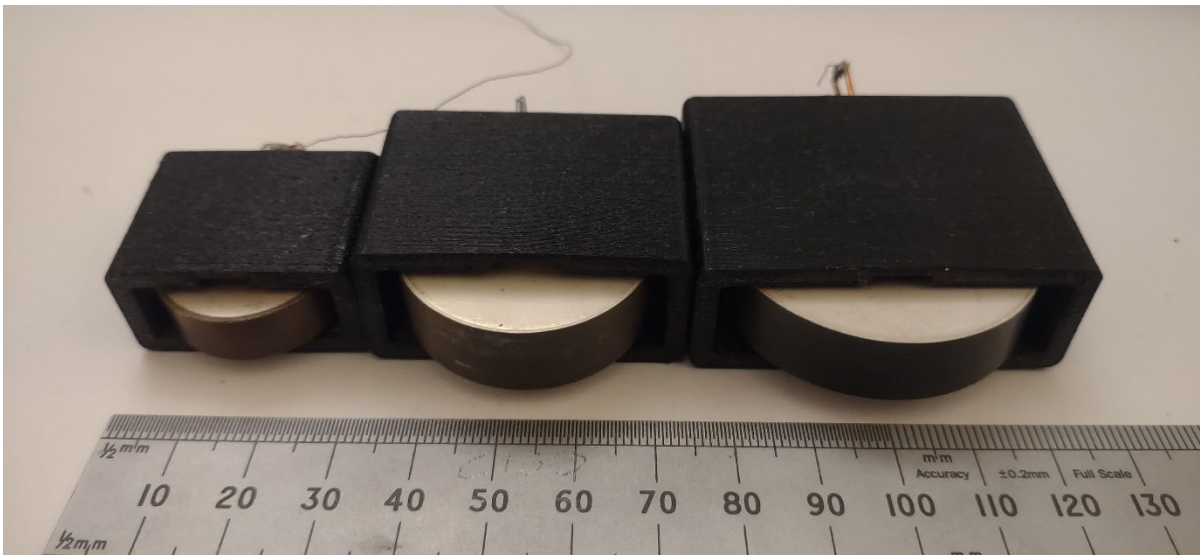

Fig. 3.10 Photograph of the SMD25T85F234S, SMD35T12S118 and SMD43T105F200S PRs from left to right in their purpose-built holders

Table 3.3 Piezoelectric resonator parameters

	SMD25T85F234S [3.2]	SMD35T12S118 [3.3]	SMD43T105F200S [3.4]
C_P (pF)	494	567	1140
R (Ω)	13.5	10.7	4.31
L (mH)	17.5	33.4	20.2
C (pF)	194	188	508
Q_{RLC}	704	1250	1460

In Chapter 4, a particle swarm optimisation method (Technique 3) is described for finding the input impedance of a piezoelectric transformer. This technique was used to determine the first resonant mode of three PRs from STEMiNC; the parameters are shown in Table 3.3, representing the values of the equivalent circuit shown in Fig. 2.11. An example of the closeness of the fit is in Fig. 3.11. These resonators and their parameters are used in Chapter 5.

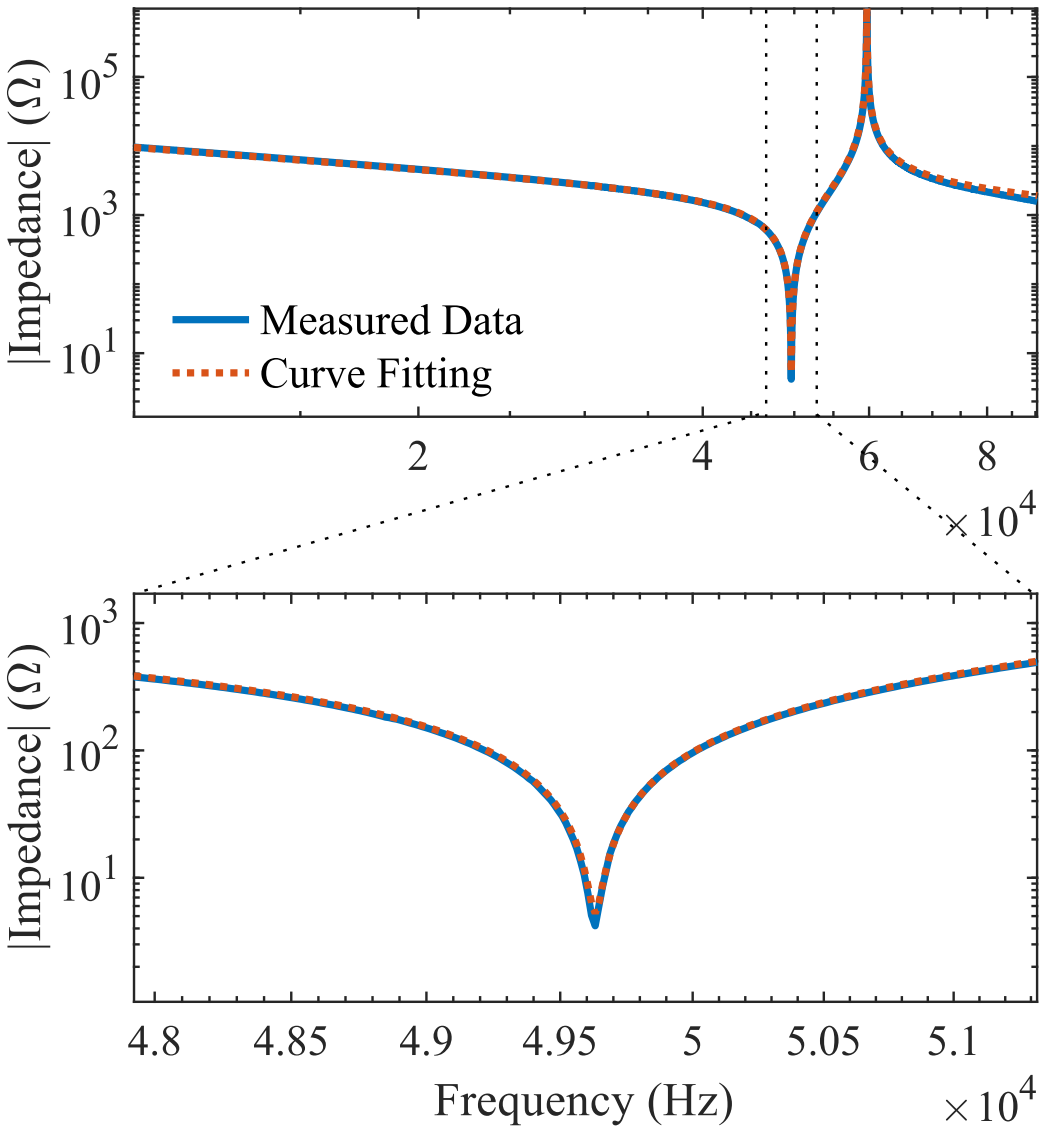

Fig. 3.11. Resonator parameterisation fit to measured data for the SMD43T105F200S.

3.5 Conventional HV Transformer

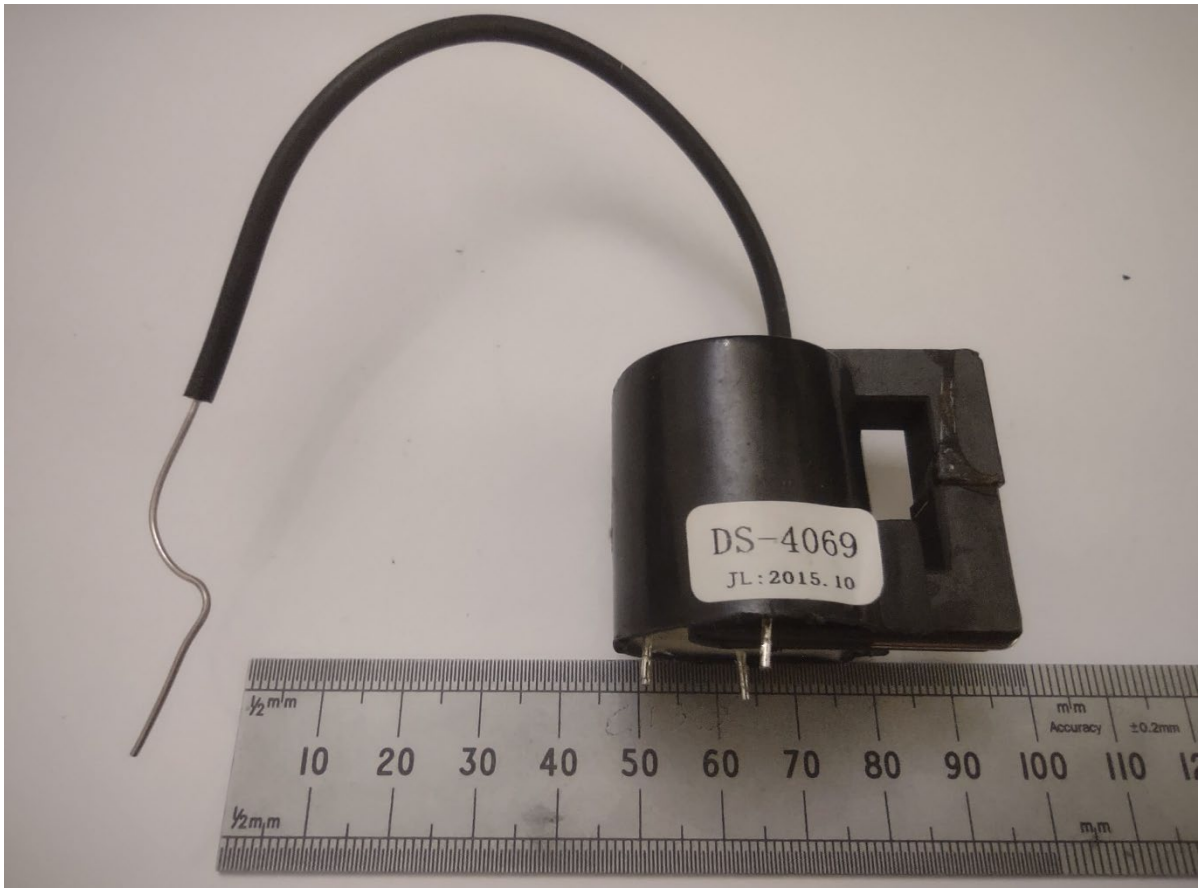

Fig. 3.12 Photograph of the HV transformer

In Section 6.3, a conventional magnetic HV transformer is required to provide voltage gain. A photograph of the transformer used is in Fig. 3.12. The frequency response of the transformer was characterised between 10 kHz and 1 MHz. This is shown in Fig. 3.13 and the equivalent circuit model is shown in Fig. 3.14. This equivalent circuit models the response up-to and including the resonant peak at 80 kHz.

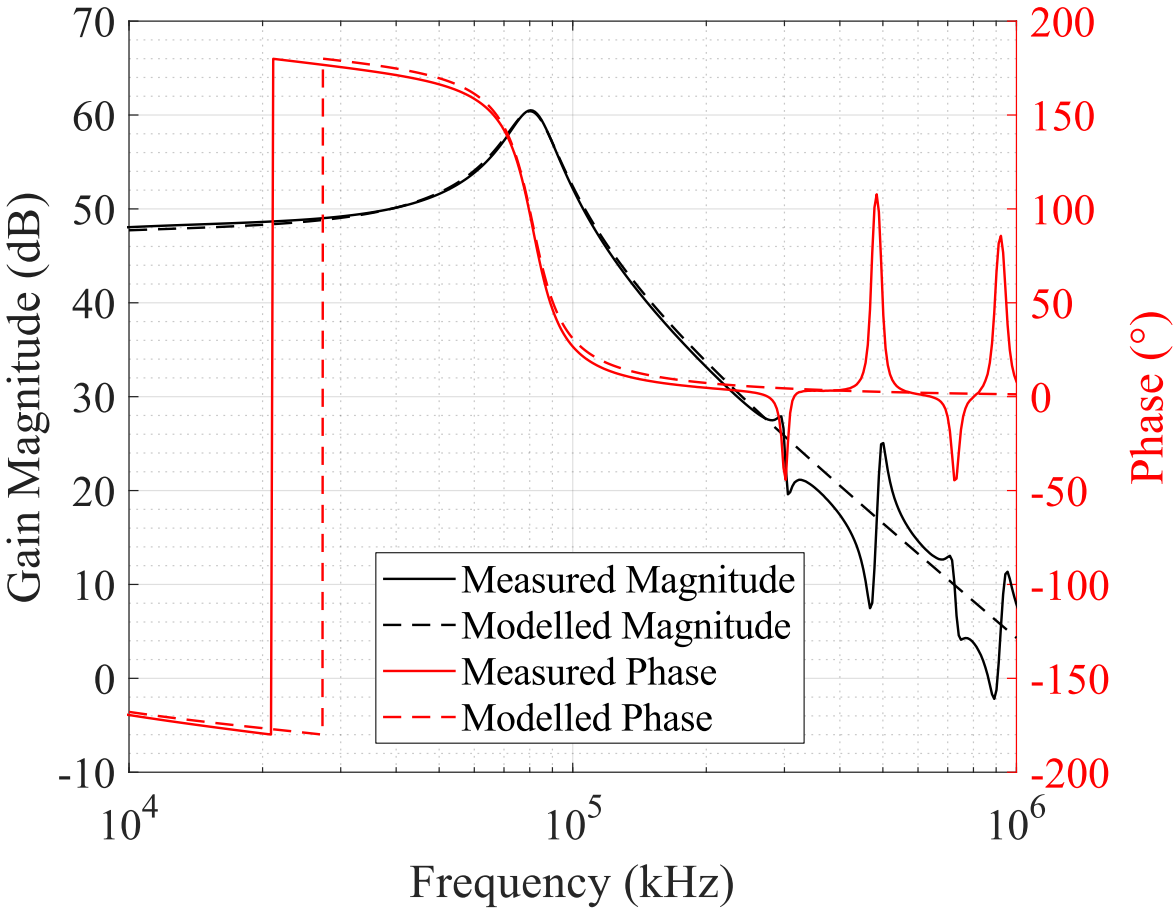

Fig. 3.13 HV transformer and equivalent circuit frequency response

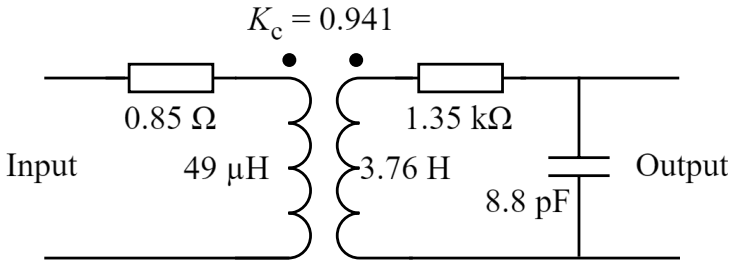

Fig. 3.14 Equivalent circuit model of the HV transformer, K_c is the transformer coupling coefficient

3.6 Low Voltage AC Inverter

The purpose of the inverter is to convert the low voltage DC input, V_{DC}, to a selective-harmonic-generated (explained in Section 6.2) or a pulse-width modulated (PWM) waveform, V_I, at a moderate voltage. This waveform can then be used to drive the piezoelectric devices or the HV transformer.

3.6.1 Hardware Description

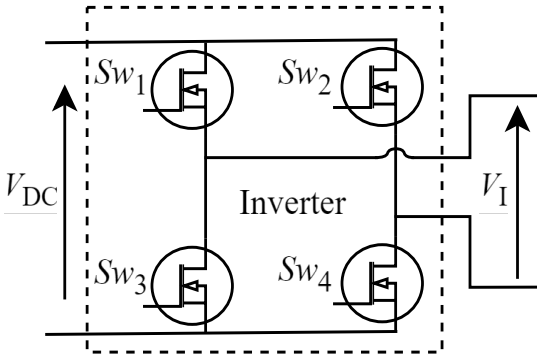

Fig. 3.15 Inverter circuit diagram

In chapters 5 and 6, a digitally controlled GaN full-bridge inverter is used (a simplified circuit diagram can be seen in Fig. 3.15). This is based on a low-voltage three-phase motor driver that had been previously designed by the author for another project. The specifications for this inverter can be seen in Table 3.4, and pictures of the front and back in Fig. 3.16.

Table 3.4 Inverter specifications

Bus voltage	48 V
GaN switches (half-bridge modules)	TI LMG5200 [3.5]
Controller IC	dsPIC33CH512MP505 [3.6]
Switch on-state resistance	15 mΩ
Switch slew-rate	50 V/ns
Switch current rating	10 A
PCB dimensions	55 mm × 32 mm

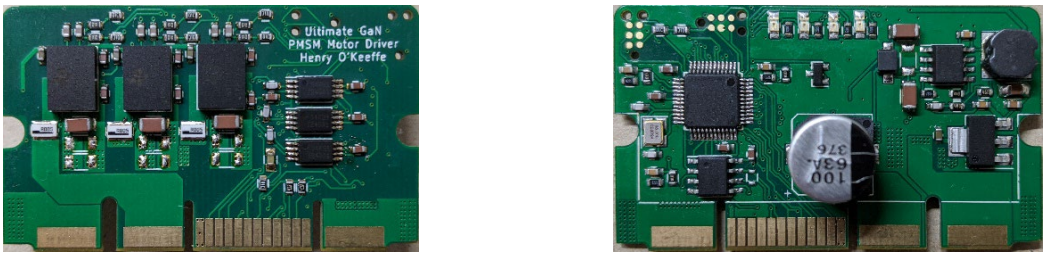

a) b)

Fig. 3.16 Photographs of the font, a) and back, b) of the GaN inverter, actual size

To communicate with the host PC (in a hardware-in-the-loop setup for example), the GaN inverter has a universal, asynchronous receive / transmit (UART), which was connected to an

FT232-RL USB-UART bridge IC, which provides universal serial bus (USB) connectivity. Since the H-bridge only required 2 of the 3 bridge inverter legs, the spare half-bridge leg was not used.

3.6.2 Microcontroller Firmware and Communications Protocol

For the work in this thesis, two different microcontroller programs were developed for the GaN inverter. They both use the same communications protocol frame structure, seen in Fig. 3.17. The frame starts with an ASCII “C” (without the quotes) and ends with “E”. After the “C”, the specific command is sent as an integer coded in ASCII, then an “R” or “W” for read operation or write operation respectively. If a “W” is sent, the data to write is sent as an ASCII encoded floating point value and followed by an “E” to end the frame. An example of a transaction (frame sent, followed by a response) might be “C10W0.145E” from host to inverter, followed by “E” sent back by the inverter to acknowledge the write operation.

"C"	Command (integer) e.g. "12"	"R" or "W" for read or write	Data (floating point) e.g. "10.253" if this is a write operation	"E"

Host to Inverter

Data (floating point) e.g. "10.253" if a read is requested	"E"

Response from Inverter

Fig. 3.17 General communications protocol frame structure

One microcontroller program is for the work in Chapter 5. This program drives the GaN MOSFETs with gate signals to create an AC pulse-train with a variable frequency, duty-cycle and dead-time between high and low side switching events (e.g. between Sw_1 turning on and Sw_3 turning off in Fig. 3.15). This program is called the inverter program and the list of commands for this program can be seen in Table 3.5.

Table 3.5 List of commands for the inverter program

Command name	Command	Units
Duty cycle	1	0-1 corresponds to 0-100% duty
Update	3	Writing 1 sets the output according to all new commands sent since the last update command
Frequency	4	Hz
Dead-time	5	0-1 corresponds to 0-100% dead-time

The other program calculates the switching angles for the selective harmonic generation (SHG) detailed in Chapter 6, and controls the LMG5200 half-bridge modules accordingly. The valid commands for this SHG program are in Table 3.6. When the command "Update" (Table 3.6) is given, the microcontroller (Table 3.4), takes several seconds to calculate the new switching angles and generate the new waveform. The more harmonics are controlled, the longer this takes. The SHG program uses minimal deadtime, in the 10s of ns.

Table 3.6 List of commands for the SHG program

Command name	Command	Units
Harmonic amplitude	1	Amplitude of the last harmonic number set, 0-1, which is scaled by the DC bus voltage
Harmonic number	2	Harmonic number to be set, starting at 1 for the first harmonic
Update	3	Writing 1 sets the output according to all new commands sent since the last update command
Fundamental frequency	4	Hz
Angle	5	Radians
Number of harmonics	6	Sets how many harmonics to control. This influences how many pulses per fundamental cycle there are. This must be set before commands 1, 2, 3 or 5.

3.7 Equipment Use

The equipment described in this chapter was used in the experimental sections of several other chapters. A breakdown of what equipment was used in what chapter can be found in Table 3.7. This table includes a basic description of other equipment not otherwise described in this chapter.

Table 3.7 Equipment cross-reference

Where equipment is used	Equipment Description	Section equipment is detailed
Chapter 4	Omicron Bode 100 impedance analyser	-
	SMMTF85P1S50 piezoelectric transformer	3.3
Section 5.2	Picoscope 6404C PC-based oscilloscope	-
	TREK 10/40A-HS HV amplifier	-
	Tektronix P6015A HV probe	-
	RSDG 830 waveform generator	-
	Coaxial reactor	3.2.1
Section 5.4	Picoscope 6404C PC-based oscilloscope	-
	Yokogawa PX8000 power analyser	-
	TTi EX354D bench PSU	-
	Tektronix P6015A HV probe	-
	2B Technologies 106-MH ozone monitor	-
	Coaxial reactor	3.2.1
	SMD43T105F200S piezoelectric resonator	3.4
	GaN Inverter	3.6
Section 6.3	Picoscope 6404C PC-based oscilloscope	-
	Yokogawa PX8000 power analyser	-
	TTi EX354D bench PSU	-
	Tektronix P6015A HV probe	-
	2B Technologies 106-MH ozone monitor	-
	Biaxial reactor	3.2.2
	Conventional transformer	3.5
	GaN Inverter	3.6
Section 6.4	Picoscope 6404C PC-based oscilloscope	-
	Picoscope 4224 PC-based oscilloscope	-
	TTi EX354D bench PSU	-
	Siglent SDM3055 digital multimeter	-
	Coaxial reactor	3.2.1
	SMSTF71P12S8 piezoelectric transformer	3.3
	GaN Inverter	3.6
	Tektronix P6015A HV probe	-
	2B Technologies 106-MH ozone monitor	-
Chapter 7	Picoscope 6404C PC-based oscilloscope	-
	TREK 10/40A-HS HV amplifier	-
	Tektronix P6015A HV probe	-
	RSDG 830 waveform generator	-
	2B Technologies 106-MH ozone monitor	-
	Bronkhorst F-201CV-20K-AAD-22-V mass flow controller	-

3.8 References

[3.1] Steiner and Martins Inc., ‘Steminc Piezoelectric Ceramic Supplier SMSTF71P12S8’, STEMINC. Accessed: Aug. 29, 2024. [Online]. Available: https://steminc.com/PZT/single-layer-piezo-transformer-71-khz-12w

[3.2] Steiner and Martins Inc., ‘Steminc Piezoelectric Ceramic Supplier SMD25T85F234S’, STEMINC. Accessed: Aug. 29, 2024. [Online]. Available: https://steminc.com/PZT/piezoelectric-disc-25x85mm-s-235-khz

[3.3] Steiner and Martins Inc., ‘Steminc Piezoelectric Ceramic Supplier SMD35T12S118’, STEMINC. Accessed: Aug. 29, 2024. [Online]. Available: https://steminc.com/PZT/piezo-ceramic-disc-35x12mm-s-190-khz

[3.4] Steiner and Martins Inc., ‘Steminc Piezoelectric Ceramic Supplier SMD43T105F200S’, STEMINC. Accessed: Aug. 29, 2024. [Online]. Available: https://steminc.com/PZT/piezo-electric-disc-43x10mm-s-200-khz

[3.5] ‘LMG5200 data sheet, product information and support | TI.com’. Accessed: Aug. 30, 2024. [Online]. Available: https://www.ti.com/product/LMG5200

[3.6] ‘dsPIC33CH512MP505’. Accessed: Aug. 30, 2024. [Online]. Available: https://www.microchip.com/en-us/product/dspic33ch512mp505#document-table

4 Piezoelectric Transformer and Resonator Equivalent Circuit Parametrisation

4.1 Introduction

This chapter describes parameterisation methods used to find the equivalent circuit parameters of piezoelectric transformers and resonators that are required for the modelling and simulation work in chapters 5 and 6.

There are several general methods of parameterising piezoelectric transformers and resonators. One approach used in [4.1] determines the model parameters using the mechanical structure of a PT combined with Legendre polynomial modelling. The work in this chapter, however, is based on fitting the electrical impedance over the desired frequency range, as previously used in [4.2] and [4.3].

Three techniques for extracting equivalent circuit parameters from piezoelectric transformers based on the Mason equivalent circuit model are explored, starting from a frequency domain analysis of the input and output impedance. Two optimisation techniques to improve the accuracy of the parameterisation are detailed and tested, each allowing multiple resonant modes to be modelled, with the aim of minimising the percentage error of the fit.

Here, three parameterisation methods are explored: technique 1 (T1), an improved parameterisation of the cost function employed in [4.2] to provide greater efficacy of the optimiser; technique 2 (T2), the incorporation of an additional step to further refine the parameters and technique 3 (T3), particle swarm optimisation (PSO) where the initial estimations of the equivalent circuit parameters are taken directly from the impedance spectrum.

4.2 Prior Work

The work presented here builds on that of Horsley, *et al.* [4.3] and method 1 from Forrester, *et al*. [4.2], where the input and output impedance spectra are fitted to the Mason equivalent circuit model shown in Fig. 2.12.

The resonant frequency, $\omega_0 = 1/\sqrt{LC}$, of L and C is determined by locating the frequency of minimum impedance measured when the output is connected to the common node (i.e. short-

circuited). Specifically, ω_0 is found by evaluating $\min\left|Z_{\text{in(s-c)M}}(\omega)\right|$ where $Z_{\text{in(s-c)M}}$ is the measured impedance looking into the input port of the PT with the output short-circuited (s-c). The resonant frequency provides the product of L and C. The resistance was found as the magnitude of impedance at the resonant frequency, $R \approx Z_{\text{in(s-c)M}}(\omega_0)$.

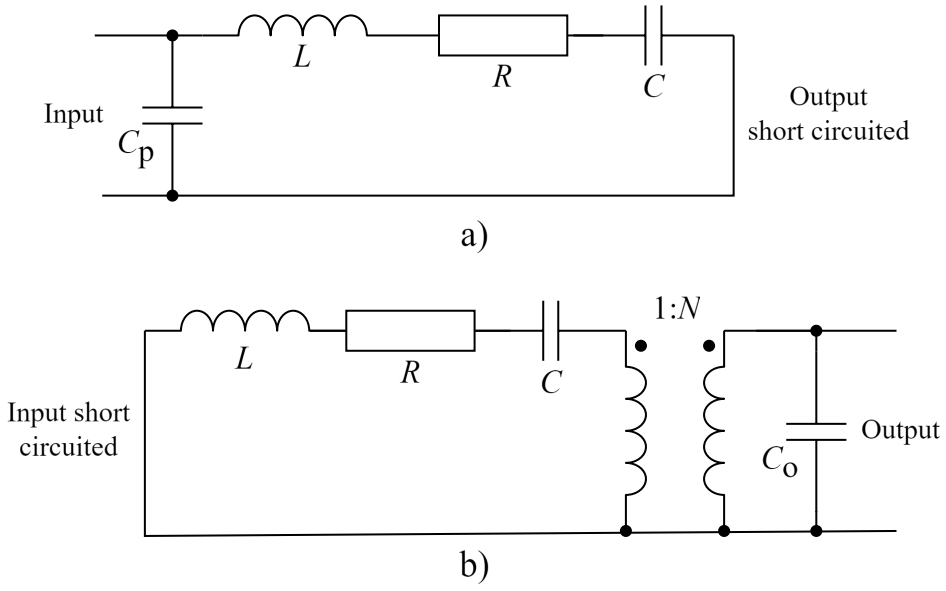

Fig. 4.1 Equivalent circuit models of the PT with a) output and b) input short circuited

Since the output is short-circuited (Fig. 4.1a), the effects of C_o and N can be neglected, leaving only C_p and one independent variable from the RLC branch to be determined. Since C_p and the RLC branch are connected in parallel it is difficult to separate them. A new parameter, β, is introduced here to represent the impedance of the RLC branch:

$$\beta = 2\pi jfL + R + \frac{1}{2\pi jfC} \tag{4.1}$$

Since ω_0 and R have already been determined from the impedance spectrum, only two variables, C_p and β, need to be obtained from a curve-fit, thereby reducing the search space. The cost function (4.2) is defined as the mean squared error between the measured impedance (M_d) and the Mason equivalent circuit calculated impedance (F_d). The summation in (4.2) is taken over the range of the reference impedance dataset (with N_D datapoints) and F_d is determined over the same range.

$$E_{\text{MS}} = \frac{\sum_{d=1}^{N_D}\left(\frac{M_d - F_d}{M_d}\right)^2}{N_D} \tag{4.2}$$

First, $M_d = |Z_{\text{in(s-c)M}}|$, and $F_d = |Z_{\text{in(s-c)}}|$, where

$$Z_{\mathrm{in(s-c)}} = \frac{1}{2\pi j f C_{\mathrm{P}} + \frac{1}{\beta}} \tag{4.3}$$

Equation (4.2) is minimised to find $\min_{C_p,\beta}(E_{\mathrm{MS}}(F_d(C_p,\beta)))$ using the Nelder-Mead method to determine the optimal values for C_{p} and β. It should be noted that the circuit in Fig. 4.1a is identical to the electrical model of a piezoelectric resonator in Fig. 2.11, making this the only step required to find the parameters for a PR.

For parameterising a PT, a similar approach can be applied to the PT output impedance by short-circuiting the input port (Fig. 4.1b) and measuring the impedance at the output port to provide the reference data $M_d = |Z_{\mathrm{out(s-c)M}}|$ and the calculated data $F_d = |Z_{\mathrm{out(s-c)}}|$ where

$$Z_{\mathrm{out(s-c)}} = \frac{1}{2\pi j f C_{\mathrm{o}} + \frac{1}{N^2\beta}} = \frac{1}{2\pi j f C_{\mathrm{o}} + \frac{1}{\beta'}} \tag{4.4}$$

Equation (4.2) can then be used to fit $Z_{\mathrm{out(s-c)}}$ and extract C_{s} and a referred value for the RLC branch impedance, β' using (4.4) which is used to calculate the turns ratio with

$$N = \sqrt{\left|\frac{\beta'}{\beta}\right|} \tag{4.5}$$

To evaluate the performance of the parameterisation, three metrics are used. The metric described (4.6) is the average magnitude of the error ratio ($E_{\%}$). Equation (4.7) describes the average absolute error (E_{abs}) and (4.8) is the coefficient of determination, R^2. N_{D} is the number of measured datapoints being fitted.

$$E_{\%} = \frac{100 \times \sum_{d=1}^{N_{\mathrm{D}}} \left|\frac{M_d - F_d}{M_d}\right|}{N_{\mathrm{D}}} \tag{4.6}$$

$$E_{\mathrm{abs}} = \frac{\sum_{d=1}^{N_{\mathrm{D}}} |M_d - F_d|}{N_{\mathrm{D}}} \tag{4.7}$$

$$R^2 = 1 - \frac{\sum_{d=1}^{N_{\mathrm{D}}} (M_d - F_d)^2}{\sum_{d=1}^{N_{\mathrm{D}}} (M_d - M_{\mathrm{m}})^2} \tag{4.8}$$

where M_{m} is the mean of the measured impedance:

$$M_{\mathrm{m}} = \frac{1}{N_{\mathrm{D}}} \sum_{d=1}^{N_{\mathrm{D}}} M_d \tag{4.9}$$

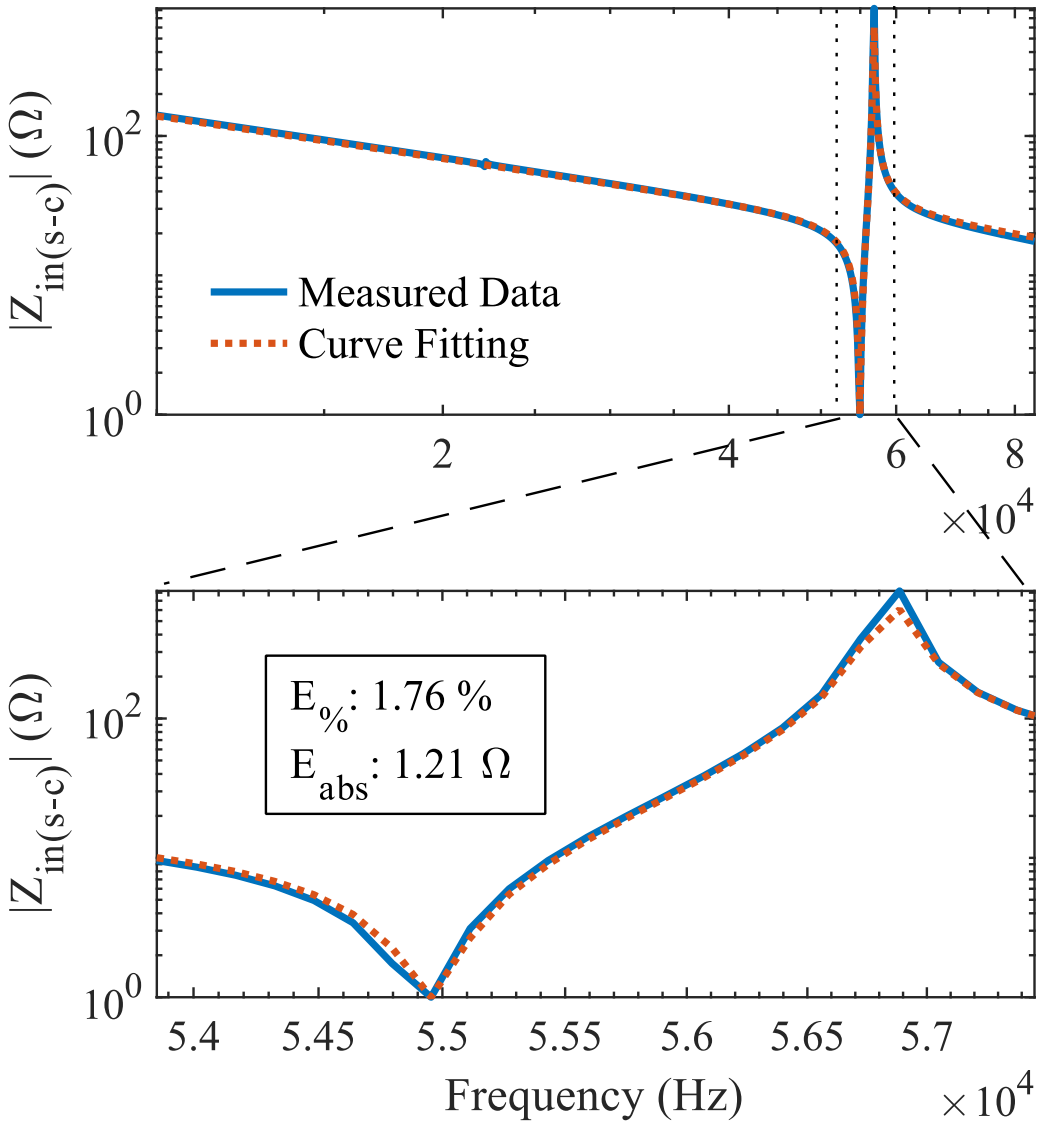

Fig. 4.2 An example curve fit for $|Z_{in(s-c)M}|$

To demonstrate this technique, frequency domain impedance data was taken from a STEMiNC SMMTF85P1S50 Rosen PT (Section 593.3) using an Omicron Bode 100 impedance analyser. 1601 data points were taken over the frequency range 10-1000 kHz with logarithmic spacing. A subset of this data covering the resonant mode(s) was used for fitting, making $N_D \approx 700$ in the example in Fig. 4.2.

Fig. 4.2 shows a Bode plot of the estimated input impedance $|Z_{in(s-c)}|$ of the PT using the curve fitting technique from [4.2], along with the measured impedance for comparison.

4.3 Proposed Optimisation Techniques

4.3.1 Technique 1 – Streamlining for Improved Convergence

Three independent variables are required to characterise the RLC branch. Method 1 in [4.2] assumes $\omega_0 L = 1/(\omega_0 C) = \beta$ to link ω_0 to L and C, with R being determined from the impedance spectrum. Since L and C are not known a priori then a large range of β values must be searched to ensure a global minimum can be found. Here, it is proposed that the characteristic impedance β may be substituted by bandwidth or Q-factor (see Fig. 4.3) to give

$$Q = \frac{f_0}{f_B} = \frac{\omega_0}{\omega_B} = \frac{1}{R}\sqrt{\frac{L}{C}} \tag{4.10}$$

where ω_B is the bandwidth and $R \approx Z_0 = Z_{in(s-c)}(\omega_0)$. Using (4.10) allows the equivalent circuit components to be written as

$$L = \frac{R}{\omega_B}, \qquad C = \frac{\omega_B}{R\,\omega_0^2} \tag{4.11}$$

Equation (4.11) is substituted into (4.1) and this is substituted into (4.3) and (4.4) to provide $Z_{in(s\text{-}c)}(C_p, R, \omega_0, \omega_B)$ and $Z_{out(s\text{-}c)}(C_o, N^2R, \omega_0, \omega_B)$ for the optimiser to work on. The optimiser is seeded with an initial value for ω_B extracted from the impedance spectrum, seen in Fig. 4.3. Using a seeded variable, ω_B, instead of the impedance of C or L at resonance reduces the search space by a significant factor and acts to decouple the interaction between the interdependent variables.

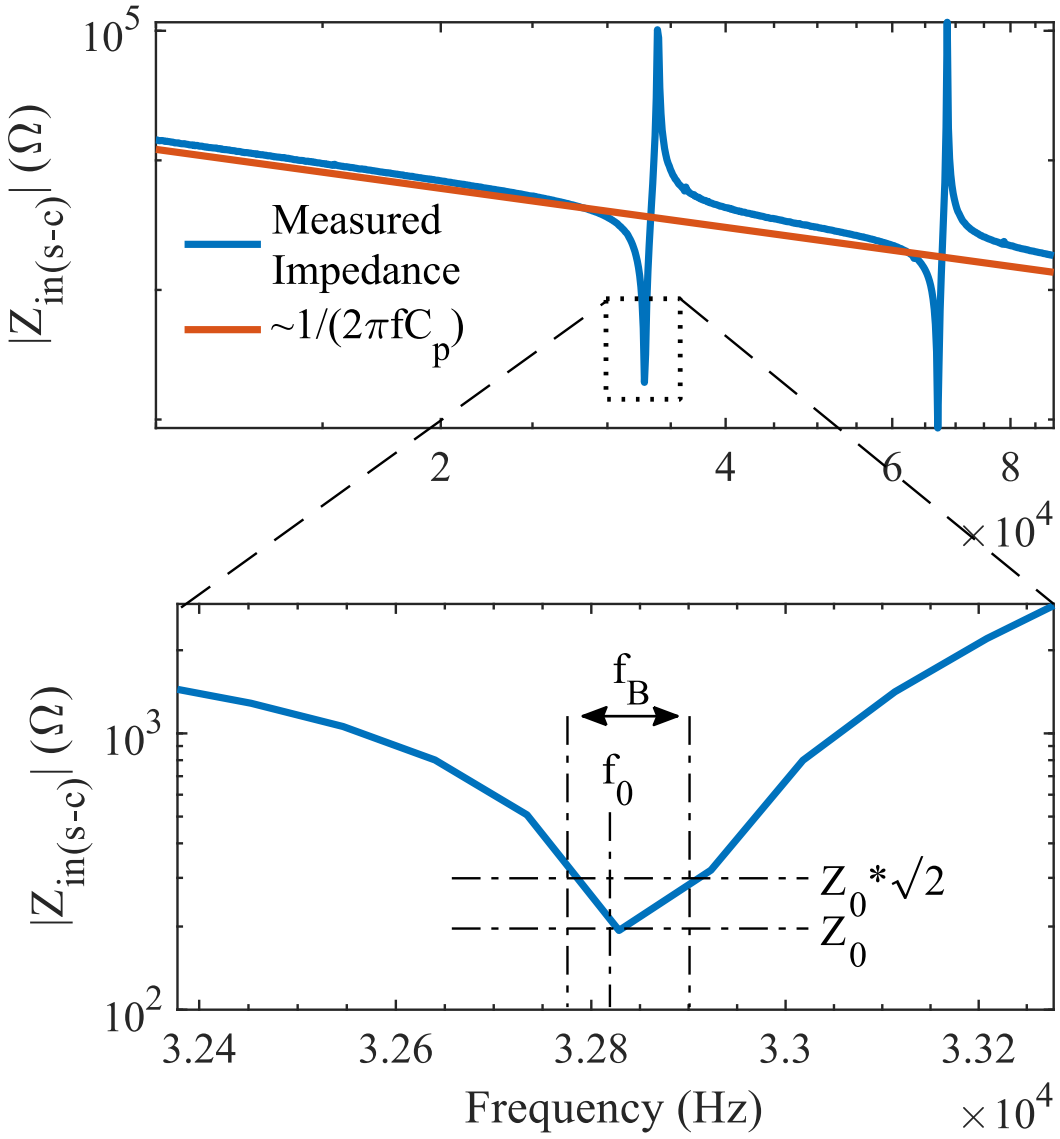

Fig. 4.3 Bandwidth estimation from a bode plot of input impedance

To further improve convergence time an initial estimate for C_p can be found by assuming the low frequency input impedance of the PT is dominated by C_p, as shown by the orange curve in Fig. 4.3. This estimated value is also used to seed the optimiser. When combined, the substitution for ω_B and seeding of the Nelder-Mead minimiser used in Section 4.2 reduced total CPU time needed for the fit in Fig. 4.2 from 47 s to 0.9 s. The minimiser was allowed a maximum of 1000 function evaluations.

Fig. 4.4 shows the steps of each parameterisation technique represented on a flowchart.

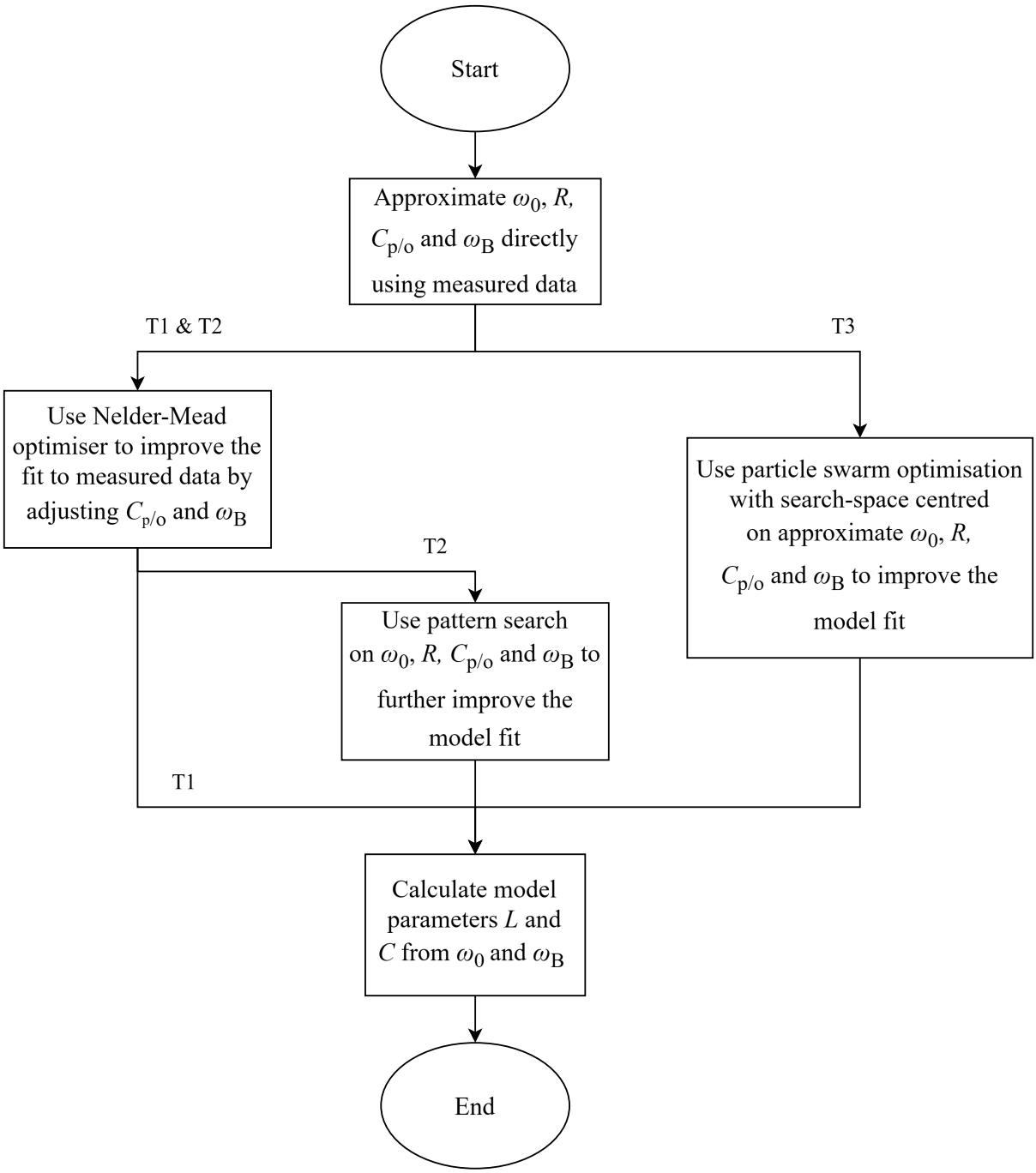

Fig. 4.4 Flowchart of parameterisation techniques. The paths of each technique are labelled T1, T2, etc.

4.3.2 Technique 2 – T1 with Pattern Search

The success of technique 1 relies on accurate values for ω_0 and R, extracted from the impedance spectrum. It was assumed C_p does not contribute to ω_0 and that R dominates the impedance at ω_0. Furthermore, T1 only optimises two parameters and therefore cannot correct for any disparity in ω_0 and R. In T2, to improve the fit of the previous technique, a

second round of optimisation was done, seeded by the results from T1. All parameters from each impedance spectrum were allowed to be adjusted to provide a global minimum using (4.2) as the cost function. Thus, the reference (measured) impedance spectra are fitted to the calculated impedance spectra evaluated using $Z_{in(s\text{-}c)}(C_p, R, \omega_0, \omega_B)$ and $Z_{out(s\text{-}c)}(C_o, N^2R, \omega_0, \omega_B)$.

For this, a pattern search (PS) optimiser from the MATLAB Optimisation Toolbox was used, which is effective for larger search spaces [4.4]. Specific optimiser settings are given in the experimental section in Section 4.4.

4.3.3 Technique 3 – Particle Swarm Optimisation (PSO)

In particle swarm optimisation, the term particle refers to a possible solution that exists in both time (iteration) and space (parameter). Multiple particles are initially randomly distributed about the search space. For each iteration, the performance of each particle is evaluated using a cost function, the velocity is updated depending on the lowest cost (error) that that particle obtained in its history, as well as the lowest cost obtained by any other particle. Over time (iterations) the particles converge on the optimal solution by traversing the search space [4.5].

The search space is centred about the initial seed values used by T1 and T2. Like T2, the reference (measured) impedance spectra are fitted to the calculated impedance spectra evaluated using $Z_{in(s\text{-}c)}(C_p, R, \omega_0, \omega_B)$ and $Z_{out(s\text{-}c)}(C_o, N^2R, \omega_0, \omega_B)$.

4.4 Experimental Evaluation of Optimisation Techniques

All three techniques were tested to determine their performance using same dataset that was used for the curve-fit shown in Fig. 4.2, where a Bode 100 impedance analyser was used to find the frequency domain impedance of a PT from STEMiNC, the SMMTF85P1S50.

T2 (pattern search) used 150 iterations, taking 10 s of CPU time (equivalent time for one core) and 2.5 s of real time with processing spread across 4 cores of a 32-core processor. PSO used 300 iterations of 500 particles, taking a CPU time of 1080 s and 45 s of real time (spread over 32 cores). The stopping conditions were chosen by experiment as the point where negligible further improvement was seen, allowing the optimisation techniques the best conditions to perform. The results can be seen in Fig. 4.5.

T3 (PSO) demonstrated the highest performance with this dataset using percentage error and absolute error metrics. T3 has a percentage error 8.4% lower than T1, and a 27% lower absolute error. The performance of T3 comes at the cost of requiring more CPU time; approximately 100 times that of T2, and more than 1000 times that of T1 alone. Here, T2 provides a good balance between a reduction in absolute error and processing time.

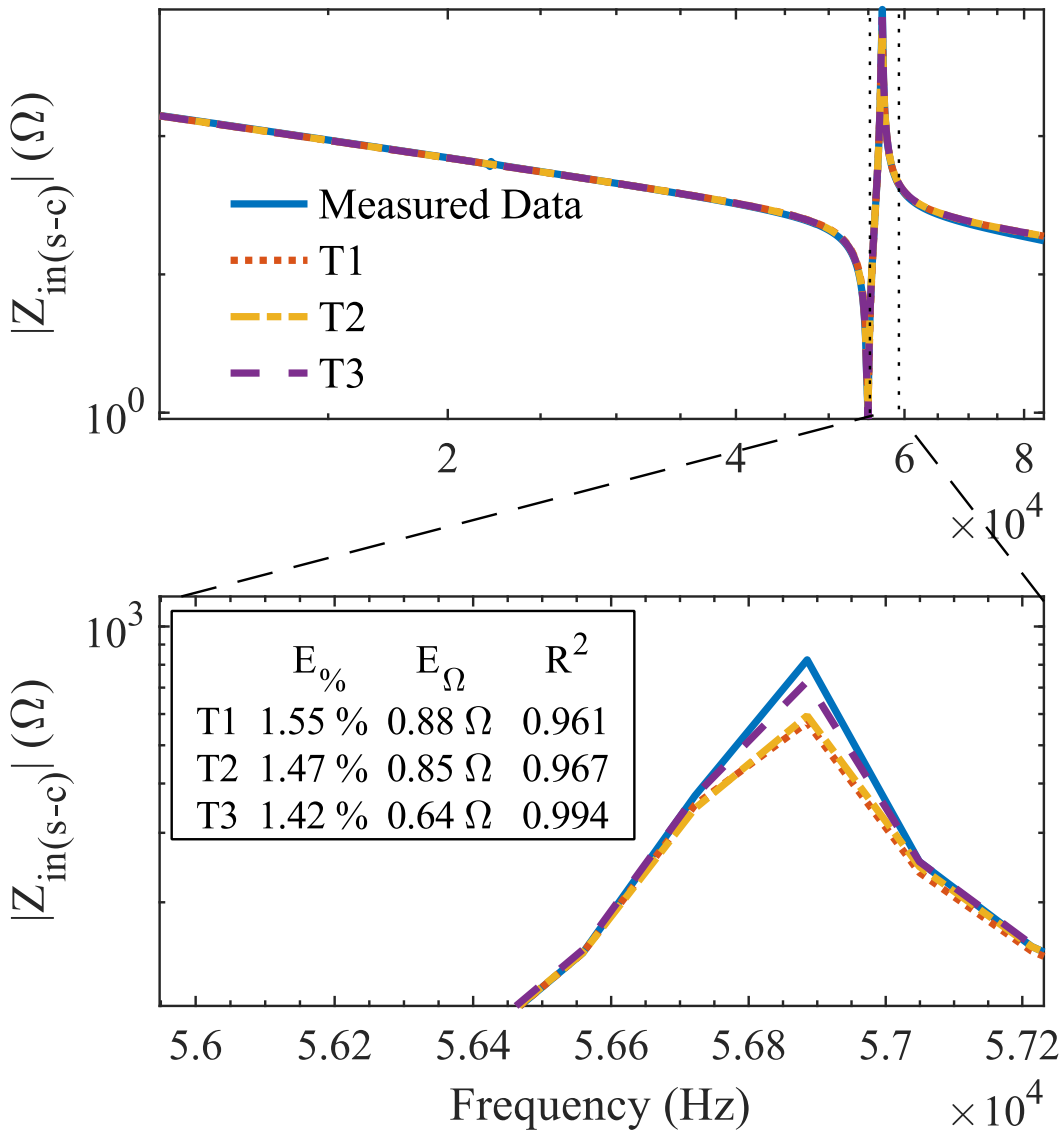

Fig. 4.5 Comparison of curve fitting, curve fitting with pattern search and particle swarm optimisation

4.5 Multiple Resonant Modes

PT are typically designed to exhibit a strong vibration mode to maximise power transfer and efficiency. However, due to material properties and their geometry PTs exhibit a range of vibration modes and it is useful to quantify these for design and control purposes.

4.5.1 Modelling Multiple Resonant Modes

The Mason equivalent circuit model in Fig. 2.12 can be extended to account for additional resonant modes by incorporating additional RLC branches. Fig. 4.6 shows an equivalent circuit for modelling $K = 2$ vibration modes.

With reference to Fig. 4.6, when the output port is short-circuited, the input impedance is characterised by the input capacitance connected in parallel with each RLC branch, representing the vibration modes of the mechanical motion. The input impedance can be calculated using (4.12), where K is the total number of resonant branches to be modelled.

$$Z_{\text{in(s-c)}} = \frac{1}{j\omega C_{\text{p}} + \sum_{k=1}^{K} \left(R_{\text{m}} + \frac{1}{j\omega C_{\text{k}}} + j\omega L_{\text{k}} \right)^{-1}} \tag{4.12}$$

Similarly, the output impedance is defined by

$$Z_{\text{out(s-c)}} = \frac{1}{j\omega C_{\text{o}} + \sum_{k=1}^{K} \left(N_{\text{k}}^2 (R_{\text{k}} + \frac{1}{j\omega C_{\text{k}}} + j\omega L_{\text{k}}) \right)^{-1}} \tag{4.13}$$

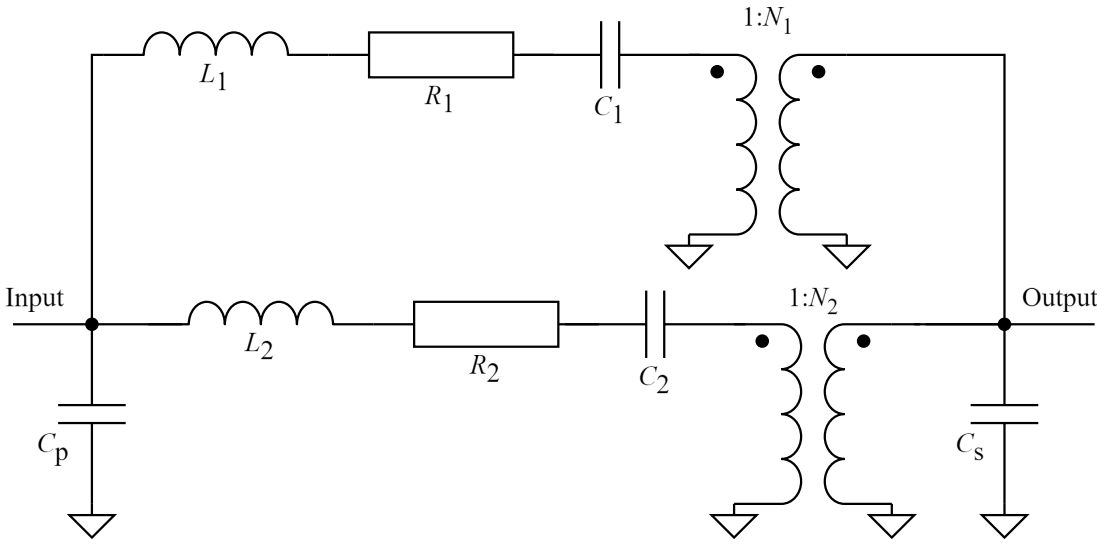

Fig. 4.6 Mason equivalent circuit model with two parallel branches

These equations allow the measured input impedance to be fitted with a model containing $3K + 1$ unknowns. The output impedance was fitted using the concepts applied in T1-3 and the square root of the ratio of the parallel branch impedances seen from either side of the device is the transformer ratio N_k, as in (4.5).

4.5.2 Curve-Fitting with Multiple Branches

The techniques described in section 3 were adapted to parameterise PTs with two active resonant modes. For T1, two curve-fit optimisation runs were performed, with run 1 having the resonant frequency (ω_0), bandwidth (ω_B) and branch resistance (R) at the first vibration mode. Run 2 used values extracted for the second vibration mode. Fixing of ω_0 and R about a vibration mode forces the minimisation algorithm to optimise the impedance error of the resonant branch at that frequency. The RLC values from each run are used to model each branch, with C_p taken as the average of the two.

As described in 4.3.2, the pattern search T2 operates on all seven parameters ($C_{p/o}$, R_1, L_1, C_1, R_2, L_2 and C_2 or their referred values) simultaneously. T2 was set to halt when the change in cost function was less than 10 parts per million (ppm) per iteration.

To apply T3 described in 4.3.3 the parameter space needs to be extended to all seven parameters and can be applied using 300 iterations with 500 particles.

4.6 Experimental Results

Seen in Table 4.1, both T2 and T3 reduce percentage error of the fit compared to T1. The average absolute error follows a similar trend to the percentage error. Table 4.1 also shows that the CPU time increases dramatically for T2 and T3 when multi-dimensional optimisation is used, with particle swarm optimisation taking several minutes to run on a high-performance system.

The PT has a high series resistance for both resonant branches (R_1 and R_2 in Table 4.1), which decreases the prominence of the peaks on the impedance plot (Fig. 4.7).

Table 4.1 Characteristics for the SMMTF85P1S50 PT

Parameter	Technique 1	Technique 2	Technique 3
C_p	30.0 nF	29.1 nF	28.8 nF
C_o	80.6 pF	78.7 pF	75.5 pF
R_1	36.4 Ω	55.5 Ω	97.0 Ω
L_1	4.56 mH	4.73 mH	4.32 mH
C_1	1.02 nF	0.968 nF	1.06 nF
N_1	23.7∠0°	24.3∠0°	19.4∠0°
R_2	16.9 Ω	20.9 Ω	26.0 Ω
L_2	1.08 mH	1.20 mH	1.05 mH
C_2	1.20 nF	1.07 nF	1.24 nF
N_2	26.1∠0°	30.2∠0°	25.2∠0°
$E_{\%(in)}$	4.40 %	1.81 %	2.50 %
$E_{\Omega(in)}$	6.43 Ω	1.06 Ω	1.23 Ω
R^2	0.9950	0.9999	0.9996
CPU time	6.9 s	207 s	1770 s

Input and output impedance spectra obtained by measurement and curve-fit are shown in Fig. 4.7 and Fig. 4.8, respectively. All three fitting methods match the resonant frequency with good accuracy, but the T1 alone does not obtain a good fit at the first anti-resonant point (shown in the lower subplot in Fig. 4.7). T2 improves the agreement at the anti-resonant point. It should be noted that the measured $Z_{out(s-c)}$ exhibits noise due to the high impedance being measured and limitations of the measurement equipment, visible in Fig. 4.8. This may have affected the performance of the optimiser.

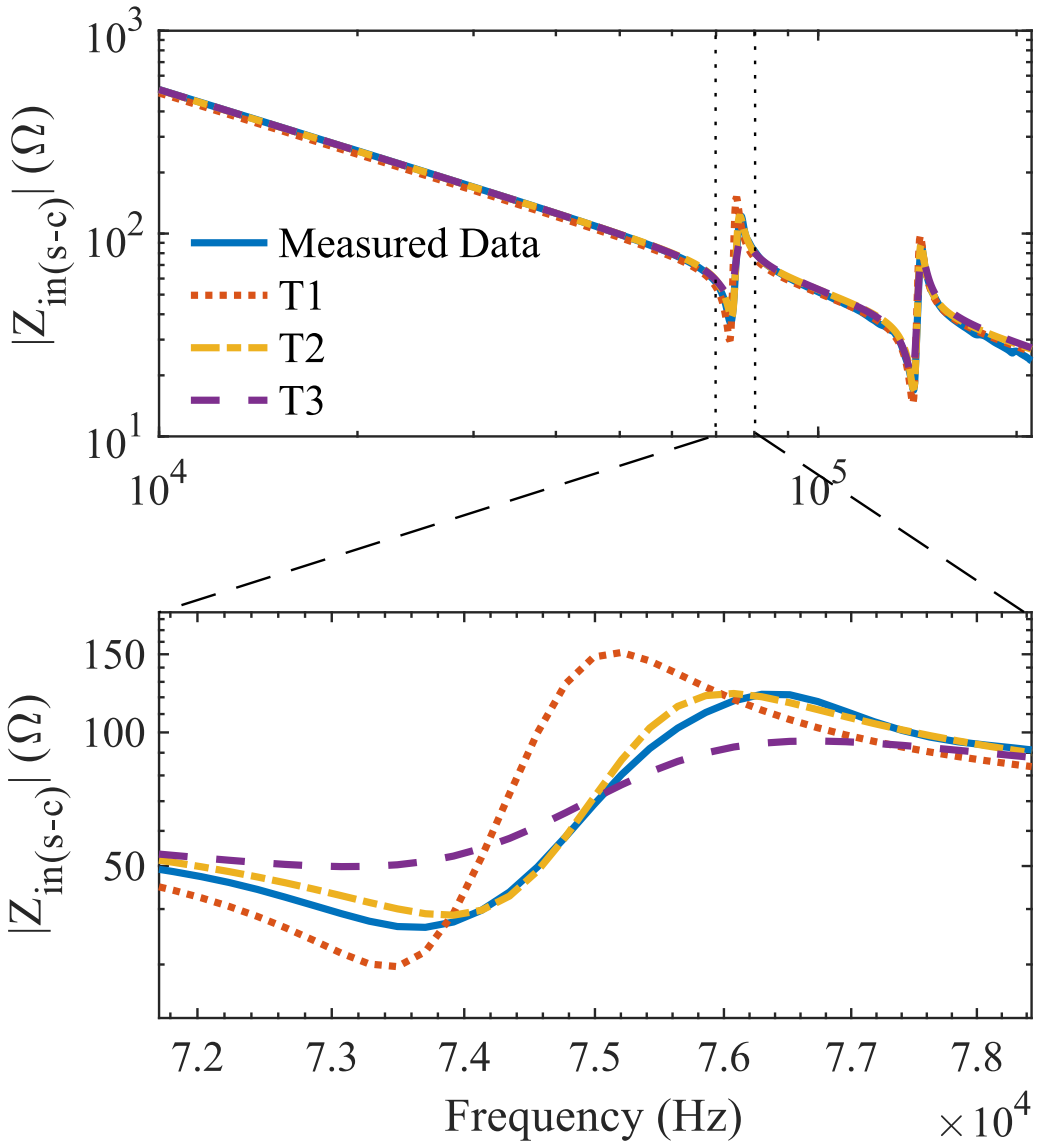

Fig. 4.7 SMMTF85P1S50 PT input impedance

In both figures, T3 has difficulty capturing behaviour about the resonant and anti-resonant frequencies. This behaviour is usually a characteristic of the optimiser becoming trapped in a local minimum. One solution would be to increase the number of particles. It should be noted that increasing the number of particles or iterations is at the cost of a greater processing time of an already computationally intensive method which takes minutes to complete, even on powerful hardware. An efficient remedy could be to seed the positions of the particles directly with values estimated from the impedance spectra.

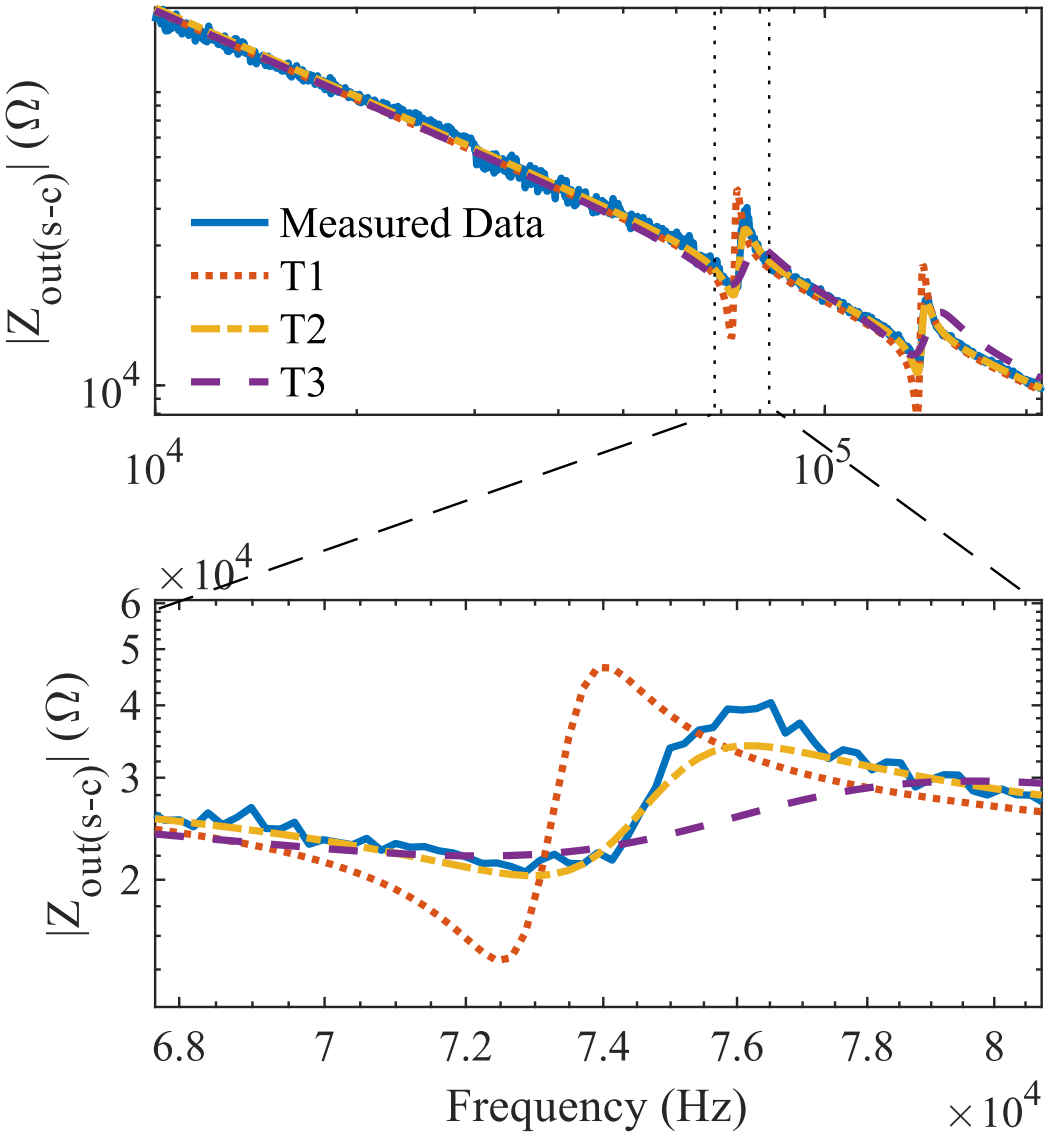

Fig. 4.8 SMMTF85P1S50 PT output impedance

4.7 Conclusion

An improved version of the curve fitting method has been demonstrated, reducing time taken to parameterise a piezoelectric transformer and extending the parameterisation to multiple resonant modes. Improvements in percentage error have been demonstrated by implementing a pattern search optimisation step after an initial reduced parameter characterisation.

Particle swarm optimisation was demonstrated as an alternative, reducing percentage error by approximately a factor of two compared to previously published techniques. In this work the pattern search optimisation technique provided greater performance than PSO while requiring an order of magnitude less CPU time.

These techniques are used to provide accurate model parameters for work in chapters 5 and 6, and this work was published in [4.6].

4.8 References

[4.1] D. J. Falimiaramanana, F. E. Ratolojanahary, J.-E. Lefebvre, L. E. Maimouni, and M. Rguiti, '2-D Modeling of Rosen-Type Piezoelectric Transformer by Means of a Polynomial Approach', *IEEE Trans. Ultrason. Ferroelectr. Freq. Control*, vol. 67, no. 8, pp. 1701–1714, Aug. 2020, doi: 10.1109/TUFFC.2020.2975647.

[4.2] J. Forrester, J. Davidson, M. Foster, and D. Stone, 'Equivalent Circuit Parameter Extraction Methods for Piezoelectric Transformers', in *21st European Conference on Power Electronics and Applications*, Genova, Italy, 2019.

[4.3] E. L. Horsley, M. P. Foster, and D. A. Stone, 'A frequency-response-based characterisation methodology for piezoelectric transformers', in *2008 2nd Electronics System-Integration Technology Conference*, Sep. 2008, pp. 959–962. doi: 10.1109/ESTC.2008.4684481.

[4.4] R. Hooke and T. A. Jeeves, '"Direct Search" Solution of Numerical and Statistical Problems', *J. ACM*, vol. 8, no. 2, pp. 212–229, Apr. 1961, doi: 10.1145/321062.321069.

[4.5] J. Kennedy and R. Eberhart, 'Particle Swarm Optimisation', in *IEEE International Conference on Neural Networks*, Perth, Australia, 1995.

[4.6] H. O'Keeffe, M. P. Foster, and J. N. Davidson, 'Parameterisation methods for piezoelecric transformer equivalent circuit models', in *11th International Conference on Power Electronics, Machines and Drives (PEMD 2022)*, Newcastle, UK: IET Digital Library, 2022, pp. 764–768.

5 Piezoelectric-Resonator-Based Power Supply for a DBD Reactor

5.1 Introduction

Chapter 4 described three parameterisation methods for piezoelectric resonators and transformers. In this chapter, parameters found using one of these methods is used to design a dielectric barrier discharge (DBD) reactor power supply for operation with a low input voltage. A piezoelectric resonator is used to provide voltage gain and high efficiency in a small volume for portable (point of use) ozone generation, suitable for the disinfection of surfaces for example. A general circuit diagram of the power supply can be seen in Fig. 5.1.

First, the coaxial DBD reactor described in Section 3.2.1 is parameterised to determine its linear-model component values. These parameters are used alongside parameters found using T3 in Chapter 4 for three different piezoelectric resonators (Section 3.4) in a mathematical model to determine the most efficient resonator and external components to realise the power supply. This power supply is coupled to the DBD reactor and tested, achieving an efficiency of 63% and an ozone generation efficacy of 67 g/kWh when operating at 4.4 W.

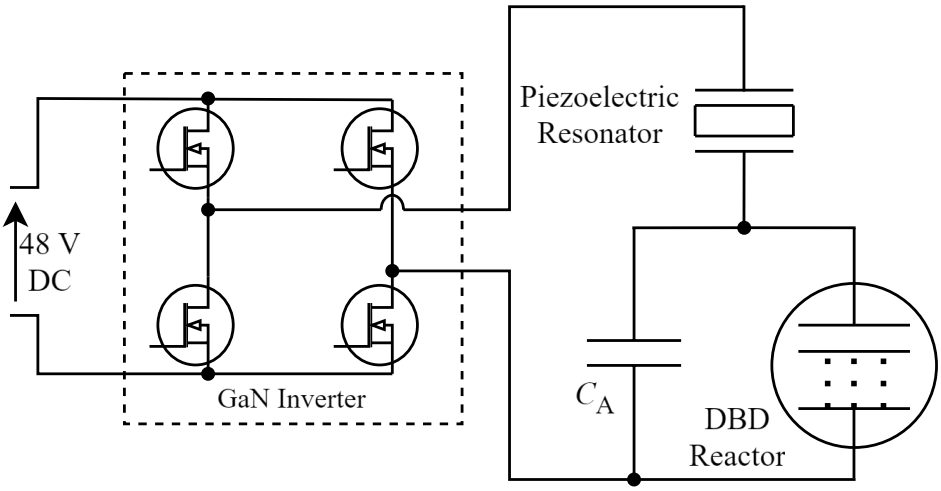

Fig. 5.1 Piezoelectric-resonator-based power supply circuit diagram

The use of a piezoelectric resonator (PR) to provide voltage gain has several advantages over a traditional electromagnetic transformer. The PR has monolithic construction for reliability, is inherently insulated against high voltage due to the ceramic material, can operate up to 300°C, and its resonant behaviour allows the power supply to operate with efficient zero-voltage switching.

5.2 Parameterisation

5.2.1 Parameterisation of the DBD Reactor

To choose the most appropriate resonator and parallel capacitance (C_A, Fig. 5.1) to achieve the needed output voltage with the highest efficiency, an accurate electrical equivalent model for the reactor is required.

The reactor was tested with the characterisation set-up shown in Fig. 5.2. These tests were performed from 10–85 kHz and 600–890 V_{RMS} to find values of R_D. To reduce degradation of the electrodes, the power was limited to 5 W.

The coaxial reactor, a Picoscope 6404C, TREK 10/40A-HS HV amplifier, Tektronix P6015A HV probe, and RSDG 830 waveform generator were used for these tests.

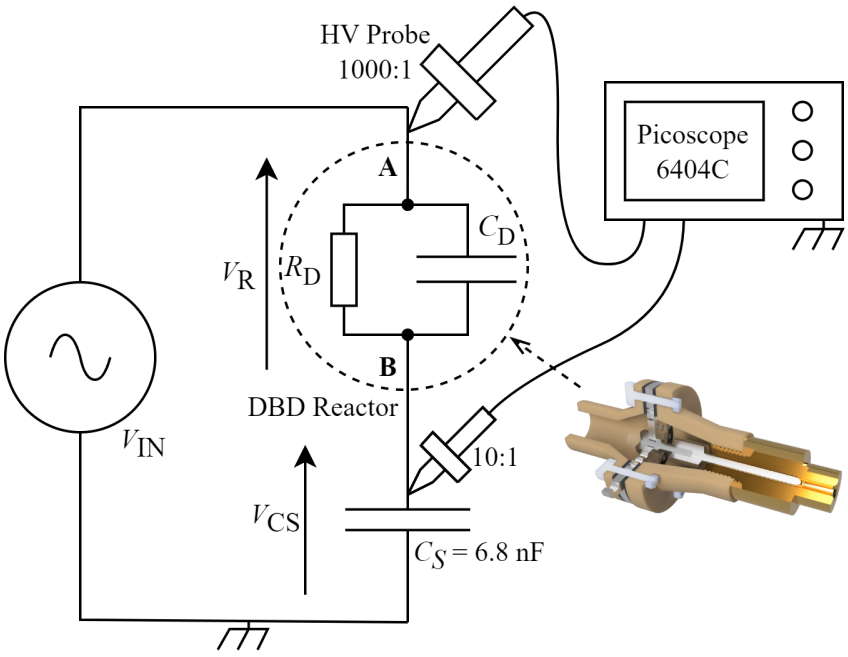

Fig. 5.2 Coaxial DBD reactor characterisation setup. The DBD reactor is represented with its linear equivalent circuit.

The time-domain measured voltages were used to calculate average power dissipated in the reactor using the Lissajous method (Section 2.3.1). This was then used with the RMS reactor voltage to calculate the R_D (the resistance of the reactor from the linearised reactor model, shown in the linearised DBD reactor model in Fig. 5.2 and Fig. 2.8) for each voltage and frequency.

Whilst the capacitance of the reactor can be calculated from its geometry, in practice there will be additional parasitic capacitance from the other parts of the reactor such as wiring.

To provide an estimation of C_D (Fig. 5.2), the effective capacitance of the reactor, C_R, was calculated from the characterisation test data using (5.1) with a V_{IN} lower than the ignition threshold (500 V_{pk}) and was found to be 11.4 pF.

$$C_R = \frac{C_S V_{CS}}{V_R} \tag{5.1}$$

Whilst in operation, charge accumulates in the reaction gap, (as highlighted in Fig. 3.2). This causes the capacitance to change under load. Other authors [5.1], [5.2], [5.3] have found that the change in C_D over the operating power range is typically <20%, depending on the type of reactor, whilst R_D can vary significantly with reactor output power. To account for this variation, expressions for R_D as a function of frequency and reactor input voltage were tested to find the best fit.

5.2.2 Exponential-Function Reactor Model

The equation (5.2) was fitted to the data from these tests using a mean-square-error cost function, introduced in Section 4.2, and a particle swarm optimiser to ensure a global best fit was found.

As Alonso, et al. in [5.3] suggest that reactor resistance should be inversely proportional to frequency, this relationship is used in both the exponential reactor model (5.2) and the power fit equation (5.3).

$$R_D = \frac{c_1}{f}\exp(c_2 V_R) \tag{5.2}$$

where c_1 and c_2 are constants chosen by the fitting algorithm which minimises the mean square error (E_{MS}). In this section, M_d is the measured $R_D(f, V_R)$ and F_d is R_D calculated with (5.2). d represents each measured position in (f, V_R) space.

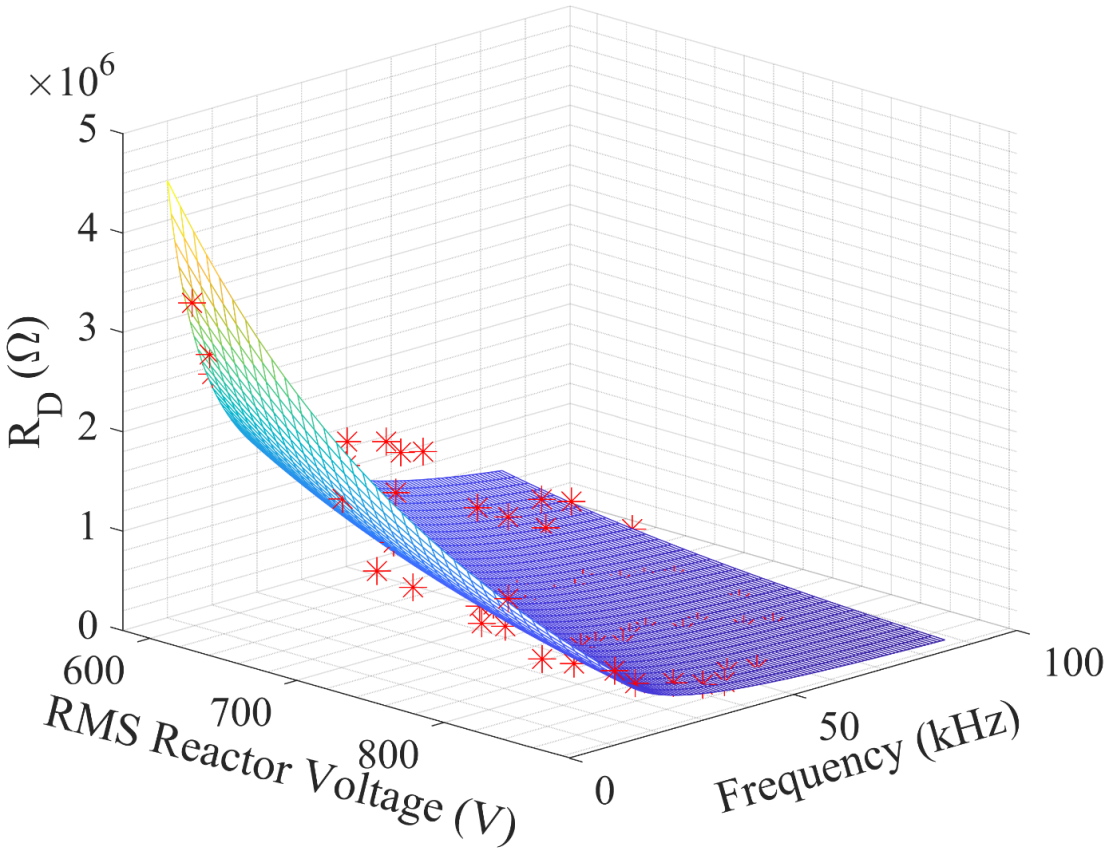

Fig. 5.3. Curve fit surface of R_D (resistance) using (5.2). Measured data points are indicated with red stars.

The curve fit can be seen in Fig. 5.3. The constants were determined to be c_1 = 1.32×10^{12} Ω.Hz.$e^{0.00585V}$ and c_2 = -0.00585 V^{-1}. The coefficient of determination (Section 4.2) R^2 = 0.885.

5.2.3 Power-Function Reactor Model

A power function was also fitted to the measured data in an attempt to find a more accurate model of the reactor.

The power fit equation (5.3) was fitted to the data from these tests using the cost function (4.2), and a particle swarm optimiser to ensure a global best fit was found.

$$R_D = \frac{c_3}{f} V_R^{c_4} \tag{5.3}$$

The curve fit can be seen in Fig. 5.4. The constants were determined to be c_3 = 1.0×10^{26} Ω.Hz.V$^{5.52}$ and c_4 = −5.52. The coefficient of determination for this fit R^2 = 0.954, indicating a better fit that obtained by the exponential equation. The power fit equation and fitted constants was chosen to model the reactor.

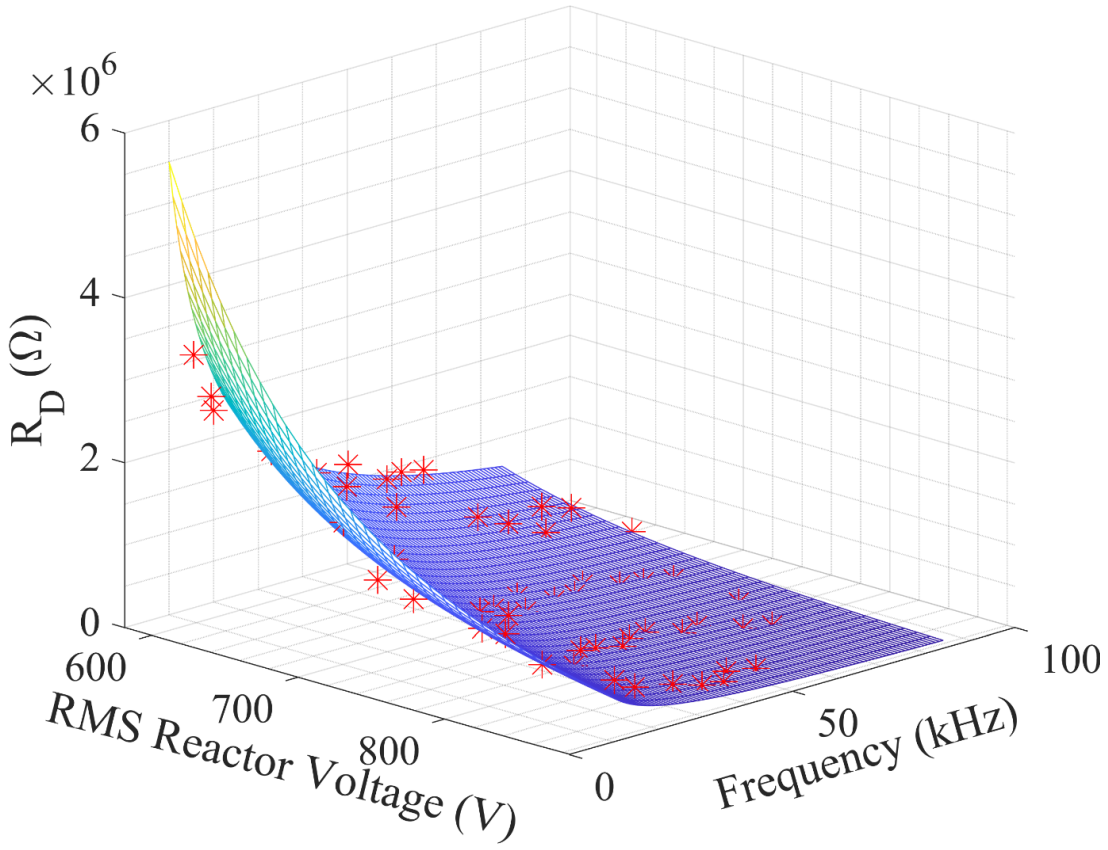

Fig. 5.4 Curve fit surface of R_D (resistance) using the power fit equation. Measured data points are indicated with red stars.

5.3 Voltage Gain

Without the inherent voltage gain of a transformer, the suitability of a piezoelectric resonator for generating high voltages for a DBD reactor is not immediately apparent. In this work, the RLC branch in the Van Dyke model (Fig. 2.11) is made to resonate with a parallel combination of the reactor capacitance, C_R, and a discrete capacitor, C_A. C_A is tuned to obtain the desired gain of the system, although this does not necessarily maximise its efficiency. The total capacitance seen by the Van Dyke model (Fig. 5.5) is $C_T = C_R + C_A$. The parameters for the Van Dyke model are shown in Table 3.3.

The complex frequency domain equation for the gain of the circuit in Fig. 5.5 is shown in (5.4).

$$\frac{V_R}{V_I} = \frac{s^3 R_D L C_P C + s^2 R R_D C_P C + s R_D (C_P + C)}{s^3 C L R_D (C_T + C_P) + s^2 C (C_T R_D R + C_P R_D R + L) + s (R_D C_T + C_P R_D + C R_D + R C) + 1} \tag{5.4}$$

where $s = j\omega$, j is the imaginary unit and ω is angular frequency, $\omega = 2\pi f$.

To calculate the frequency at which the maximum gain occurs, (5.3) was substituted into (5.4) to eliminate R_D:

$$V_{\mathrm{R}}{}^{1-c_4} = \frac{-2\pi j c_3 V_{\mathrm{I}}}{\omega\left(\frac{j(jCL\,\omega^2 + CR\omega - j)}{\omega(jC + jC_{\mathrm{P}} - jCC_{\mathrm{P}}L\omega^2 - CC_{\mathrm{P}}R\omega)} - \frac{V_{\mathrm{R}}{}^{c_4}\, 2\pi c_3\,(2\pi j a\, C_{\mathrm{T}} V_{\mathrm{R}}{}^{c_4} - 1)}{\omega\left(C_{\mathrm{T}}{}^2 V_{\mathrm{R}}{}^{2c_4}(2\pi c_3)^2 + 1\right)}\right)(2\pi c_3 C_{\mathrm{T}} V_{\mathrm{R}}{}^{c_4} - j)} \tag{5.5}$$

This equation is transcendental and requires solving numerically. Two nested Nelder-Mead optimisers (Section 4.2) were used to maximise V_{R} for a given V_{I} = 48 V_{pk} by varying the frequency, ω. The inner optimiser was used to solve (5.5) for V_{R}, whilst the outer optimiser operated on the frequency.

Output power, P_{O} is defined as the power dissipated by R_{D},

$$P_O = \frac{|V_{\mathrm{R}}|^2}{R_{\mathrm{D}}} \tag{5.6}$$

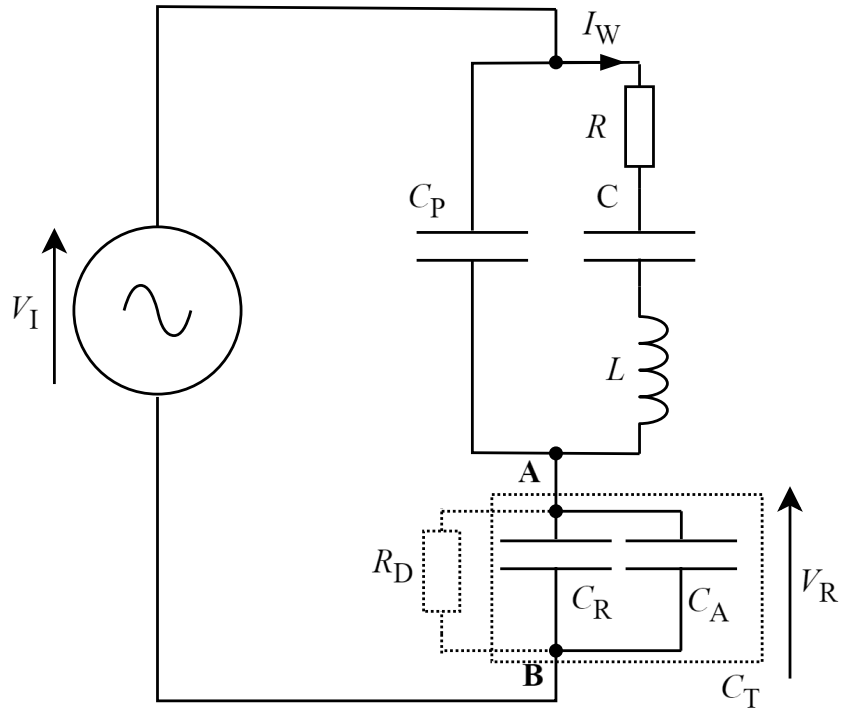

Fig. 5.5. PR Van Dyke model with power supply, series capacitance (C_{A}) and DBD reactor model (C_{R} & R_{D}).

The only other source of power dissipation in the PR Van Dyke model shown in Fig. 5.5 is R. The waste power dissipated in this resistor is given by,

$$P_{\mathrm{W}} = |I_{\mathrm{W}}|^2 R \tag{5.7}$$

I_{W} was formulated in terms of V_{I},

$$I_{\mathrm{W}} = \frac{sV_{\mathrm{I}}C(sR_{\mathrm{D}}C_{\mathrm{T}} + 1)}{1 + s^3 CLR_{\mathrm{D}}(C_{\mathrm{T}} + C_{\mathrm{P}}) + s^2 C(R(C_{\mathrm{T}} + C_{\mathrm{P}})R_{\mathrm{D}} + L) + s\big((C + C_{\mathrm{T}} + C_{\mathrm{P}})R_{\mathrm{D}} + CR\big)} \tag{5.8}$$

The efficiency, η, can then be calculated from P_{O} and P_{W}:

$$\eta = \frac{P_O}{P_O + P_W} \tag{5.9}$$

These calculations were performed for each resonator with a range of C_T values to analyse the effects of C_T on output power and efficiency. These results can be seen in Fig. 5.6, Fig. 5.7 and Fig. 5.8.

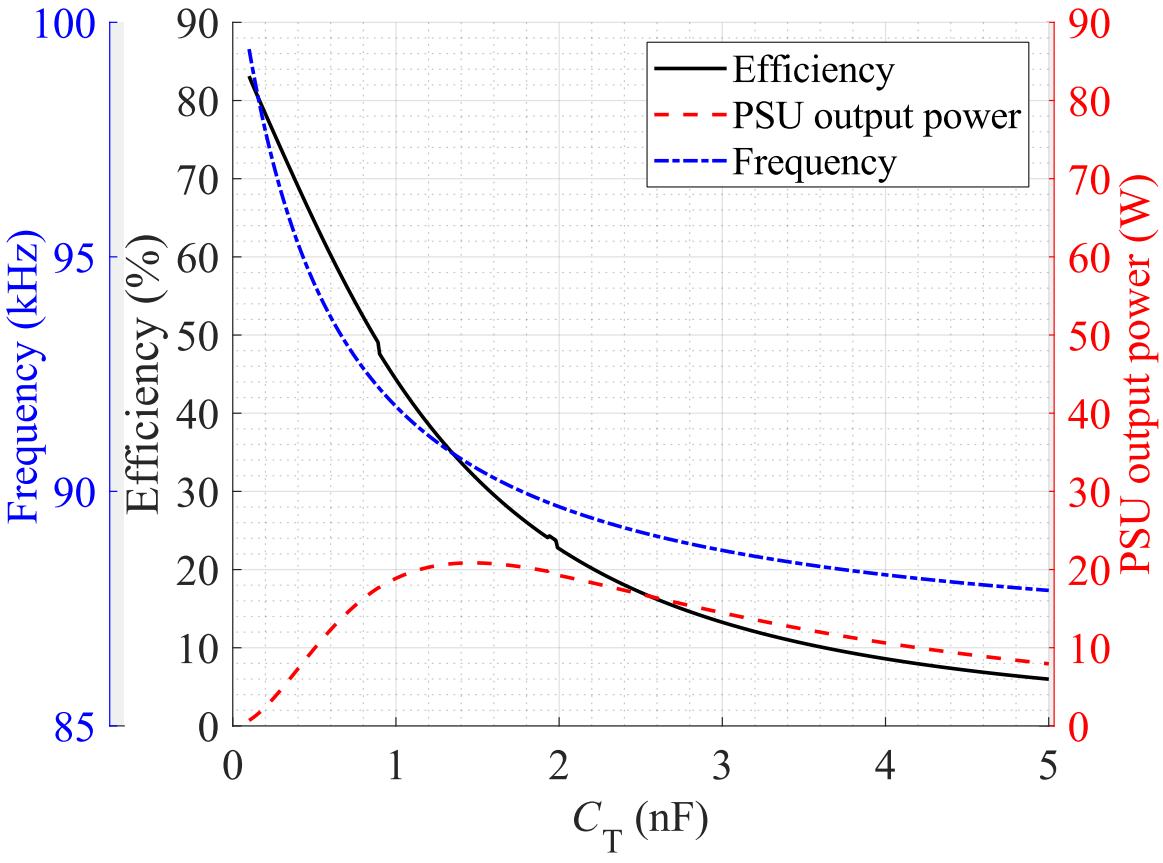

Fig. 5.6. Simulated effect of C_T choice on maximum power, efficiency, and frequency for the SMD25T85F234S resonator

Comparison of the results for the three PRs in Fig. 5.6, Fig. 5.7 and Fig. 5.8 shows that the largest resonator, SMD43T105F200S with the highest Q-factor and lowest impedance at resonance (seen in Table 3.3) exhibits a higher maximum power and higher efficiency than the other two resonators. For this reason, this resonator was chosen for the final design.

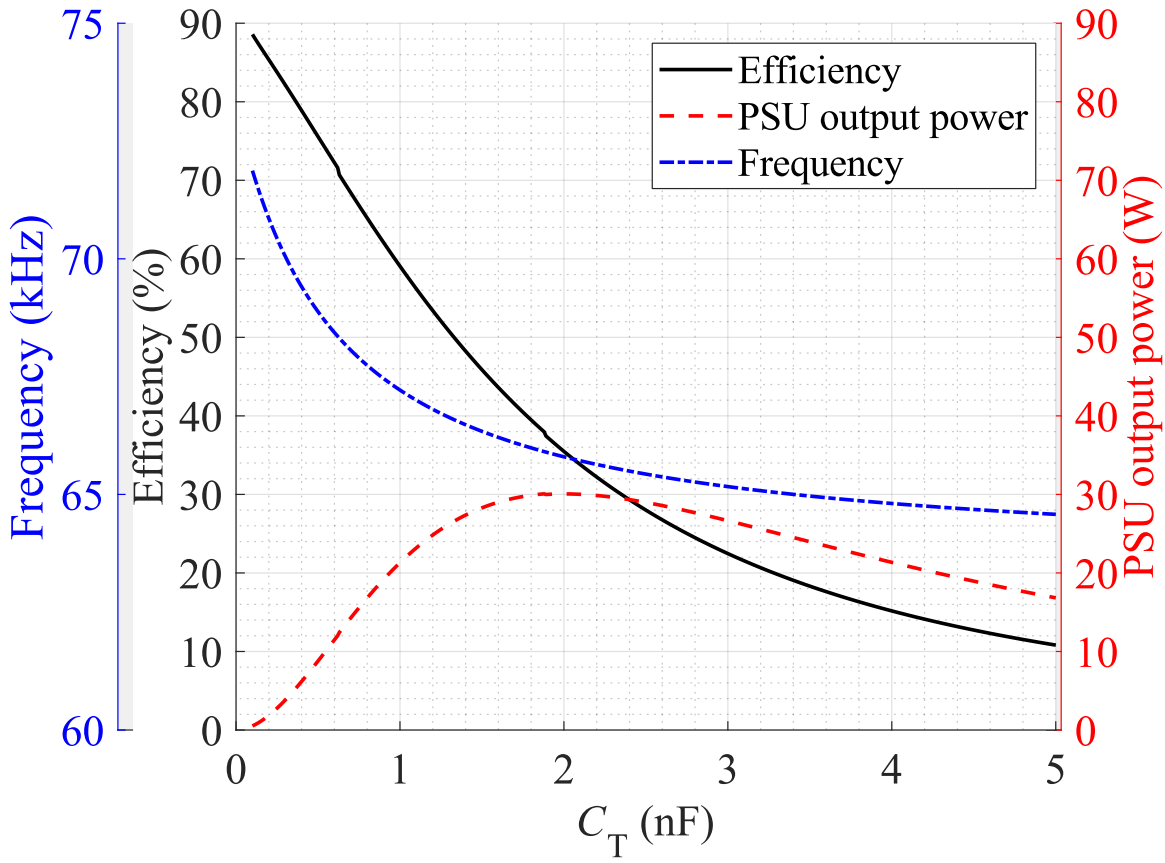

Fig. 5.7. Simulated effect of C_T on maximum power, efficiency, and frequency for the SMD35T12S118 resonator

As the power rating of the reactor is 5 W (Table 3.1), the power supply can be designed for this power, maximising efficiency because the efficiency and power have an inverse relationship as C_T is increased (Fig. 5.8). 5 W corresponds to a C_T of ~500 pF, an efficiency of 88% and frequency of 56.7 kHz. C_A was chosen to be 500 pF as C_R is negligible for this reactor.

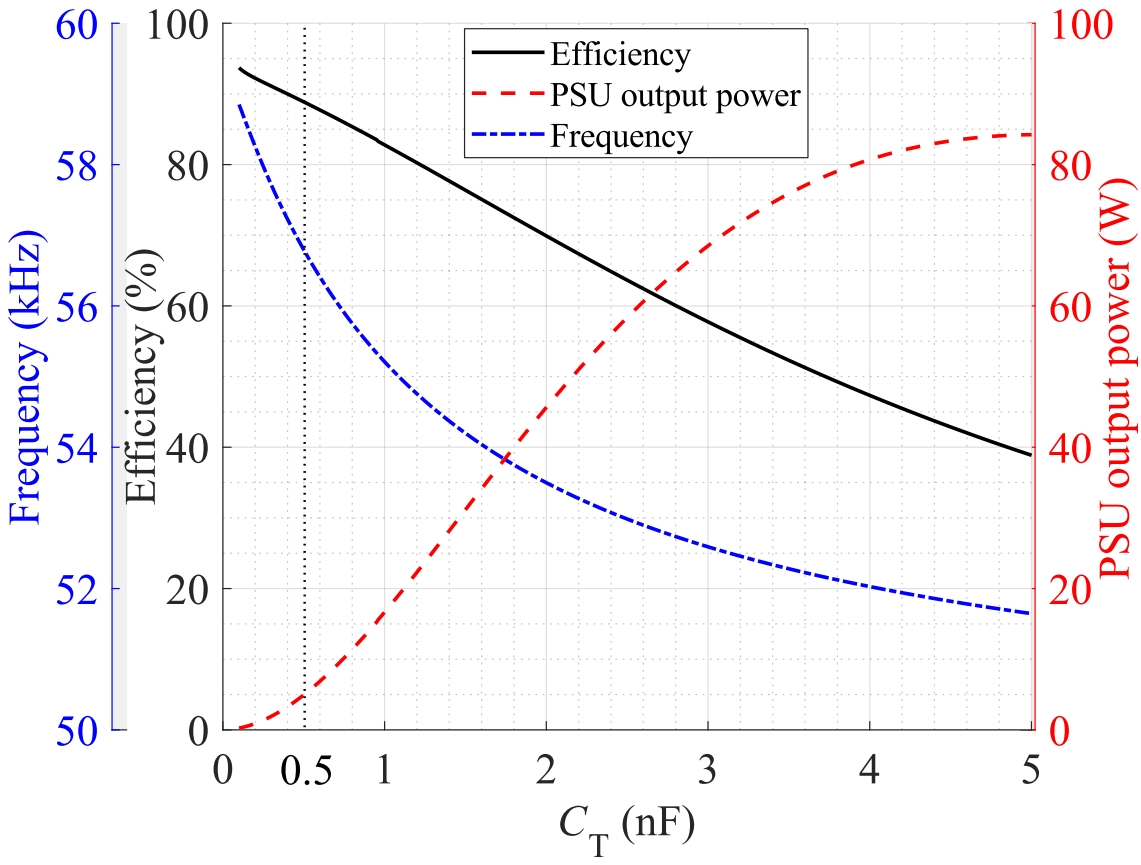

Fig. 5.8 Simulated effect of C_T on maximum power, efficiency, and frequency for the SMD43T105F200S resonator.

5.4 Experimental Validation

To validate the design process, the system was tested using the setup shown in Fig. 5.9. The additional equipment used over previous tests was a Yokogawa PX8000 power analyser to assess the performance of the inverter, and a 48 V DC supply to power the system. The connection of this test equipment necessitated wires approximately 50 cm in length. These have a parasitic inductance on the order of microhenries represented by L_P in Fig. 5.9.

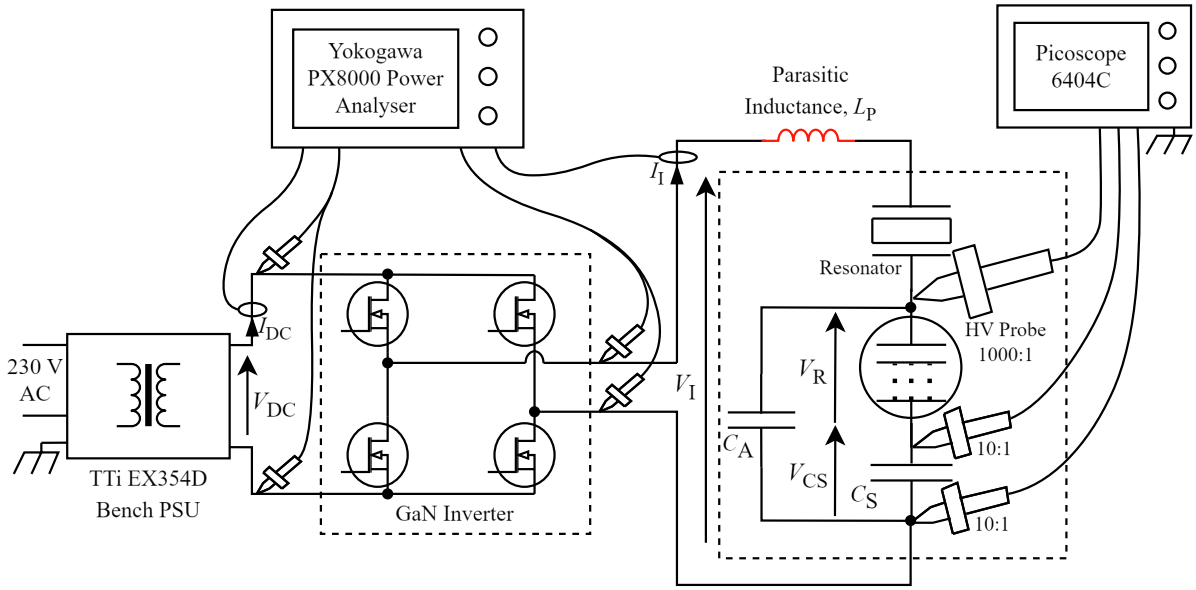

Fig. 5.9. Experimental test set-up

To drive this system, any voltage source with an AC component can be used: any DC voltage component will be blocked by the resonator and only spectral components around the resonant frequency will contribute significantly to the reactor power.

In this chapter a GaN inverter is used, described in Section 3.6. A half-bridge could alternatively be used but has half the output voltage of a full bridge. The half bridge is generally cheaper but requires higher resonant system gain, reducing overall system efficiency.

A duty cycle of 50% was used in this experiment and frequency, f, was adjusted to change the resonant behaviour of the system, change the amplitude of V_R, and by extension the reactor power, P_R. To reduce the switching losses associated with switching a capacitive load, a deadtime of 10% was used. The deadtime allows energy to be recovered from the PR acoustic wave to charge the capacitance on the output of the inverter during this dead time.

The PX8000 was used to measure the voltage and current at the input and output of the inverter (V_{DC}, I_{DC}, V_I, I_I). In each test, data was captured over a period of 10 ms (~500 cycles) to ensure accurate power measurement with the Lissajous technique.

Fig. 5.10 shows the waveforms of the inverter output current and voltage when operating with an output power of 0.4 W. The 10% deadtime allows the resonant current (leading the voltage by approximately 90°) to charge the capacitance present on the output of the inverter, causing the inverter output current to drop and the output voltage to rise to the bus voltage

during the deadtime, achieving zero-voltage switching (ZVS). Also visible is a high frequency component: ringing resulting from the change in current (0.2 A) through the resonator and parasitic inductance (L_P) in a short period of time (100 ns).

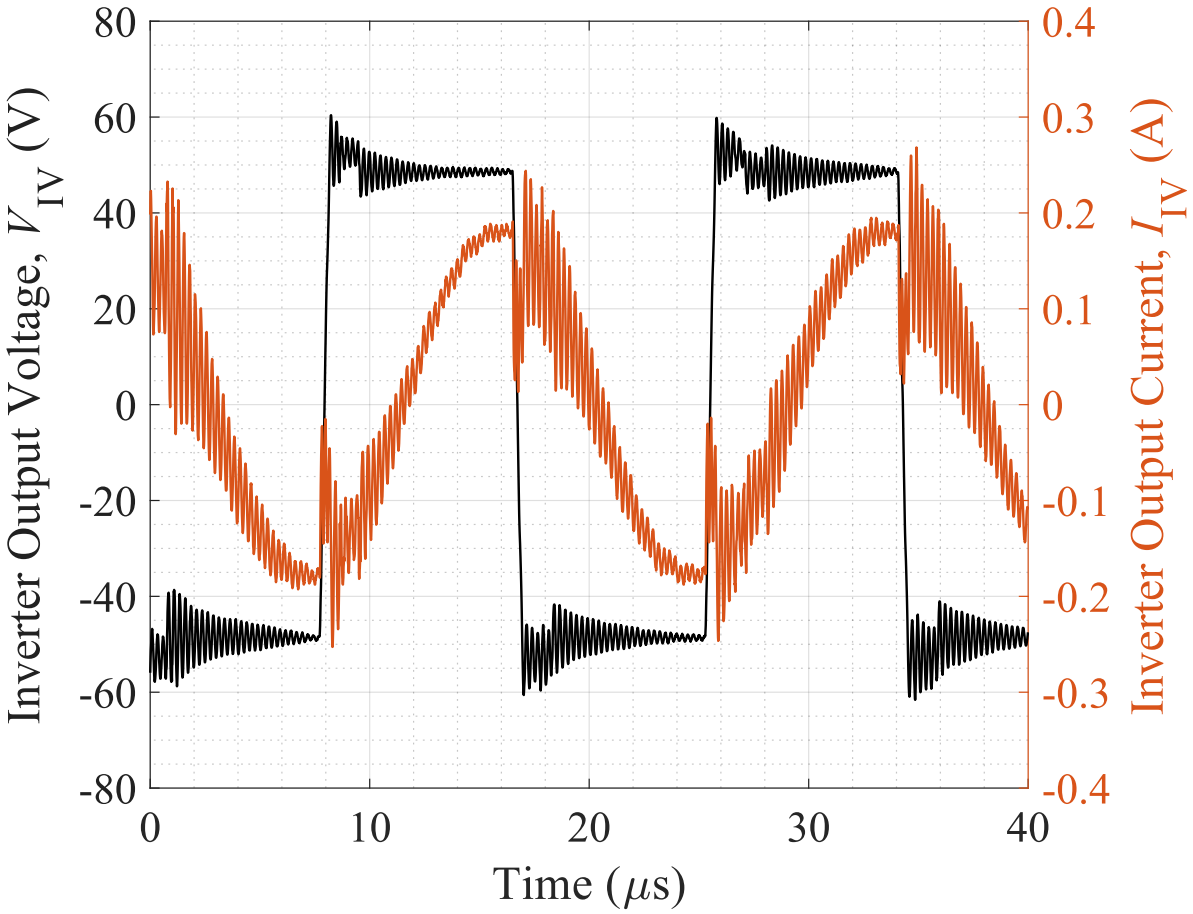

Fig. 5.10 Inverter waveforms, P_O = 0.4 W.

Fig. 5.11 shows these waveforms during operation at P_O = 4.4 W. The voltage-leading phase shift has now increased to 150° and there is less current available during the deadtime to charge C_P, the input capacitance of the PR (Fig. 5.5). By the end of the deadtime, C_P has charged with V_I nearly at V_{DC} as the output current crosses 0 at 19 µs. This operating condition represents a limit to the maximum output power of the system whilst still maintaining ZVS.

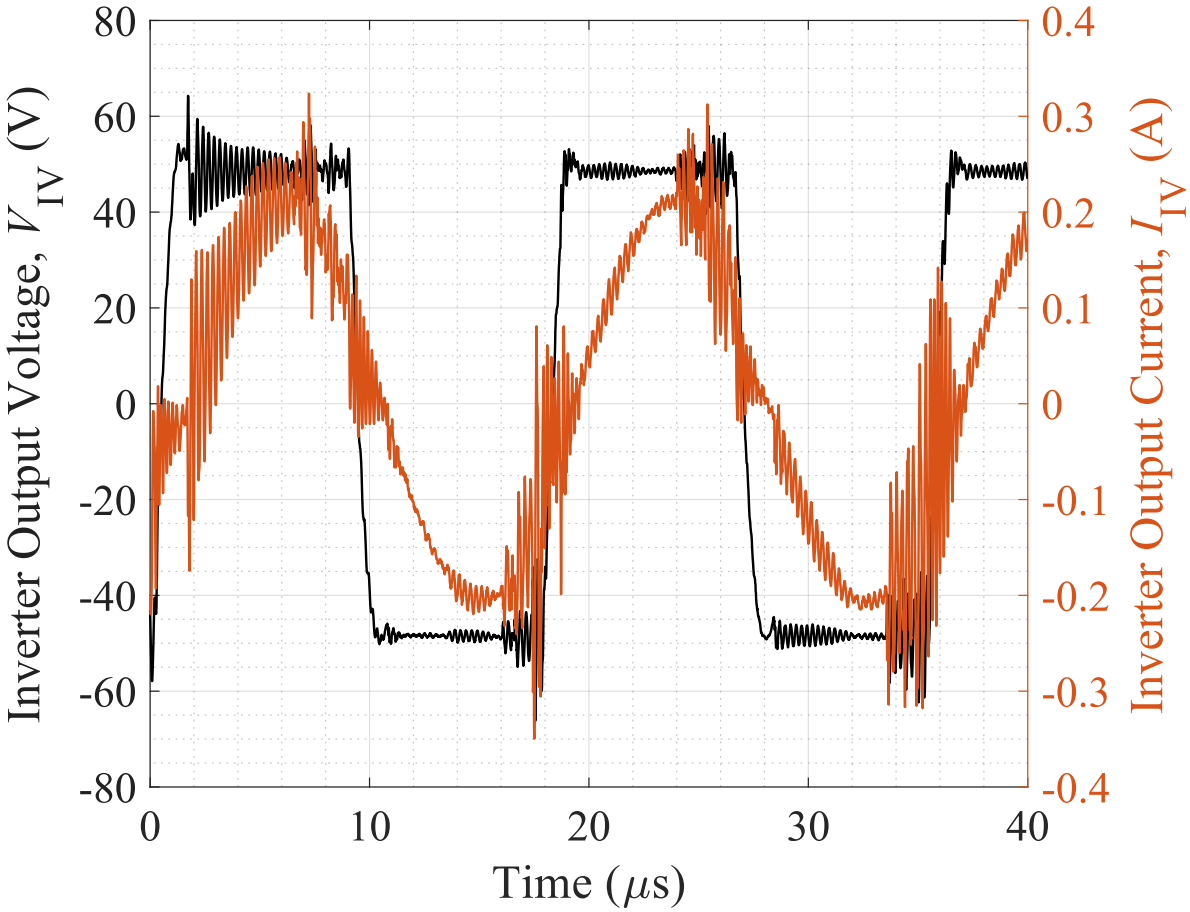

Fig. 5.11. Inverter waveforms, P_O = 4.4 W.

At 4.4 W there is significant discharge in the reactor. This causes noise on the current and voltage waveforms in Fig. 5.11, seen periodically before commutation at 16 µs for example. There is also generally less ringing at this power level as the reactor current is lower during commutation, resulting in a lower $\mathrm{d}I_I/\mathrm{d}t$.

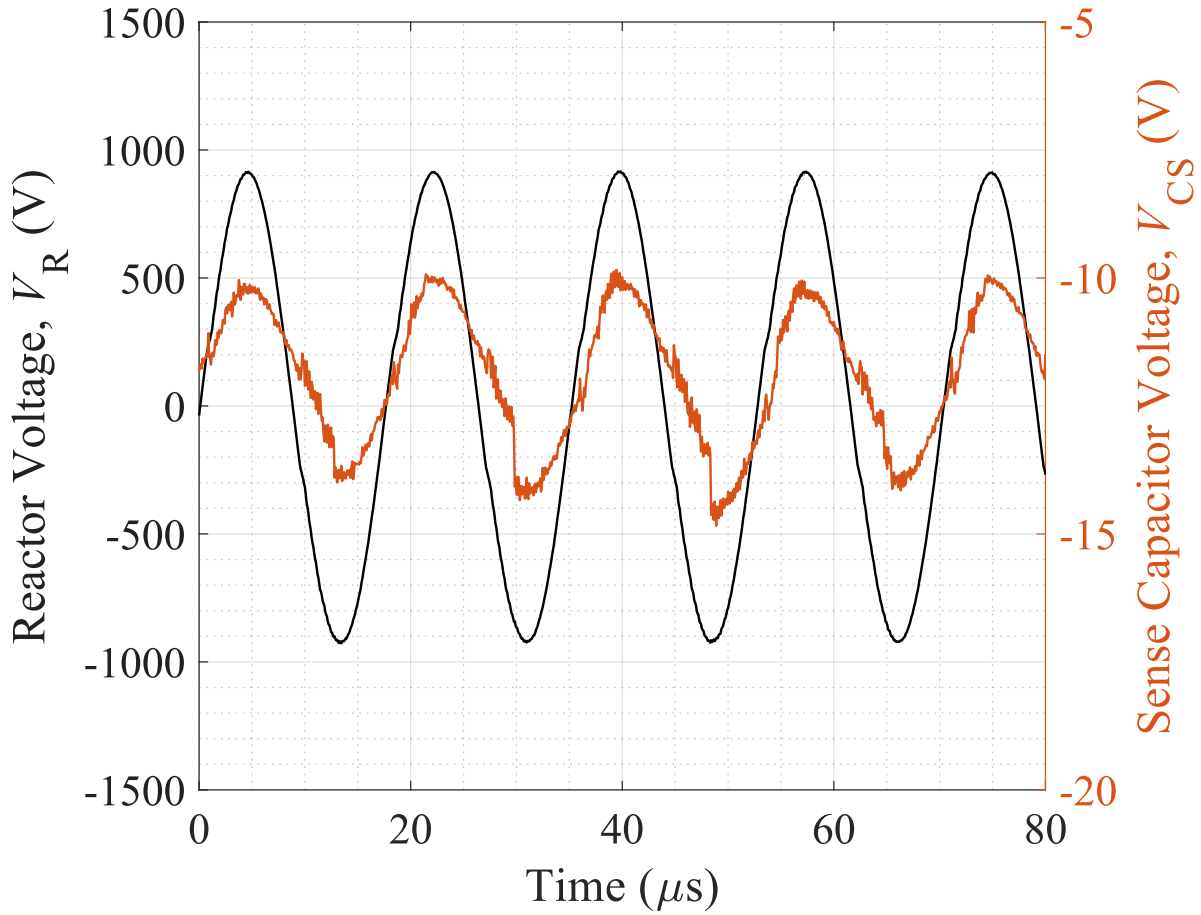

Fig. 5.12. Reactor waveforms at 0.4 W reactor power.

Fig. 5.12 and Fig. 5.13 show the voltage waveforms on the reactor, V_R, and the current sense capacitor, V_{CS}, for tests at 0.4 W and 4.4 W of reactor power respectively. These signals are digitally low-pass filtered in post-processing with a linear roll-off from 12.5 MHz to 108 MHz, above which it has an attenuation of >60 dB. This was done to reduce high-frequency noise caused by the discharge in the reactor.

V_R is sinusoidal, with a small distortion twice per cycle during the dead time (at 10 µs in Fig. 5.12, for example). V_{CS} shows noise from the discharge, visible as many regions of high $\mathrm{d}V/\mathrm{d}t$. When one plasma streamer is formed, the conducting channel often prompts nearby charged regions to discharge, resulting in a cascade effect. As these discharges are very short (~10 ns) in duration, this cascade is also very short. This results in a large ΔV_{CS} over a short time, seen at 30 µs and 47 µs in Fig. 5.13, for example.

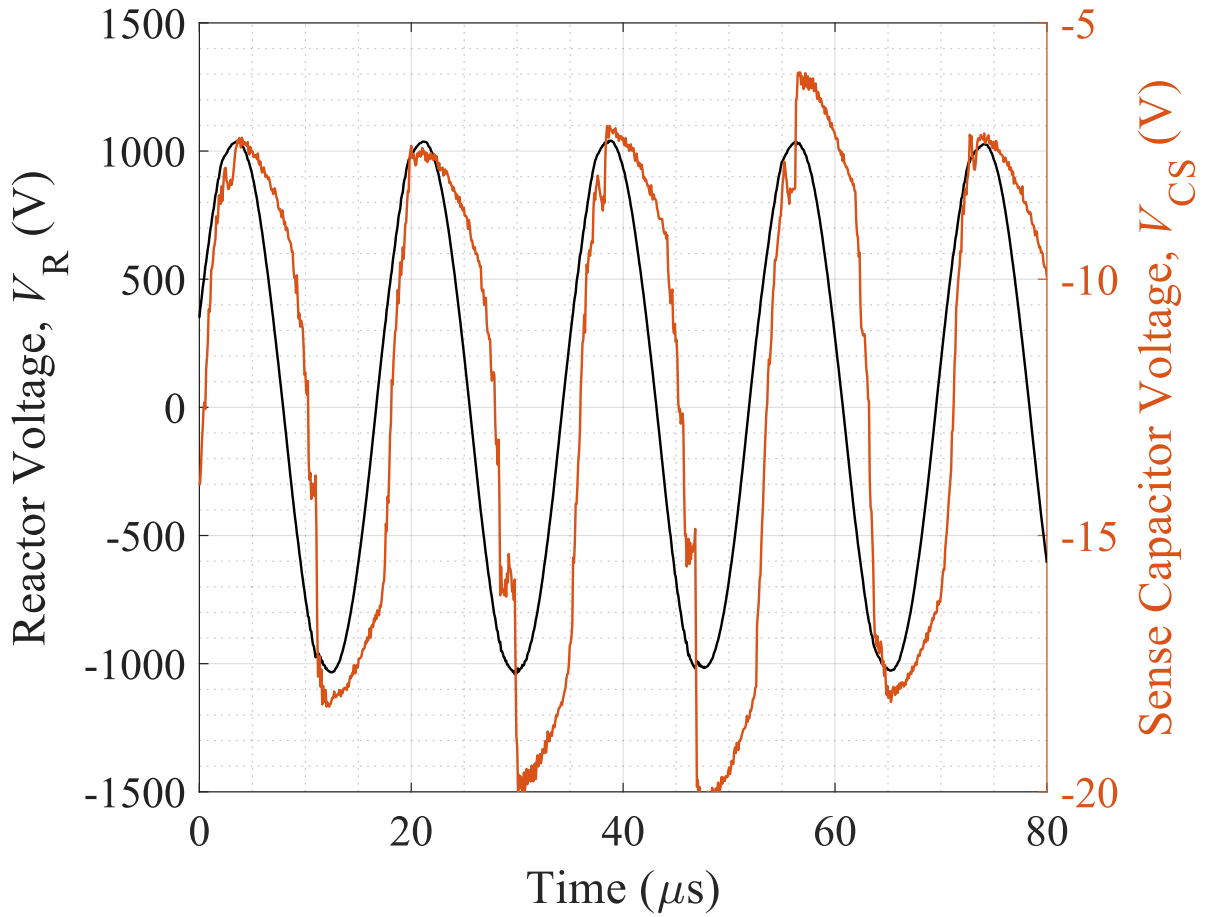

Fig. 5.13. Reactor waveforms at 4.4 W reactor power.

Fig. 5.12 and Fig. 5.13 show a DC offset on V_{CS}. Since the reactor electrodes are asymmetrical, the DC offset is thought to be due to charge build-up on the dielectric. To test this hypothesis, two pairs of electrodes were used: a pair of identical alumina-coated electrodes of the type described in Section 3.2.1, and a set of one coated and one uncoated electrode.

A sinusoidal voltage of approximately 600 V_{pk} at 20 kHz was applied to the electrodes, and the DC offset of V_{CS} was measured over 40 cycles. The pair of identical (symmetrical) electrodes had a DC offset voltage of −0.022 V, whilst the coated / uncoated (asymmetrical) set had a DC offset of 0.2 V, approximately ten times higher than the symmetrical test.

Fig. 5.14 shows the variation in power and voltage over the frequency range 56.75 kHz to 56.95 kHz. This is sufficient to change the reactor input power approximately linearly from 0.4 W to 4.4 W, with reactor voltage also varying approximately linearly over the range 647 V_{RMS} to 746 V_{RMS}. This allows the reactor power to be inferred from the reactor voltage.

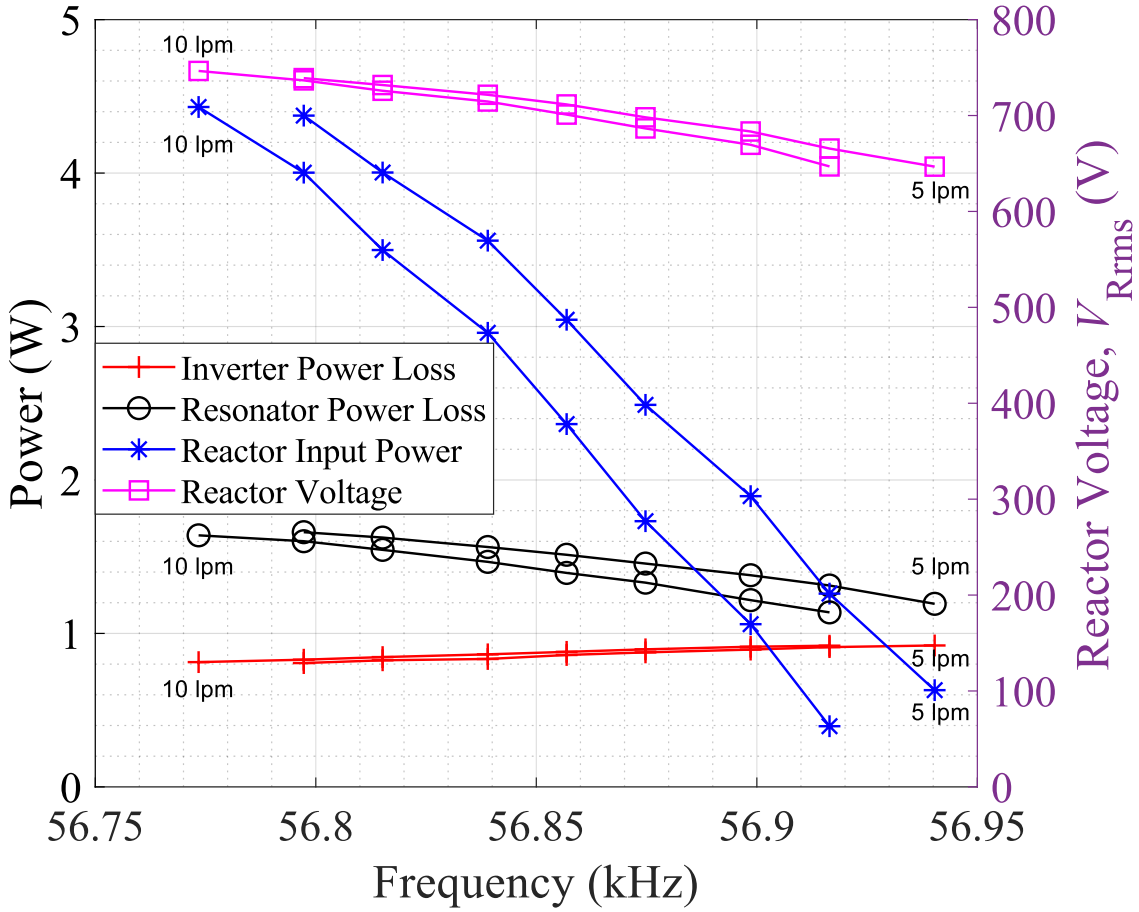

Fig. 5.14. Reactor voltage and power distribution as frequency is varied.

The change in power and voltage for a given frequency when the flowrate is increased from 5 to 10 litres per minute (lpm) is seen in Fig. 5.14. This change suggests that there is a relationship between the flowrate and the performance of the reactor. It follows that the parameters in the electrical model of the reactor, C_D and R_D, change with flowrate, perhaps due to the increased flow causing individual discharges to be extinguished faster.

The power loss distribution in Fig. 5.14 shows the power loss in the inverter reduces as frequency decreases and power increases. The power loss in the resonator increases with reactor power more slowly than the reactor power itself, meaning efficiency is increasing with reactor power. The system reaches a total efficiency of 63%, with all support circuity (microcontroller, etc.) included in the inverter losses. Considering the resonator alone, the efficiency is 72%.

The system's overall efficiency has a positive trend with reactor power and ozone production, reaching a peak efficiency at the maximum power rating of the reactor, suggesting that this efficiency could be improved further at the expense of a loss of ZVS (as most of the input

power is delivered to the reactor, it is likely that despite the reduced efficiency of the inverter, the overall efficiency would increase due to the increased reactor (output) power).

Fig. 5.15 shows the performance of the DBD reactor. The tests at 10 lpm had increased reactor efficacy, η_r, a ratio of the generated mass of ozone and the energy delivered to the reactor defined as,

$$\eta = \frac{m_{O_3}}{E} \tag{5.10}$$

where m_{O_3} is the mass of ozone produced and E is the energy consumed by the reactor (η_r) or the whole system (η_s).

The reactor also has a lower ozone concentration probably due to the greater flow also reducing reactor temperatures. The results demonstrate that the reactor is most efficacious at a lower power. This is most likely due to the reduced heating causing less ozone to be destroyed after it is produced as ozone is destroyed at higher temperatures [5.4].

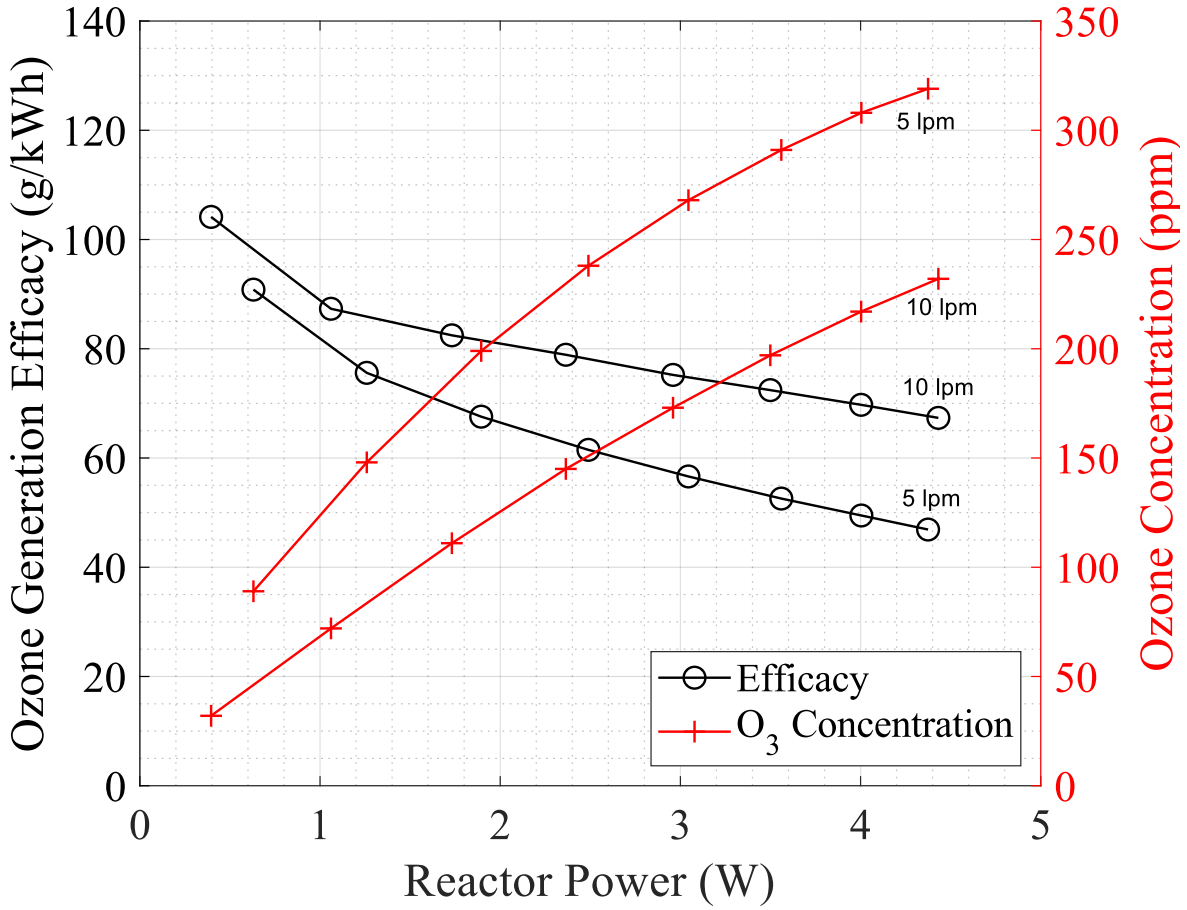

Fig. 5.15. Measured performance of the DBD reactor.

5.5 Conclusion

This chapter describes the use of a PR as a device for driving a dielectric barrier discharge and briefly explores the effects of electrode symmetry on the DC offset voltage of the current sense capacitor. The use of a PR as an energy converter offers several advantages over conventional power supplies, including high efficiency and the ability to operate at high frequencies for increased ozone production. The results show that the system achieves 63% efficiency with a reactor voltage of over 740 V_{RMS} at 56.8 kHz.

The voltage and power vary linearly with frequency, simplifying control, whilst the reactor is most effective at lower power levels due to reduced heating and a smaller percentage of ozone being destroyed after it is produced. The results demonstrate the potential of the PR-based power supply as a viable alternative to conventional power supplies for DBD reactors.

5.6 References

[5.1] P. Hothongkham and V. Kinnares, 'High-voltage high-frequency power supply using a phase-shifted PWM full bridge inverter fed ozone generator with constant applied electrode voltage', in *The 2010 International Power Electronics Conference - ECCE ASIA*, Sapporo, Japan, 2010.

[5.2] J. Alonso, J. Cardesin, E. Corominas, M. Rico-Secades, and J. Garcia, 'Low-power high-voltage high-frequency power supply for ozone generation', *IEEE Trans. Ind. Appl.*, vol. 40, no. 2, pp. 414–421, 2004.

[5.3] J. M. Alonso, M. Valdés, A. J. Calleja, J. Ribas, and J. Losada, 'High Frequency Testing and Modeling of Silent Discharge Ozone Generators', *Ozone Sci. Eng.*, vol. 25, no. 5, pp. 363–376, 2003, doi: 10.1080/01919510390481685.

[5.4] H. Itoh, M. Taguchi, and S. Suzuki, 'Thermal decomposition of ozone at high temperature leading to ozone zero phenomena', *J. Phys. Appl. Phys.*, vol. 53, no. 18, p. 185206, 2020, doi: 10.1088/1361-6463/ab71a9.

6 Selective Harmonic Generation for DBD Reactors

6.1 Introduction

In this chapter, a biharmonic waveform composed of the sum of two sinusoidal components, a 1st and 2nd harmonic (Fig. 6.1) is used to explore how changing the frequency spectrum of the reactor input waveform affects the efficacy (5.10) of the reactor (η_r) and the overall system efficacy, η_s.

A technique related to selective harmonic elimination, termed selective harmonic generation (SHG) is presented as a means of creating a pulse-train containing precisely controllable harmonics up to the switching frequency. Harmonics above this frequency are assumed to be filtered out (attenuated) by inductive components of the circuit. To create the biharmonic waveform, the first two harmonics are controlled in accordance with the experiments, whilst the remaining controllable harmonics are eliminated.

Two experiments are performed with different voltage gain devices. Experiment 1 uses a conventional high-voltage transformer (described in Section 3.5), whilst experiment 2 uses a piezoelectric transformer (described in Section 3.3). For both experiments, a GaN inverter (described in Section 3.6) is used to provide the bipolar pulse train.

This chapter has two main aims: to investigate whether pulse waveforms can be tailored to optimise reactor performance by controlling their frequency spectrum and to determine the performance of the proposed approaches (in experiment 1 and experiment 2) in providing the required waveforms.

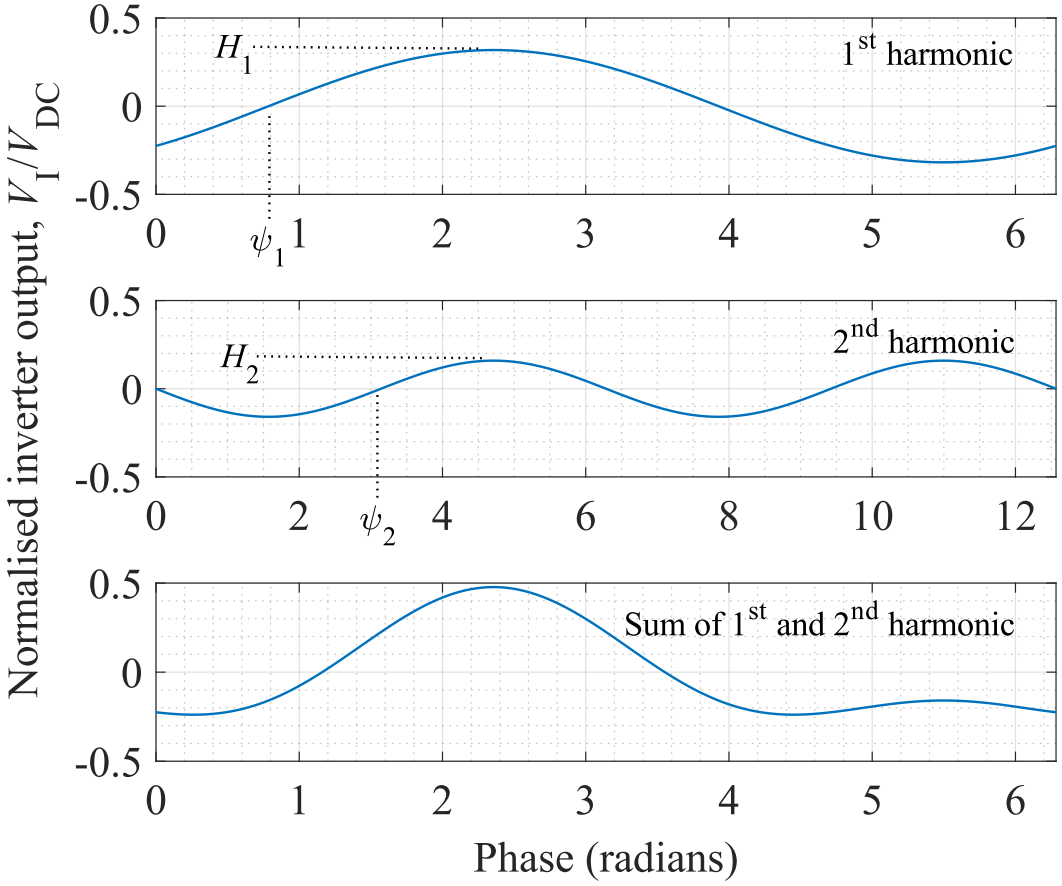

Fig. 6.1 Biharmonic waveform decomposed into first and second harmonics.

6.2 Selective Harmonic Generation

The PT is driven by a GaN H-bridge inverter (Fig. 6.2). This inverter can generate a pulse train with the output voltage, $V_I = -V_{DC}$, 0 or V_{DC}. An example pulse train is given in Fig. 6.3.

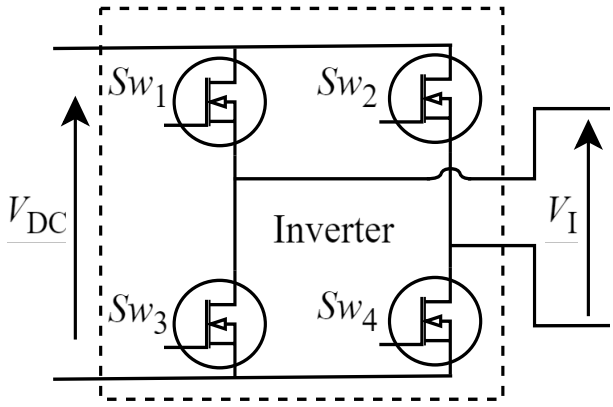

Fig. 6.2 Inverter circuit diagram

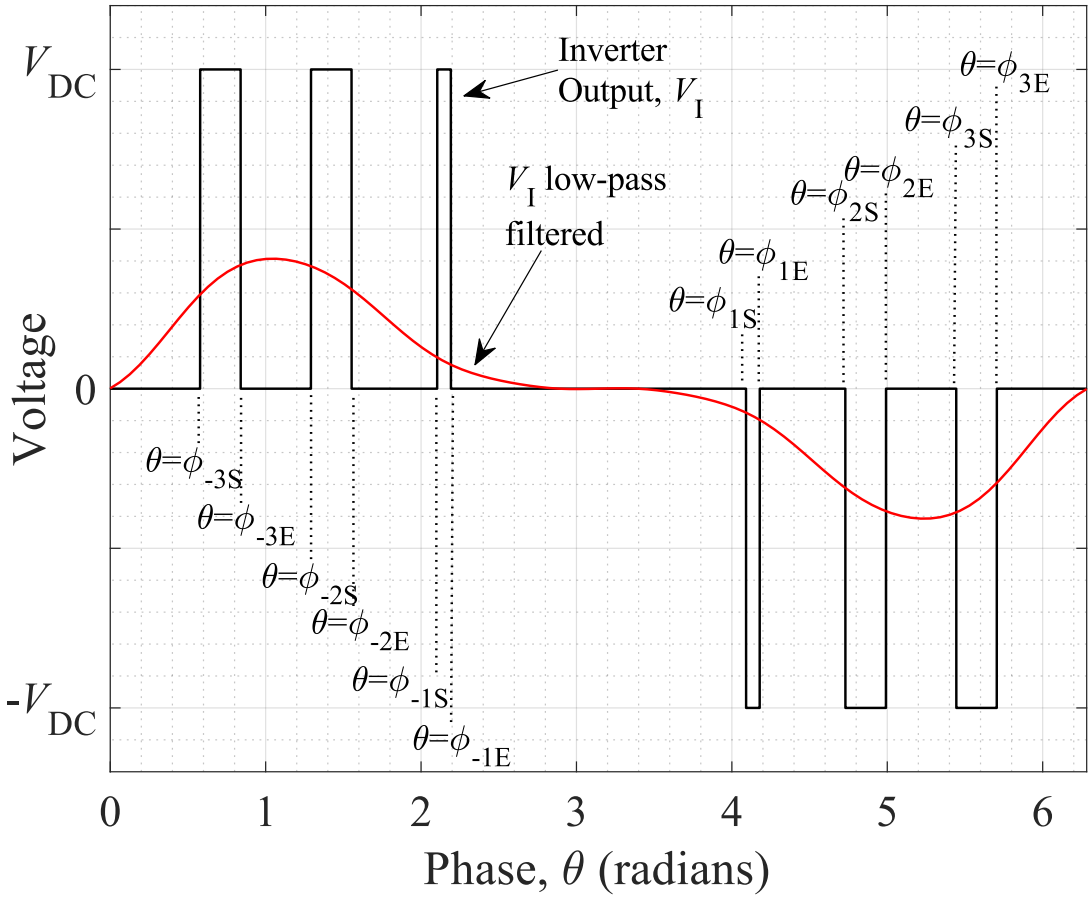

Fig. 6.3 Example pulse-train waveform containing first and second harmonic content.

In the analysis that follows it is assumed that the pulse train is divided into N_p pulses per cycle, where N_p is an even number. Fig. 6.3 shows an example inverter waveform with N_p=6. ϕ_{Sa} represents the start angle of pulse a, and ϕ_{Ea} represents the end of pulse a such that the duration of pulse 1 is $\phi_{S1} - \phi_{E1}$. When $a < 0$ the pulses are positive and phase angle $\theta < \pi$. When $a > 0$, the pulses are negative and $\theta \geq \pi$. There is no pulse at $a = 0$.

When $\phi_{Sa} < \theta < \phi_{Ea}$ and $\theta < \pi$, Sw_1 and Sw_4 of the H-bridge inverter shown in Fig. 6.2 are on and the inverter output voltage $V_I = V_{DC}$. During the negative half-cycle when $\phi_{Sa} < \theta < \phi_{Ea}$ and $\theta \geq \pi$, Sw_2 and Sw_3 are on and $V_I = -V_{DC}$. Otherwise, Sw_3 and Sw_4 are on, and $V_I = 0$.

The pulse-train in Fig. 6.3 can be low-pass filtered (red waveform), to eliminate uncontrolled higher harmonics. These higher harmonics are illustrated in the frequency domain in Fig. 6.4. The switching frequency, the frequency of pulses in the pulse train, is represented by f_{sw}, and is equal to the fundamental frequency multiplied by N_p.

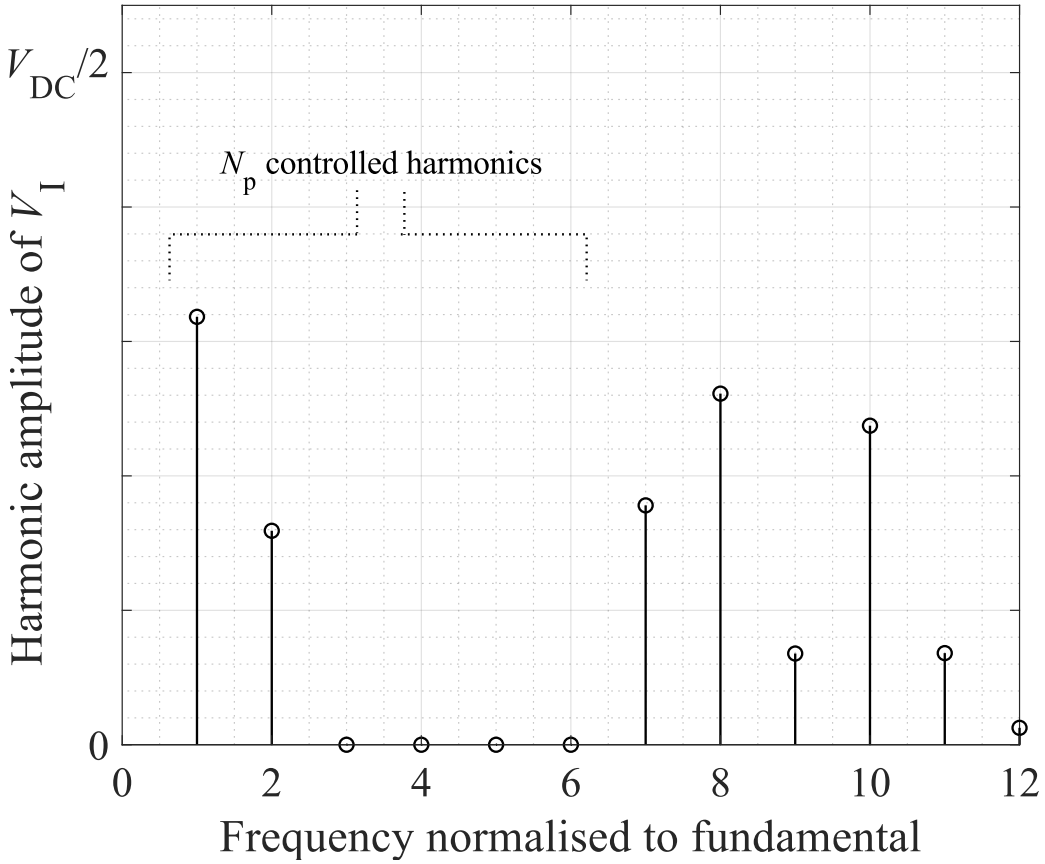

Fig. 6.4 Frequency domain representation containing first and second harmonic content.

Both SHE and SHG are based on the Fourier-series expansion of a bipolar pulse-train, like the pulse train shown in Fig. 6.3. The sine-cosine form of the Fourier series is

$$S(\theta) = A_0 + \sum_{n=1}^{\infty} (A_n \cos(n\theta) + B_n \sin(n\theta)) \tag{6.1}$$

where

$$A_0 = \frac{1}{2\pi} \int_0^{2\pi} s(\theta)\, \mathrm{d}\theta \tag{6.2}$$

$$A_n = \frac{1}{\pi} \int_0^{2\pi} s(\theta) \cos(n\theta)\, \mathrm{d}\theta \tag{6.3}$$

$$B_n = \frac{1}{\pi} \int_0^{2\pi} s(\theta) \sin(n\theta)\, \mathrm{d}\theta \tag{6.4}$$

A_n and B_n represent the orthogonal contributions of the n^{th} harmonic, A_0 represents the DC offset of the waveform.

The waveform function $S(\theta)$ is given by

$$S(\theta) = \begin{cases} V_{\mathrm{DC}}, & \phi_{\mathrm{S}a} < \theta < \phi_{\mathrm{E}a} \text{ and } a < 0 \\ -V_{\mathrm{DC}}, & \phi_{\mathrm{S}a} < \theta < \phi_{\mathrm{E}a} \text{ and } a > 0 \\ 0, & \text{otherwise} \end{cases} \tag{6.5}$$

Equation (6.5) can be substituted into (6.3) and the integration evaluated to give

$$A_n = \frac{1}{n\pi} \sum_{a=-\frac{N_p}{2}}^{\frac{N_p}{2}} \mathrm{sgn}(a)\, \gamma(n\phi_{\mathrm{S}a}, n\phi_{\mathrm{E}a}) \tag{6.6}$$

where N_p is the number of pulses per cycle and

$$\gamma(\phi_\mathrm{S}, \phi_\mathrm{E}) \equiv V_{\mathrm{DC}}(\sin(\phi_\mathrm{S}) - \sin(\phi_\mathrm{E})) \tag{6.7}$$

Similarly,

$$B_n = \frac{1}{n\pi} \sum_{a=-\frac{N_\mathrm{p}}{2}}^{\frac{N_\mathrm{p}}{2}} \mathrm{sgn}(a)\, \lambda(n\phi_{\mathrm{S}a}, n\phi_{\mathrm{E}a}) \tag{6.8}$$

where,

$$\lambda(\phi_\mathrm{S}, \phi_\mathrm{E}) \equiv V_{\mathrm{DC}}(\cos(\phi_\mathrm{E}) - \cos(\phi_\mathrm{S})) \tag{6.9}$$

Since the goal of SHG is to a design a pulse waveform to exhibit specific harmonic content, the values of A_n and B_n are known. The problem is to determine the required switching angles to generate the desired harmonics $A_{1,2,3\ldots}$ and $B_{1,2,3\ldots}$.

$$\boldsymbol{G}(\boldsymbol{\phi}_m) = \begin{bmatrix} \gamma(\phi_{\mathrm{S}1}, \phi_{\mathrm{E}1}) + \gamma(\phi_{\mathrm{S}2}, \phi_{\mathrm{E}2}) \ldots - \gamma(\phi_{\mathrm{S}-1}, \phi_{\mathrm{E}-1}) - \gamma(\phi_{\mathrm{S}-2}, \phi_{\mathrm{E}-2}) \ldots - \pi A_1 \\ \gamma(2\phi_{\mathrm{S}1}, 2\phi_{\mathrm{E}1}) + \gamma(2\phi_{\mathrm{S}2}, 2\phi_{\mathrm{E}2}) \ldots - \gamma(2\phi_{\mathrm{S}-1}, 2\phi_{\mathrm{E}-1}) - \gamma(2\phi_{\mathrm{S}-2}, 2\phi_{\mathrm{E}-2}) \ldots - 2\pi A_2 \\ \gamma(3\phi_{\mathrm{S}1}, 3\phi_{\mathrm{E}1}) + \gamma(3\phi_{\mathrm{S}2}, 3\phi_{\mathrm{E}2}) \ldots - \gamma(3\phi_{\mathrm{S}-1}, 3\phi_{\mathrm{E}-1}) - \gamma(3\phi_{\mathrm{S}-2}, 3\phi_{\mathrm{E}-2}) \ldots - 3\pi A_3 \\ \vdots \\ \lambda(\phi_{\mathrm{S}1}, \phi_{\mathrm{E}1}) + \lambda(\phi_{\mathrm{S}2}, \phi_{\mathrm{E}2}) \ldots - \lambda(\phi_{\mathrm{S}-1}, \phi_{\mathrm{E}-1}) - \lambda(\phi_{\mathrm{S}-2}, \phi_{\mathrm{E}-2}) \ldots - \pi B_1 \\ \lambda(2\phi_{\mathrm{S}1}, 2\phi_{\mathrm{E}1}) + \lambda(2\phi_{\mathrm{S}2}, 2\phi_{\mathrm{E}2}) \ldots - \lambda(2\phi_{\mathrm{S}-1}, 2\phi_{\mathrm{E}-1}) - \lambda(2\phi_{\mathrm{S}-2}, 2\phi_{\mathrm{E}-2}) \ldots - 2\pi B_2 \\ \lambda(3\phi_{\mathrm{S}1}, 3\phi_{\mathrm{E}1}) + \lambda(3\phi_{\mathrm{S}2}, 3\phi_{\mathrm{E}2}) \ldots - \lambda(3\phi_{\mathrm{S}-1}, 3\phi_{\mathrm{E}-1}) - \lambda(3\phi_{\mathrm{S}-2}, 3\phi_{\mathrm{E}-2}) \ldots - 3\pi B_3 \\ \vdots \end{bmatrix} = \mathbf{0} \tag{6.10}$$

In (6.10), (6.6) and (6.8) are represented together as a system of equations, $\boldsymbol{G}(\boldsymbol{\phi}_m)$, where $\boldsymbol{\phi}_m$ is the vector of switching angles and $\mathbf{0}$ is the zero vector.

The system in (6.10) has $2N_\mathrm{P}$ equations in $2N_\mathrm{P}$ unknowns (the switching angles). This system is non-linear, but can be solved numerically using Newton's method:

$$\boldsymbol{\phi}_{m+1} = \boldsymbol{\phi}_m - \left(\frac{\partial \boldsymbol{G}(\boldsymbol{\phi}_m)}{\partial \boldsymbol{\phi}_m}\right)^{-1} \boldsymbol{G}(\boldsymbol{\phi}_m) \tag{6.11}$$

where m is the iteration.

The initial conditions, $\boldsymbol{\phi}_0$, were estimated by pulse-width modulating (PWM) a time-domain representation of the waveform to be generated: this time-domain representation is divided into N_p equally spaced sections, representing the period of the modulated waveform. The amplitude at the centre of each section is the centre-aligned duty cycle for that period.

For convenience, each harmonic is converted from polar form using (6.12) for use in (6.10).

$$\begin{aligned} A_n &= H_n \sin(\psi_n) \\ B_n &= H_n \cos(\psi_n) \end{aligned} \tag{6.12}$$

To ensure dominance of the fundamental harmonic, $H_1 \geq 2H_2$. Violating this inequality may result in extra negative pulses in the region $\theta > \pi$ and extra positive pulses in the region $\theta < \pi$, invalidating the waveform definition, (6.5), for the modulated waveform.

To ensure that the harmonics converge closely to the desired values, 15 iterations of Newton's method are carried out using 64-bit precision. The SHG microcontroller program uses minimal deadtime, in the 10s of ns. This is facilitated by the use of fast GaN devices in the inverter and allows the generated pulse-train to closely match the waveform function (6.5).

6.3 Experiment 1

6.3.1 Experimental Setup

The physical system consists of a GaN H-Bridge inverter described in Section 3.6, driving a HV transformer, connected via a current-sense capacitor to the reactor. The electrical set-up diagram is shown in Fig. 6.5 and the inverter specifications are in Table 3.4. The biaxial reactor used is described in Section 3.2.2. The ozone output was measured with a 2B Technologies 106 ozone monitor.

The frequency response of the transformer is shown in Fig. 3.13. To obtain high gain at the second harmonic, a fundamental frequency of 35 kHz for all tests was chosen.

Power to the reactor was measured using the Lissajous technique (Section 2.3.1). The dry air feedstock was set at a flowrate of 0.5 ℓpm.

The number of pulses per cycle, $N_p = 10$, allowing the uncontrolled higher harmonics to be attenuated by approximately 30 dB compared to the gain at the fundamental frequency.

To prevent a waveform being generated with a DC offset ($A_0 \neq 0$) which could lead to transformer core saturation, $\psi_n = 0 \ \therefore A_n = 0$ and only B_1 and B_2 are varied. This results in the waveforms being rotationally symmetrical around $\theta = \pi$, and therefore $A_0 = 0$.

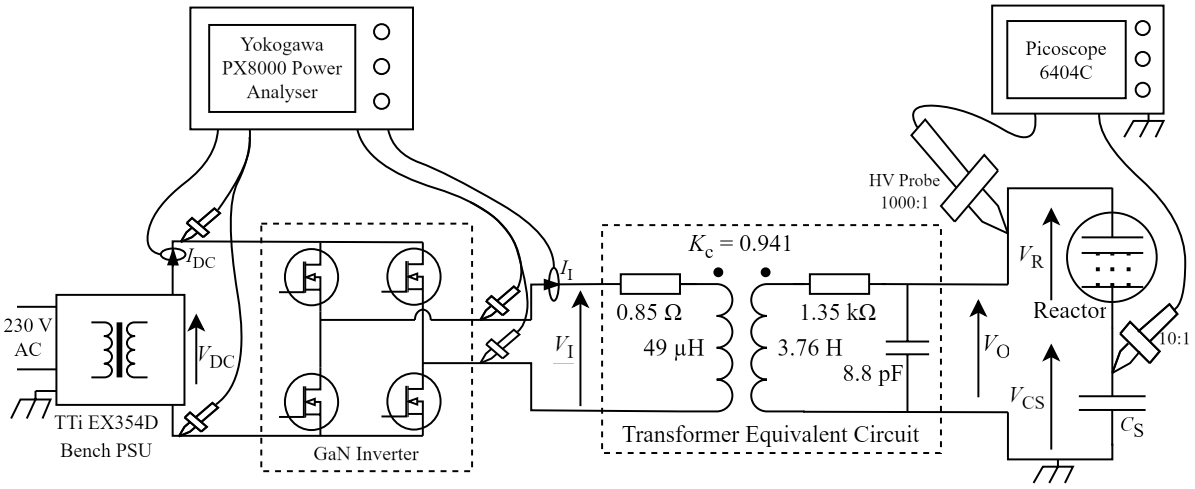

Fig. 6.5 Experimental setup for experiment 1

6.3.2 Experimental Results

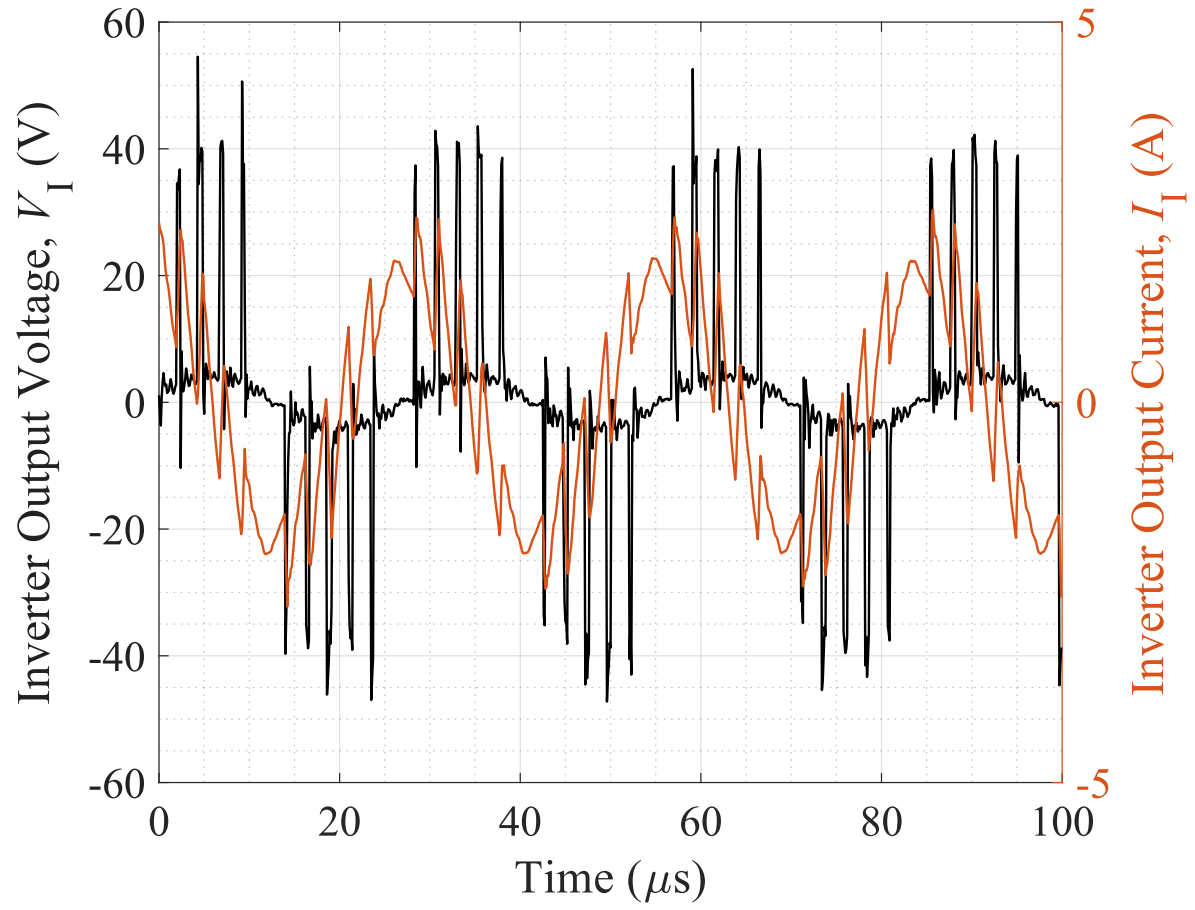

Fig. 6.6 Inverter output voltage V_I and current I_I when $B_1 = 0.23 V_{DC}$, $B_2 = 0$

For these tests, B_1 was adjusted from $0.114V_{DC}$ to $0.228V_{DC}$ and B_2 between 0 and $0.114V_{DC}$, whilst ensuring $2B_2 \leq B_1$.

Fig. 6.6 shows the inverter output current and voltage with no second harmonic. The pulses can clearly be seen extending to ±48 V. The 350 kHz triangle wave contribution to the 35 kHz current waveform (orange) is due to switching frequency exciting the step-up transformer.

Fig. 6.7 shows the waveforms when the second harmonic is set to 50% of the 1st harmonic. The second harmonic is visible in the current waveform as well as the high-frequency ripple.

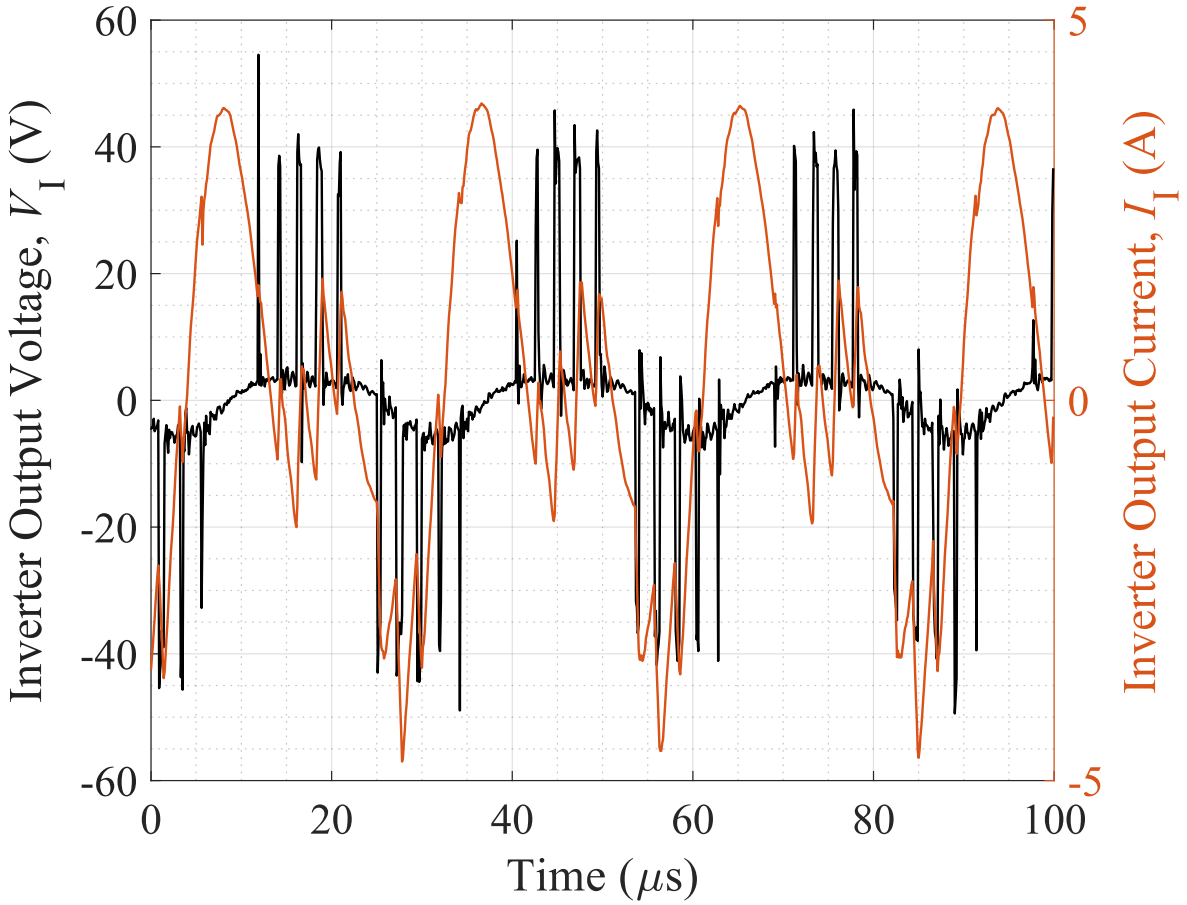

Fig. 6.7 Inverter output voltage V_I and current I_I when $B_1 = 0.23V_{DC}$, $B_2 = 0.115V_{DC}$

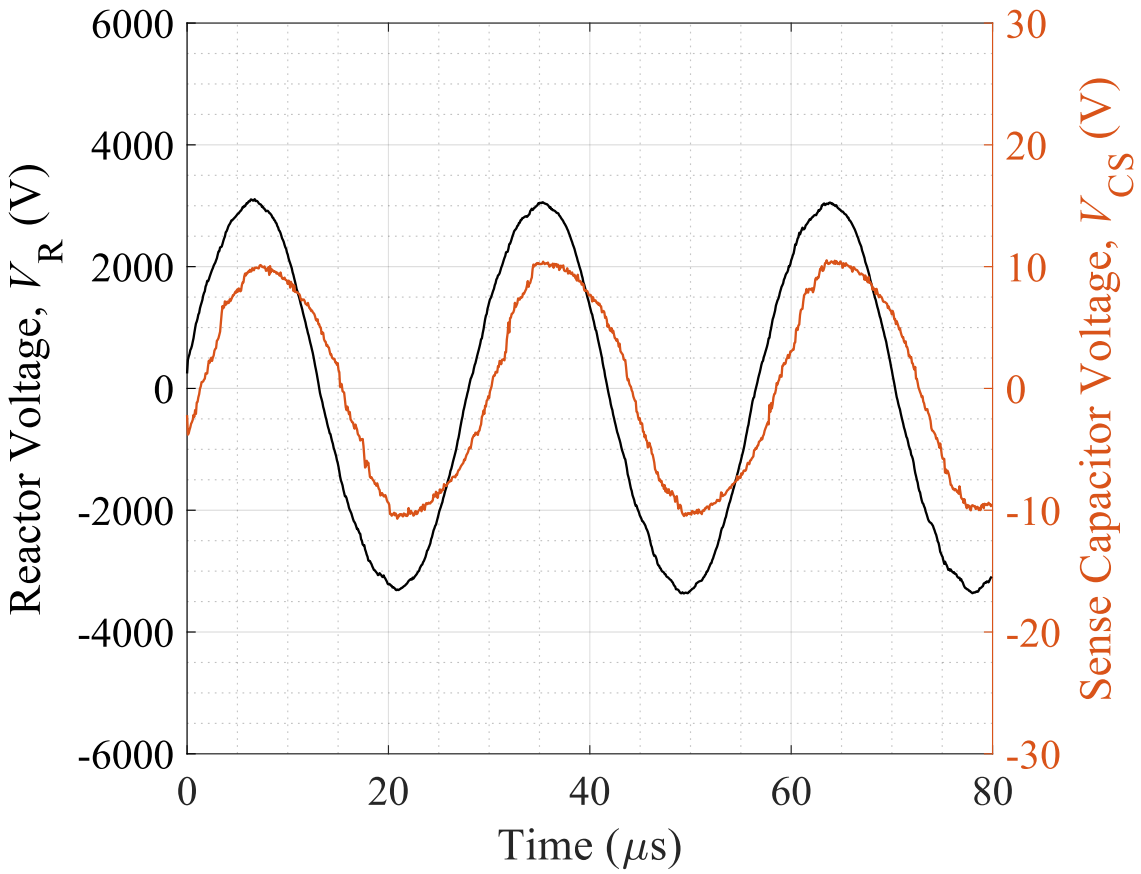

Fig. 6.8 Reactor voltage V_R and current sense capacitor voltage V_{CS} when $B_1 = 0.23 V_{DC}$, $B_2 = 0$

Fig. 6.8 and Fig. 6.9 show the reactor waveforms for the same conditions as in Fig. 6.6 and Fig. 6.7. The transformer has filtered out the high-frequency harmonics, leaving the waveforms closer to the desired pure 1st and 2nd harmonics. As there is discharge in the reactor during both tests, both Fig. 6.8 and Fig. 6.9 show noise due to discharge in the reactor.

The spectral content of the transformer output voltage is shown in Fig. 6.10. Harmonics above the second are attenuated by over 20 dB compared to the fundamental. When $B_2 = 0$, the uncontrolled second harmonic (V_{O2}) is 80 V_{pk} compared to the fundamental 3.2 kV_{pk}. When $B_2 = 0.115 V_{DC}$, V_{O2} = 1.3 kV_{pk}, less than the 1.6 kV_{pk} predicted by difference between B_1 and B_2. This could be due to the increased RMS voltage increasing the power in the reactor, increasing the current and the voltage drop across parasitic components in the transformer.

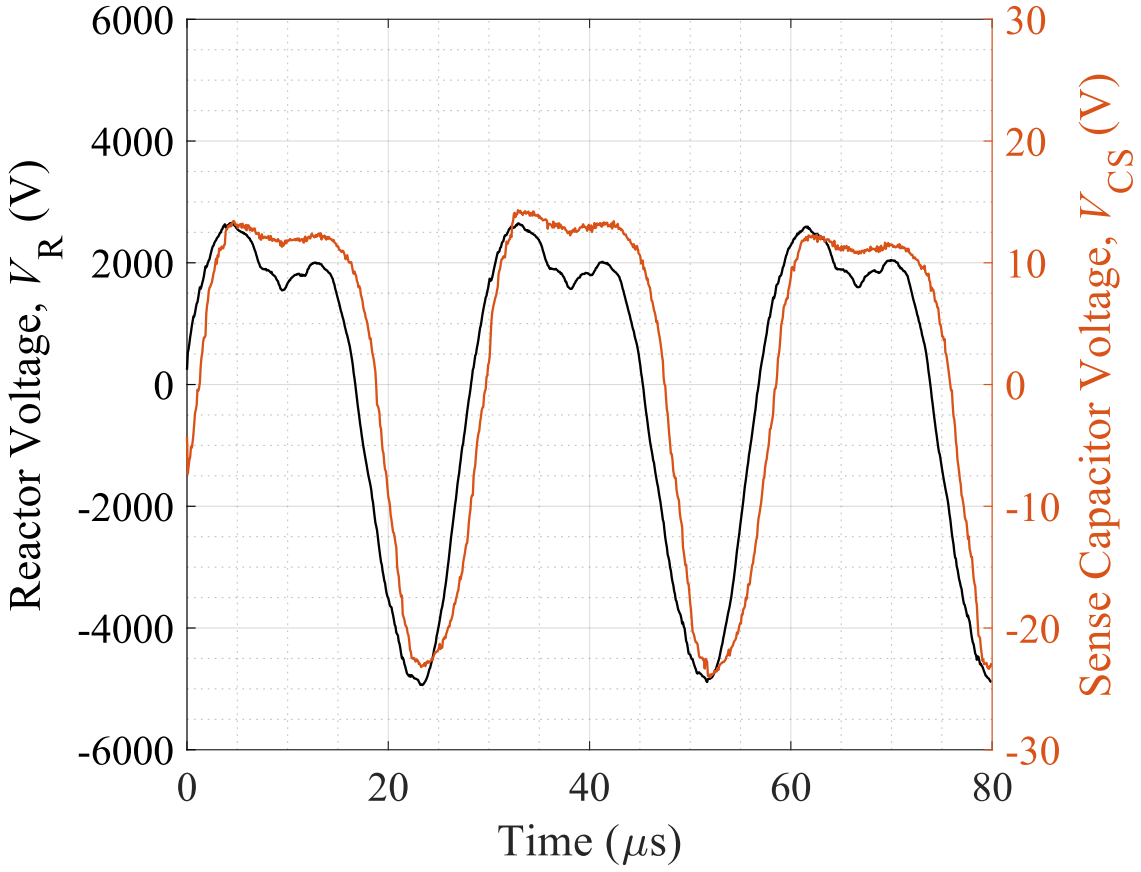

Fig. 6.9 Reactor voltage V_R and current sense capacitor voltage V_{CS} when $B_1 = 0.23V_{DC}$, $B_2 = 0.115V_{DC}$

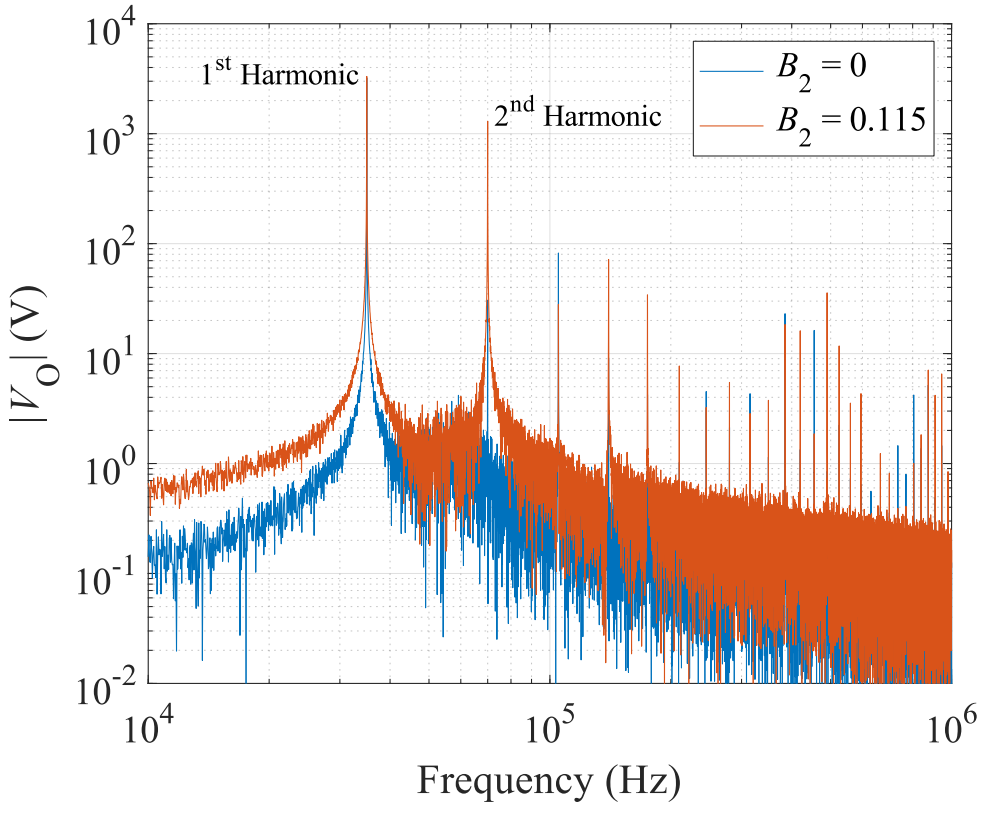

Fig. 6.10 Transformer output voltage ($V_{O\,pk}$) in the frequency domain when $B_1 = 0.23V_{DC}$

6.3.3 Investigation into Reactor Performance

Fig. 6.11 shows power delivered to the reactor over the test-range of 1st and 2nd harmonic magnitudes where the horizontal axis is the amplitude of the first harmonic component of the output voltage and the vertical axis is the second harmonic. Power increased as both the magnitude of the 1st and 2nd harmonic were increased, reaching a peak of approximately 6 W. As the 1st harmonic of the output voltage (V_{O1}) was increased and the power in the reactor increased, V_{O2} reduced, perhaps due to the increased current as discussed previously.

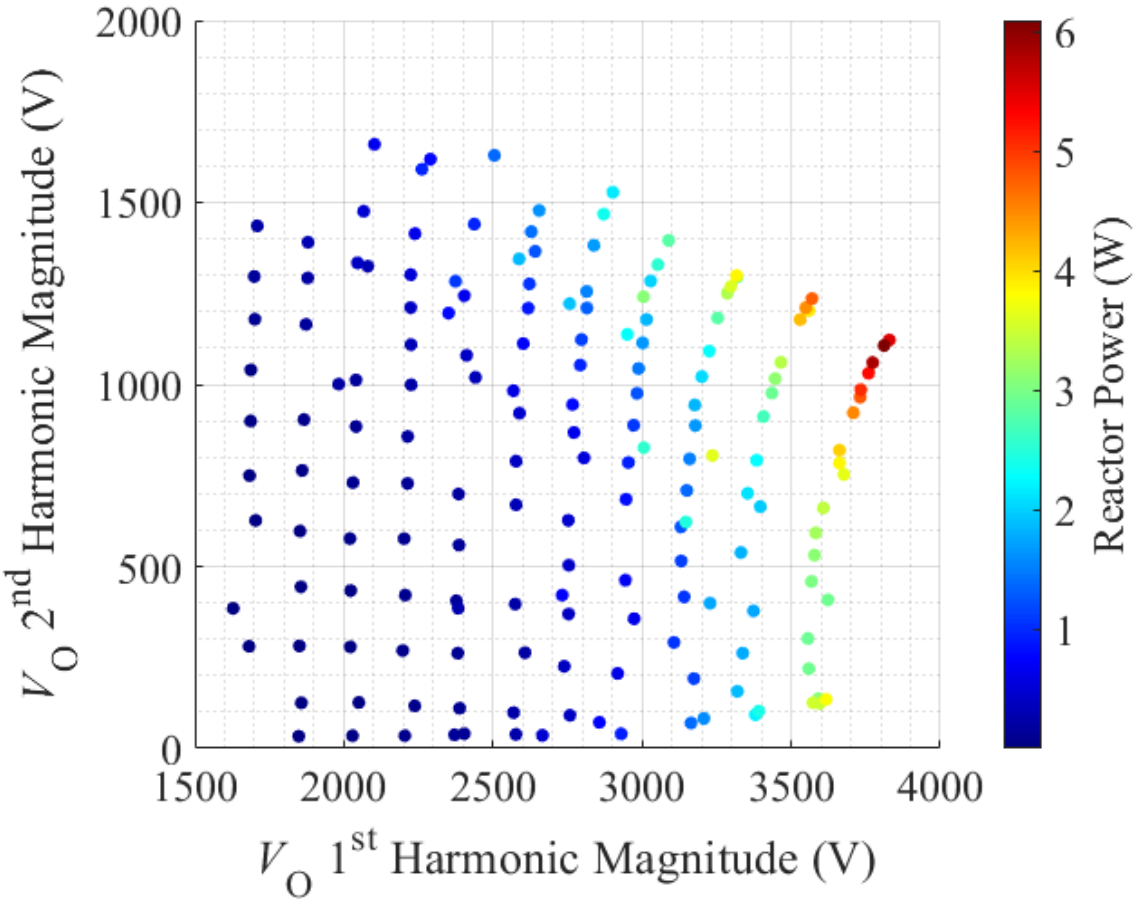

Fig. 6.11 Reactor power as a function of the 1st and 2nd harmonic voltage

The ozone concentration obtained from these tests is presented in Fig. 6.12. The maximum ozone concentration was obtained with V_{O1} = 3 kV_{pk} and V_{O2} = 1.25 kV_{pk}, at 175 ppm (parts per million).

The ozone concentration increases as both harmonic voltages are increased, then decreases sharply when V_{O1} > 3.5 kV_{pk} and V_{O2} > 750 V_{pk}. This is thought to be due to heating in the

reactor causing ozone to be destroyed after production as ozone is highly reactive and degrades quickly at high temperatures [6.1].

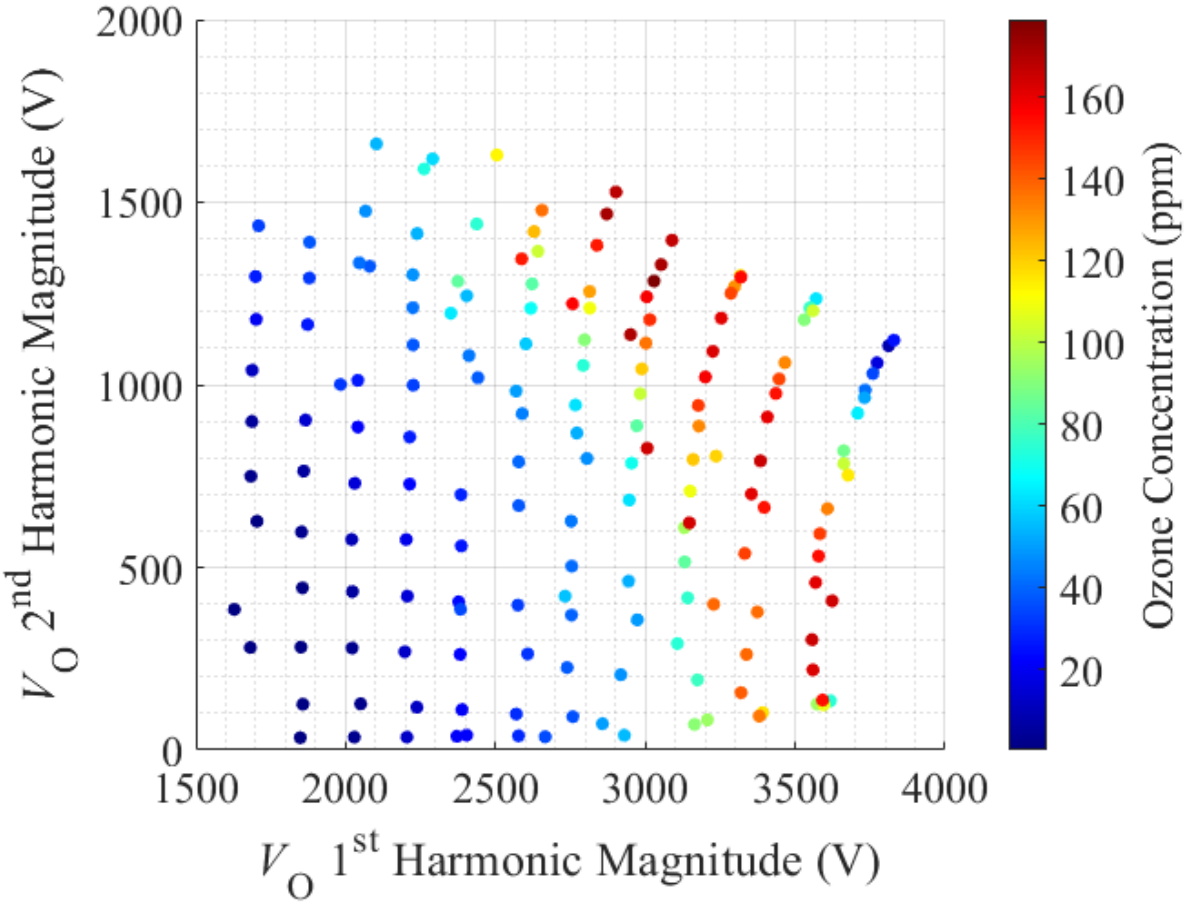

Fig. 6.12 Ozone concentration as a function of the 1st and 2nd harmonic voltage

Fig. 6.12 shows that high concentrations (~150 ppm) can be obtained using V_{O1} = 3.5 kV_{pk} and V_{O2} = 100 V_{pk}, by using V_{O1} = 3 kV_{pk} and V_{O2} = 1.3 kV_{pk}, or some combination within this range. Fig. 6.13 shows that, over the same range, the reactor efficacy changes from 57 ppm/W when $V_{O2} \ll V_{O1}$ to 78 ppm/W with significant 2nd harmonic, suggesting that, in this system, efficacy can be improved by adding 2nd harmonic content to the waveform whilst slightly decreasing the fundamental amplitude.

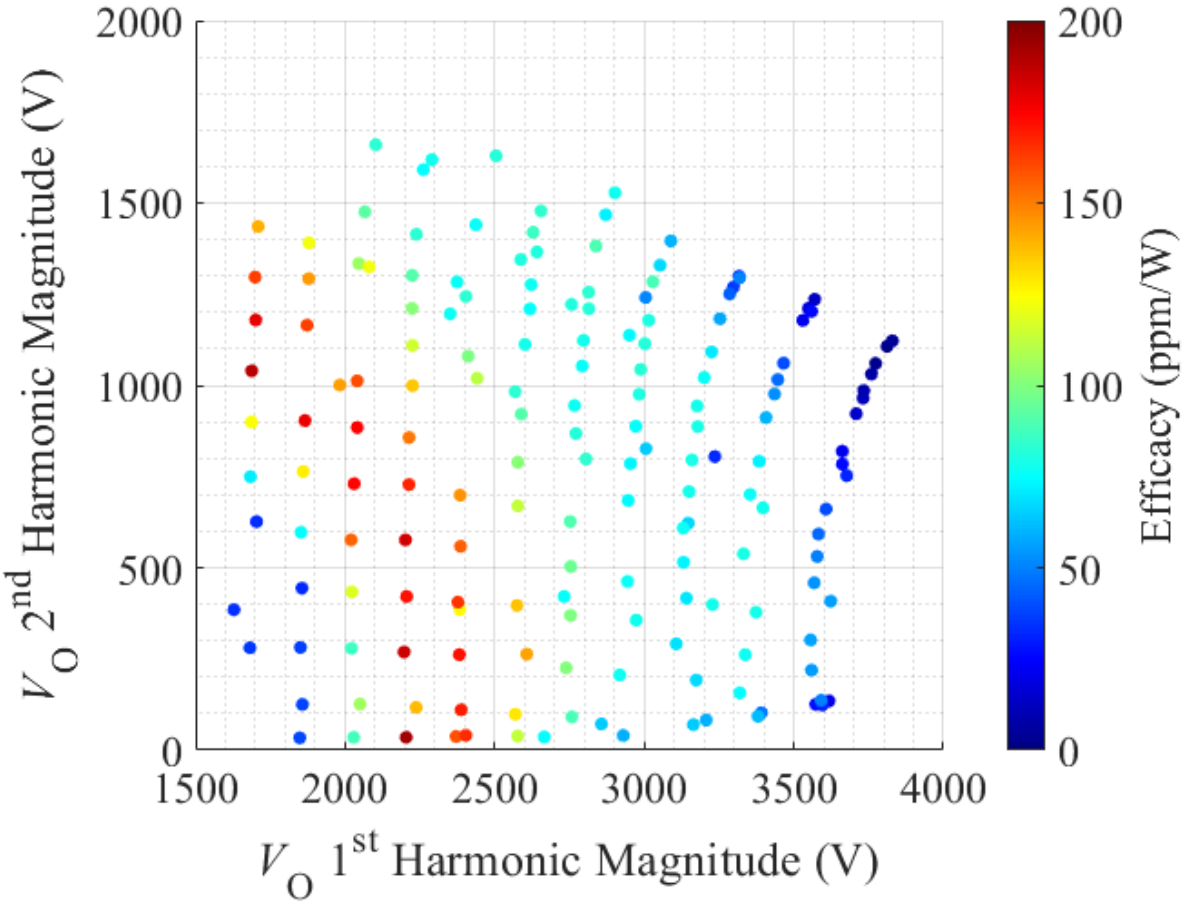

Fig. 6.13 Reactor efficacy as a function of the 1st and 2nd harmonic voltage

Fig. 6.13 shows the efficacy of the reactor (a measure of the reactor performance in ppm/W) over the same tests. The efficacy peaks at relatively low voltages, around V_{O1} = 2.25 kV_{pk} and V_{O2} = 600 V_{pk}. When combined with the ozone concentration data from Fig. 6.12, this represents a trade-off between efficacy and ozone concentration; the highest efficiency can only be obtained at low concentrations.

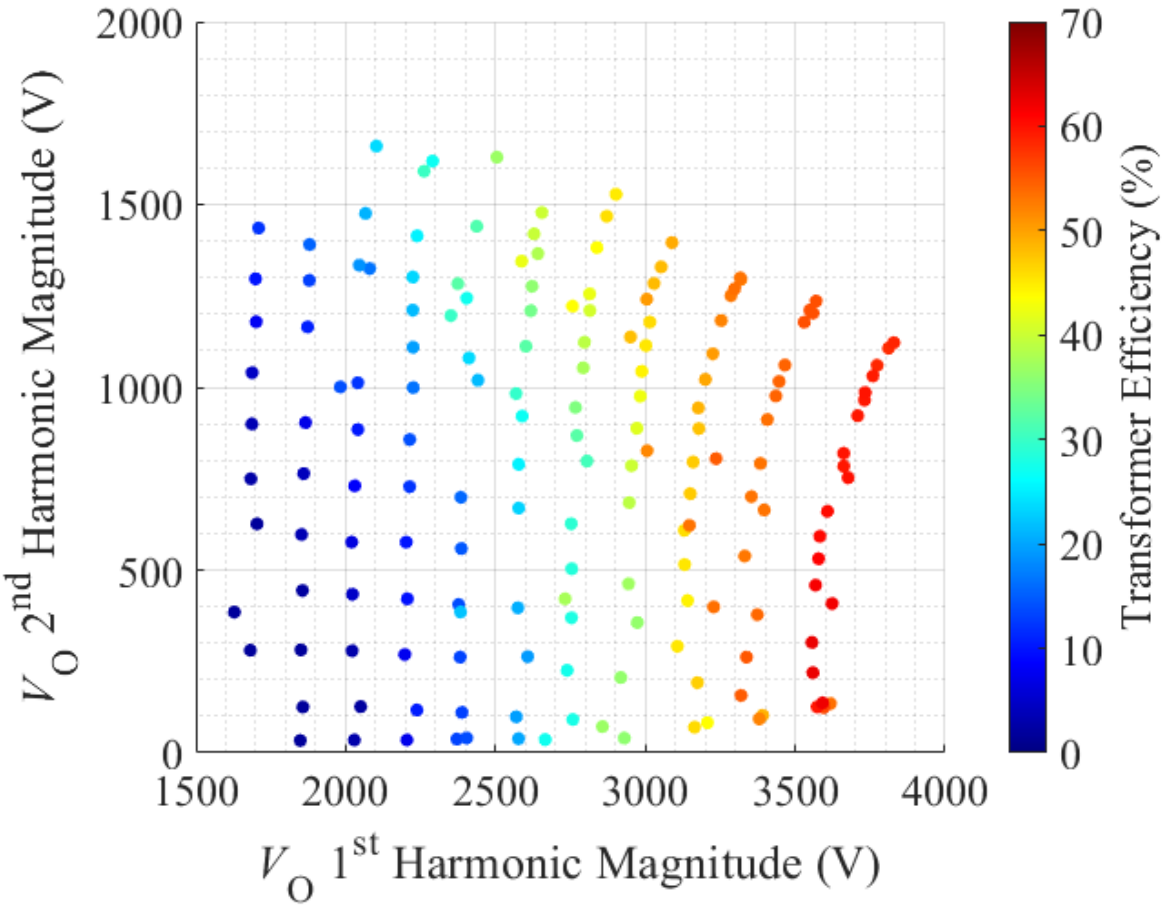

Fig. 6.14 Transformer efficiency as function of the 1st and 2nd harmonic voltage

Fig. 6.14 shows how the transformer efficiency varies with voltage. This figure shows a similar trend to the reactor power in Fig. 6.11, suggesting that the transformer losses are dominated by losses associated with reactive current, rather than the load current. A better selection of transformer or operating frequency may help increase this efficiency.

6.4 Experiment 2

6.4.1 Experimental Setup

The experimental system shown in Fig. 8 consists of a GaN H-Bridge inverter driving a piezoelectric transformer, which is represented by its equivalent circuit, via a current sense resistor, R_S, and series inductor, L_I. The SMSTF71P12S8 PT output is connected via a current-sense capacitor, C_S to the reactor. The SMSTF71P12S8 PT equivalent circuit was found using the "PSO" technique (T3) described in Chapter 4. The inverter specifications are shown in Table 3.4. A diagram of the coaxial reactor used is shown in Fig. 3.3. The ozone output was again measured with a 2B Technologies 106 ozone monitor.

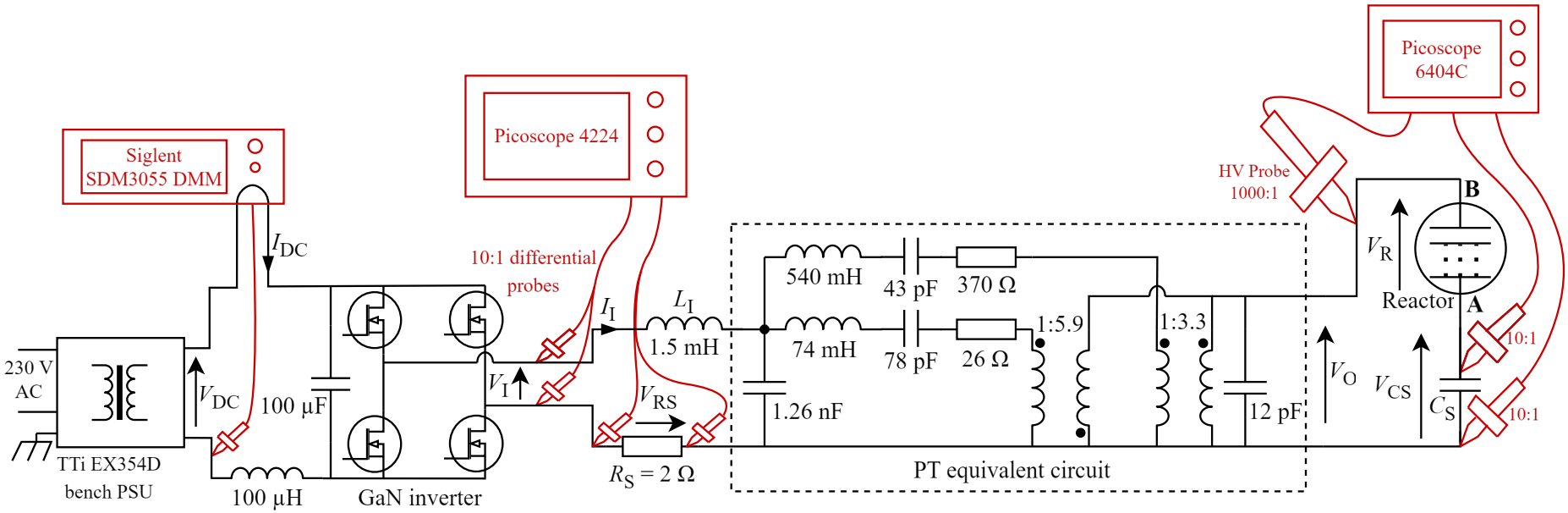

Fig. 6.15 Experimental setup for experiment 2. Measurement equipment is coloured red.

The frequency response of the PT is shown in Fig. 3.7. Peaks in the gain at the first, second and third resonant modes can be seen at approximately 35, 70 and 105 kHz, the first two having significantly higher magnitude than the third. To obtain high gain at the second harmonic, a fundamental frequency of 35 kHz for all tests was chosen.

To reduce the losses in the inverter associated with hard switching a capacitive load, a 1.5 mH inductor L_I was added in series with the PT input, seen in Fig. 6.15. This allows the significant harmonics above the switching frequency, f_{sw} = 350 kHz to be attenuated by L_I, whilst the gain at the first and second harmonics remains high.

The input power to the PT (P_I) was measured with a current sense resistor, R_S = 2 Ω and differential probes were used to measure the inverter output voltage (V_I) and the current-sense resistor voltage (V_{RS}). Equation (6.13) was then used to calculate average power from the recorded waveforms.

$$P_I = \frac{1}{TR_S} \int_{t=0}^{T} (V_I(t) - V_{RS}(t)) V_{RS}(t)\, dt \tag{6.13}$$

where T is the time-period over which the data was taken.

Power to the reactor (P_R) was again measured using the Lissajous technique described in Section 2.3.1. The dry air feedstock was set at a flowrate of 1 ℓpm.

For the experimental tests, a parametric sweep was performed with three variables, H_1, H_2 and ψ_2. H_1 was adjusted in the range $0.15V_{DC}$ to $0.76V_{DC}$, H_2 was adjusted from 0 to $0.38V_{DC}$, ψ_1 = 0, and ψ_2 was adjusted in 4 steps: 0, 90°, 180° and 270°. The input voltage to the inverter, V_{DC}, was maintained at 48 V. In this experiment, N_P = 10.

6.4.2 Experimental Results

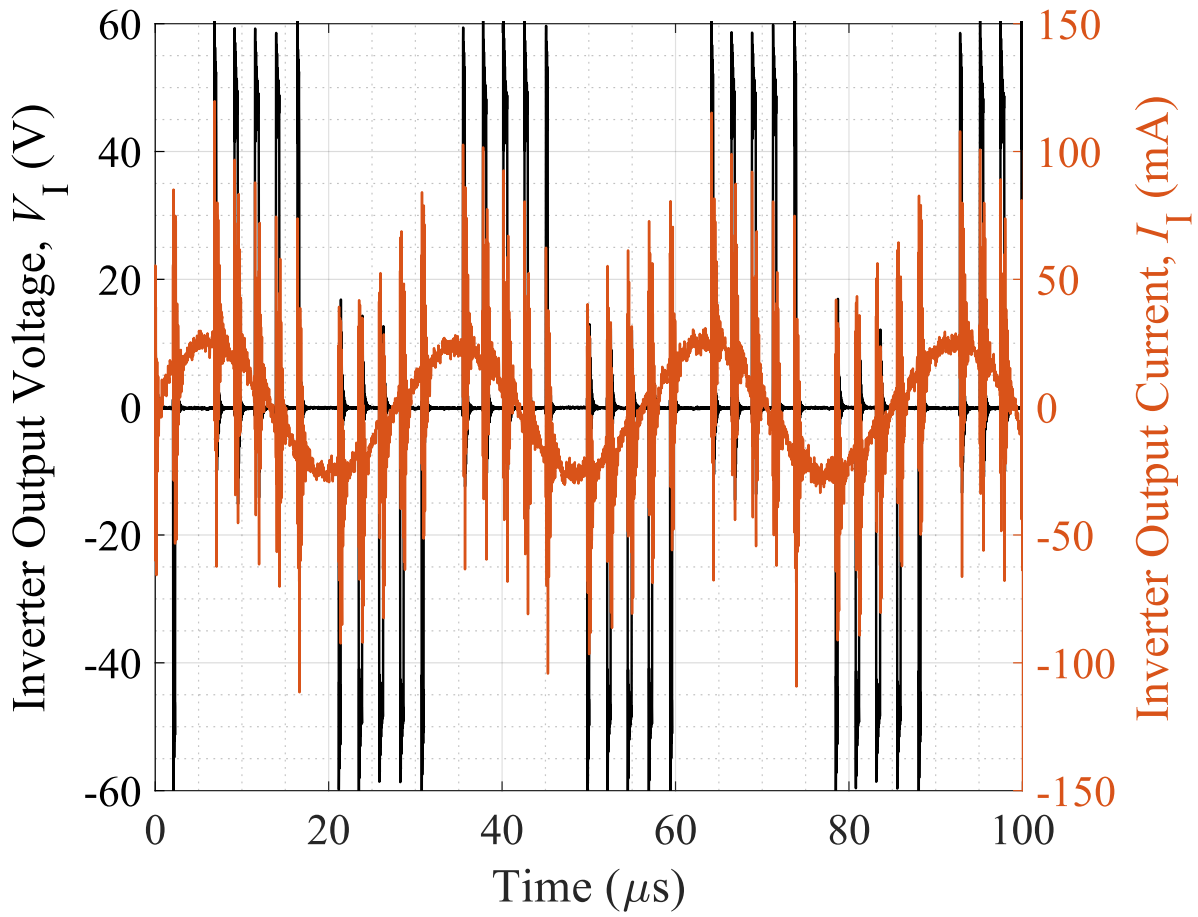

Fig. 6.16 Time domain waveform for the inverter output. $H_1 = 0.19V_{DC}$, $H_2 = 0$, $\psi_2 = 0$

Fig. 6.16 shows the inverter output voltage (V_I) and current (I_I) in the time domain for the case where $H_1 = 0.19V_{DC}$ and $H_2 = 0$. The switching at 350 kHz is visible, causing ripple on the current waveform, which is otherwise sinusoidal.

The PT output voltage (V_O) and current sense capacitor voltage (V_{CS}) for these conditions can be seen in Fig. 6.17. The peak PT output voltage is 650 V, below the plasma ignition threshold, so no noise from dielectric discharge is present on either waveform in Fig. 6.17.

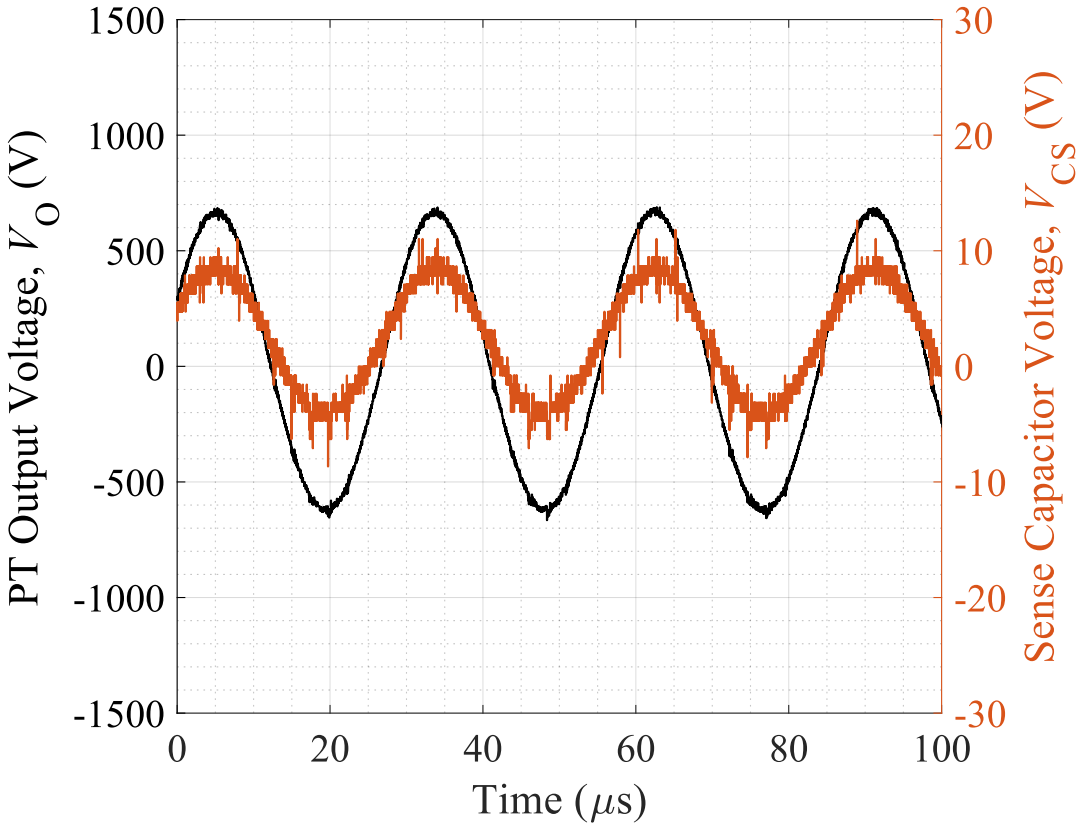

Fig. 6.17 Time domain waveform for the PT output. $H_1 = 0.19V_{DC}$, $H_2 = 0$, $\psi_2 = 0$

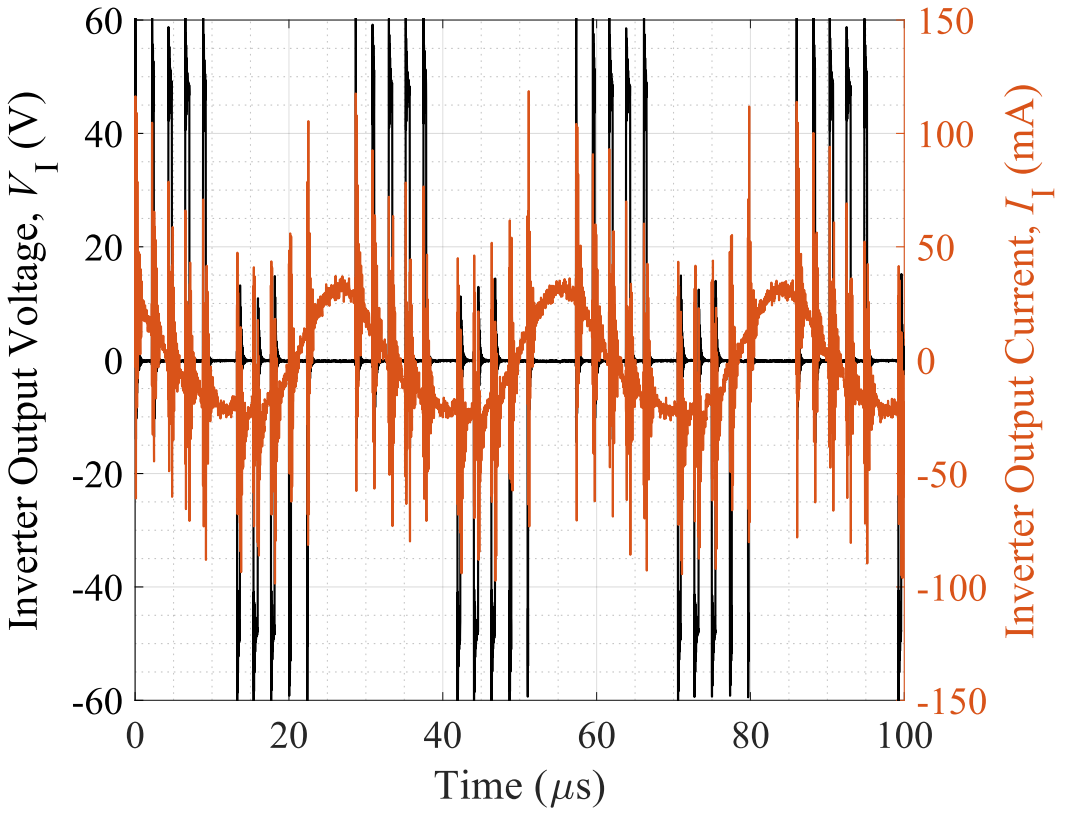

Fig. 6.18 Time domain waveform for the inverter output. $H_1 = 0.19V_{DC}$, $H_2 = 0.1V_{DC}$, $\psi_2 = 0$

Fig. 6.18 and Fig. 6.19 show the inverter output and PT output voltage waveforms respectively for the case where $H_2 = 0.1V_{DC}$. The effect of the second harmonic content is manifest as different zero-voltage periods between the positive and negative half-cycles shown in Fig. 6.18 and as the non-sinusoidal reactor voltage in Fig. 6.19.

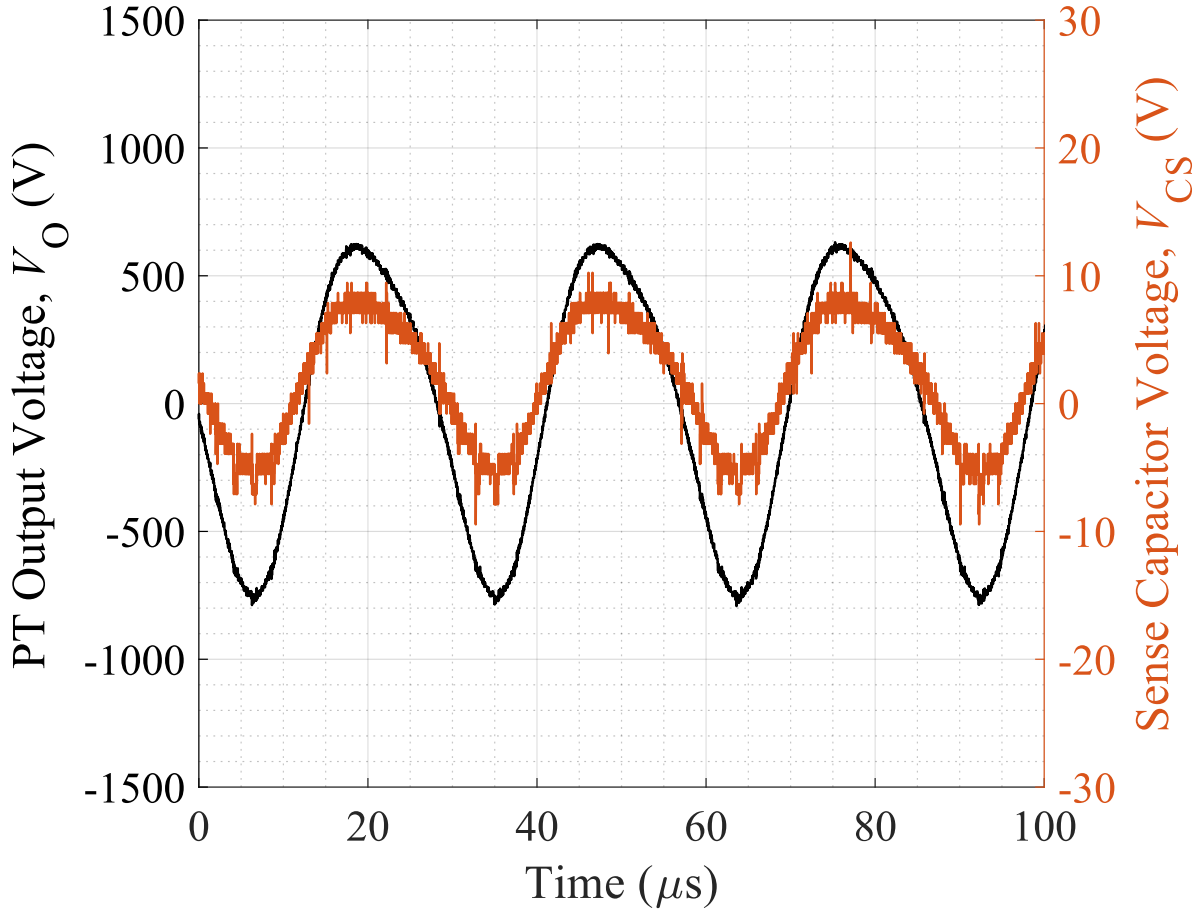

Fig. 6.19 Time domain waveform for the PT output. $H_1 = 0.19V_{DC}$, $H_2 = 0.1V_{DC}$, $\psi_2 = 0$

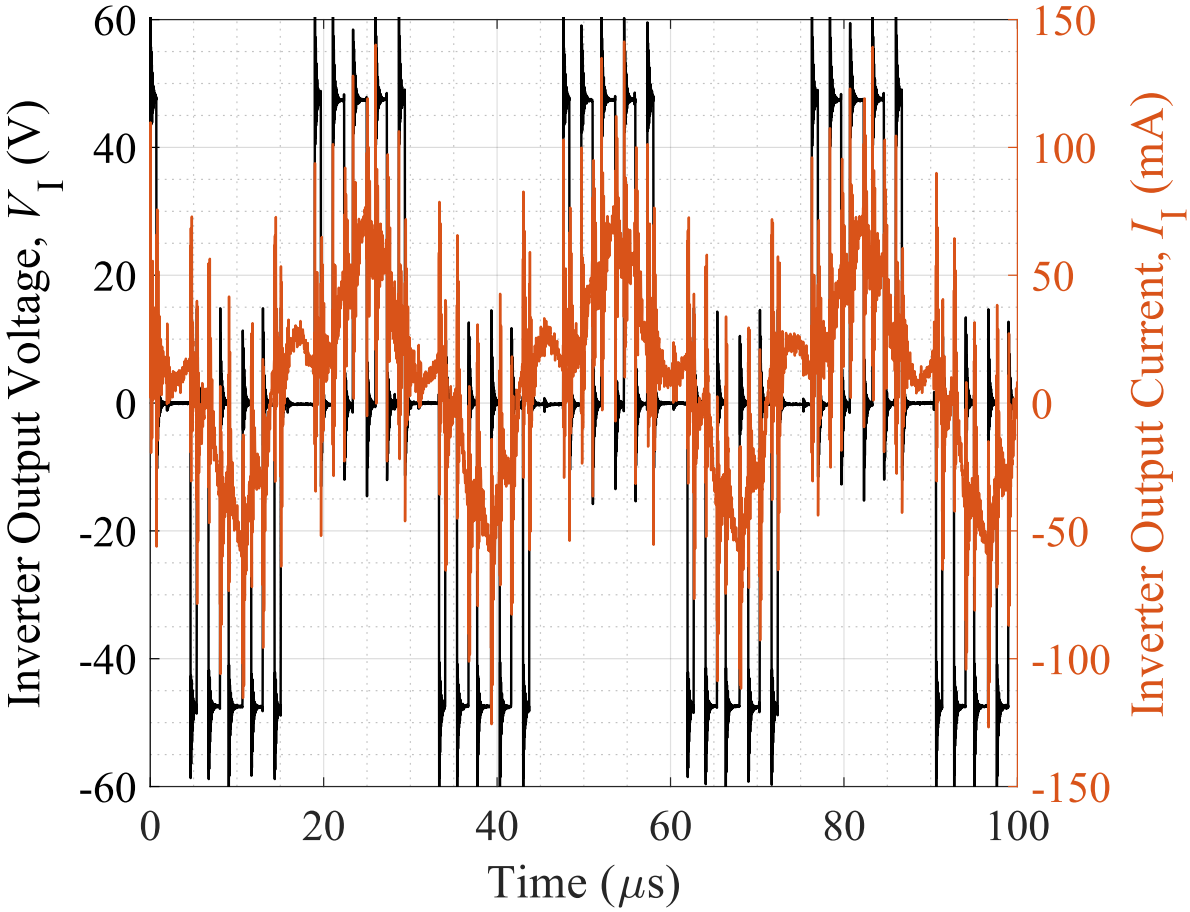

Fig. 6.20 Time domain waveform for the inverter output. $H_1 = 0.64V_{DC}$, $H_2 = 0$, $\psi_2 = 0$

Fig. 6.20 shows the inverter output voltage and current when $H_1 = 0.64V_{DC}$. The PT output voltage (Fig. 6.21) is sufficient to form plasma in the gas gap.

The output impedance of a PT is low at the resonant frequencies of the PT; however, away from these frequencies, the output impedance is significantly higher. The plasma discharges, drawing current with a wide range of spectral content, cause voltage fluctuations on the output of the PT which are seen several times per cycle (Fig. 6.21). Increasing H_1 by a factor of three to $0.64V_{DC}$ increased V_O by a factor of approximately two, demonstrating the non-linearity of the system.

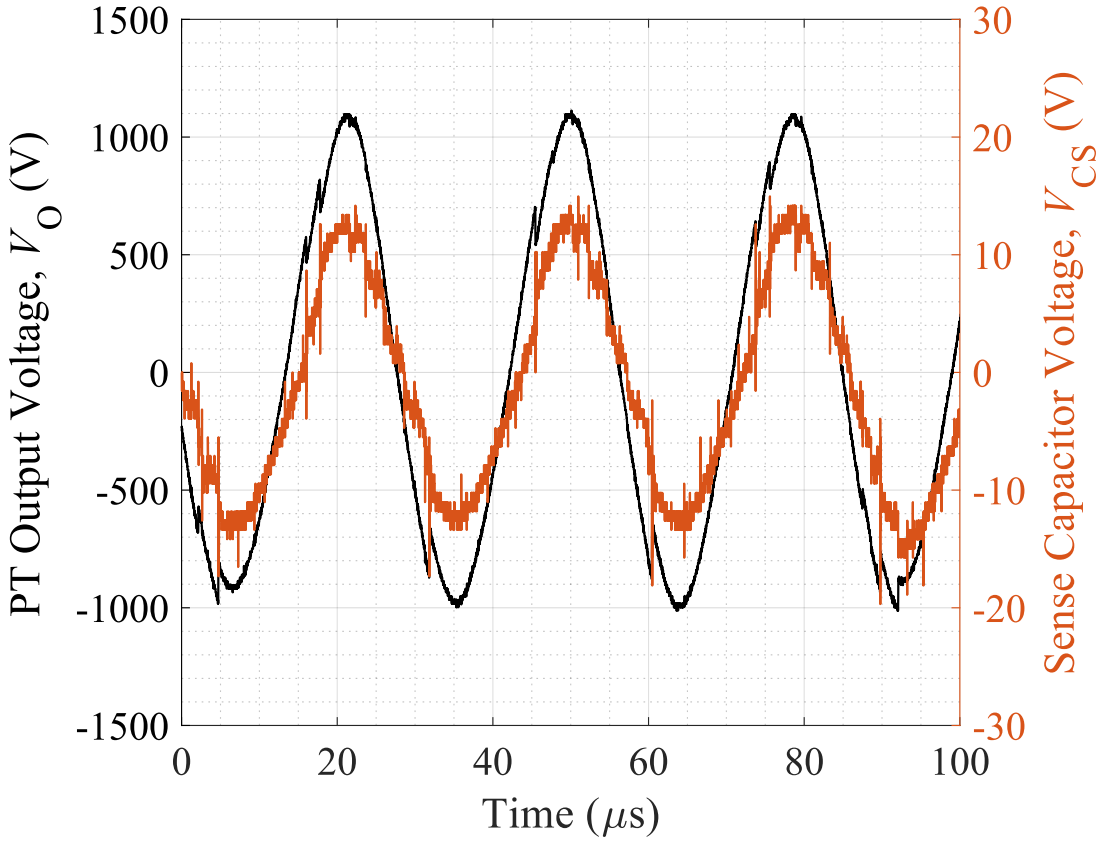

Fig. 6.21 Time domain waveform for the PT output. $H_1 = 0.64V_{DC}$, $H_2 = 0$, $\psi_2 = 0$

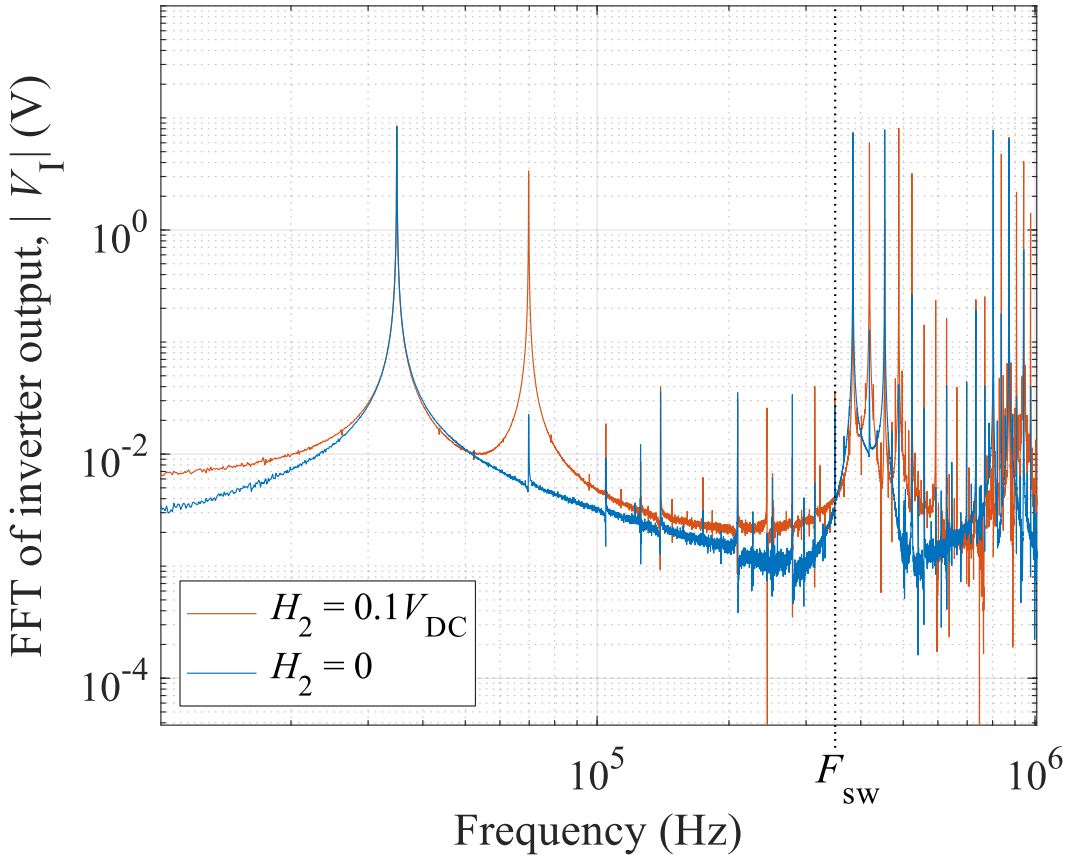

Fig. 6.22 Inverter output frequency spectra for $H_1 = 0.19V_{DC}$

Fig. 6.22 shows the output spectra for the inverter with the first harmonic amplitude set to $H_1 = B_1 = 0.19V_{DC}$. With $H_2 = 0$ (blue curve) the measured first harmonic inverter output voltage, $V_{I1} = 8.4\ V_{pk}$, approximately 90% of the designed value of $H_1 = 9.12\ V_{pk}$.

There is no harmonic content above 40 mV_{pk} from the second harmonic up to and including the tenth harmonic. With $H_2 = 0.1V_{DC}$, the inverter output has measured second harmonic content $V_{I2} = 3.36\ V_{pk}$, 70% of the designed value ($H_2 = 4.8\ V_{pk}$), with low spectral content up to f_{sw}, marked on Fig. 10.

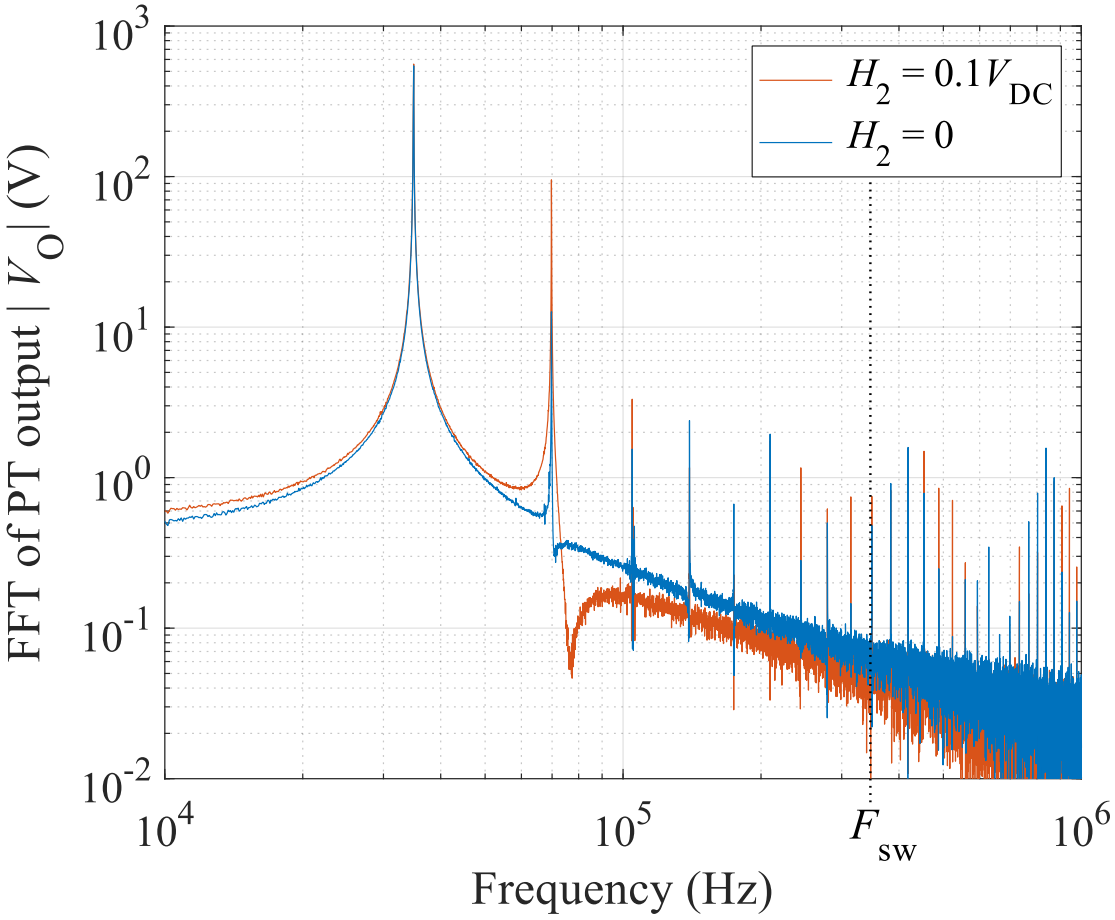

Fig. 6.23 PT output frequency spectra for $H_1 = 0.19V_{DC}$.

Fig. 6.23 shows frequency spectra for the output of the PT (V_O) without discharge. The higher harmonics (frequencies greater than f_{sw}) are significantly attenuated compared to the inverter output spectra in Fig. 6.22.

The frequency spectra of the PT output voltage during reactor operation are shown in Fig. 6.24. The plasma contributes to the second, third and higher-order harmonics. The stochastic nature of the discharge [6.2] also contributes to the higher noise floor when compared to the test without discharge in Fig. 6.23.

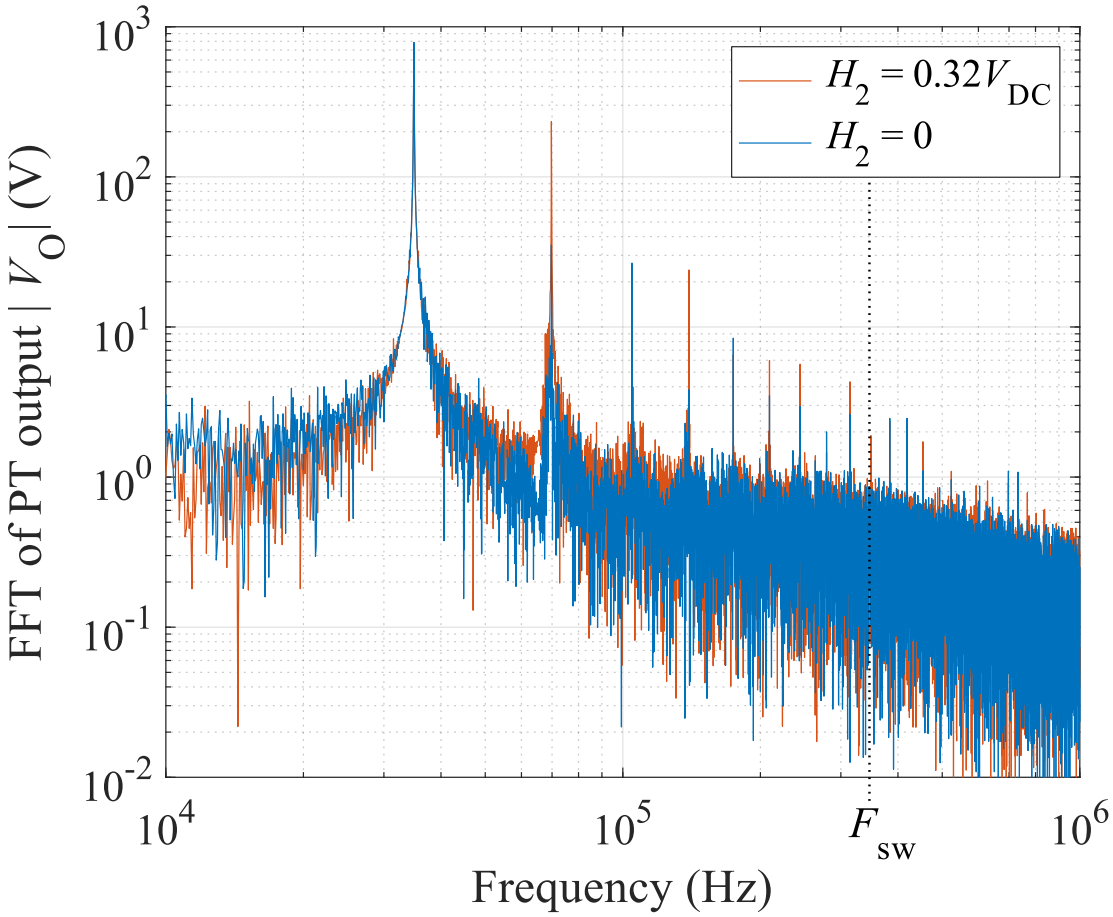

Fig. 6.24 PT output frequency spectra for $H_1 = 0.64V_{DC}$.

Fig. 6.16 to Fig. 6.24 demonstrate the ability of SHG and the PT to provide a controllable waveform for the reactor. What follows is an investigation into the effects of H_1, H_2 and ψ_2 on the power and ozone generation efficacy for specific combinations of these parameters using a hardware-in-the-loop parametric sweep.

6.4.3 Investigation into Reactor Performance

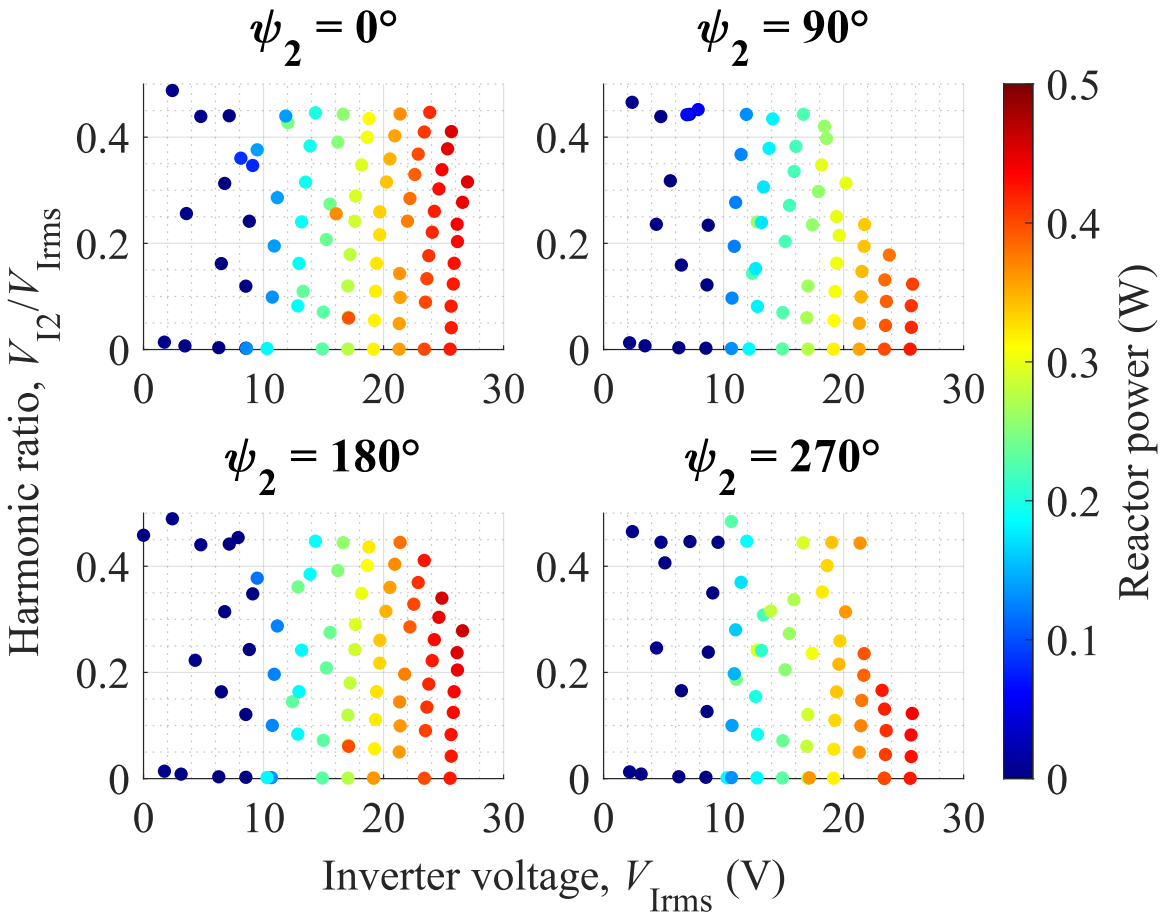

Fig. 6.25 Reactor power vs inverter output voltage and harmonic ratio.

Fig. 6.25 shows the measured reactor power for the parametric sweep tests. The horizontal axis shows RMS voltage at the output of the inverter, V_{Irms} considering only the measured peak values of the first and second harmonics,

$$V_{Irms} = \sqrt{V_{I1}^2 + V_{I2}^2} \tag{6.14}$$

This is equivalent to total harmonic distortion RMS (THD_R) when only first and second harmonics are considered. The vertical axis is the ratio of second harmonic content to the RMS voltage, V_{I2}/V_{Irms}, termed the "harmonic ratio".

Fig. 6.25 shows a positive trend of power with inverter voltage, V_{Irms}, and no discernible trend with the second harmonic ratio.

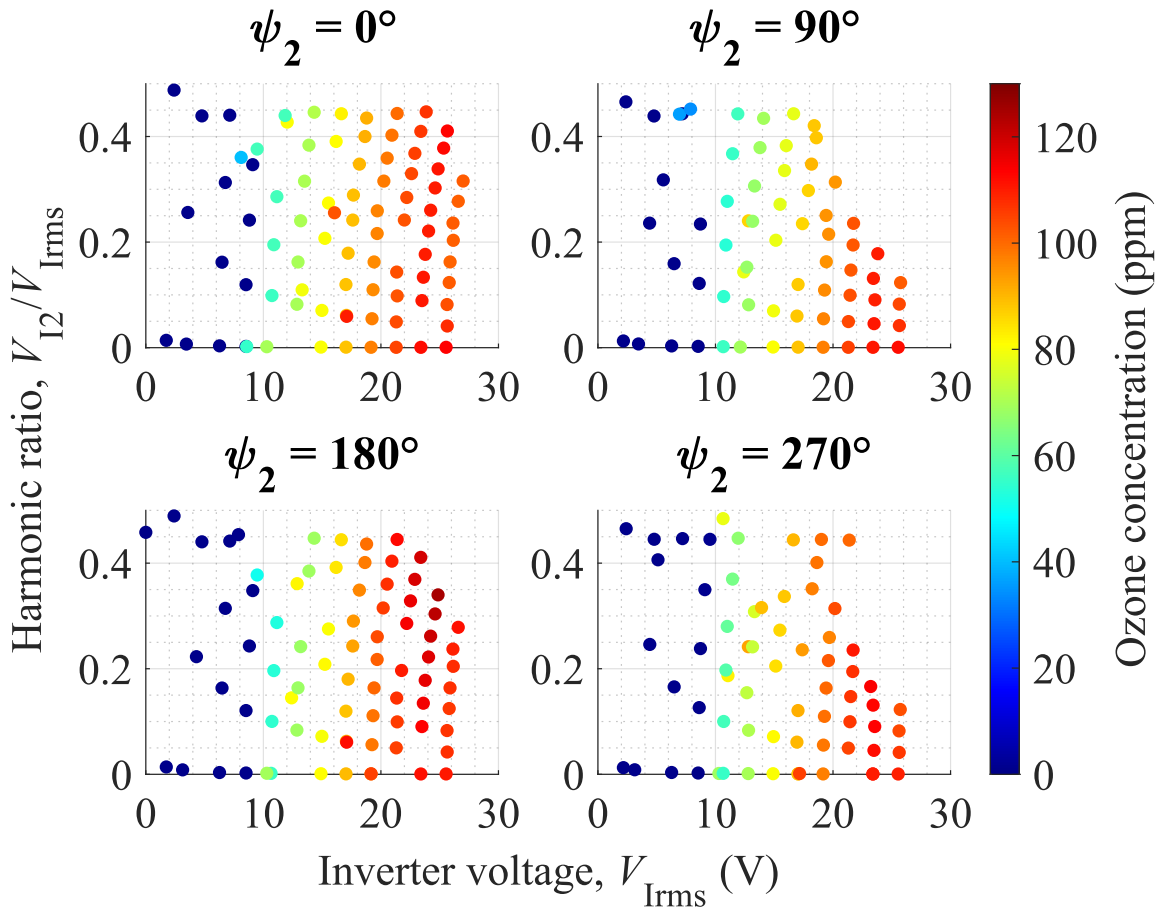

Fig. 6.26 Ozone concentration vs inverter output voltage and harmonic ratio.

Fig. 6.26 shows how the ozone concentration varies over the same tests. A similar trend to Fig. 6.25 is seen, however, at $\psi_2 = 180°$, a slight positive trend of ozone concentration with the harmonic ratio is seen at higher inverter voltages. This indicates the highest efficacy is in the region around $V_{I2}/V_{Irms} = 0.3$ and $V_{Irms} = 25$ V for $\psi_2 = 180°$, shown in Fig. 6.27.

The positive trend in ozone concentration with inverter voltage breaks down at higher voltages. The increased reactor power causes increased ozone destruction, limiting the quantity of ozone which escapes the gas gap. This destruction increases exponentially with absolute temperature [6.1]. In extremis, additional reactor power can reduce ozone concentration.

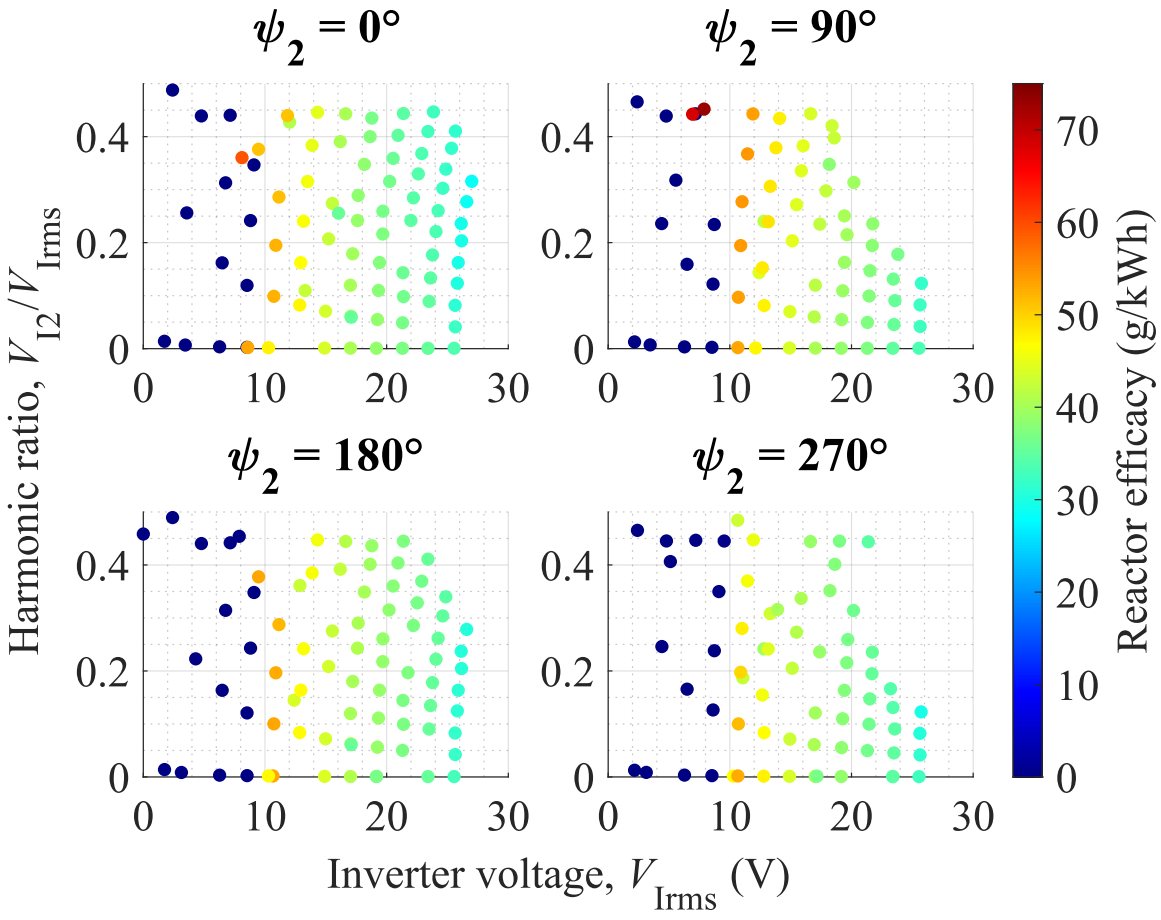

Fig. 6.27 Reactor efficacy (η_r) vs inverter output voltage (V_I) and harmonic ratio.

The reactor efficacy can be seen in Fig. 6.27. The highest efficacy is obtained at the threshold of plasma ignition (around V_{Irms} = 9 V): at lower inverter output voltages, there is no plasma, no ozone and necessarily 0 efficacy. As little as 1 V above this threshold, little plasma is produced, perhaps only one streamer per cycle. The low energy plasma allows the gas temperature to remain near room temperature and minimises the destruction of ozone due to heating, maximising ozone efficacy.

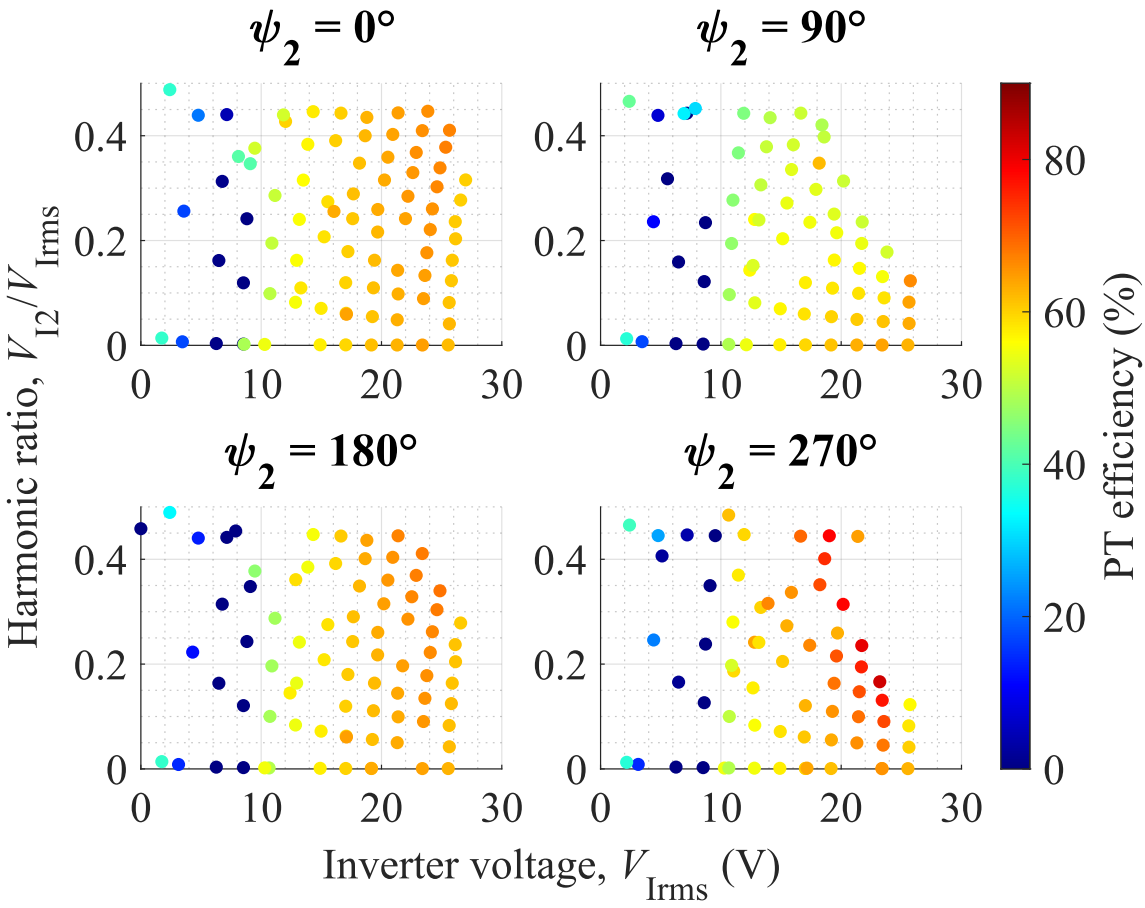

Fig. 6.28 PT efficiency vs inverter output voltage and harmonic ratio.

The efficiency of the PT is shown in Fig. 6.28. The efficiency follows a similar trend to the ozone concentration for ψ_2 = 0 and 180°, suggesting it has no-load losses and losses associated with the output current, in the same way as a conventional transformer [6.3].

At ψ_2 = 90°, however, the efficiency of the PT is much lower than the other second harmonic phase angles tested, and at 270°, the efficiency is higher. Despite this higher efficiency, the system efficacy remains low due to losses in the inverter (Fig. 6.29).

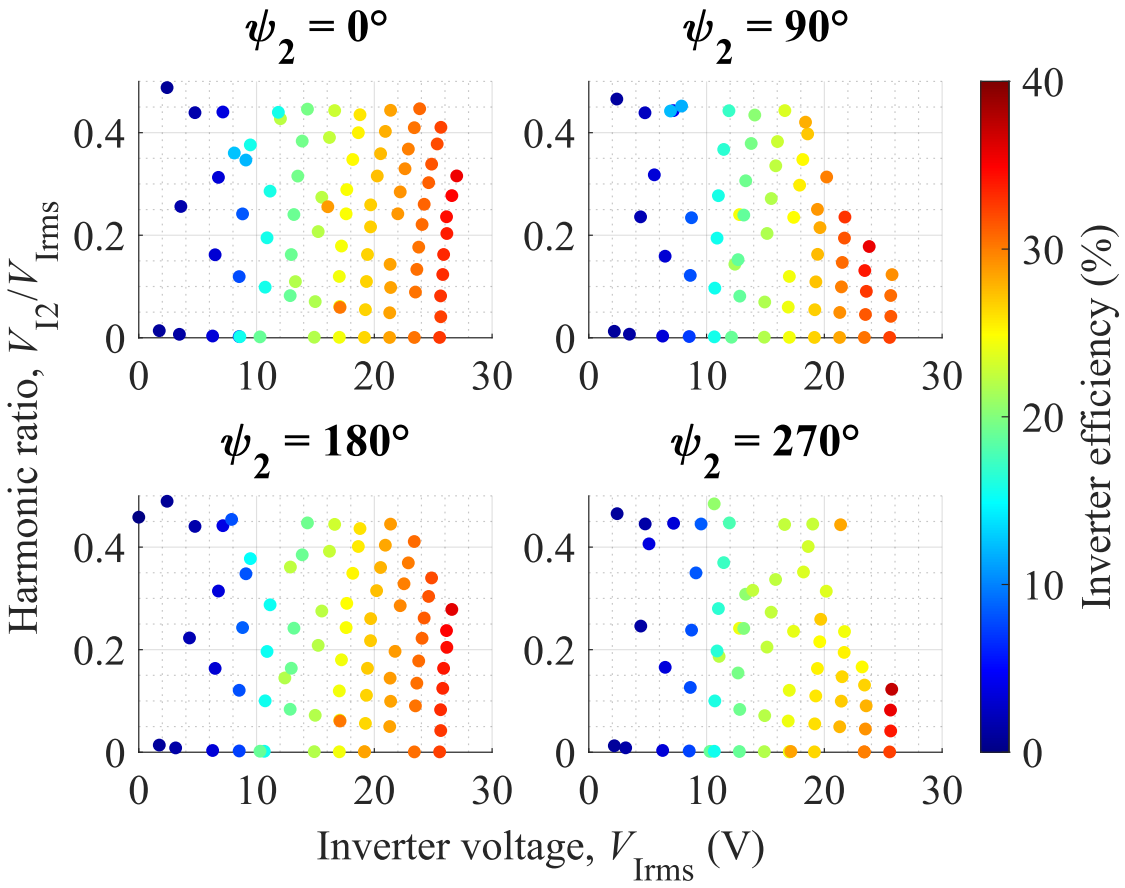

Fig. 6.29 Inverter efficiency vs inverter output voltage and harmonic ratio.

Inverter efficiency includes the power drawn by all the components in the system, including gate drives, the microcontroller used to calculate the switching angles, and the losses of the auxiliary PSU used to provide power for the 12 V and 3.3 V rails. This results in relatively high system power consumption independent of output power and an inverter efficiency that increases with output voltage (and by extension, output power). No attempt has been made to optimise the performance of these elements.

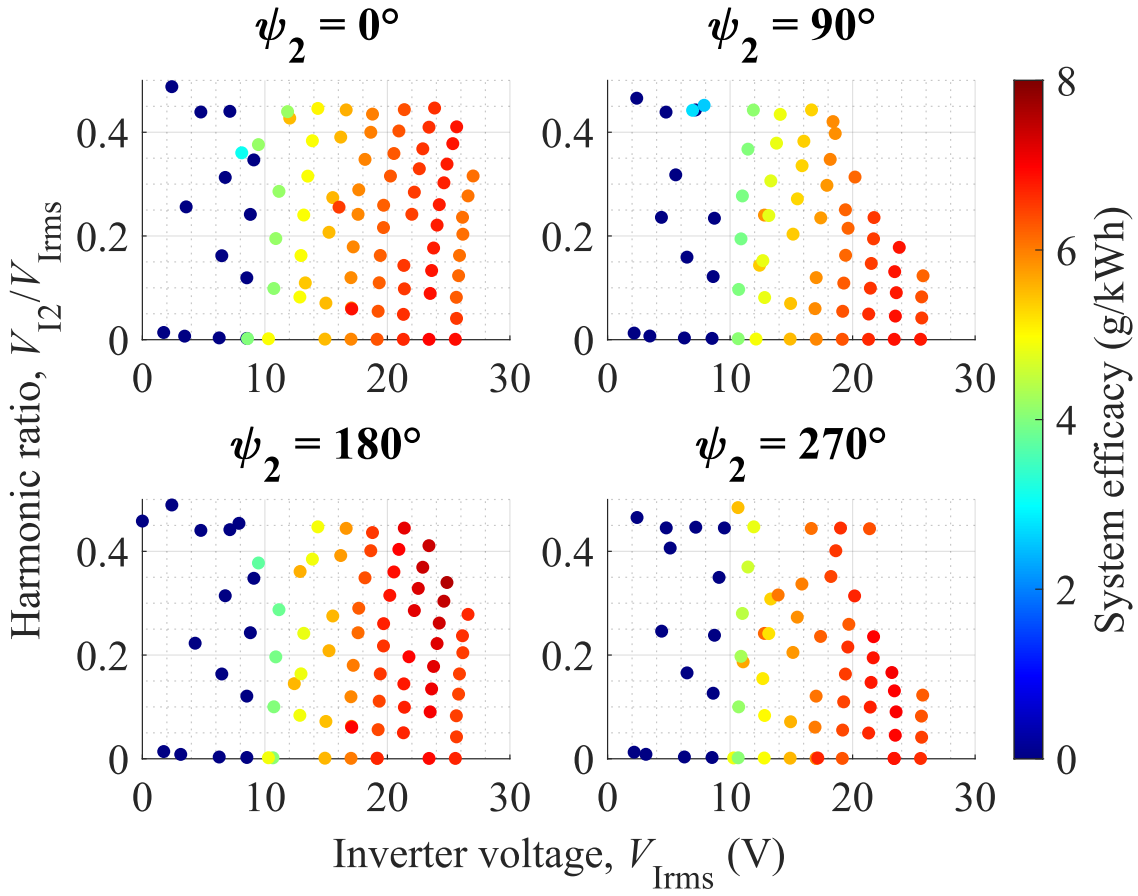

Fig. 6.30 System efficacy (η_s) vs inverter output voltage (V_{Irms}) and harmonic ratio.

Fig. 6.30 shows the overall system efficacy (η_s) across all tests. The highest efficacy is obtained at $V_{I2}/V_{Irms} \approx 0.3$ and $V_{Irms} \approx 25$ V_{rms} for $\psi_2 = 180°$. This corresponds to the region of higher reactor efficacy (η_r) at the higher ozone concentration shown in Fig. 6.26.

The trends in system and reactor efficacy are different, therefore the highest system efficacy is not the same as the highest reactor efficacy. To maximise system efficacy, the electronics and reactor must be designed and tested in tandem.

6.5 Conclusion

In this chapter, a technique has been demonstrated for generating a tailored waveform for plasma generation in dielectric barrier discharge reactors by controlling two sine-wave harmonics and supressing low-order overtones. This technique, SHG, has been demonstrated to produce waveforms with harmonics close to their controlled values when used with a low voltage GaN inverter and a conventional transformer.

A piezoelectric-transformer-based power supply was also used as the supply for a DBD reactor, and its performance was evaluated under a range of operating conditions.

In experiment 1, some additional second harmonic content was shown to increase the efficacy of the reactor from 57 to 78 ppm/W when high ozone concentration (~150 ppm) is required. A peak quantitative efficacy of 12.2 g/kWh was obtained with the reactor in this system.

The system in experiment 2 achieved an efficacy of 7.6 g/kWh with high second harmonic content at a phase angle of 180° with respect to the fundamental, showing that a biharmonic waveform allows for higher performance that a purely sinusoidal one. The lower efficacy of the system in experiment 2 could be due to the different reactor. The thinner dielectric of the coaxial reactor used in experiment 2 compared to the biaxial reactor in experiment 1 could be a source of dielectric loss at high frequencies, and the design of this reactor makes it difficult to ensure perfectly parallel (or concentric) electrode faces.

The larger reactor and power supply used in experiment 1 may be more suitable for bench-top applications, whereas the more compact coaxial reactor and PT used in experiment 2 could make it more suitable for hand-held ozone generation.

The work has potential applications across multiple fields such as machine drives, as well as in a PT-based PSUs for DBD reactors where a PT was demonstrated to operate efficiently at two resonant modes simultaneously.

6.6 References

[6.1] H. Itoh, M. Taguchi, and S. Suzuki, ‘Thermal decomposition of ozone at high temperature leading to ozone zero phenomena’, *J. Phys. Appl. Phys.*, vol. 53, no. 18, p. 185206, 2020, doi: 10.1088/1361-6463/ab71a9.

[6.2] W. H. Tay, S. S. Kausik, C. S. Wong, S. L. Yap, and S. V. Muniandy, ‘Statistical modelling of discharge behavior of atmospheric pressure dielectric barrier discharge’, *Phys. Plasmas*, vol. 21, no. 11, p. 113502, Nov. 2014, doi: 10.1063/1.4901250.

[6.3] Y. H. Su, Y. P. Liu, D. Vasic, F. Costa, W. J. Wu, and C. K. Lee, ‘Study of a piezoelectric transformer-based DC/DC converter with a cooling system and current-doubler rectifier’, *Smart Mater. Struct.*, vol. 22, no. 9, p. 095005, Sep. 2013, doi: 10.1088/0964-1726/22/9/095005.

7 Targeted-Waveform Optimisation for Ozonising Dielectric Barrier Discharge Reactors

7.1 Introduction

This chapter presents a method for maximising the efficacy of ozone production by dielectric barrier discharge (DBD). By developing an optimiser-based hardware-in-the-loop system, the effects of varying input waveform parameters and the flowrate of the input gas on the reactor conditions are explored with greater fidelity than in previous literature.

The waveform used is biharmonic, consisting of the sum of two sinewaves (Fig. 7.1) and allows a greater number of explorable parameters. The performance of the reactor, evaluated using the parametric sweep technique, is compared to that of a hybrid optimiser combining particle swarm optimisation and pattern search.

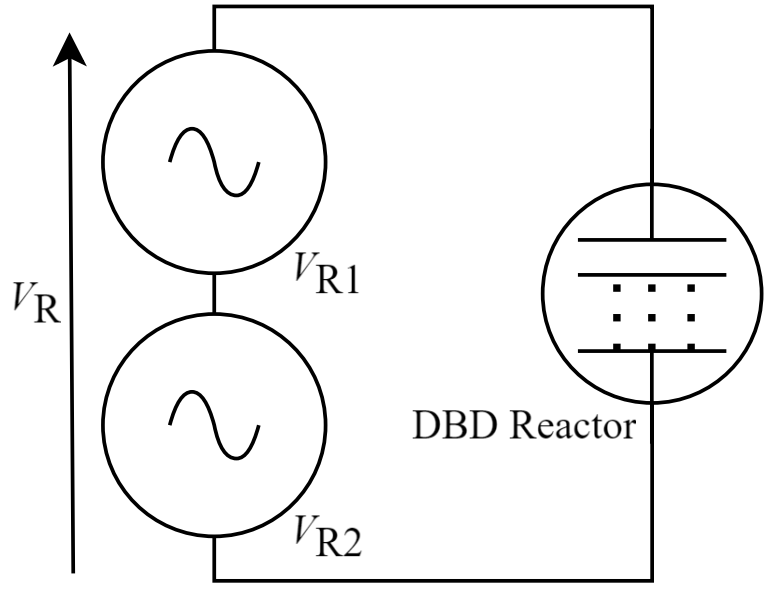

Fig. 7.1 Simplified experimental schematic

Two metrics are targeted: ozone concentration to power ratio (ppm/W) and ozone quantity for a given energy (g/kWh). Thus, the characteristics of the input voltage waveform and flow rate are adjusted to target high ozone generation efficacy for the reactor used in the experiment.

7.2 DBD waveform

The RMS biharmonic waveform for the reactor input voltage (V_{Rrms}) consists of a 1st (fundamental) and 2nd harmonic, termed V_{R1} and V_{R2} respectively. The reactor voltage, V_{Rrms}, is

$$V_{\mathrm{Rrms}} = \sqrt{V_{\mathrm{R1}}^2 + V_{\mathrm{R2}}^2} \tag{7.1}$$

where $V_{\mathrm{R1}}(\mathrm{t}) = \sqrt{2}V_{R1}\sin(2\pi ft)$ and $V_{\mathrm{R2}}(\mathrm{t}) = \sqrt{2}V_{R2}\sin(4\pi ft + \Psi_2)$ (i.e. $V_{\mathrm{R2}}(\mathrm{t})$ is twice the frequency of $V_{\mathrm{R1}}(\mathrm{t})$ and phase-shifted by Ψ_2). The waveform and its three parameters, V_{R1}, V_{R2} and Ψ_2 were chosen to give the waveform a wide range of possible waveshapes, whilst being easy to generate using selective harmonic generation (Chapter 6) or off-the-shelf equipment, as in this chapter. These parameters can be seen in the time domain waveforms shown in Fig. 7.2. The fundamental frequency, *f*, of this waveform is kept constant.

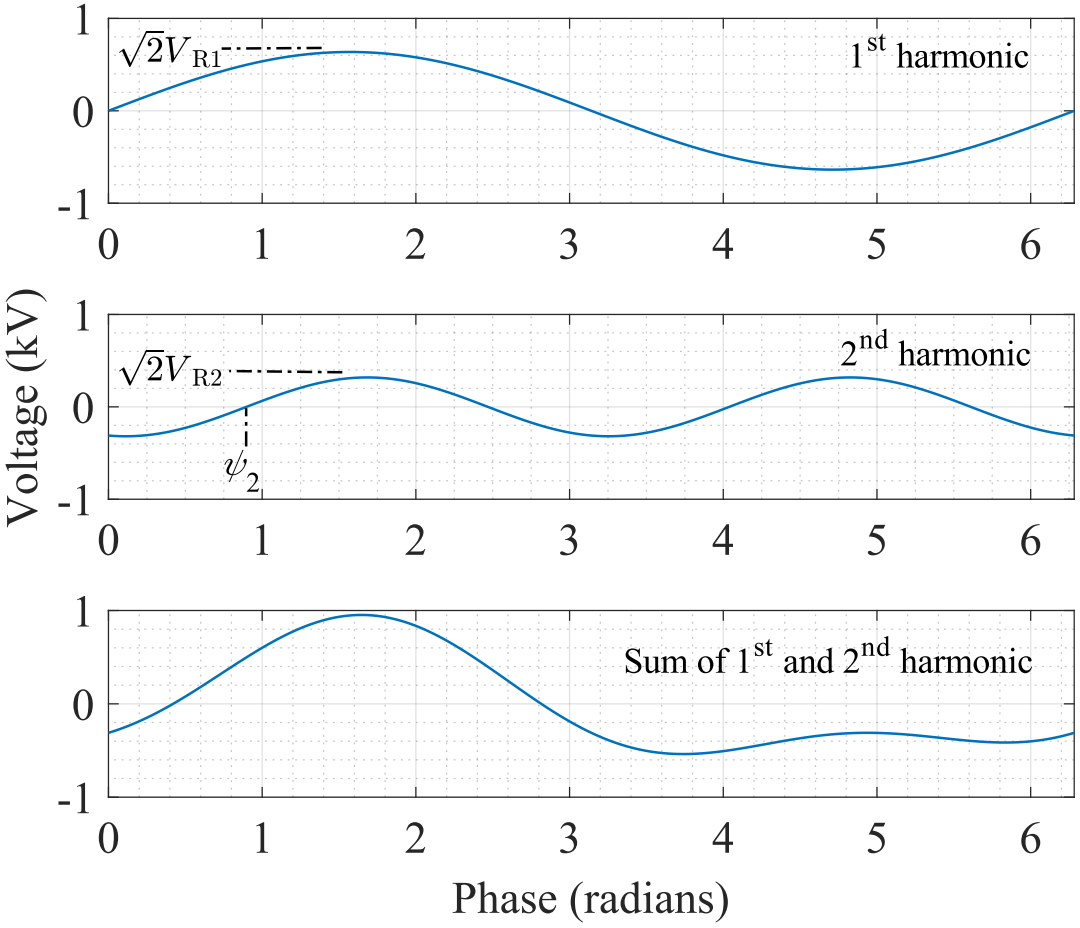

Fig. 7.2 Biharmonic waveform decomposition showing the first and second harmonics and their sum.

7.3 Experimental Setup

To test how the optimisers can be used to adjust the operating conditions of a reactor to improve performance, three experiments were conducted for each of three targeting methods:

Experiment 1 – parametric sweep: variation of four parameters; flowrate (F_A), V_{R1}, V_{R2} and ψ_2, with linearly spaced test points for each parameter, resulting in 256 tests.

Experiment 2 – Optimisation for concentration efficacy: using the Matlab Optimisation Toolbox with a swarm size of 20 particles and a maximum of 6 iterations including the starting point. The optimiser was allowed to vary the 4 parameters to maximise the reactor output concentration efficacy, η_c, in ppm/W. The most optimal solution was then given as the starting point to a PS optimiser which ran for a further 150 tests, for 270 tests in total.

Experiment 3 – Optimisation for ozone quantity: using the same optimiser as experiment 2, but maximising ozone quantity, η_q, in g/kWh, rather than ppm/W.

The fundamental frequency, f, of the waveform was kept constant at 10 kHz for all experiments to limit the number of parameters that are to be tested. The amplitude of each harmonic was limited to approximately 3.2 kV_{RMS}, subject to further limitation by the HV amplifier. Flowrate, F_A, ranged from 0.1-10 ℓpm (litres per minute), and phase was varied through 360°.

For all three experiments, and for each unique set of variables, two sets of data were obtained: A steady-state ozone reading from 5 consecutive measurements averaged over a 10 second period, and an oscillogram of the electrical waveforms.

The Lissajous method [7.1] described in Section 2.3.1 was used to calculate the reactor power due to its superior accuracy compared to methods using direct current measurement [7.2]. The equipment used can be found in Table 7.1 and the experimental set-up used is shown in Fig. 7.3.

Table 7.1 Experiment apparatus

Ozone monitor	2B Technologies 106-MH
Oscilloscope	Picoscope 6404E
High voltage probe	Tektronix P6015A
Waveform generators	RS RSDG830
HV amplifier	Trek 10/410 A-HS
Mass flow controller	Bronkhorst F-201CV-20K-AAD-22-V

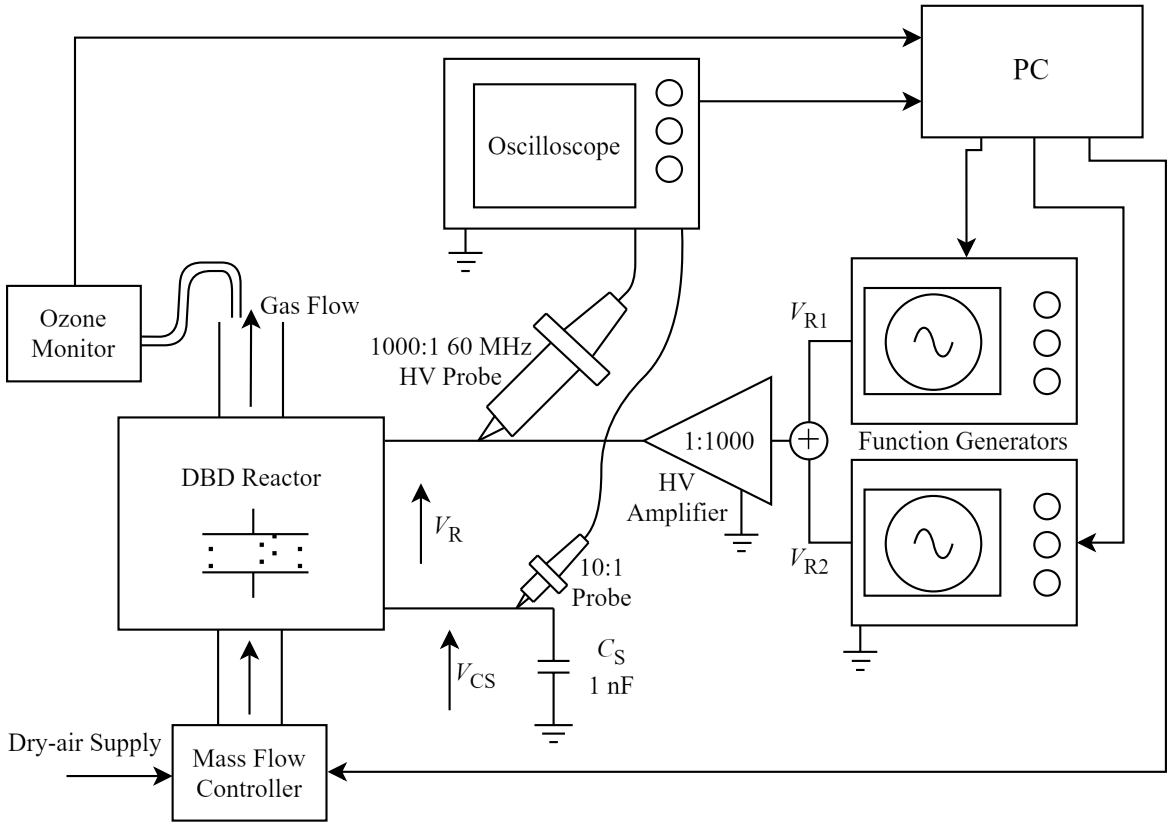

Fig. 7.3 Experimental set-up diagram

The reactor is driven by a HV amplifier, the input signal of which is the sum of waveforms from the two synchronised waveform generators, one operating at the first harmonic (10 kHz) and the other at the second harmonic (20 kHz). The design and operation of the reactor is explained in Section 3.2.2. An oscilloscope is used to monitor and record the voltage on the input of the reactor and the current sense capacitor via an HV probe and 10:1 voltage probe respectively. An ozone monitor records the concentration of ozone in the gas flow on the output of the reactor, whilst a mass flow controller (MFC) controls the dry air input to the

reactor. A PC controls the MFC and the waveform generators, whilst capturing data from the oscilloscope and ozone monitor (Table 1).

A flowchart of the optimisation process can be seen in Fig. 7.4. The first stage, particle swarm optimisation, can be seen on the left of the figure and pattern search is on the right. A description of these optimisation algorithms can be found in Section 2.9.

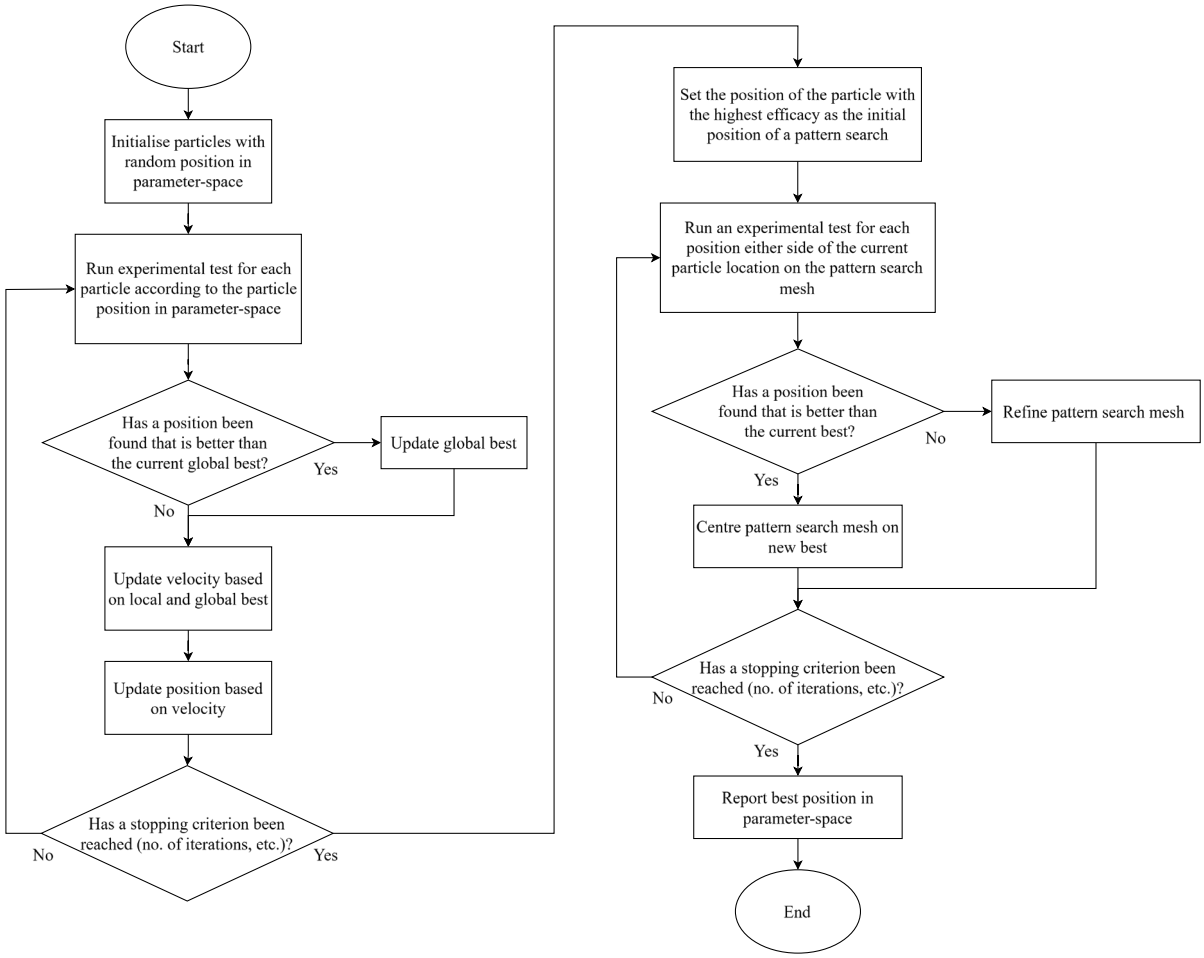

Fig. 7.4 Optimisation process flowchart

7.4 Experimental Results

Fig. 7.5 shows the reactor input power against the four controlled parameters. For Fig. 7.5-Fig. 7.6, the harmonic voltage ratio (V_{R2}/V_R), second harmonic phase (ψ_2) and flowrate (F_A) are the horizontal axes of the three subplots, whilst the reactor voltage (V_{R2}) is the vertical axis. In these figures, the experimental data (dots) for all three experiments are shown on the same plots, giving a total of 796 data points. The data has been binned with the colour indicating the maximum value in a given region. Each test, providing one data point, took approximately 30 s to complete.

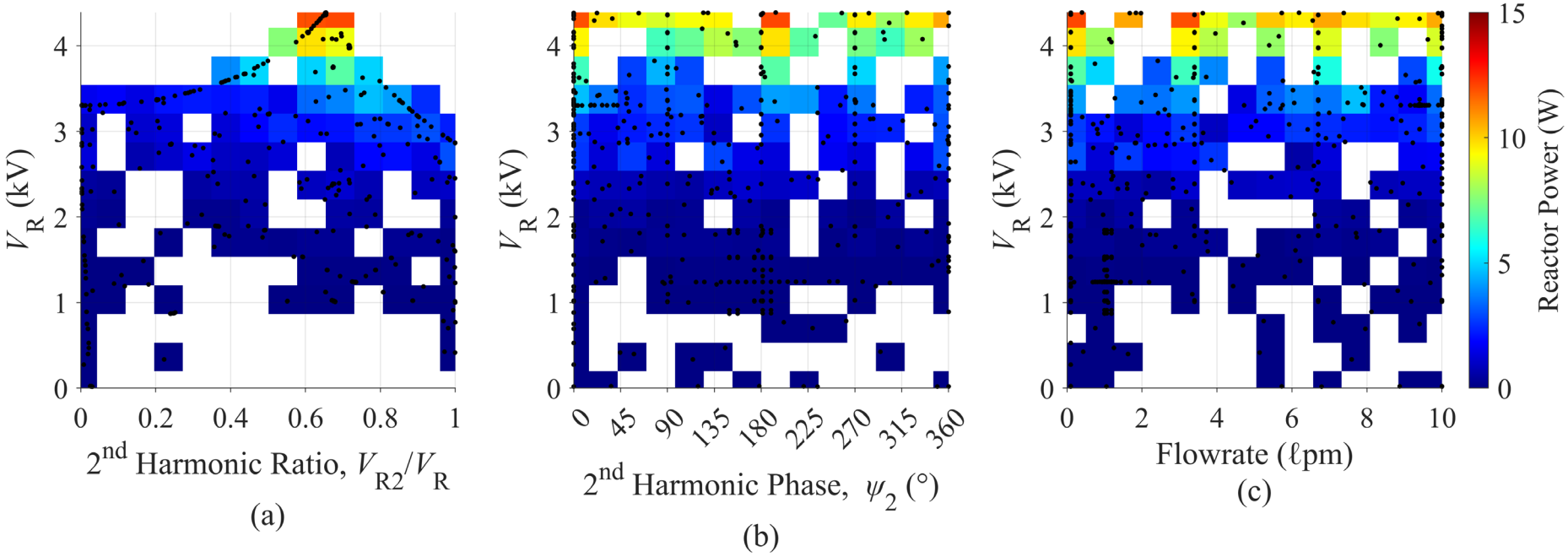

Fig. 7.5 Reactor power with reactor voltage and the three controlled parameters combining the three experiments. Dots represent the experiment datapoints, the colour represents the highest datapoint in each bin.

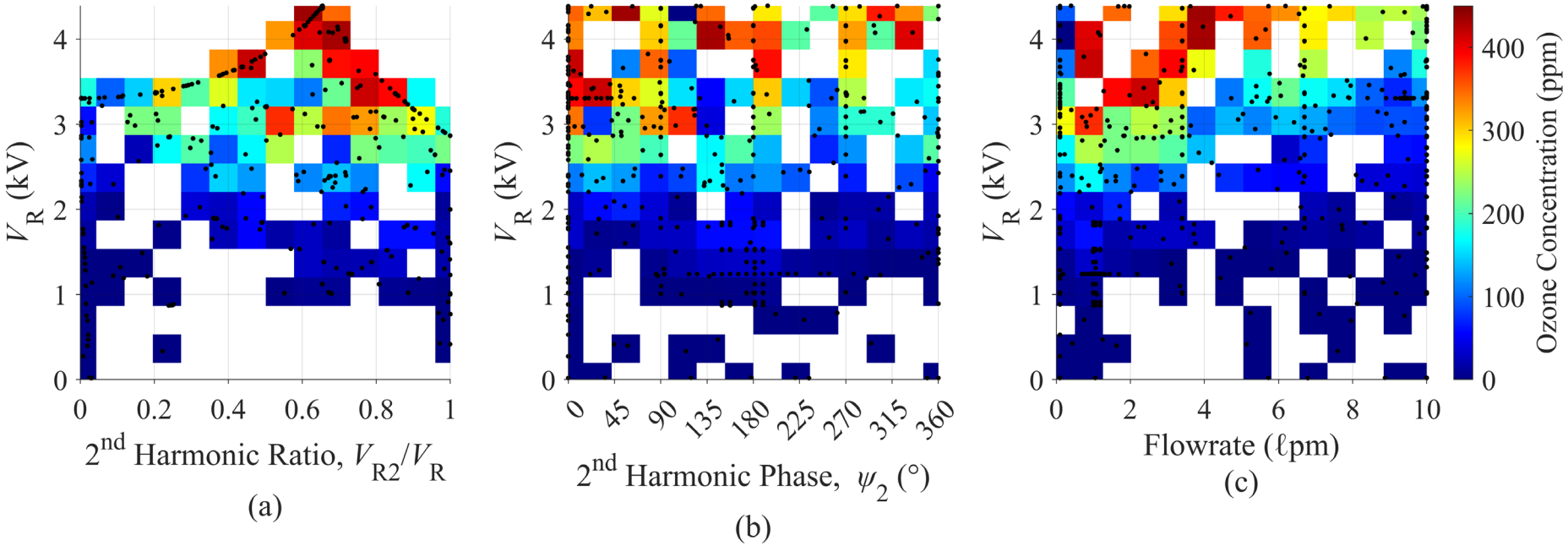

Fig. 7.6 Ozone concentration with reactor voltage and the three controlled parameters combining the three experiments. Dots represent the experiment datapoints, the colour represents the highest datapoint in each bin.

The positive correlation of power and voltage shown in Fig. 7.5a is evident, as expected from [7.3] for waveforms with frequencies in the tens of kHz.

It can also be seen that the 2nd harmonic voltage results in a greater power in the reactor than a 1st harmonic of the same voltage. This is also in accordance with the literature, as power should be approximately proportional to frequency [7.4].

Reactor power vs. ψ_2 and V_{Rrms} plot shown in Fig. 7.5b indicates higher reactor power around $\psi_2 = 0°$ and $\psi_2 = 180°$ compared to $\psi_2 = 90°$ and $\psi_2 = 270°$.

Fig. 7.5c shows the effect of flowrate and reactor voltage on reactor power. A weak negative trend is seen, where flowrate and power have an inverse relationship; with V_{Rrms} approximately constant at 4400 V, the reactor power decreases from 11.9 to 10.5 W when flowrate is increased from 0.1 to 10 ℓpm. This could be due to the increased flow increasing the pressure in the reactor slightly, resulting in an increase in the breakdown voltage of the air feedstock (seen with dry air in [7.5]) and reducing the number of discharges per second.

The effect of the second harmonic, V_{R2}, on the ozone concentration at the output of the reactor can be seen in Fig. 7.6a. This graph shows the same trend as Fig. 7.5a, suggesting that the ozone concentration and reactor power are positively correlated. In this figure, however, there are datapoints that do not fit this trend, the orange square at ($V_{R2}/V_{Rrms} = 0.5$, $V_{Rrms} = 3$ kV) for example, where ozone concentration is higher than might be expected from Fig. 7.5.

These outliers are due to the variations from the other two parameters; Fig. 7.6b shows how the ozone concentration varies with 2nd harmonic phase angle and shows a similar trend to the power in Fig. 7.5b, with more outliers, as the ozone concentration is heavily dependent on the flowrate, as seen in Fig. 7.6c.

The flow of the feedstock helps remove heat from the reactor and, as the decomposition of ozone has a strong positive correlation with temperature [7.6], very low flowrates (<1 ℓpm) cause a sharp decrease in ozone concentration, as seen in Fig. 7.6c. Outside this region, ozone concentration decreases with flowrate as the plasma produces a similar amount of ozone, but it becomes diluted with more air infeed. This relationship is not linear, however, with the ozone concentration only decreasing by approximately a factor of two at 10 ℓpm compared to the concentration at 2 ℓpm. This is perhaps due to the increased cooling reducing the decomposition of ozone [7.6] at higher flowrates.

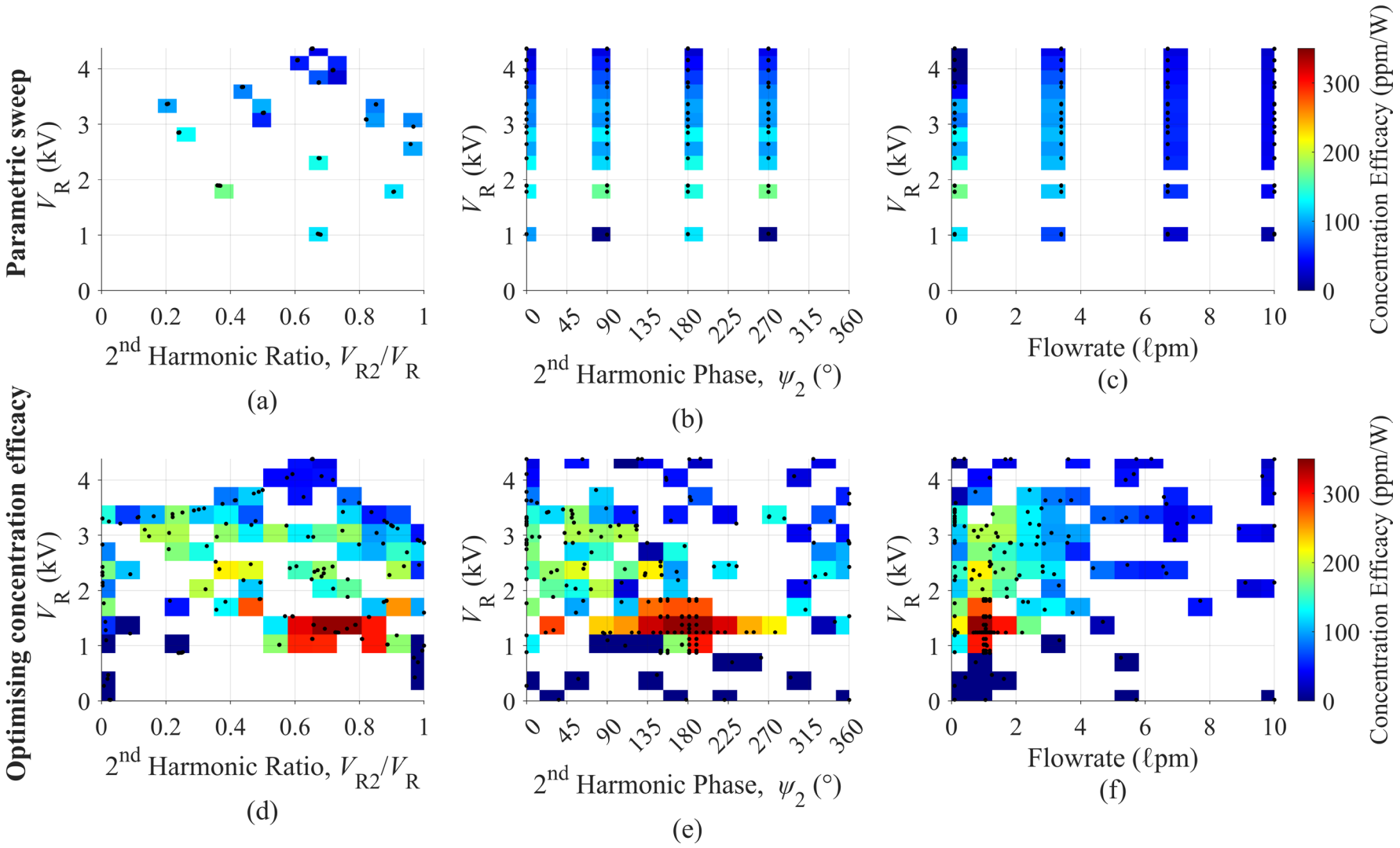

Fig. 7.7 Ozone concentration efficacy, η_c (ppm/W) with reactor voltage and the three controlled parameters the parametric sweep and concentration efficacy optimisation. Dots represent experiment datapoints, the colour represents the highest datapoint in each bin.

Fig. 7.7a and d show how the concentration efficacy varies with the harmonic ratio for each of the three experiments. A comparison of these three sub-plots illustrates the effectiveness of the optimisation algorithm targeting this metric. A cluster of datapoints in the high-efficacy region around (V_{R2}/V_{Rrms} = 0.75, V_{Rrms} = 1.2 kV) in Fig. 7.7d represent the final iterations of the optimisation algorithm, as it converges to the optimal solution.

The voltages chosen by the optimiser result in V_{Rrms} reaching just above the plasma ignition threshold and corresponds to an ozone concentration of 10 ppm.

Fig. 7.7e shows the optimiser targeting concentration efficacy converging on a small region of high efficacy around (ψ_2 = 180°, V_{Rrms} = 1.2 kV).

A region of higher concentration efficacy is also shown in Fig. 7.7f. A flowrate of ~1.2 ℓpm has been identified by the optimisation algorithm as having the highest efficacy, and refinement attempts around this flowrate in the parameter-space show an area of high concentration efficacy between about 0.7 and 1.5 ℓpm.

Taken together, Fig. 7.7d, e and f clearly show how the optimiser explores the search space and converges on the optimum solution, which could be missed with a simple parametric sweep (Fig. 7.7a, b and c). The optimiser found an operating point at (V_{R2}/V_{Rrms} = 0.75, ψ_2 = 180°, F_A = 1.2 ℓpm, V_{Rrms} = 1.2 kV) with a maximum concentration efficacy of 343 ppm/W compared to 170 ppm/W obtained from the parametric sweep.

Fig. 7.8a and d show the effect of the harmonic ratio on quantitative efficacy. Efficacy is zero where the reactor voltage is lower than the ignition threshold (V_{Rrms} < 0.8 kV), as there is no plasma. It can also be seen that there is lower efficacy where V_{Rrms} > 4 kV across the three sub plots. Elsewhere in the plot, the quantitative efficacy is high on average, the parametric sweep in Fig. 7.8a showing consistently high efficacy with a slight trend favouring a low second harmonic ratio. During the quantitative efficacy experiment shown in Fig. 7.8d, the optimiser converged on a point with no second harmonic (V_{R2}) content and the highest achievable voltage for this second harmonic content, V_{Rrms} = 3.3 kV.

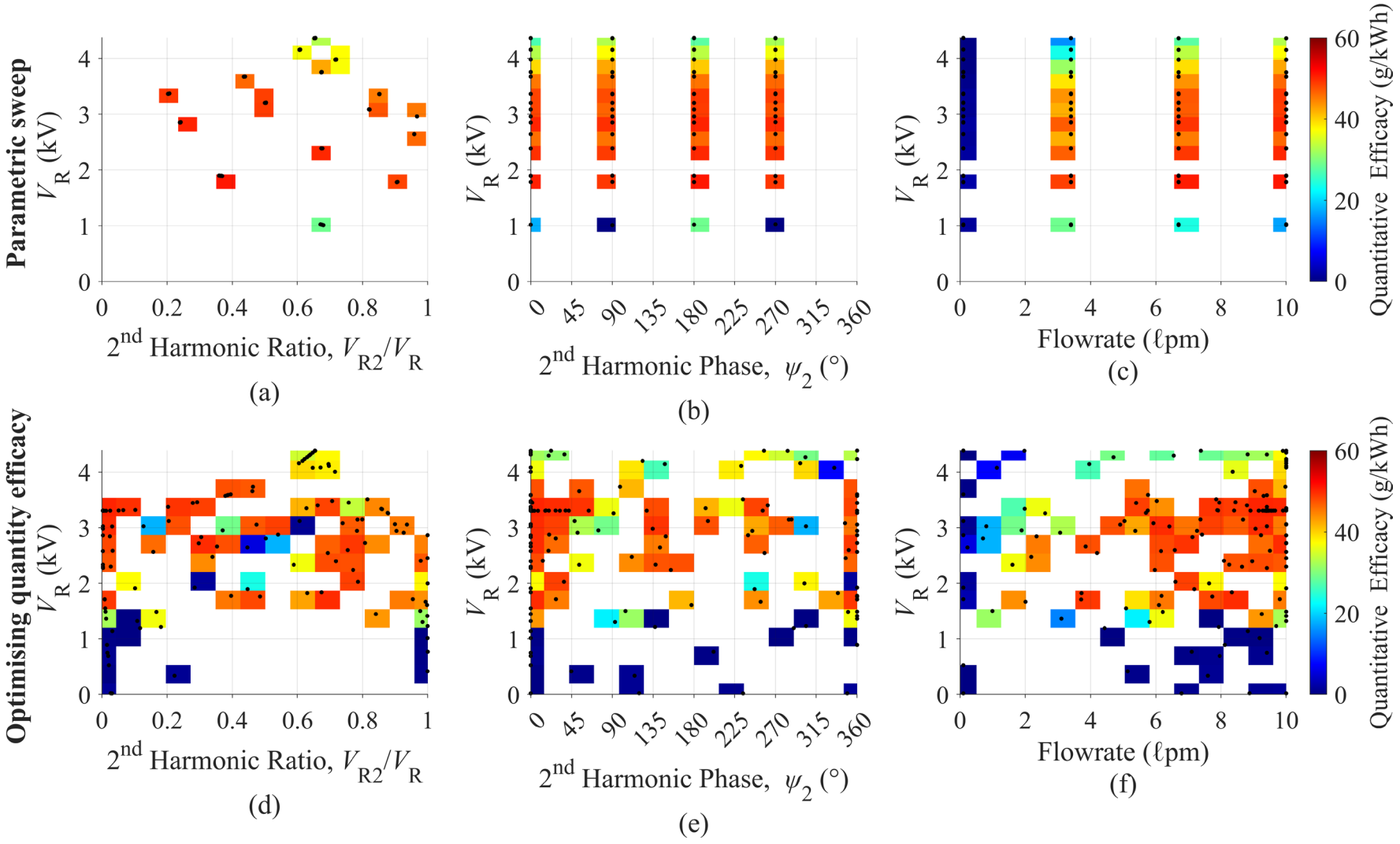

Fig. 7.8 Ozone quantitative efficacy, η_q (g/kWh) with reactor voltage and the three controlled parameters for the parametric sweep and quantity efficacy optimisation. Dots represent experiment datapoints, the colour represents the highest datapoint in each bin.

No clear effect of the second harmonic phase angle, ψ_2 on the quantitative efficacy can be seen in Fig. 7.8b or c. When V_{R2} is close to 0, ψ_2 has little to no effect. However, the optimiser still attempts to optimise its value, resulting in redundant tests where the optimiser walks along the $V_{R2}/V_{Rrms} = 0$ axis.

Fig. 7.8c and f show a positive correlation between quantitative efficacy and flowrate, due to the increased cooling effect of the higher flow preventing ozone decomposition, as already discussed. A cluster of datapoints in Fig. 7.8f can be seen around the optimiser's final position ($V_{R2}/V_{Rrms} = 0$, $\psi_2 = 0°$, $F_A = 9.5$ ℓpm, $V_{Rrms} = 3.3$ kV).

Fig. 7.9 shows how the best (maximum) efficacy found by the hybrid optimiser is improved as the optimiser iterates. The concentration efficacy in the upper plot shows continual, large improvements over time, whereas the quantitative efficacy shows very little improvement after the first few iterations.

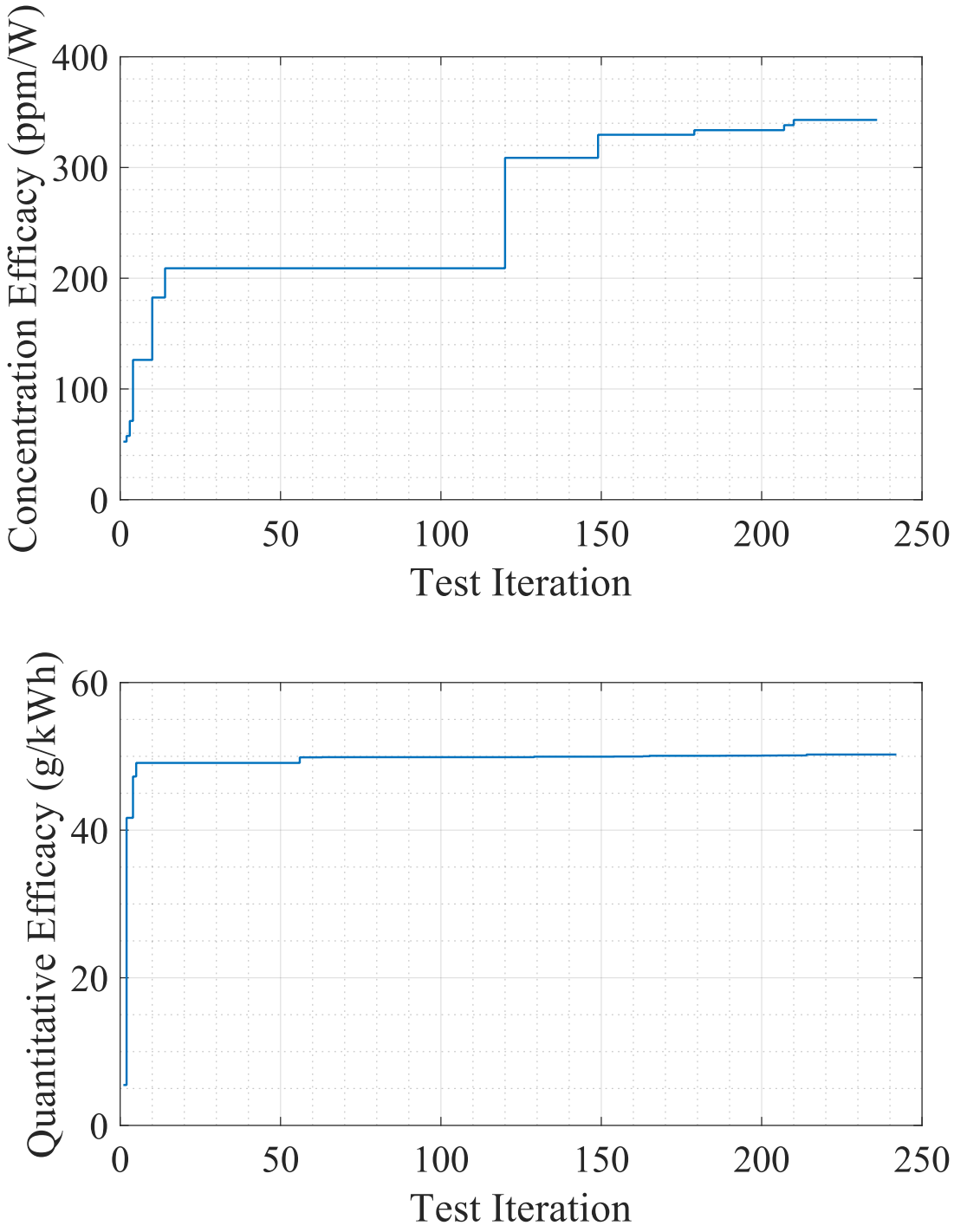

Fig. 7.9 Cumulative best optimiser results for each test iteration, for concentration efficacy (upper) and quantitative efficacy (lower)

Table 7.2 Summary of results

Test	No. of tests per experiment	Maximum concentration efficacy (ppm/W)	Maximum quantitative efficacy (g/kWh)
Parametric sweep	256	169.9	50.87
Concentration efficacy optimisation	270	343.0	52.54
Quantitative efficacy optimisation	270	246.8	50.24

Table 7.2 shows a summary of results. All three experiments have a similar number of tests, and therefore took a similar amount of time, approximately a minute per datapoint, totalling approximately 4.5 hours per experiment.

Due to the number of parameters to cover, only 4 data points on each parameter could be covered with a reasonable number of tests: $4^4 = 256$ tests. This has limited the area that could be covered by the parametric sweep.

Each of the three experiments had a similar maximum quantitative efficacy, with the optimisation intended to target this metric finding the lowest, at 50.2 g/kWh. This may be due to the large number of datapoints already close to the optimum resulting in a lack of a clear relationship between many of the parameters and the target metric, suggesting for that these parameters may have little dependence on this target metric (quantitative efficacy) for the reactor and the reaction conditions used in these experiments.

7.5 Conclusion

A hardware-in-the-loop (HIL) optimisation approach to targeted waveform ozone generation has been presented in this chapter. The technique optimised the amplitude and phase difference of a biharmonic waveform at a fixed frequency. This was compared to a parametric sweep of equivalent complexity and shows an improvement in the identified optimum operating conditions.

The biharmonic waveform was composed of fundamental and second harmonic voltages, allowing independent variation of the amplitudes of these harmonic components and the phase angle of the second harmonic to tailor reactor conditions. In both experiments the optimiser was allowed to vary flow rates between 0.1 to 10 litres per minute and manipulate three waveform parameters including the first and second harmonic voltage and phase angle of the second harmonic. Ozone concentration (ppm) and reactor power (W) were recorded and used as feedback for the HIL system.

Reactor performance was explored using a parametric sweep technique and a hybrid optimiser targeting ozone concentration efficacy per watt (ppm/W) in one experiment, and optimising for maximum g/kWh, the mass of ozone produced per kWh of energy consumed in a second experiment. The quantitative efficacy optimisation performed poorly. Many positions in parameter-space had similarly high-efficacy and it seems this led to the optimiser being unable to find a clear maximum.

For the concentration efficacy tests, however, the hybrid optimiser technique resulted in a clearly defined set of parameters that obtain an efficacy of 343 ppm/W compared to 170 ppm/W in the parametric sweep, demonstrating the promise of this hardware-in-the-loop approach for optimising chemical production by dielectric barrier discharge reactors.

7.6 References

[7.1] F. Peeters and T. Butterworth, 'Electrical Diagnostics of Dielectric Barrier Discharges', in *Atmospheric Pressure Plasma - From Diagnostics to Applications. IntechOpen*, 2018. doi: 10.5772/intechopen.80433.

[7.2] T. Homola, V. Prukner, P. Hoffer, and M. Šimek, 'Multi-hollow surface dielectric barrier discharge: an ozone generator with flexible performance and supreme efficiency', *Plasma Sources Sci. Technol.*, vol. 29, no. 9, p. 95014, 2020, doi: 10.1088/1361-6595/aba987.

[7.3] M. Ponce, J. Aguilar, J. Fernandez, E. Beutelspacher, J. M. Calderon, and C. Cortes, 'Linear and non linear models for ozone generators considering electrodes losses', in *2004 IEEE 35th Annual Power Electronics Specialists Conference*, Piscataway NJ: IEEE, 2004, pp. 810-814 Vol.1. doi: 10.1109/PESC.2004.1355853.

[7.4] U. Kogelschatz, 'Dielectric-barrier Discharges: Their History, Discharge Physics, and Industrial Applications', *Plasma Chem. Plasma Process.*, vol. 23, no. 1, pp. 1–46, 2003.

[7.5] Z. Fan, H. Yan, Y. Wang, Y. Liu, H. Guo, and C. Ren, 'Breakdown characteristics of atmospheric dielectric barrier discharge in gas flow condition', *Phys. Plasmas*, vol. 25, no. 5, p. 053517, May 2018, doi: 10.1063/1.5018331.

[7.6] H. Itoh, M. Taguchi, and S. Suzuki, 'Thermal decomposition of ozone at high temperature leading to ozone zero phenomena', *J. Phys. Appl. Phys.*, vol. 53, no. 18, p. 185206, 2020, doi: 10.1088/1361-6463/ab71a9.

8 Conclusion and Future Work

The work in this thesis contributes to the development of efficient power supplies and optimisation techniques for high-efficacy DBD ozonisers, focusing on controllable waveform generation. The research has introduced improved parameterisation methods for piezoelectric transformers and resonators, a novel piezoelectric resonator-based power supply design for operation with low input voltage, selective harmonic generation (SHG) technique to precisely control the frequency spectrum of reactor input waveforms, and global optimisers using hardware in the loop tuning biharmonic input waveform parameters.

The first major contribution of this thesis is the development of improved parameterisation techniques for piezoelectric devices, allowing them to be used to design novel DBD reactor power supplies. The work presented in Chapter 4 demonstrates an improved curve fitting method, increasing the accuracy of piezoelectric device parameterisation and extending the parameterisation to multiple resonant modes. The use of particle swarm optimisation (PSO) was also shown to provide greater accuracy than previously published techniques.

The second major contribution is the design and development of a novel piezoelectric-resonator-based DBD reactor power supply for operation with low input voltage. A dielectric barrier discharge reactor was parameterised to determine its equivalent linear-model component values, which were used in conjunction with parameters from three different piezoelectric resonators to optimise the design for maximum efficiency. The largest resonator with the highest Q-factor and lowest impedance at resonance exhibited the highest maximum power and highest theoretical efficiency.

The power supply was tested in conjunction with the DBD reactor to determine both the performance of the power supply and the efficacy of the reactor with this high-frequency sinusoidal waveform. The results of these tests show that the power supply achieves a 63% efficiency when considering both the piezoelectric resonator and the inverter, whilst the reactor achieved an efficacy of 105 g/kWh at the highest flow rate and lowest power levels. This power supply could be employed in small hand-held devices for DBD reactors producing ozone or excited argon for medical applications, for example.

The third major contribution is the development of the technique called selective harmonic generation to create a periodic pulse-train containing precisely controllable harmonics up to and including the switching frequency. In this work, this technique was used for the

optimisation of reactor performance by controlling the frequency spectrum of the input waveform.

A computer-controlled GaN inverter was used to produce pulse-trains with the desired harmonic content using SHG. The output of this inverter was then used to drive both a piezoelectric transformer and a conventional transformer with high efficiency. The experimental tests show that SHG with a low-voltage GaN inverter can produce waveforms with harmonics close to the desired values. The outputs of the voltage magnification devices were coupled to DBD reactors and were shown to provide a higher reactor efficacy than a waveform with only a fundamental frequency. This technique could be used in large reactors for wastewater treatment, where it has the potential to significantly improve efficiency.

The fourth major contribution is the development of a hardware-in-the-loop hybrid global optimiser approach, integrating particle swarm optimisation and pattern search for improved parameter selection over a simple parametric sweep. This approach is used to optimise the biharmonic-waveform harmonic amplitudes as well as the phase difference of the second harmonic and the flowrate of the air feedstock to tailor reactor conditions.

The results of this research demonstrate that using a biharmonic waveform improves ozone generation concentration efficacy compared to a purely sinusoidal one. The hybrid optimiser approach is shown to be effective in finding optimal operating conditions when there is an optimum point to be found, with a significant improvement in identified optimum operating conditions compared to a parametric sweep with an equivalent number of experimental measurements. This optimiser-based technique can also be used with large reactors, and coupled with SHG or otherwise, could further improve the efficacy of the reactor and power supply as a system.

This work has made significant contribution to the development of efficient power supplies for high-efficacy DBD ozonisers. The research has demonstrated the potential of using piezoelectric devices, selective harmonic generation, and hybrid optimisation approaches to improve ozone production efficacy. These findings have implications for reducing energy consumption costs associated with both small and large-scale DBD reactor operation and can be applied to various fields such as water treatment, surface disinfection, healthcare, and environmental remediation. The developed technologies offer opportunities for more energy-efficient operation and reduced operational costs in various industrial processes involving DBD reactors.

8.1 Future work

This work also provides interesting opportunities for further research:

The accurate modelling of multiple resonant modes in piezoelectric devices, coupled with the successful driving of PTs at multiple resonant modes in Chapter 6 suggest that perhaps other PT-based power supply topologies may benefit from the deliberate injection of harmonics to the input waveform.

It could also be beneficial to investigate the use of SHG techniques in other fields where precise control over the frequency spectrum is required. For example, the injection of phase-shifted third harmonics could help reduce third-harmonic distortion from an H-bridge or 3-phase full-bridge. Electrical machines such as switched-reluctance machines might also be able to benefit from a non-sinusoidal waveform generated with SHG.

Other future research could include the design and optimisation of a reactor and power supply as a system, with a focus on increasing efficiency. Often research concentrates on optimising one part of a system, however the work in Chapter 6 shows that with some types of power supply and reactor, the system's most efficient operating point is not necessarily the same as the most efficient operating point when only considering the reactor, for example.

More directly inspired research could include exploring the use of different waveforms in optimising DBD reactor efficacy or metrics in other DBD-related applications like the intensity of DBD lamps or DBD-pumped lasers. The resonator-based power supply in Chapter 5 could be made to operate with no additional capacitor if the reactor is designed to provide the required capacitance on its own.